

Modeling of Inductive Contactless Energy Transfer Systems

THÈSE N° 5486 (2012)

PRÉSENTÉE LE 25 SEPTEMBRE 2012

À LA FACULTÉ DES SCIENCES ET TECHNIQUES DE L'INGÉNIEUR

LABORATOIRE D'ACTIONNEURS INTÉGRÉS

PROGRAMME DOCTORAL EN SYSTÈMES DE PRODUCTION ET ROBOTIQUE

ÉCOLE POLYTECHNIQUE FÉDÉRALE DE LAUSANNE

POUR L'OBTENTION DU GRADE DE DOCTEUR ÈS SCIENCES

PAR

Pascal MEYER

acceptée sur proposition du jury:

Prof. J. Jacot, président du jury
Prof. Y. Perriard, directeur de thèse
Dr B. Dehez, rapporteur
Prof. P.-A. Farine, rapporteur
Dr D. Ladas, rapporteur



ÉCOLE POLYTECHNIQUE
FÉDÉRALE DE LAUSANNE

Suisse
2012

Un Tiens vaut, ce dit-on, mieux que deux Tu l'auras ;
L'un est sûr, l'autre ne l'est pas.
— Jean de La Fontaine

Whatever you can do or dream you can, begin it.
Boldness has genius, power and magic in it.
— William Hutchison Murray

Remerciements

Tout d'abord, je tiens à remercier Yves qui m'a donné l'opportunité de faire ce travail de recherche au LAI avec une grande liberté et autonomie. Il a réussi à instaurer dans ce laboratoire une atmosphère à la fois stimulante d'un point de vue intellectuel et ouverte à un esprit de franche camaraderie, offrant un cadre de travail absolument exceptionnel.

Bien sûr, toute l'équipe du LAI y contribue largement. En particulier, un grand merci à Paolo pour sa sagacité, sa disponibilité, et surtout sa science qu'il prodigue avec allégresse. En travaillant avec lui, j'ai appris qu'il n'y a pas de problème insoluble lorsqu'il s'agit de bricoler, réparer, souder, tourner, fraiser, prototyper,...

Je tiens aussi à remercier Mika, un peu agressif lorsqu'il brandit son stylo rouge, mais toujours (ou presque) juste lorsqu'il s'attelle à améliorer une publication ou à solutionner des problèmes scientifiques. Une pensée aussi pour Christian, avec qui j'ai toujours eu plaisir à converser de sujets techniques ou actuels et qui n'aura eu de cesse de m'étonner par sa culture et son savoir.

Je remercie également les doctorants et collègues qui ont tous, à leur manière, un petit grain de folie susceptible d'égayer une pause, une sortie ou un repas. Je pense aux anciens espagnols (José et Pinot), à toute la clique tessinoise (Sebi, Ale, Omar), à Markus, Joël, Chris, Tophe, Romain, Shi Dan et Xinchang. Enfin, à Greg, avec qui j'ai partagé les études, les voyages, le vin, le bureau, l'appartement, une pimpante CBR rouge et d'épiques combats de boxe...

Je tiens spécialement à remercier mes parents, Jojo et Gérard, qui m'ont toujours encouragé et soutenu durant mes études et ce travail de thèse. Un merci aussi à mes frères et ma sœur, Fred, Sandra et RV, avec qui je partage le même goût des bonnes choses que la vie peut offrir et cet insatiable désir de profiter de l'instant présent. Enfin, une mention toute spéciale pour Sindy, qui a eu la patience et la gentillesse de me supporter durant ma phase de rédaction, et qui fait de chaque jour passé à ses côtés un mixte d'émerveillement et d'aventure.

Neuchâtel, 29 Août 2012

P. M.

Abstract

In the domain of electronic devices and especially desktop peripherals, there is an industrial trend which consists in removing the cables that pollute our domestic and professional environments. In this sense, wireless communication protocols are already massively widespread while the power supplies still use wires or batteries. To address this problem, alternative solutions must be investigated such as contactless energy transfer (CET).

In a broad sense, CET is a process that allows to bring electrical energy from one point to another through a given medium (generally air or vacuum) and at a certain distance. Inductive CET means that the intermediate form of energy is the magnetic induction, generated from primary coils excited by high-frequency alternating currents and collected in secondary coils by induced voltages. Most of existing approaches to design CET systems are applicable to only single applications and do not include an optimization method. For this reason, the present thesis focuses on the modeling, design and optimization of inductive CET systems.

Using the coreless transformer as the central part of CET systems, an equivalent electric model is derived from the theory of conventional transformers. The absence of ferrite core gives rise to a specific characteristic, which is to have large leakage inductances compared to the main one. In order to circumvent this issue, using a high frequency together with a resonant circuit allow to enhance the effect of the mutual inductance and to transfer power with an excellent efficiency. Different parts of the coreless transformer are addressed separately.

First, an accurate modeling of DC resistances, self and mutual inductances is proposed. Then, the equivalent electric circuit is resolved and the different compensation topologies for the resonant circuit are discussed. Finally, the AC resistance is computed using a 2D finite element modeling that takes into account the skin and proximity effects in the conductors. So as to exploit optimally FEM simulations, a complete output mapping together with a specific interpolation strategy are implemented, giving access to the AC resistance evaluation in a very short time. As a result, all the models are implemented in a way that makes them highly

adaptable and low-consuming in term of computing resources.

Then a sensitivity analysis is performed in order to restrict the variation range of different parameters and to provide a general and intuitive understanding of inductive CET. After that, an optimization method using genetic algorithms (GAs) is presented. The main advantage of GAs is that the number of free parameters does not change the complexity of the algorithm. They are very efficient when a lot of free parameters are involved and for optimizations where the computing time is a key factor. As existing GAs failed to converge properly for different tested CET problems, a new one is developed, that allows to optimize two objective functions in the same time. It is thus a multiobjective genetic algorithm (MOGA) and has been successfully applied to the design of different CET systems.

Finally, in order to validate the models and optimization methods proposed along the thesis, several prototypes are built, measured and tested. Notably, a CET table that allows to supply simultaneously different peripherals is fabricated. By analyzing in real time the current amplitude in the primary coils, an efficient sensorless detection of the peripherals is implemented. Digital control techniques have enabled the autonomous management of the detection and the local activation of the table. These results contribute to the future development of robust and efficient CET tables.

Keywords: Contactless energy transfer, coreless transformer, high-frequency effects, skin and proximity effects, 2D finite element modeling, genetic algorithms, optimization, coils arrays, sensorless detection.

Résumé

Le monde des appareils électroniques et en particulier des périphériques d'ordinateur est gouverné par une tendance industrielle aspirant à éliminer les câbles qui infestent aussi bien les milieux domestiques que professionnels. Dans cette optique, les protocoles de communications sans fil sont déjà profondément implantés tandis que l'alimentation électrique a encore recours aux câbles et aux batteries. Des recherches de solutions alternatives doivent donc être entreprises, à l'instar de la transmission d'énergie sans contact (TESC).

Au sens large, la TESC est un procédé qui consiste à transporter de l'énergie d'un circuit électrique à un autre, à travers une certaine distance et dans un milieu tel que l'air ou le vide. La TESC par induction indique que la forme intermédiaire de l'énergie est celle d'un champ magnétique. Elle est issue de bobines primaires parcourues par un courant alternatif à haute fréquence et récoltée dans des bobines secondaires sous forme de tensions induites. La plupart des méthodes existantes pour le dimensionnement de tels systèmes sont uniquement applicables à des systèmes isolés et n'incluent pas de procédé d'optimisation. Pour cette raison, la présente thèse se consacre à la modélisation, le dimensionnement et l'optimisation de systèmes de TESC par induction.

Plaçant le transformateur sans fer au cœur de la méthode de conception, un modèle électrique équivalent est créé en se fondant sur la théorie des transformateurs conventionnels. L'absence de fer leur confère une propriété particulière qui consiste à avoir de grandes inductances de fuite et par conséquent une inductance principale relativement faible. Ce problème est contourné en augmentant la fréquence de fonctionnement et en intégrant des circuits résonnants. De cette manière, l'effet de l'inductance mutuelle est amplifié et le transfert d'énergie peut être exécuté à des rendements excellents. Les différentes parties du transformateur sans fer sont étudiées séparément.

Une première partie se consacre à la modélisation précise des résistances à basse fréquence (DC), des inductances propres et des inductances mutuelles. Ensuite, le circuit équivalent des transformateurs sans fer est résolu en tenant compte des différentes topologies existantes

pour les circuits résonants. Finalement, les résistances à haute fréquence (AC) sont calculées en utilisant la modélisation par éléments finis (MEF 2D) capable de prendre en charge les effets de peau et de proximité dans les conducteurs. Afin d'exploiter de manière optimale les simulations de la MEF, une stratégie de balayage complet de l'espace de recherche ainsi qu'une technique d'interpolation spécifique ont été mises au point, permettant l'évaluation de la résistance AC en un temps extrêmement court. Ainsi, les différents modèles sont implémentés d'une manière telle qu'ils sont très flexibles et peu coûteux en temps de calcul.

Ensuite, une analyse de sensibilité des paramètres est effectuée afin de réduire au maximum leur plage de variation et également afin d'insuffler au lecteur une compréhension globale et intuitive de la TESC. Une méthode d'optimisation utilisant les algorithmes génétiques (AGs) est présentée. Le principal atout des AGs, comparativement à d'autres algorithmes existants, réside dans le fait que le nombre de paramètres libres n'influe pas sur leur complexité. Ils sont en outre très efficaces lorsque le nombre de paramètres libres est important et que le temps de calcul est un point critique. Dans la mesure où la convergence d'AGs préalablement développés n'a pas abouti à des résultats satisfaisants lorsqu'ils ont été appliqués à des problèmes de TESC, un nouveau AG a été développé. Ce dernier est capable d'optimiser deux objectifs en même temps, et à ce titre, est appelé algorithme génétique multi-objectif (AGMO). Il a été appliqué avec succès à la conception de plusieurs systèmes de TESC.

Finalement, pour valider les différents modèles et la méthode d'optimisation, plusieurs prototypes ont été réalisés, mesurés et testés. Le plus important d'entre eux est sûrement une table à induction qui permet l'alimentation simultanée de plusieurs périphériques d'ordinateur. Une analyse en temps réel de l'amplitude du courant circulant dans les bobines primaires permet la détection sans capteur des périphériques. Par le biais de techniques de contrôle numérique, un microcontrôleur gère de manière autonome la détection et l'activation localisée de la table à induction. Ces résultats contribuent au futur développement de systèmes robustes et efficaces impliquant la TESC.

Mots-clés : Transmission d'énergie sans contact, transformateur sans fer, effets haute-fréquence, effet de peau, effet de proximité, modélisation par éléments finis 2D, algorithmes génétiques, optimisation, matrice de bobines, détection sans capteur.

Contents

Remerciements	v
Abstract (English/Français)	vii
Contents	xi
List of figures	xv
List of tables	xxi
1 Introduction	1
1.1 Contactless energy transfer	2
1.2 Scope of the thesis	3
1.2.1 Historical context and current state	3
1.2.2 Technical and industrial background	4
1.3 State of the art	5
1.3.1 Fixed position systems	6
1.3.2 Free position systems	12
1.3.3 Discussion	19
1.4 Motivations and objectives	19
1.5 Thesis structure	20
2 Coreless transformer modeling	23
2.1 Introduction	24
2.2 Coreless transformer modeling	25
2.2.1 Resistance	26
2.2.2 Magnetic flux density	26
2.2.3 Inductances	27
2.2.4 Coupling factor and quality factor	32
2.2.5 Validation and measurements	33
2.3 Equivalent electric circuit modeling	40
2.3.1 General electric circuit	42

xi

Contents

2.3.2	The four topologies	45
2.3.3	Discussion	50
2.4	Conclusion	50
3	High frequency effects	51
3.1	Introduction	52
3.1.1	Definition of the skin and proximity effects	52
3.1.2	Equivalent electric circuit of a coil	53
3.1.3	Joule losses and efficiency issues	56
3.1.4	Problem definition	56
3.2	First numerical method	59
3.2.1	Current density modeling	59
3.2.2	Resistance calculation	61
3.2.3	Internal self inductance calculation	62
3.2.4	Validation and measurements	63
3.3	Numerical modeling using FEM	65
3.3.1	Introduction	65
3.3.2	Geometrical structure and model of a coil	65
3.3.3	Meshing of the conductors	67
3.3.4	Physical and electrical definition	68
3.3.5	Validation and measurements	70
3.4	Discussion	70
3.5	Exploitation of FEM simulations	72
3.5.1	Design of experiments	72
3.5.2	Complete output mapping	74
3.6	Effective impact of the high frequency on CET	76
3.7	Overall conclusion	77
4	Design and optimization of CET systems	79
4.1	Problem definition	80
4.2	Sensitivity analysis	83
4.2.1	Analyzis context	83
4.2.2	Effect of the number of turns	83
4.2.3	Effect of the track width	85
4.2.4	Effect of the space between tracks	85
4.2.5	Effect of the size of the coils	86
4.2.6	Effect of the displacement of the secondary coil	87
4.2.7	Effect of the frequency	88
4.2.8	Discussion	90
4.3	Optimization methods	91
4.4	Genetic algorithms	92
4.4.1	Generalities	92
4.4.2	Genetic algorithm implementation	93

4.4.3	Genetic algorithm testing	94
4.5	Multiobjective genetic algorithms	98
4.5.1	Pareto optimality	98
4.5.2	Generalities	99
4.5.3	Multiobjective genetic operators	100
4.5.4	Multiobjective genetic algorithm implementation	102
4.5.5	MOGA testing	103
4.6	Design of the CET table	107
4.6.1	Context and specifications	107
4.6.2	Choice of the coils geometry	108
4.6.3	Choice of the compensation topology	109
4.6.4	CET table Optimization	110
4.7	Overall conclusion	115
5	Experimental results and prototypes	117
5.1	Inductive notebook charger	118
5.1.1	Context and specifications	118
5.1.2	The coreless transformer	118
5.1.3	Electronics	120
5.1.4	Measurements	122
5.1.5	Conclusion	126
5.2	CET table	127
5.2.1	Introduction	127
5.2.2	First measurements	128
5.2.3	Second prototype	130
5.2.4	Supply strategy	131
5.2.5	Primary coils array circuit	134
5.2.6	Peripheral detection	138
5.2.7	Secondary coils circuit	142
5.2.8	Third prototype	144
5.3	Estimation of the magnetic field	146
5.4	Conclusion	148
6	Conclusion	149
6.1	Overview	149
6.2	Main results and innovative contributions	150
6.3	Outlook and perspectives	151
A	Electric Modeling Equations	153
A.1	Series Compensated Secondary: Voltage Source Behavior	153
A.2	Parallel Compensated Secondary: Current Source Behavior	154
A.3	Behavior of the four topologies	156

Contents

B Numerical methods for the integral	159
B.1 Integral method	159
B.2 Approximated integral method	160
B.3 Geometrical mean distance method	161
B.4 Linear resistance and internal self inductance for circular cross-section conductors	164
C Genetic algorithms implementation and test functions	165
C.1 Genetic operators	165
C.1.1 Individual evaluation	165
C.1.2 Constraints management	166
C.1.3 Selection	167
C.1.4 Crossover	168
C.1.5 Mutation	168
C.1.6 Replacement	169
C.1.7 Genetic algorithm termination	169
C.2 Multiobjective test functions	169
C.2.1 Unconstrained test functions	169
C.2.2 Constrained test functions	169
D Notebook charger: Preliminary study and electronics	173
D.1 Energy chain	173
D.2 Charger and notebook specifications	174
D.2.1 Coils	174
D.2.2 Electrical requirements	174
D.2.3 Input voltage of the coreless transformer	175
D.2.4 Output voltage of the coreless transformer	176
D.2.5 Summary	177
D.3 Electronics	178
E CET table: electronics	181
E.1 Primary coils array implementation	181
E.2 Detection method implementation	182
E.3 Secondary circuit implementation	183
Bibliography	185
Curriculum Vitae	195

List of Figures

1.1	Principle of contactless energy transfer by induction.	3
1.2	Pictures of the <i>Alto</i> platform. (a) Without notebook [1]. (b) With notebook [2].	5
1.3	Principle of an induction cooker.	6
1.4	(a) Coreless transformer structure of the TET system for artificial heart supply, showing the amorphous magnetic coils [87]. (b) Coreless transformer structure of the TET for the electrical stimulation system [105].	8
1.5	(a) One of the first prototypes involving a CET system to charge a mobile phone [34]. (b) Inductively charged mouse from A4 Tech [8]. (c) Portable Powermat station that allows to charge up to three devices simultaneously.	9
1.6	(a) Coreless transformer using a track of primary coils. (b) Coreless Transformer using a meander shaped primary coil. (Adapted from [82].)	13
1.7	(a) An illustration of four primary coils with the free moving secondary one. (b) Focus on a single primary coil with its smaller sensing coils. (Taken from [104].)	14
1.8	(a) Secondary coil above nine primary coils [37]. (b) Contactless planar actuator with a manipulator for different applications such as measurement, inspection or manufacturing tasks on the moving platform [39].	15
1.9	(a) Schematic view of the CET desktop showing the clusters of three activated primary coils, each of them being 120° shifted in phase [115]. (b) The array of primary hexagon spiral windings used in the prototype of the CET desktop presented in [114].	15
1.10	Pictures of the prototype used for the measurements made in [131]. (a) Primary array showing the ferrite cores inside each primary coil. (b) Secondary coil with the ferrite plate.	16
1.11	(a) Three layers of hexagonal coils used for the modeling and simulation in [78]. (b) Picture showing a mobile phone being charged by a three-layer primary coils array (taken from [67]).	17
2.1	General coreless transformer system.	24
2.2	Equivalent electric circuit of a coil at low frequency.	25
2.3	Spatial configuration of a straight conductor of finite length.	28

List of Figures

2.4	Computation of the mutual inductance. Here, two square coils with a single closed turn are represented, but eq. (2.8) can be applied to any conductor shape.	30
2.5	Computation of the self inductance.	31
2.6	Top views of (a) a rectangular coil and (b) a hexagonal coil. Cross-sections of (c) a PCB coil and (d) a coil with conventional or Litz wires.	34
2.7	(a) Magnetic flux densities generated by coil 5 when it is excited by a 1 A current. Computed with the Biot-Savart's law (a) and with the FEM software (b) at a height of $z = 5$ mm. Computed with the Biot-Savart's law (c) and with the FEM software (d) at a height of $z = 1$ mm.	36
2.8	Self inductance computed as a function of the step size for coil 2 (a) and for coil 5 (b).	37
2.9	(a) Mutual inductance computation between coils 1 and 2. (b) Mutual inductance computation between coils 5 and 6.	38
2.10	(a) Measured and computed mutual inductance between coils 1 and 2. (b) Measured and computed mutual inductance between coils 5 and 6.	41
2.11	Electric circuit of the coreless transformer.	42
2.12	(a) Step 2: Simplification of the secondary circuit. (b) Step 3: Reflected impedance of the secondary circuit. (c) Step 4: Total equivalent impedance of the coreless transformer.	44
2.13	(a) Series-Series (SS) topology. (b) Parallel-Series (PS) topology. (c) Series-Parallel (SP) topology. (d) Parallel-Parallel (PP) topology.	46
3.1	Equivalent electric circuit of a coil at high frequency.	53
3.2	Typical impedance of a coil versus the frequency, with hypothetical values $R = 1 \Omega$, $L = 5 \mu\text{H}$, $C = 10 \text{ pF}$ (a) Real part. (b) Imaginary part.	55
3.3	Typical variation of the resistance versus the frequency for coils 5, 7 and 10. . .	58
3.4	Typical variation of the self inductance versus the frequency for coils 5, 7 and 10.	58
3.5	Conductor of rectangular cross-section.	60
3.6	Comparison between the analytical solution and the numerical one for the linear resistance (a) and for the linear internal inductance (b). The linear resistance and the linear internal inductance are normalized to the DC value.	63
3.7	Comparison between the numerical solution and the measurements on (a) coil 4, (b) coil 5, (c) coil 7, and (d) coil 10.	64
3.8	Geometrical design of a coil with Flux2d.	66
3.9	Intensity of the magnetic flux density around the coil showing the boundary condition of the design.	67
3.10	Magnetic field lines zoomed in the conductors region.	68
3.11	Meshing of the intermediate box and the conductors.	69
3.12	Current density distribution in the conductors at (a) 200 kHz and (b) 5 MHz. . .	69
3.13	Comparison between measured and computed AC resistance. The AC resistance is normalized to the DC resistance. (a) Coil 4, (b) Coil 5, (c) Coil 6, (d) Coil 7, (e) coil 10, (f) coil 11.	71

3.14	Discrepancy between FEM simulations and the complete output mapping used with the closest pick strategy. A total of 2000 samples randomly generated in the experimental domain have been evaluated.	75
3.15	Discrepancy between FEM simulations and the complete output mapping with interpolation. The results obtained from the model with interactions and without interactions are compared. The same 2000 samples as in Fig. 3.14 have been evaluated.	76
3.16	Computed quality factor for different coils.	77
3.17	Efficiency and power losses versus the frequency for the coreless transformer made of coils 5 and 6. Dashed curves show the case where the HF effects are not taken into account, and plain curves when they are.	78
4.1	(a) Mutual inductance, (b) output power, and (c) efficiency versus the number of primary turns and the number of secondary turns.	84
4.2	(a) Mutual inductance, (b) output power, and (c) efficiency versus the primary track width and the secondary track width.	86
4.3	(a) Mutual inductance, (b) output power, and (c) efficiency versus the primary inter-track space and the secondary inter-track space.	87
4.4	(a) Mutual inductance, (b) output power, and (c) efficiency versus the primary coil size and the secondary coil size.	88
4.5	(a) Mutual inductance, (b) output power, and (c) efficiency versus the displacements x_d and y_d of the secondary coil.	89
4.6	(a) Output power and (b) efficiency versus the operating frequency.	90
4.7	Schematic description of a conventional GA.	93
4.8	Power losses versus output power for different solutions obtained from two runs of optimization and with different values of α	97
4.9	Output power versus α showing the fluctuations of the solutions obtained with the second run.	97
4.10	Explanation of the Pareto optimality. Here, the point D dominates the points E and F, because its two objectives are better. A and B belong to the set of Pareto optima, because no other solution dominates them.	98
4.11	Schematic description of the MOGA implemented for CET systems.	100
4.12	Multiplication coefficient evolution.	104
4.13	Obtained Pareto optimal solutions with <i>NSGAimp</i> and Matlab's NSGA-II on (a) <i>ZDT1</i> , (b) <i>ZDT2</i> , (c) <i>ZDT3</i> , (d) <i>ZDT4</i>	105
4.14	(a) Obtained Pareto optimal solutions with <i>NSGAimp</i> and Matlab's NSGA-II on <i>Constr.</i> (b) Obtained Pareto optimal solutions with <i>NSGAimp</i> on <i>Tnk</i>	106
4.15	Pareto optimal solutions obtained for three successive runs of <i>NSGAimp</i> on the problem <i>Probl</i>	106
4.16	Arrays of (a)-(b) circular coils, (c) hexagonal coils, (d)-(e) square coils. (f) Two layers of primary square coils.	109
4.17	(a) Single-transistor converter. (b) Full-bridge converter	110

List of Figures

4.18 (a) Position P_1 , (b) position P_2 , (c) position P_3	111
4.19 (a) Position P_a , (b) position P_b , (c) position P_c	112
4.20 Results of three optimization runs giving the total output power ($-O_1$) versus the total Joule losses (O_2).	114
5.1 The CET system for the CET notebook charger.	119
5.2 (a) Top view and (b) side view of the full-bridge converter.	121
5.3 The output rectifier with the series compensation capacitor and the smoothing capacitor.	122
5.4 Measurement of the input voltage and the current in the primary coil when no load is present.	123
5.5 (a) Measurement of the input voltage and the current in the primary coil when the coreless transformer is loaded by a resistor of 5Ω without the rectifier. (b) Measurement of the voltage and the current in the load.	124
5.6 (a) Measurement of the input voltage and the current in the primary coil when the coreless transformer is loaded by a resistor of 5Ω with the rectifier. (b) Measurement of the voltage at the input of the secondary rectifier and the current in the secondary coil.	125
5.7 Efficiency and DC voltage level versus the load resistance.	126
5.8 (a) Picture of the prototype without the notebook. (b) Picture of the prototype while charging the notebook battery.	127
5.9 (a) The array of 9 coils. (b) The array of 18 coils.	128
5.10 Picture of the setup with the array of 18 coils.	129
5.11 Load voltage versus the displacement along X axis and along Y axis. (a) Calculated and (b) measured over an array of 9 coils. (c) Calculated and (d) measured over an array of 18 coils distributed into two shifted layers.	130
5.12 (a) Top view and (b) bottom view of the prototype.	132
5.13 General strategy used for the CET table.	133
5.14 Different time scales for the signals applied to the primary coils array.	134
5.15 Primary circuit schematic.	135
5.16 Single-transistor converter.	136
5.17 (a) Good scenario with two loads and two activated coils. (b) Bad scenario with two loads and four activated coils.	137
5.18 (a) Signal generated on the gate of the MOSFET. (b) Input voltage and primary coil current.	137
5.19 Circuit implemented for the estimation of the current.	139
5.20 (a) Current generated by the voltage supply. (b) Voltage provided to the A/D converter of the DSP.	140
5.21 Current delivered by the DC voltage supply over a large time scale showing a few short detection phases between the supply phases with no load (a), one load (b), and two loads (c). View of the current during a single detection phase with no load (d), one load (e), and two loads (f).	141

5.22 Zoom on the second coil scanning with and without load.	142
5.23 Secondary circuit scheme for the speaker providing a 5 V (DC) output.	142
5.24 (a) Voltage and current measured on a load of 10 Ω without rectifier. (b) Voltage and current measured at the input and at the output of the rectifier loaded by a resistor of 10 Ω	143
5.25 Picture of the primary coils array and the secondary coil.	145
A.1 Behavior of the coreless transformer (coils 5 and 6) when the load resistance varies from 10 to 100 Ω	154
A.2 Behavior of the coreless transformer (coils 5 and 6) when the load resistance varies from 10 to 100 Ω	155
A.3 Behavior of the coreless transformer (coils 5 and 6) when the load resistance varies from 10 to 100 Ω . (a)-(b) PS topology, (c)-(d) PP topology.	157
A.4 Behavior of the coreless transformer (coils 5 and 6) when the load resistance varies from 10 to 100 Ω . (a)-(b) SS topology, (c)-(d) SP topology.	158
C.1 (a) Pareto front line of (a) <i>ZDT1</i> , (b) <i>ZDT2</i> , (c) <i>ZDT3</i> , (d) <i>ZDT4</i>	171
C.2 (a) Pareto front line of (a) <i>Constr</i> , (b) <i>Tnk</i>	171
D.1 Energy chain for the CET system of the notebook.	174
D.2 Electronic schematic from the grid to the primary coil. The secondary side is not shown.	175
D.3 Schematic view of the rectified and smoothed voltages.	176
D.4 Schematic view of the AC voltage at the converter output.	177
D.5 (a) Electronic schematic of the secondary circuit. (b) Equivalent circuit.	178
D.6 (a) Top view and (b) side view of the full-bridge converter.	179
D.7 The output rectifier with the series compensation capacitor and the filter capacitor.	180
E.1 Photograph of the primary electronic circuit and a portion of the primary coils array.	181

List of Tables

1.1	Summary of the main characteristics of some CET fixed charging applications available on the market or found in literature. The size of the coils is given by the external diameter for the circular coils and by the external lengths for square or rectangular coils.	11
1.2	Summary of the main characteristics of some CET free charging systems found in literature. The size of the coils is given by the external diameter for the circular or hexagonal coils and by the external lengths for square or rectangular coils. .	18
2.1	Calculated DC internal self inductance for conductors of rectangular cross-section with different aspect ratios.	31
2.2	Geometric parameters	34
2.3	Characteristics of the experimental coils	35
2.4	Self inductance computations as a function of the step size.	37
2.5	Computation time for different cases issued from Fig. 2.9(b).	38
2.6	Results of the self inductance computations and measurements	39
2.7	Results of the mutual inductance computations and measurements.	40
2.8	Electric parameters.	41
3.1	Input parameters for the FEM simulations	66
3.2	Variation range of the input parameters	73
4.1	Free parameters of CET systems.	82
4.2	Free parameters.	107
4.3	Output parameters.	107
4.4	Electric specifications of the mouse, keyboard and loudspeaker	108
4.5	Input parameters for the CET table.	114
4.6	Output parameters for the CET table.	114
5.1	Specifications of the CET notebook charger demonstrator	118
5.2	Final design of the coreless transformer for the Notebook.	120
5.3	Calculated and measured parameters of the coreless transformer.	120

List of Tables

5.4	Electrical values of the coreless transformer.	123
5.5	Electrical values of the coreless transformer.	124
5.6	Electrical values of the coreless transformer.	125
5.7	Geometrical parameters of the coils for the second prototype.	131
5.8	Power and efficiency measurements	144
5.9	Parameters of the primary and secondary coils	145
5.10	Measured and calculated electric parameters of the third prototype.	146
5.11	Estimation of the magnetic flux density at different points above the two CET prototypes.	147
C.1	Unconstrained test functions that are often used to evaluate MOGAs.	170
C.2	Constrained functions that are often used to evaluate MOGAs.	170
D.1	Main components of the full-bridge converter	178
D.2	Components used in the rectifier.	180
E.1	Description of the main components used in the primary circuit.	182
E.2	The main components used in the detection circuit.	182
E.3	Description of the main components used in the primary circuit.	183

Introduction

Summary

1.1 Contactless energy transfer	2
1.2 Scope of the thesis	3
1.2.1 Historical context and current state	3
1.2.2 Technical and industrial background	4
1.3 State of the art	5
1.3.1 Fixed position systems	6
1.3.2 Free position systems	12
1.3.3 Discussion	19
1.4 Motivations and objectives	19
1.5 Thesis structure	20

This first chapter gives the general aspects related to this thesis. The first section introduces the reader to the world of contactless energy transfer (CET), through a large panel of different technologies associated to CET and then by focusing on the most interesting one for this thesis, that is electromagnetic coupling. An overview of the commercially available devices and a state of the art of the recent researches are summarized in the second part of the chapter. Then, the strategy and the main objectives for designing and optimizing CET systems are described. Finally this first chapter ends with the outline of the whole dissertation.

1.1 Contactless energy transfer

Contactless Energy Transfer refers to a really broad and vague concept if not bounded by a specific context. In its large meaning, contactless energy can take the form of electricity, light, heat or even sound and wind. The contactless transfer involves a starting point (source) and an ending point (receiver) without intermediate material that would be intentionally added to achieve some purpose. In the scope of this thesis, the starting and ending points are both characterized by electric energy, with in between no additional wires or material.

Light energy transfer can be obtained by photons travel from a source such as the sun or a laser, to a receiver that is generally a photovoltaic cell. The advantage of the laser as a source is that it provides a very directional illumination thanks to its high degree of temporal and spatial coherence. However, the efficiency of light energy transfer is very low, because the losses at each step of the transfer processes are important, namely in the source, in the air and in the receiver. Furthermore, the economical aspects are not attractive [45]. For these reasons, light energy is interesting only for applications that require a transfer over a very large distance, for example in the space.

The microwaves can also transfer energy over a relatively large distance that can be greater than the emitter and receiver sizes. They are electromagnetic waves ranging from 1 GHz to 300 GHz and are used for far-field energy transfer [83]. The most common source for domestic applications is the magnetron thanks to its unexpensive cost, but high frequency waves can be also generated by antennas. The receiver is a rectenna which is actually an antenna with a rectifier used to convert microwaves into DC electricity. The main drawbacks of this technology are the health risks and the relatively low efficiency that can be obtained.

The most used way to transfer contactless energy is the magnetic induction whose principle is shown in Fig. 1.1. It uses near-field electromagnetic waves in the range of frequencies between 10 kHz and a few MHz. The characteristic distance of transfer is the same order as the size of the receiver (secondary coil) and the emitter (primary coil). Such CET systems are based on the coreless transformers theory. The working principle consists in applying a high frequency current in a primary coil. In the surrounding air, it generates a magnetic field that induces a voltage to a secondary coil if placed in proximity. It is necessary to operate at high frequency because coreless transformers suffer from weak mutual coupling. To enhance the coupling between primary and secondary, both coils must be well aligned and the air gap must be as small as possible.

With this description, a distinction can be made between inductive CET and RFID systems. Indeed, the former involves a transfer of power through a relatively short distance as defined above, while the latter is used to transfer information (with power generally lower than

100 mW) through a large distance.

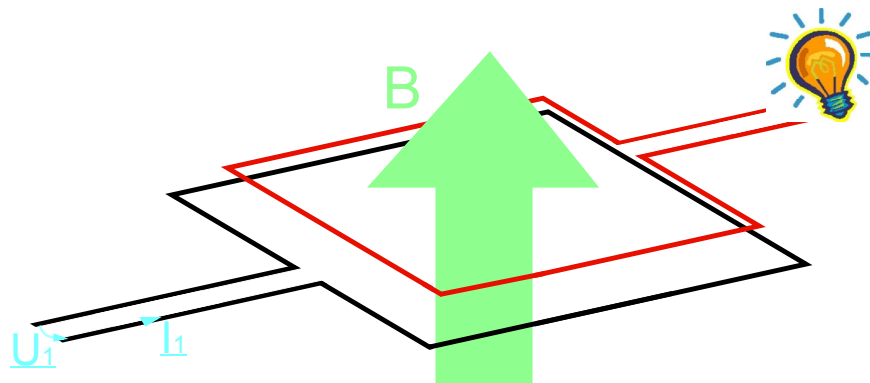


Figure 1.1: Principle of contactless energy transfer by induction.

1.2 Scope of the thesis

1.2.1 Historical context and current state

Nicola Tesla proposed the first theories of CET in 1899-1900. He carried out various wireless transmission and reception experiments through air or matter. At his Colorado Springs laboratory, he experimented for example a remote supply of 200 light bulbs through the ground from a distance of about 40 km [14].

The first reported researches on the so-called energy transport by inductive coupling date from the 1960s [71]. Although the principle of inductive CET was known for a long time, this technology has remained immature for a long time as the first industrial applications appear in the 1990s with the electric toothbrushes. Even nowadays the number of electric devices supplied by inductive CET is relatively low. This absence is probably due to the lack of standards and regulations for this technology, and also to the uncertainty from the average population concerning the inherent health dangers.

In 1998, a scientific committee has published general guidelines [25] to avoid any kind of health risks concerning the exposure of the population to electromagnetic fields. Basically these recommendations provide the restrictions for the public exposure as a function of the operating frequency, the immersed body proportion and the size of the coils. However, in practice, they are not relevant according to [10]. Therein, a study on the maximum power transfer, based on these restrictions, shows that common applications including coils size of 40 mm to 100 mm could transfer no more than about 30 mW, which is roughly two orders of

magnitude lower than existing products on the market. This statement will be assessed later in this thesis work.

In late 2008, the Wireless Power Consortium (WPC) has been created in order to unify the powering protocols related to inductive CET systems. At that time the consortium consisted of the gathering of 8 companies that are active in the domain of CET technologies. Thanks to its great success, it counted 100 companies in October 2011. Basically the WPC aims to set *the standard for interoperable wireless charging* [18]. In July 2010, a three-part document has been finalized, in which the new standard, called 'Qi', is designed for electronic devices up to 5 W. Practically it means that all receivers stamped with the Qi logo can be supplied by all transmitters also stamped with the same logo. In this sense the Qi sign stands for the emblematic figure of interoperability and compatibility between the different devices.

1.2.2 Technical and industrial background

More and more electric applications require an energy transfer without wires and contacts. Especially in the domain of desktop applications such as computer peripherals, wireless technologies (Bluetooth, ZigBee, RF, IR, WiFi) that allow transfer of information are very trendy, while the supplying process uses massively wires or batteries. In a desktop environment, removing the cables between the power source and electronic devices would be convenient. It would allow to gain a certain amount of place and to clean the surface from wires pollution. In this context, the contactless energy transfer by inductive coupling meets more and more success. Some products are already available for a few applications, such as mice or mobile phones. However, a full platform enabling to supply simultaneously several consumers is still not to be reported.

In the framework of a collaboration between Logitech SA and the Laboratory of Integrated Actuators (LAI), CET systems are studied for notebook and desktop applications.

This collaboration is divided into two different practical applications:

1. The **inductive notebook charger** is aiming to realize the prototype of a CET system from a platform to a static notebook. The said platform is a product already available on the market under the commercial name *Alto* (Fig. 1.2);
2. The **CET table** is aiming to realize a prototype of a CET system embedded in a table in order to supply multiple desktop peripherals.

Logitech [9] is a Swiss company developing and marketing products such as peripheral devices for PCs, including mice, keyboards, loudspeakers, microphones and webcams. They are



Figure 1.2: Pictures of the *Alto* platform. (a) Without notebook [1]. (b) With notebook [2].

responsible in the above-mentioned projects for providing the equipment (*Alto* platform, peripherals, ...) and sharing their know-how on hardware and manufacturing of electronic peripherals.

The LAI has conducted numerous projects linked to CET. As representative examples, a few projects are chosen and briefly described here. The first one is the *Serpentine* project [55], [56]. A power of 2.5 kW was provided to an electric vehicle through a coreless transformer composed of a linear track of primary coils and a single secondary coil.

The second application concerns a project in collaboration with *Hilti* [29]. The goal was to add new functions to a drill machine, such as a bidirectional communication between the main tool and the accessories. The main challenge was to simultaneously transfer power (25 W) and information. Therefore two pairs of windings were used with extremely low mutual effects in order to make both functions as decoupled as possible.

The third application refers to the *ColoStim* project. The goal of the project was to electrically stimulate the colon of people suffering from severe motility troubles. Using classical electric stimulators often causes problems due to the presence of wires. In order to resolve this problem, a new device using inductive CET is designed in [57], [58]. The primary is worn around the patient's torso and multiple secondary windings (0.1 W) are implanted all along the colon so as to stimulate the peristaltic waves.

1.3 State of the art

CET systems can be classified into two categories. The first one concerns fixed position systems wherein the devices to be supplied are static. The second one concerns the free

position systems involving devices that can be freely moved on the charging surface. With such a definition, it is obvious that the inductive notebook charger belongs to the first one and the CET table to the second one.

1.3.1 Fixed position systems

The fixed position system is the simplest inductive CET method. Nowadays, it involves almost all the existing industrial applications. It usually charges one load and the energy is transferred from a single primary coil to a single secondary coil. Furthermore, both coils have to be approximatively the same size and well aligned to ensure a good mutual coupling, a sufficient amount of transferred energy and a good efficiency.

Induction cookers

Fixed CET is traditionally the method used in induction cookers, except that the secondary coil is replaced by the cooking vessel made of ferromagnetic and conductive metal. The initial researches and patents date from the early 1900s, but the first production of induction cookers was performed in the 1970s by the *Westinghouse Electric Corporation* [15]. Nowadays, many manufacturers are present on this market, such as *Bosch, Miele, Siemens, Electrolux,...*

The principle of the induction heating is shown in Fig. 1.3. The magnetic field generated by the primary coil creates Eddy currents in the pot that cause the heating Joule effect. The wires of the primary coils generally exhibit a flat and spread geometry in order to enhance the distribution of the magnetic field that reaches the cooking vessel. The transferred power is in the order of 1 to 2 kW and the operating frequency is situated in a range from 20 kHz to 50 kHz.

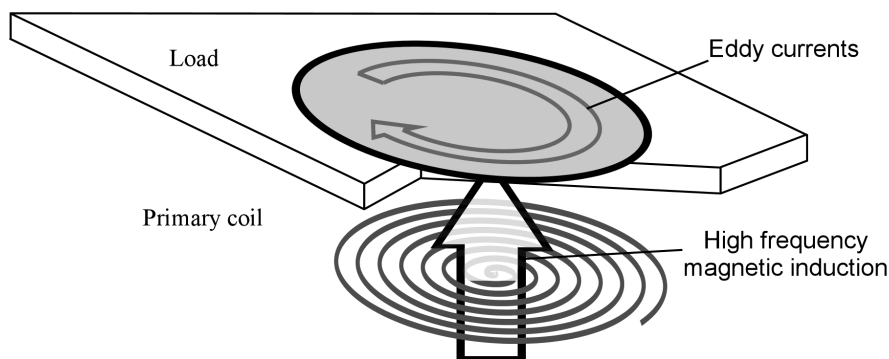


Figure 1.3: Principle of an induction cooker.

Electric toothbrushes

Inductive CET is interesting for applications that require no exposed electrical contacts, such as devices that are used in a moist environment or even immersed in water. Since the early 1990s, rechargeable toothbrushes (for example from the Oral-B brand [7]) use this technology that allows to enclose and therefore fully insulate the wires. It gives the advantage to protect the user against electric shocks due to apparent contacts and to prevent short-circuits that could damage electronics. The system generally includes a ferromagnetic core that increases the coupling between the coils. The operating frequency is around 10 kHz or more, and the transferred power is between 10 and 15 W. Similar CET systems are also integrated into electric shavers.

Transcutaneous energy transfer

In the medical domain, CET can be used to supply surgically implanted devices, where it is specifically called *transcutaneous energy transfer* (TET).

For instance, the use of heart assist devices to circumvent left ventricular dysfunctions has been proven to be beneficial for the patients [101]. However, conventional ways to supply them can develop additional risks associated to the apparition of infections as the wires are passed through the skin. To solve this problem, a novel resonant converter with its coreless transformer is designed in [129] and allows to supply a prototype of such a heart assist device. The amount of transferred power is 10 W and the operating frequency is 205.1 kHz.

In [86],[87], a TET system is designed for an implantable artificial heart. Therein, the main constraint is that the primary coil has to be placed near the secondary one in order to have a good coupling. The operating frequency is 50 kHz and the amount of transferred power is 20 W. The coreless transformer includes two circular spiral coils whose mechanical structure is maintained by radial amorphous fibers. These fibers make the coils flexible and contain magnetic material that is supposed to improve the energy transfer by concentrating the flux through the coils (*c.f.* Fig. 1.4(a)). Furthermore, a special focus is made on the temperature rise of the secondary coil, which is a critical issue for *in vivo* applications.

Finally, TET is used in [105] to supply electrodes that aim to generate electrical stimulations in order to restore the movement of limbs paralysed by injured spinal cord. The primary coil has a solenoid shape and is placed around the said limb. The secondary coils have spiral shapes and are connected to the electrodes, as shown in Fig. 1.4(b). Two different frequencies of 96 kHz and 387 kHz are tested, and the transferred power is not indicated but estimated to be less than 1 W for each electrode.

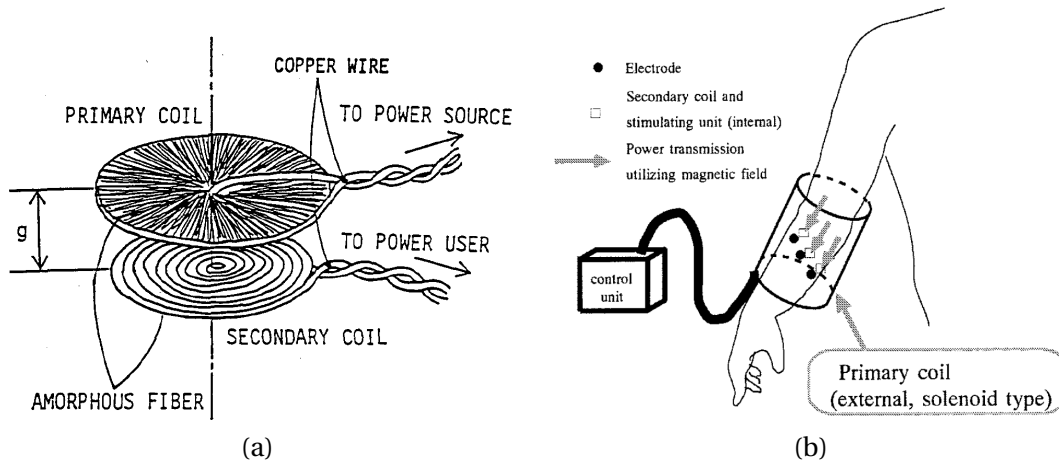


Figure 1.4: (a) Coreless transformer structure of the TET system for artificial heart supply, showing the amorphous magnetic coils [87]. (b) Coreless transformer structure of the TET for the electrical stimulation system [105].

Desktop peripherals and mobile phones

The first CET studies dedicated to mobile phones were realized in the early 2000s. For example, the prototype of a small platform allowing to recharge a mobile phone battery is proposed in [33], [34]. A picture of the prototype is given in Fig. 1.5(a). The coreless transformer is made of printed circuit board (PCB) coils that have to be precisely aligned to start the charging process. The operating frequency is ranged between 920 and 980 kHz, and the power transferred to the battery is 3.3 W, but the transformer has been tested to transfer up to 24 W.

More recently, many desktop applications have been marketed. An example of existing CET application is the battery-free optical mouse from A4 Tech [8] (*c.f.* Fig. 1.5(b)). Instead of batteries, the mouse uses inductive CET to provide energy via the included mouse pad, which is connected to a computer USB port. Mice are very low powered devices, generally the amount of transferred power is less than 1 W. In a similar way, the HP Touchstone is a small dockstation powered by the USB port and can transfer the power (5 W) to recharge a phone or a Palm device [6].

Concerning systems involving CET to multiple devices, many products are commercially available. They remain in this category of fixed position charging because they do not offer the possibility to supply the devices freely placed on the whole surface, but only at predefined places. For example, the first CET table developed by Fulton Innovation under the denomination of *eCoupled* allows to transfer energy to multiple but fixed devices [5]. This application has the ability to communicate with the devices thanks to a process specifically developed by Fulton, which allows to transfer the exact amount of power required by each load on the

platform.

Other companies are present on this market with similar platforms and applications, such as Qualcomm with the eZone charger [16], Mojo Mobility with the MojoPad [17], Homedics with its Powermat product line [12]. The common points to these applications are the low power devices that they can supply (generally less than 5 W), the predetermined position of the devices on the platform and the integrated intelligence that detects and recognizes the devices.

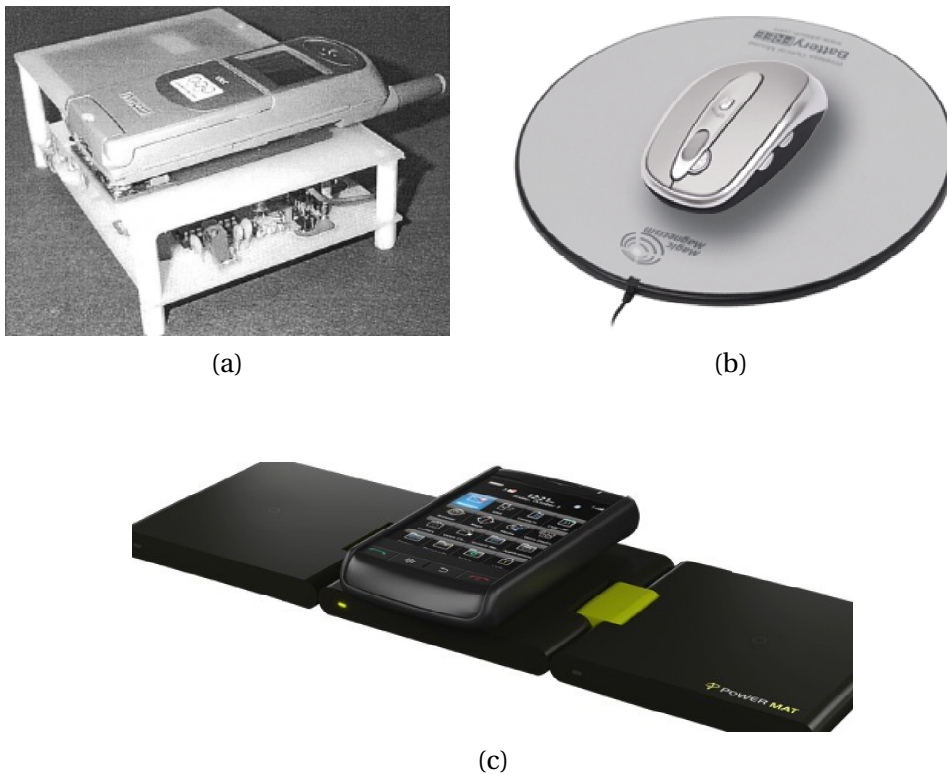


Figure 1.5: (a) One of the first prototypes involving a CET system to charge a mobile phone [34]. (b) Inductively charged mouse from A4 Tech [8]. (c) Portable Powermat station that allows to charge up to three devices simultaneously.

Electric vehicles

A new niche market that may explode in the future for fixed positioning CET systems is the electric vehicles charging. Many researches are ongoing in this domain [49], [127], [124], prototypes are being tested by Siemens or BMW [4], and some applications are on the verge to be commercially available [3], [19]. For instance, the typical specifications for a prototype (such as the one developed in [127]) consist of transferring a power of 30 kW to the vehicle

Chapter 1. Introduction

battery. The operating frequency is 20 kHz. The main issue here comes from the large airgap of 45 mm which makes the coupling low.

As a conclusion for the fixed position systems, a summary of the most noteworthy applications encountered in this section is given in Table 1.1 with their main specifications. A remark should be made about the efficiency of such CET systems. Strangely, efficiency issues are rarely discussed in literature, especially for low-consuming applications. It is probably due to the fact that it is not an attractive point for inductive CET. Furthermore, when they are mentioned, their application is often blurry and it is difficult to determine what they take into account. Thereby, the efficiency is just mentioned in parentheses in table 1.1 when the information is available and the values have to be taken with caution.

Table 1.1: Summary of the main characteristics of some CET fixed charging applications available on the market or found in literature. The size of the coils is given by the external diameter for the circular coils and by the external lengths for square or rectangular coils.

Application	Author / Company	Ref.	Year	Coils	Frequ.	Power	Specifics
Induction cookers	Westinghouse Corp.	[15]	1973-1975	Circular - spiral ~150-300 mm	20-50 kHz	1-2 kW ($\eta = 84\%$)	No secondary coil Ferromagnetic metal
				Circular - square ~20mm	10 kHz	10-15 W	Ferromagnetic core
Electric tooth-brushes	Oral-B Philips Sonicare	[7], [11]	~1990	Litz wires	205.1 kHz	10 W ($\eta = 84.5\%$)	-
				Circular ~20-30 mm			
Transcutaneous energy transfer	Wu <i>et al.</i>	[129]	2009	Circular - spiral 114 mm	50 kHz	20 W ($\eta = 90\%$)	Flexible coils Radial magnetic fibers
	Matsuki <i>et al.</i>	[86], [87]	1990-1992	Primary Circular - solenoid 55 mm	96 kHz	< 1 W	Primary coil around the arm
	Sato <i>et al.</i>	[105]	2001	Secondary Circular - spiral 11.5 mm			
	Choi <i>et al.</i>	[34]	2004	PCB coils Circular - spiral 35 mm	920-980 kHz	24 W ($\eta = 57\%$)	-
Desktop peripherals Mobile phones	A4 Tech	[8]	-	Circular ~200 mm (Prim.) ~30 mm (Sec.)	-	< 1 W	Primary coil supplied by USB port
	Powermat	[12]	-	Square ~10 mm	-	< 5 W	Up to three devices si- multaneously charged
Electric vehi- cles	Wang <i>et al.</i>	[127]	2005	Rectangular 800 × 600 mm ²	20 kHz	30 kW	Large air gap

1.3.2 Free position systems

The free position systems are more complex and elaborated than the fixed ones. They generally can charge one or multiple loads on a large area, whatever their position. They are made of multiple primary and secondary coils that can be distributed in one or multiple layers. Besides, they often integrate a detection system that allows to activate only the primary coils located under the loads. Until now, no such manufactured system does exist, but many projects are in the research phase.

Single primary coil configuration

At first thought, the most simplistic way to supply multiple loads that can be freely moved on a large surface consists in using a single primary coil that encompasses the whole useful area. However, this leads to two main problems. First, it is difficult to ensure that the same amount of energy is transferred for every position of the loads. Secondly, as the primary coil is much larger than the secondary ones, their coupling is very low which obviously makes it more difficult to transfer large amounts of energy.

In [77], such a system is proposed to transfer simultaneously from 2 to 12 W to four loads at an operating frequency of 418 kHz. The design of the primary coil is based on a magnetic field approach. Indeed the intensity of the magnetic field is almost uniform thanks to the use of two layers of primary coils different in shape and size. The main drawback of this design procedure comes from the relatively small charging surface that has to be limited in order to ensure a sufficient power to be transferred. The prototyped primary platform has a size of 126 mm × 97 mm and the secondary coils have a size of 60 mm × 30 mm.

Two-dimensional primary coils

Unlike the electric vehicles presented in section 1.3.1, CET can be used to supply the vehicles while they are moving. It allows to remove or drastically reduce the weight of the batteries. These CET systems generally integrate a track of primary coils wherein the vehicle is constrained to remain.

In [82] a study linked to the *Serpentine* project is conducted. A power of 2.5 kW is transferred at about 100 kHz to an electric vehicle through a coreless transformer composed of a linear track of primary coils (placed in the ground) and a single secondary coil (placed at the vehicle chassis). The structure of the coreless transformer is shown in Fig. 1.6(a). The supply strategy consists in activating only the two primary coils that are closest to the secondary one, and the operating frequency is continuously adapted thanks to a maximum power point tracking

(MPPT) method.

For the *Swissmetro* project [13], a primary coil of meander shape is considered in [82]. The principle of the CET system is shown in Fig. 1.6(b). The supply strategy consists in applying a DC current in the meander primary coil so that an induced voltage is generated into the secondary coils only when they are moving. The frequency of the CET system is then dependent on the vehicle speed and on the distance between the transverse segments of the primary coil. The resulting operating frequency for the proposed solution is 1.5 kHz at full speed. Furthermore, multiple secondary coils are distributed all along the *Swissmetro* structure, each of them receiving 5 kW. Although this solution was estimated to be physically feasible, it was abandoned at an early stage as the huge required volume of copper led to excessive costs.

Another study involving the meander type coils is proposed in [103]. Therein the effort is made on trying to minimize the variation of the voltage induced in the secondary coil along its course. The operating frequency is 100 kHz and the transferred power is not indicated.

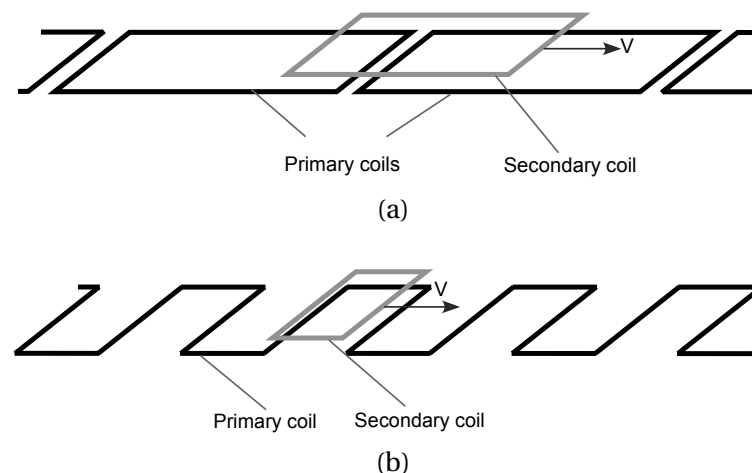


Figure 1.6: (a) Coreless transformer using a track of primary coils. (b) Coreless Transformer using a meander shaped primary coil. (Adapted from [82].)

Primary coils arrays

A method that is widely used to transfer energy over a large surface consists in using arrays of primary coils. For such systems, a strategy to detect the presence of the load(s) is generally integrated so as to supply only the primary coils that are situated in their vicinity.

In [104], a CET is designed to provide 200 W at 100 kHz to an electric vehicle. The primary coils configuration is not only a two-dimensional track as for the previous examples. It is made of multiple rectangular coils above which the secondary coil can be freely moved. A detection

strategy is integrated to the system to selectively activate the primary coils. It uses much smaller sensing coils situated at the periphery of each primary coil to detect the presence of the load. The coil configuration and the sensing coils are shown in Fig. 1.7.

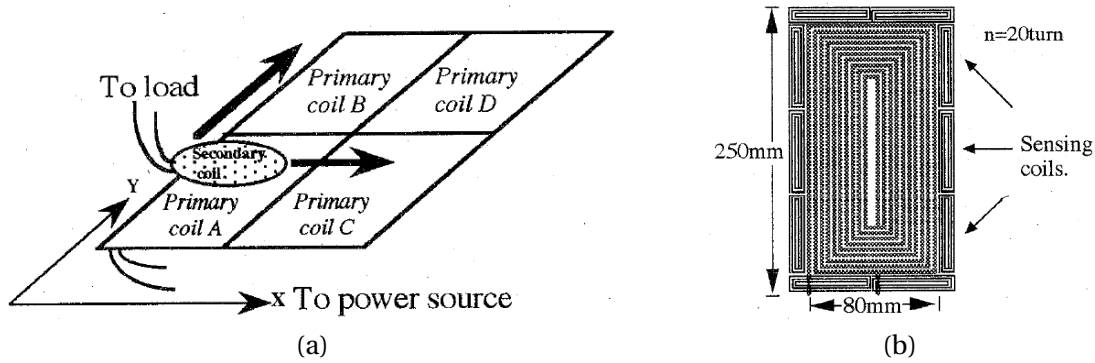


Figure 1.7: (a) An illustration of four primary coils with the free moving secondary one. (b) Focus on a single primary coil with its smaller sensing coils. (Taken from [104].)

Arrays of square primary coils are a very common structure to generate a magnetic field. It is used to supply a moving load in [38], [37], where the secondary coil is the size of about four primary coils, and the primary side is composed of nine coils, as shown in Fig. 1.8(a). The operating frequency is 100 kHz and the transferred power is estimated to be around 250 W. In order to ensure the desired amount of transferred power, the voltage supply is continuously adjusted during movement of the secondary coil. Furthermore, the moving load has to be levitated and propelled by the primary coils array. To achieve this, each secondary coil is equipped with a permanent magnet that plays a crucial role for the levitation function. An optimisation of this system is proposed in [39], in order to supply a large contactless planar actuator. A schematic view of this actuator is shown in Fig. 1.8(b). Therein, the coils are made of Litz wires and their required number has to be largely increased in order to supply the actuator over the required area. The Litz wires are used to reduce the resistance of the coils at high frequency, which thus allows to lower the heat generation that is a critical issue for this application.

A contactless energy transfer that uses an array of hexagonal coils is proposed in [115]. It is used to supply different desktop peripherals. The operating frequency is 150 kHz and the transferred power is not explicitly specified, but can be guessed from the application to be in the order of 5 W. Clusters of three primary coils are excited by a current with the same amplitude but with a phase shift of 120 degrees (*c.f.* Fig. 1.9(a)). This allows to reduce the stray magnetic field. It is also shown that secondary topologies with multiple small coils are better suited than a single large coil. But for this application, the maximum power efficiency of

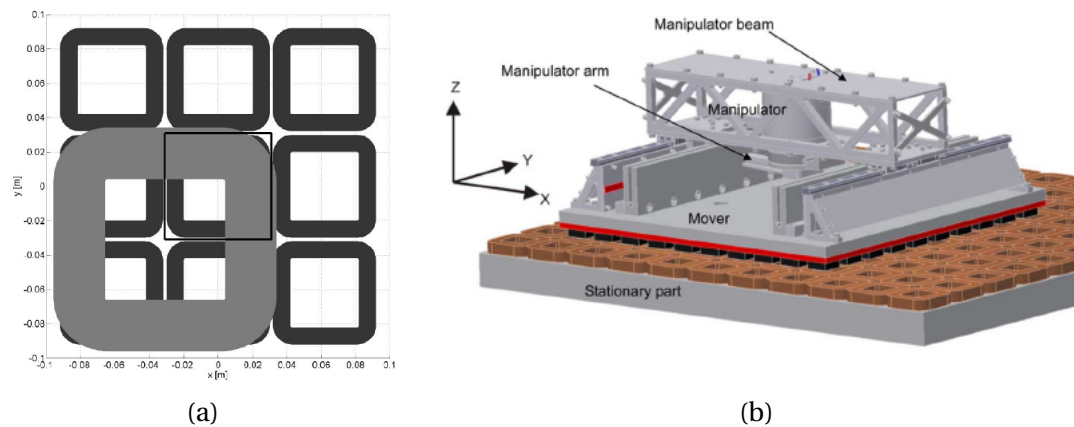


Figure 1.8: (a) Secondary coil above nine primary coils [37]. (b) Contactless planar actuator with a manipulator for different applications such as measurement, inspection or manufacturing tasks on the moving platform [39].

13% is relatively low. In [114], they still use their three-phase configuration to reduce the stray magnetic field, but change the strategy of the CET by using larger secondary coils than the primary ones, which ensures a larger minimal mutual coupling. Furthermore, the efficiency and power transfer are slightly improved. The operating frequency is increased to 2.77 MHz and it is possible to transfer up to 8 W to the loads.

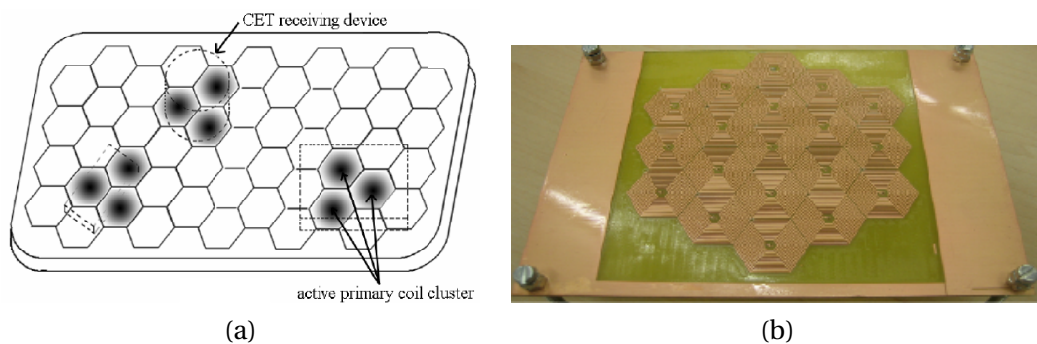


Figure 1.9: (a) Schematic view of the CET desktop showing the clusters of three activated primary coils, each of them being 120° shifted in phase [115]. (b) The array of primary hexagon spiral windings used in the prototype of the CET desktop presented in [114].

In [62], a completely different design for a CET desktop is presented. The primary is composed of an array of small circular coils. The energy is transferred from multiple primary coils to a larger secondary one. The detection strategy consists in sending information from the secondary to the primary. To detect the secondary device, the primary coils turn into a signal-reception mode and the secondary coil changes into a signal-emission mode to determine its

exact position. Two different frequencies are used. The detection system works at 500 kHz and the power transfer at 100 kHz. Up to 50 W can be transferred this way. The measurements show a CET efficiency of $85\% \pm 5\%$ depending on the location of the secondary. However, the major drawback comes from the detection system, since it needs the integration of more electronics on the secondary device, which is inconvenient for small peripherals.

Finally, in [130],[131], another structure for the primary coils array is proposed. A study on the best arrangement of shapes for primary and secondary coils is performed. It aims to ensure a good efficiency, whatever the position of the device. As a result, this paper states that the best solution is an hexagonal packing of circular primary windings coiled around a ferrite core, and a larger secondary circular spiral coil designed so that it covers at least one primary coil wherever it is placed on the surface. The system is able to detect the device and generate the charging magnetic field only within the covered area of the secondary coil. The operating frequency is 150 kHz and the transferred power is 5 W. Practical measurements show an efficiency in the range of 86% to 89%. A picture of the prototype is given in Fig. 1.10. On the one hand this system is convenient because it needs only one primary layer, but on the other hand it requires a three-dimensional ferromagnetic structure that cannot be realized with PCB coils.

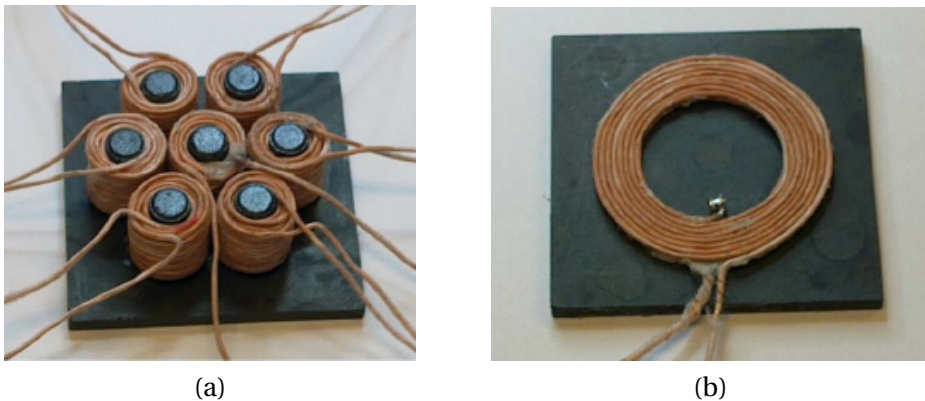


Figure 1.10: Pictures of the prototype used for the measurements made in [131]. (a) Primary array showing the ferrite cores inside each primary coil. (b) Secondary coil with the ferrite plate.

Multiple layers of primary coils arrays

In single layered primary coils arrays, the main difficulty comes from the drop of magnetic field intensity between the coils, which may lead to an insufficient amount of energy transfer if the secondary coil is located just at this position. Using multiple layers of primary coils arrays allows to circumvent this problem.

For example, in [24] a study on different array structures is shown. Two shapes (square and hexagonal) are taken into account, and different multilayer arrangements are tested. This paper presents only a preliminary study on the best primary coil array structures for a battery charging platform, so that no power or frequency considerations are investigated. The result shows that three layers of shifted hexagonal coils or two layers of shifted square coils are the best solutions. However, although simulations provide interesting results, the experimental measurements remain quite far from simulations.

In order to generate an uniform flux density over the whole surface, a three-layer array of hexagonal PCB coils (Fig. 1.11(a)) is simulated and measured in [67], [78]. This application is designed to charge different electronic devices such as mobile phones or Palm devices. The transferred power is about 5 W at a 130 kHz frequency. An interesting development concerns the connexions and the activation strategy of the primary coils. Multiple coils, that belong to one or different layers, are connected in series. Thereby, clusters of primary coils can be activated. For example they propose so-called columns of six coils spread over two layers, and each column can be separately activated. This simplifies the modeling and the supply of their CET platform. A picture of a prototype is given in Fig. 1.11(b).

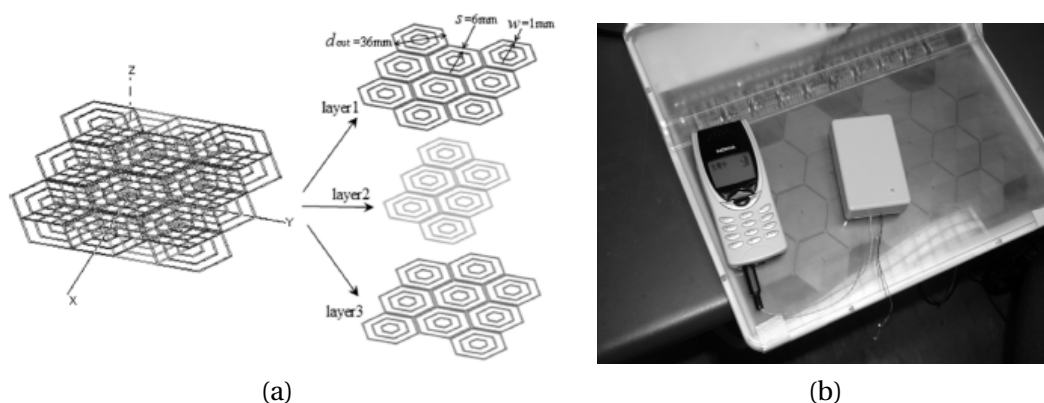


Figure 1.11: (a) Three layers of hexagonal coils used for the modeling and simulation in [78]. (b) Picture showing a mobile phone being charged by a three-layer primary coils array (taken from [67]).

As a conclusion for the free position systems, a summary of the most noteworthy applications encountered in this section is given in Table 1.2 with their main specifications. Concerning efficiency issues, the same remark as for Table 1.1 can be made. The values of efficiency are given in parentheses when they are available and have to be considered with caution.

Table 1.2: Summary of the main characteristics of some CET free charging systems found in literature. The size of the coils is given by the external diameter for the circular or hexagonal coils and by the external lengths for square or rectangular coils.

System	Author	Ref.	Year	Prim. coils	Sec. coils	Frequ.	Power	Specifics
Single primary coil	Liu <i>et al.</i>	[77]	2008	Rectangular 126 × 97 mm ²	Rectangular 60 × 30 mm ²	418 kHz	2-12 W ($\eta = 80\%$)	Up to four loads simultaneously charged
	Macabrey <i>et al.</i>	[82], [55]	1997	Rectangular 1 × 0.3 m ²	Rectangular 0.9 × 0.3 m ²	~100 kHz	2.5 kW ($\eta = 95\%$)	Large airgap of 55 mm
2D coils	Macabrey <i>et al.</i>	[82]	1998	Meander type Width: 0.3 m Half period: 1 m	Rectangular 1 × 0.3 m ²	~1.5 kHz	5 kW	Large airgap of 50 mm
	Sato <i>et al.</i>	[104]	1996	Rectangular 250 × 80 mm ²	Circular 80 mm	100 kHz	200 W ($\eta = \sim 80\%$)	Small sensing coils at the periphery of prim. and sec. coils
Primary coils arrays One layer	de Boeij <i>et al.</i>	[37]	2006	Square 60 mm	Square 130 mm	100 kHz	~250 W ($\eta = 95\%$)	Permanent magnets inside the sec. coils
	Sonntag <i>et al.</i>	[114]	2008	Hexagonal 25 mm	Hexagonal 40 mm	2.77 MHz	≤ 8 W	PCB coils
	Hatanaka <i>et al.</i>	[62]	2002	Circular	Circular	100 kHz	50 W ($\eta = 85\%$)	-
	Zhong <i>et al.</i>	[130], [131]	2002	Circular ~22 mm	Circular ~8 mm	150 kHz	5 W ($\eta = 85\%$)	Larger sec. coils than prim. ones Ferromagnetic structures
Primary coils arrays Multiple layers	Achterberg <i>et al.</i>	[24]	2008	Square 30 mm hexagonal 30 mm	Hexagonal 35 mm	10 kHz	-	PCB coils
	Hui <i>et al.</i>	[67], [78]	2007	Hexagonal 36 mm	Hexagonal 36 mm	195 kHz	1.5-4 W	PCB coils

1.3.3 Discussion

Beyond the technical aspects, this section shows that there is no limit to the scope of the coils shape and configuration. They can be of meander type or of spiral type, planar or three-dimensional. Many shapes exist, such as circular, square, rectangular, hexagonal, . . . and nothing prevents from possibly generating new exotic geometries. They can be made of usual wires, Litz wires or PCB tracks. In array configurations, the coils can be placed in different arrangements and in different number of layers. This diversity gives a huge freedom to the designer, which is both an advantage and a challenge. The former because it opens the field of research into an infinite panel of possibilities, and the latter because it is impossible to consider every possibility.

Fortunately, this state of the art also highlights the limitations of different CET methods and therefore can orient towards the most favorable solutions. For fixed position charging, the most appropriate technique consists, with regard to the different presented applications, in using one primary coil and one secondary coil that are similar in shape and in size. This provides a high magnetic coupling which is the prerequisite to transfer the maximal power with a good efficiency.

For the free position charging, primary coils arrays are the most appropriate solution, and using larger secondary coils is interesting since it allows to integrate only one of them to each load, instead of multiple smaller ones. Furthermore, the PCB support without the addition of ferromagnetic structures offers, in our opinion, a great manufacturing benefit.

1.4 Motivations and objectives

As pointed out in the state of the art of the last section, an industrial application of a fully operational desktop able to supply multiple peripherals over a large area does not exist yet. The main goal of this thesis is to propose a design methodology of such CET systems.

Furthermore, optimizations for CET systems do exist but are only applicable to specific and isolated cases. This work aims to propose a design methodology that integrates an optimization of CET systems. With the developments presented in this thesis, it should be possible to perform an optimal CET design for different ranges of power, different coils configurations and different distances between the primary and secondary coils.

To be optimal, the CET system has to minimize losses in the coils and in the electronic components. Therefore, the resistance of the coils has to be accurately modeled in order to determine the inherent losses. This leads to issues linked to the use of high frequency currents in the coreless transformers, namely the skin effect and the proximity effect. These effects

are responsible for an increase of the resistance of the coils with the frequency. However they are most often neglected in the literature concerning CET systems design, and when they are taken into account, some assumptions are made that are difficult to justify for optimization purposes. Therefore an accurate modeling of these effects and their impact on the resistance of the coils is necessary to achieve an effective optimization.

With the coreless transformers and the high frequency effects accurately modeled, an optimization method can be used. For CET systems, the number of parameters that are involved is relatively high, and it may be interesting to optimize different objectives according to the application. For example, if a great amount of power is to be transferred, it could be advantageous to maximize the efficiency of the system. However, when the size of the coils has to remain small, in order to integrate them in electronic devices, the configuration (shape, number, arrangement, ...) that allows the maximal power transfer has to be researched. Therefore, a study has to be performed so as to identify the parameters to be optimized.

Many optimization methods exist and can be investigated. In electronic and electromagnetic design, a method that gains more and more success is the genetic algorithms (GAs). Its greatest advantage is to reach an optimal solution with lower cost of computation time than for conventional methods such as the gradient methods or response surface methods. Furthermore, it is well suited for problems involving a lot of parameters and also multiple objectives to optimize. An effective GA has to be developed and adapted in a way that makes it applicable to any CET system.

Finally, two different prototypes have to be built, as presented in section 1.2.2. The first one, that is the inductive notebook charger, will allow to verify the accuracy of the modeling and is above all challenging in terms of electronics. For the second prototype, that is the CET table able to supply different peripherals, two main challenges have to be fulfilled. First, the system has to be able to provide continuously a minimal amount of power at every position on the CET surface. Secondly, the prototype has to integrate an autonomous control unit that is able to detect the position of the peripherals and to control the activation of the energy transfer only where required.

1.5 Thesis structure

The thesis presents the modeling, optimization and implementation of different CET systems. It is divided into four main chapters in addition to the introduction and conclusion.

In the present chapter is given a general introduction on CET with a state of the art of the field and the main objectives of the thesis research.

Chapter 2 is dedicated to the modeling of the coreless transformers. First the “magnetic” part of the modeling allows to calculate resistances and inductances of the coils based on the geometry of the coreless transformers. Then the “electric” part allows to determine power magnitudes, current and voltage intensities, based on the resolution of an equivalent electric circuit of coreless transformers. Concepts of resonance and reactive power compensation are introduced then.

Chapter 3 deals with the high frequency effects in the coils. After defining the problem and providing the main inherent hypotheses to resolve it, two methods to compute the AC resistances that vary with the frequency are provided. The first one is based on the resolution of Maxwell’s equations in a particular case, and the second one is derived from finite-element-method (FEM) simulations. The issue of losses in the coils is then addressed and the impact of the high frequency is discussed.

Chapter 4 is probably the most important one because it provides innovative tools to design and optimize different CET systems. In the first part, a sensitivity analysis of the main parameters of coreless transformers is presented. This allows to identify the ones that need to be optimized, as well as their variation range. In the second part, the optimization method itself is described. The main concepts of genetic algorithms and, in particular, multiobjective genetic algorithms are introduced. The implementation of a new algorithm based on a very common one (called NSGA-II) is then presented. It integrates notably several improvements that make it highly efficient. It is then tested with some often-used functions for multiobjective algorithms evaluation, and successfully applied to different CET problems.

Chapter 5 presents the different prototypes built during this thesis work. The design the electronics are discussed in details. Notably, for the CET table, the strategy used to control the detection and the local activation of the table is thoroughly presented.

Chapter 6 ends with a general overview of the results obtained in this thesis. The perspectives and main contributions are also analyzed.

Coreless transformer modeling

Summary

2.1 Introduction	24
2.2 Coreless transformer modeling	25
2.2.1 Resistance	26
2.2.2 Magnetic flux density	26
2.2.3 Inductances	27
2.2.4 Coupling factor and quality factor	32
2.2.5 Validation and measurements	33
2.3 Equivalent electric circuit modeling	40
2.3.1 General electric circuit	42
2.3.2 The four topologies	45
2.3.3 Discussion	50
2.4 Conclusion	50

This chapter presents the fundamental aspects associated to CET systems. The concept of coreless transformer is introduced, and the modeling of the parameters linked to the geometry of the coils is proposed. The electric modeling is then described for different possible configurations and allows to calculate the power transferred to a load and determine efficiency issues.

2.1 Introduction

Basically, a CET system that involves a primary and a secondary coil is none other than a transformer. As it has no ferromagnetic structure, it is called in this thesis a coreless transformer. The theory of transformers can then be adapted and applied to CET systems, but a main difference distinguishes coreless transformers from conventional ones. Indeed, they suffer from weak mutual coupling. This is circumvented by operating at high frequencies (generally from 100 kHz to a few MHz) so as to enhance the mutual effect. Consequently, coreless transformers are characterized by high leakage inductances, which gives rise to a large reactive power that in turn generates additional losses. To solve this problem, a resonant circuit is implemented on both primary and secondary sides, by adding resonant capacitors (in series or in parallel).

The global energy chain for an usual CET system is represented in Fig. 2.1. Each part requires a special attention to design an efficient CET. At a first stage, the energy is generally provided by a DC voltage supply. A high frequency voltage is then generated by a high frequency converter. The energy is then passed through the coreless transformer, from the primary coil to the secondary coil and their respective resonant circuits. The voltage thus obtained has to be rectified so as to make it exploitable by the load.

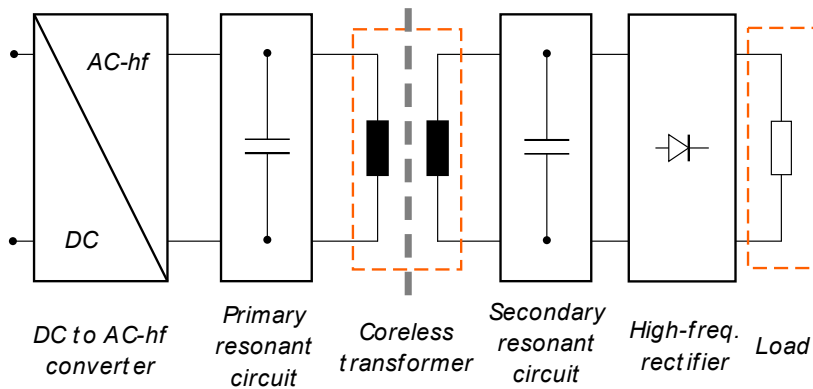


Figure 2.1: General coreless transformer system.

The aim of this chapter is to establish the modeling of coreless transformers in order to design and optimize CET systems. It is developed in a general way that ideally makes it applicable to all possible cases. Some parts of it have been published in [90], [88]. All coils types (solenoid, spiral, ...), all coils materials (Litz wires, PCB tracks, ...), all coils geometries (circular, square, rectangular, hexagonal, ...) can be modeled. The transformer configuration can as well be freely chosen so that the primary and the secondary coils may be close or distant, aligned or misaligned, and even different in shape or type.

The design of the coreless transformer is based on its equivalent circuit modeling. First the main components of the coreless transformer have to be calculated, such as inductances and resistances. Then, the electric circuit can be resolved. The design of the coreless transformers is therefore split into two main parts:

1. **The magnetic part:** With the geometry of the coreless transformer completely defined, it is possible to compute inductances and resistances of the coils. This part concerns the coreless transformer itself where the electromagnetic conversion takes place, and its modeling is presented in section 2.2. In this chapter, the skin and proximity effects are not taken into account. Only the formulations for DC resistance and inductance are presented. However, for high frequencies, these effects can not be neglected. This issue is discussed in chapter 3.
2. **The electric part:** Once inductances and resistances are accurately computed, an equivalent electric model of the coreless transformer can be generated. The resonant circuit plays here a significant role, and different possible configurations (series or parallel in the primary or in the secondary) can be considered. Currents, voltages, power, and efficiency involved in different components of the coreless transformer can thus be calculated. As a prerequisite, the value of the load, the amplitude of the input voltage (or current) and the power to be transferred have to be determined, according to the application and the specifications. The electric modeling is presented in section 2.3.

2.2 Coreless transformer modeling

At low frequencies (less than 200 kHz), the coils can be regarded as a resistor and an inductor in series, as illustrated in Fig. 2.2. The coupling between the primary coil and the secondary coil is represented by the mutual inductance. This section aims to calculate those different elements.

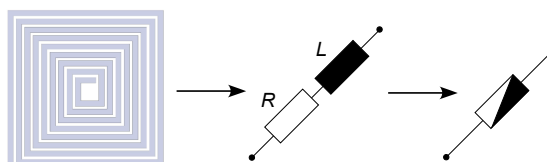


Figure 2.2: Equivalent electric circuit of a coil at low frequency.

2.2.1 Resistance

It is important to calculate the resistance of the primary and secondary coils in CET systems, because they represent the main limitation for the power that can be transferred. Actually, if resistances were zero, the efficiency of the coreless transformer would be 100 % and there would be no limitation to the amount of power that could be transferred. However, coils resistances generate heat due to Joule effect, and this heat has to remain at an acceptable level. Minimizing the Joule losses is then a crucial point while designing CET systems, in terms of efficiency and transferable power.

The resistance of a coil exhibits a DC behavior at DC and low frequencies (≤ 200 kHz). It means that the current is uniformly distributed over the cross-section of the conductor. The DC resistance R_{DC} of a coil is given by the well-known formula:

$$R_{DC} = \frac{\rho l}{S} \quad (2.1)$$

where ρ is the resistivity of the conductive material ($\rho = 17$ n Ω m for the copper at 21°C), l is the length of the conductor and S is the cross-section area of the conductor.

The DC resistance is often sufficiently accurate to design coreless transformers, and many examples found in literature simply neglect the high-frequency effects. Their impact on the resistance value mainly depends on the size of the cross-section and the frequency. To give an idea on the orders of magnitude, in a circular wire with a radius of 1 mm for example, they become noticeable at about 10 kHz [117]. Up to a frequency of 200 kHz, the influence of the high-frequency effects is generally insignificant when using PCB windings [51], [50] or Litz wires [118], [117].

2.2.2 Magnetic flux density

The magnetic flux density \mathbf{B} is a vector field that is created by a current in a conductor. It is related to the magnetic field \mathbf{H} through the magnetic permeability μ that characterizes the medium in which the conductor is situated:

$$\mathbf{B} = \mu \mathbf{H} = \mu_0 \mu_r \mathbf{H} \quad (2.2)$$

where μ_0 is the permeability of free space and μ_r the relative permeability of the magnetic medium. In coreless transformers, the coils are situated in the air for which the relative permeability is approximated to unity. With this, the magnetic flux density and the magnetic field are equivalent for coreless transformers, except for units. The \mathbf{B} -field is expressed in Tesla [T], and the \mathbf{H} -field is expressed in Ampere per metre [A/m].

It is interesting to compute the magnetic flux density in CET systems for three reasons. First, for health considerations, they can be used to foresee electromagnetic radiations that are generated by the conductors and then to verify if they fulfill regulation conditions. Secondly, the magnetic flux density can be used as a design tool for CET systems, like in [77], [24], [78]. By investigating its distribution over one or multiple coils, it is possible to avoid local drops of field intensity and consequently to ensure a minimal magnetic flux density everywhere. Finally, it is a part of a solution that leads to inductance calculation, as it will be shown in section 2.2.3.

The analytical solution for the magnetic flux density \mathbf{B} is given by the Biot-Savart's law [32]:

$$\mathbf{B} = \frac{\mu_0 I}{4\pi} \oint_C \frac{d\mathbf{l} \times \mathbf{R}}{R^3} \quad (2.3)$$

where I is the current in the conductor, C is the integration path of the conductor, R is the distance between the elementary integration length $d\mathbf{l}$ and the point where the magnetic flux density is evaluated. For example, this integral is easily solved for a straight conductor of finite length. Assuming that the primary and secondary coils are parallel to the (x, y) plane, only the \mathbf{B} -field in the z -direction has a contribution to CET. For a straight segment parallel to y -axis, such as the one shown in Fig. 2.3, the magnetic flux density in the z -direction is evaluated at a position (x, y, z) by [53], [82]:

$$B_z(x, y, z) = \frac{\mu_0 I}{4\pi} \left(\frac{l_2 - y}{\sqrt{(l_1 + x)^2 + z^2 + (l_2 - y)^2}} + \frac{l_2 + y}{\sqrt{(l_1 + x)^2 + z^2 + (l_2 + y)^2}} \right) \left(\frac{l_1 + x}{(l_1 + x)^2 + z^2} \right) \quad (2.4)$$

where l_2 is half the length of the segment and l_1 its distance from the y -axis. For simple coils such as square ones or hexagonal ones, this equation has to be adapted and applied to each segment. The addition of their individual contribution gives then the magnetic flux density generated by the coil. For more complex geometries, the same strategy is applied: The conductor is divided into multiple segments that have to be sufficiently small so as to be considered as straight. The magnetic flux density is then calculated at a position (x, y, z) by summing the contributions of all small segments.

2.2.3 Inductances

In literature, inductances calculations have been a lot explored, but most of the time, the developed solutions are only applicable to specific coil shapes:

- circular coils in [123], [68], [69];
- rectangular coils in [60];

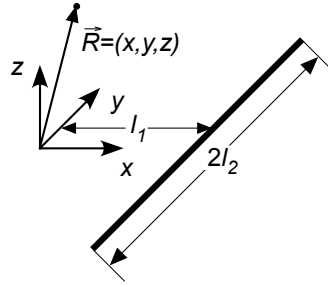


Figure 2.3: Spatial configuration of a straight conductor of finite length.

- square coils in [27],[80];
- square, hexagonal, octagonal and circular in [94], but the model requires adjustments for each individual case.

The aim here is to describe an analytical model that can be applied to any coils. So far, two different methods can be used. The first one consists in using the magnetic flux density and Stokes' theorem [90]. The second one consists in using Neumann's formula [117], [113].

Mutual inductance

The mutual inductance in a CET system is a crucial point, because it defines its ability to transfer power. It is an image of the mutual coupling and of the link between the primary and the secondary coils. It contains the information of how they influence each other in a coreless transformer.

Stokes' theorem

With this method, the strategy consists first in calculating the mutual inductance between two single-turn coils. These coils can be approximated by two closed loops. Their mutual inductance is then calculated using the Stokes' theorem and the magnetic vector potential:

$$M = \frac{1}{I_1} \oint_{C_2} \mathbf{A}_1 \cdot d\mathbf{l}_2 = \frac{1}{I_1} \iint_{S_2} \nabla \times \mathbf{A}_1 \cdot d\mathbf{S} = \frac{1}{I_1} \iint_{S_2} \mathbf{B}_1 \cdot d\mathbf{S} \quad (2.5)$$

Here, \mathbf{A}_1 is the magnetic vector potential and \mathbf{B}_1 is the magnetic flux density issued from the primary coil current I_1 . S_2 is the area delimited by the secondary coil. The analytical solution for \mathbf{B}_1 is given by eq. (2.3). This equation has to be numerically integrated on the area delimited by the second coil in order to evaluate the mutual inductance between the two coils.

For primary and secondary coils that have more than one turn, the total mutual inductance L_{12} is obtained by summing mutual inductances between each possible pair of turns:

$$L_{12} = \sum_{i=1}^{n_1} \sum_{j=1}^{n_2} M_{ij} \quad (2.6)$$

where n_1 is the number of primary turns, n_2 the number of secondary turns, and M_{ij} the mutual inductances between the i -th primary turn and the j -th secondary turn. The required number of iterations is therefore equal to $n_1 \cdot n_2$, and the computation resource may become heavy above a certain amount of turns.

It is then possible to use the equivalent spire method, which consists in concentrating all the primary turns in one equivalent turn and repeating the process for the secondary coil. In this case, each turn of the primary coil is assumed to be traversed by an identical magnetic flux, and the same goes for the secondary coil. The mutual inductance M_{eq} between the equivalent primary turn and secondary one can then be seen as the mutual permeance between the primary and secondary coils. The resulting value for the mutual inductance between the two coils is given by:

$$L_{12} = n_1 \cdot n_2 \cdot M_{eq} \quad (2.7)$$

This allows to reduce drastically the computation resources, but in return the result suffers from a lower accuracy, especially if the turns of one of the coils are distant from each other.

Neumann's formula

The second method for inductance calculations is given by Neumann's formula [31], [113]. It provides the analytical equation for the mutual inductance between two coils of any shape:

$$L_{12} = \frac{\mu_0}{4\pi} \oint_{C_2} \oint_{C_1} \frac{dl_2 \cdot dl_1}{R} \quad (2.8)$$

where C_1 is the integration path of the primary conductor, C_2 is the integration path of the secondary conductor, and R is the distance between the two elementary integration lengths dl_1 and dl_2 . A schematic view of two coils and their different parameters is given in Fig. 2.4.

The Neumann's formula is complicated to use directly. It can be evaluated in two steps. First, the magnetic vector potential is calculated as follows:

$$\mathbf{A}_1 = \frac{\mu_0 I_1}{4\pi} \oint_{C_1} \frac{dl_1}{R} \quad (2.9)$$

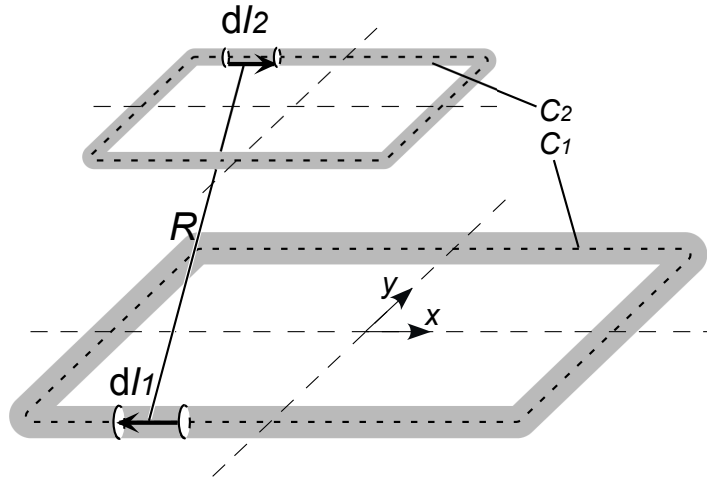


Figure 2.4: Computation of the mutual inductance. Here, two square coils with a single closed turn are represented, but eq. (2.8) can be applied to any conductor shape.

Then, the mutual inductance is expressed as a function of the vector potential:

$$L_{12} = \frac{1}{I_1} \oint_{C_2} \mathbf{A}_1 \cdot d\mathbf{l}_2 \quad (2.10)$$

Self inductance

The self inductance of a coil characterizes its ability to generate a magnetic field. It is important for CET systems since it influences the power that can be transferred and plays an important role to achieve a resonance phenomenon.

The evaluation of self inductances is performed in a similar way as the mutual inductance, but the problem of the singularity present in (2.3) or (2.8) when $R = |\mathbf{R}| = 0$ has to be addressed. As in [117], it is circumvented by splitting the self inductance into two parts:

$$L_1 = L_i + L_e \quad (2.11)$$

where L_e is the external inductance and L_i the internal inductance. The external inductance can as well be expressed by Stokes' theorem or Neumann's formula, but unlike for the mutual inductance, C_2 is the integration path on the wire surface, as illustrated in Fig. 2.5.

The internal part is at it largest at a low frequency and decreases when the frequency increases.

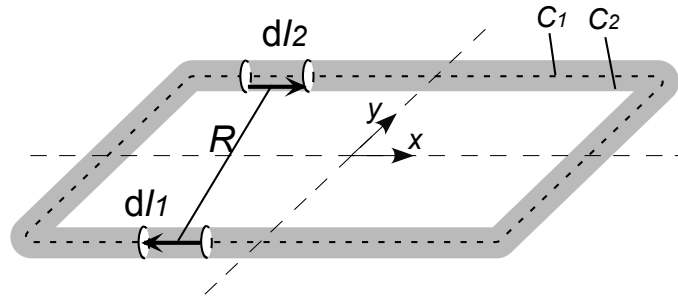


Figure 2.5: Computation of the self inductance.

Generally, the internal self inductance is one or two orders of magnitude lower than the external one. For example in [117], the DC internal part is calculated for a conductor of circular cross-section using Ampere’s law and the energy stored in a coil [32], [97], as follows:

$$L_{i,DC} = \frac{\mu_0 l}{8\pi} \tag{2.12}$$

With this, at DC frequency, the internal self inductance is equal to 50 nH/m and is independent on the radius of the conductor. With the development that will be presented in chapter 3, it is possible to determine the internal induction for a rectangular cross-section. For reader’s interest, table 2.1 gives the values of internal inductance for rectangular cross-sections of different aspect ratios and at DC frequency.

Table 2.1: Calculated DC internal self inductance for conductors of rectangular cross-section with different aspect ratios.

Aspect ratio	1:1	1.2	1:5	1:10	1:15
Internal self inductance [nH]	48	43	27	16	11

Numerical implementation

Equations (2.8), (2.9) and (2.10) have no analytical solutions except for very specific cases such as circular coils, and so they can not be solved by direct means. A numerical solution must be applied. Therefore, the contours of both primary and secondary coils are divided into small segments and the integrals are approximated by sums. These equations are then rewritten under their discretized form.

The discretized forms for Biot-Savart’s law (2.3), Neumann’s formula (2.8), the magnetic vector

potential (2.9) and (2.10) are respectively given by:

$$\mathbf{B} = \frac{\mu_0 I}{4\pi} \sum_{C_1} \frac{\Delta \mathbf{l}_1 \times \mathbf{R}}{R^3} \quad (2.13)$$

$$L_{12} = \frac{\mu_0}{4\pi} \sum_{C_2} \sum_{C_1} \frac{\Delta \mathbf{l}_2 \cdot \Delta \mathbf{l}_1}{R} \quad (2.14)$$

$$\mathbf{A}_1 = \frac{\mu_0 I_1}{4\pi} \sum_{C_1} \frac{\Delta \mathbf{l}_1}{R} \quad (2.15)$$

$$L_{12} = \frac{1}{I_1} \sum_{C_2} \mathbf{A}_1 \cdot \Delta \mathbf{l}_2 \quad (2.16)$$

Here, the infinitesimal vectors $d\mathbf{l}_1$ and $d\mathbf{l}_2$ from integral formulations become respectively the vectors $\Delta \mathbf{l}_1$ and $\Delta \mathbf{l}_2$ whose discretization length, also called step size, has to be judiciously chosen.

Indeed, the crucial point concerning the discretized model is to set the correct step size. There is a trade-off between the computation time and the resulting accuracy. In [117], experimental rules are defined in order to choose the largest step size providing a solution with an acceptable error. Nevertheless, the impact of the step size on the obtained results is more deeply analyzed in section 2.2.5.

2.2.4 Coupling factor and quality factor

Two more parameters are often used to describe coreless transformers. The first one is the coupling factor that can be expressed as follows:

$$k = \frac{L_{12}}{\sqrt{L_1 L_2}} \quad (2.17)$$

where L_{12} is the mutual inductance between the primary and secondary coils, L_1 , and L_2 are their respective self inductances. In conventional transformers, this value is close to 1, but for coreless transformers a coupling factor around 0.5 (when the coils are well aligned) is very

good, and for applications involving a large air gap, its value is often below 0.1.

The second one is the quality factor of a coils:

$$Q = \frac{\omega L_1}{R_1} \quad (2.18)$$

where ω is the pulsation associated to the operating frequency. This factor is an image of the quality of a given coil. It defines its capacity to generate a large magnetic field and low losses. According to [18], a quality factor below 10 represents a really poor coil that should be avoided for CET, and values around 100 are excellent for industrial applications.

2.2.5 Validation and measurements

In order to validate the modeling of coreless transformers, a series of verifications are undertaken. Therefore multiple experimental coils are used for measurements and comparisons with the modeling. Before entering these considerations, it is necessary to define the main parameters that are involved in coreless transformers so as to be able to describe correctly the geometry of experimental coils.

To validate the modeling of the coreless transformers, two coils shapes (rectangular and hexagonal) and two types of wires (Litz wires and PCB tracks) are considered. Furthermore, their size is chosen in order to cover a large range of possible solutions.

Geometric parameters

The coils have different geometric parameters depending on whether they are rectangular or hexagonal and whether they are made of PCB tracks or Litz wires. These differences are shown in Fig. 2.6, and the parameters involved in coreless transformers are defined in Table 2.2. Except for g , indices 1 or 2 can be attached to all parameters. They represent respectively the primary and the secondary coil. Besides those parameters could be also added the misalignment of the secondary coil compared to the primary one. Assuming the coils are parallel to the (x, y) plane, the misalignment is defined by the displacements x_d and y_d . As a result they are zero when the centers of the coils are superimposed.

Experimental coils

The characteristics of the experimental coils used in the following sections are presented in Table 2.3. The two first proposed coils are rectangular shaped, made of Litz wires and their size is rather large compared to the others. In fact, they are respectively the primary and the

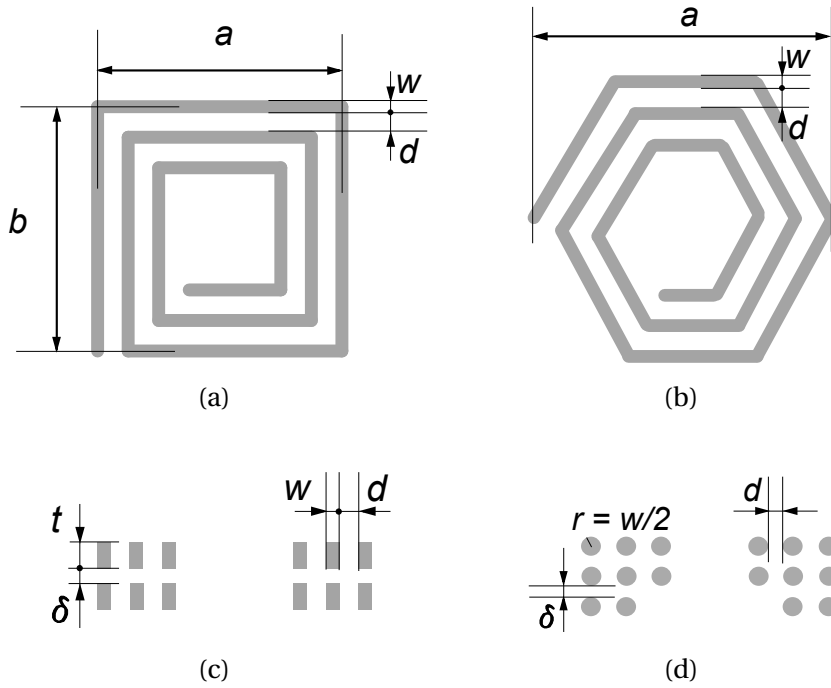


Figure 2.6: Top views of (a) a rectangular coil and (b) a hexagonal coil. Cross-sections of (c) a PCB coil and (d) a coil with conventional or Litz wires.

Table 2.2: Geometric parameters

Parameter	Definition	
n	Number of turns	
N	Number of layers for the turns distribution	
d	Space between two turns	
δ	Space between two layers	
g	Air gap	
	Rectangular Shape	Hexagonal Shape
a	First side length	Diameter
b	Second side length	-
	Rectangular Cross-section	Circular Cross-Section
w	Track width	-
t	Track thickness	-
r	-	Wire radius

secondary coils used in the prototype of the inductive notebook charger. The other ones are all made of PCB. Coils 3 to 6 are square, and coils 7 to 10 are hexagonal.

Table 2.3: Characteristics of the experimental coils

	Type	n	N	a [mm]	b [mm]	w [mm]	t [μm]	r [mm]	d [mm]	δ [mm]
1	Litz	1	1	220	140	-	-	1.0	-	-
2	Litz	10	3	220	140	-	-	1.0	0	0
3	PCB	16	1	50	50	1.0	105	-	0.5	-
4	PCB	28	2	30	30	0.5	105	-	0.5	0.6
5	PCB	18	2	40	40	1.5	105	-	0.5	0.2
6	PCB	20	2	40	40	1.0	105	-	0.5	0.2
7	PCB	10	1	34.64	-	0.2	35	-	0.8	-
8	PCB	10	1	34.64	-	0.9	35	-	0.1	-
9	PCB	5	1	50	-	1.5	105	-	0.5	-
10	PCB	15	1	50	-	0.5	105	-	0.5	-

Magnetic flux density validation

The computed magnetic flux density (2.3) is verified by comparing it with results obtained from magneto-static FEM simulations. Assuming the coils parallel to the (x, y) plane, only the z -component of the magnetic flux density is evaluated. Its distribution is compared using coil 5 for two different heights.

First, the distribution of the magnetic flux density computed with (2.3) at a height of $z = 5$ mm over the coil 5 when it is excited by a current of 1 A is shown in Fig. 2.7(a). It is compared to FEM simulation in Fig. 2.7(b). The results show a good agreement since the relative difference between computed and simulated values remains below 2 %. The maximal difference is obtained in the center of the coil, where the intensity of the magnetic flux density is the highest.

Then, a second comparison is made with the same conditions but at a height of $z = 1$ mm over the coil 5. The results computed with (2.3) and simulated are respectively given in Fig. 2.7(c) and (d). The relative difference remains below 9 %, and the maximal values are obtained at the corners of the most internal turns. This difference can be explained by the very short distance of evaluation and by the approximation of (2.3), where the wires are considered as infinitely thin filaments. So all the current is concentrated in these filaments, and this results in a larger magnetic field intensity just over them, especially when the distance of evaluation is short.

Inductances: step size definition

In order to find the good compromise between accuracy and time computation, the step size for the numerical implementation of inductances presented in section 2.2.3 is analyzed through two sets of computations.

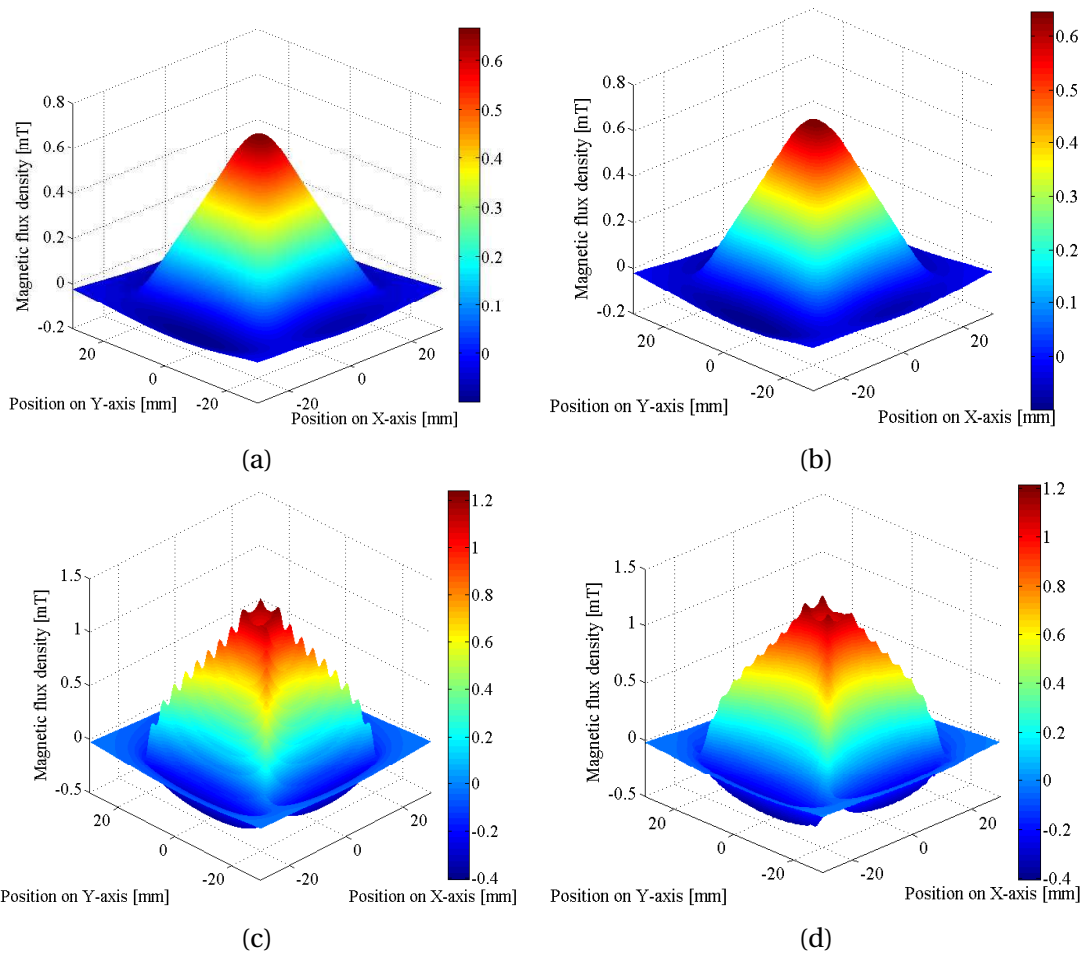


Figure 2.7: (a) Magnetic flux densities generated by coil 5 when it is excited by a 1 A current. Computed with the Biot-Savart's law (a) and with the FEM software (b) at a height of $z = 5$ mm. Computed with the Biot-Savart's law (c) and with the FEM software (d) at a height of $z = 1$ mm.

In the first set of computations, the effect of the step size on the self inductance is analyzed. In Fig. 2.8, the self inductances of coils 2 and 5 are plotted as a function of the step size. In both cases, the self inductance converges when the step size becomes sufficiently small. For coil 2 (Fig. 2.8(a)), which has a relatively large size, the self inductance converges to a value of $49.12 \mu\text{H}$, and a step size of 10 mm still provides a good approximation resulting in a relative difference of 1.02 % with the convergence value. For coil 5 (Fig. 2.8(a)), which is much smaller, the model converges to a self inductance of $68.90 \mu\text{H}$, and a relative difference of 0.73 % is obtained with a step size of 1 mm. More values of computed self inductances with their corresponding relative difference with the converged result are given in Table 2.4. In brief, it can be stated that the correct step size changes according to the dimensions of the concerned coil.

2.2. Coreless transformer modeling

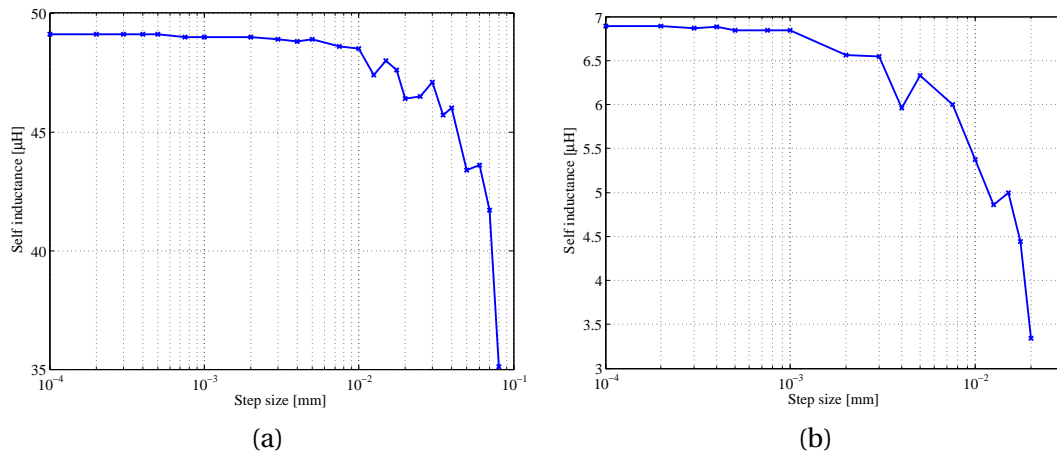


Figure 2.8: Self inductance computed as a function of the step size for coil 2 (a) and for coil 5 (b).

Table 2.4: Self inductance computations as a function of the step size.

	Step size [mm]	0.1	0.5	1.0	2.0	5.0	10.0	20.0	50.0
Coil 2	Computed self inductance [μH]	49.1	49.1	49.0	49.0	48.9	48.6	46.4	43.4
	Relative difference [%]	0	0	0.20	0.20	0.41	1.02	5.50	11.61
Coil 5	Computed self inductance [μH]	68.9	68.4	68.4	65.6	63.3	53.7	33.4	-
	Relative difference [%]	0	0.73	0.73	4.79	8.13	22.06	51.52	-

In the second set of computations, the effect of the step size on the mutual inductance is analyzed. Fig. 2.9(a) shows the mutual inductances between coils 1 and 2 as a function of the air gap. They are computed using Stokes' theorem (2.5) and Neumann's formula (2.14). The former is solved using directly the function *dblquad* from the MATLAB toolbox, and the later is solved with different step sizes. The results show that both approaches provide equivalent results for small step sizes. More specifically, for step sizes smaller or equal to 10 mm, the relative difference using Stokes' theorem is much smaller than 1 %.

Fig. 2.9(b) shows the mutual inductances between coils 5 and 6 as a function of a lateral displacement x_d . Only a positive displacement along the X axis is considered for symmetry reasons. The results show that Stokes' theorem and Neumann's formula with a step size of 1 mm provide equivalent results with a relative difference much smaller than 1 %. For a step size of 10 mm, the difference becomes more noticeable, that is about 13.7 % when x_d is equal

Chapter 2. Coreless transformer modeling

to zero, but it decreases when x_d becomes larger.

It is also interesting to compare the computation time between Stokes' and Neumann's approaches and for different step sizes. The goal is to obtain accurate values (with a relative difference smaller than 1 %) in the shortest computation time. The interest comes from that it allows to gain a considerable time in an optimization process that may require more than 10^5 inductances computations (see chapter 4). In Fig. 2.9(b), nine different positions are evaluated for the mutual inductance computations. The computation time is compared in Table 2.5 for both approaches and for different step sizes. Hence, the discretized model is really interesting, even for small step sizes, because it provides accurate and quick results.

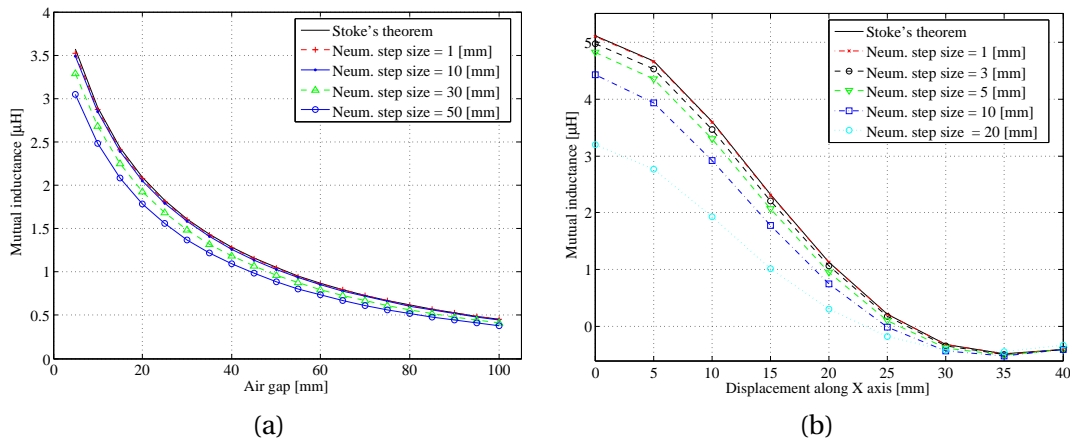


Figure 2.9: (a) Mutual inductance computation between coils 1 and 2. (b) Mutual inductance computation between coils 5 and 6.

Table 2.5: Computation time for different cases issued from Fig. 2.9(b).

Neumann's formula Step size = 10 mm	Neumann's formula Step size = 1 mm	Neumann's formula Step size = 0.1 mm	Stokes' theorem
~ 1 s	5 s	43 s	278 s

As a conclusion, it can be stated that the dimensions of the coils have a major impact on the choice of the step size which must be fixed accordingly. For the mutual inductance, the larger the distance between the coils (lateral or vertical), the lower is the impact of the step size.

However, the step size is more critical for the self inductance computation, as seen through the two sets of computations. As a global rule, we consider the results of an inductance computation as accurate enough when the step size does not cause an error greater than 1 % in comparison with its value of convergence. In all cases encountered in this work, a step size of 0.5 mm for the mutual inductances and a step size of 0.1 mm for the self inductances fulfil

by far this condition while considering coils with an external size greater or equal to 20 mm. Thereby, those step sizes are used by default in this thesis or it is mentioned otherwise.

Inductance measurements

The inductances are measured with a HP Precision LCR Meter 4284A (20Hz-1MHz) at 200 kHz. Litz wires are used as connection cables from the coils to the LCR Meter, and they are reduced to their shortest length so as to minimize their effect on the measurement. Generally, their contribution to the total inductance is insignificant, as their length is much shorter than the one of the coil track. But in the following measurements, they are taken into account. The inductance of connection cables is evaluated by measuring it on a twisted pair of straight Litz wires of 1 mm radius, resulting in a linear inductance of $0.6 \mu\text{H}/\text{m}$. For instance, the contribution of the connection cables for coils 3 to 6 is much smaller than 1 % of the total self inductance and can be therefore neglected. This is due to the high number of turns which ensures a long length of track. For coils 1 and 2, the inductance of the connection cables corresponds respectively to 12.9 % and 0.4 % of the total inductance. Because the coil 1 has only a single turn, the length of the connection cables are significant compared to the length of the coil itself, and as a result, their effect on the total inductance cannot be neglected.

In Table 2.6, the measured self inductances of coils 1 to 10 are compared with the computed ones. For the measurements, the inductance of the connection cables is subtracted. The relative error between measurements and computations with Neumann's formula is also provided. Measured and computed results are in good agreement as relative errors remain smaller than 6 %.

Table 2.6: Results of the self inductance computations and measurements

Coil #	Stoke	Neumann	Measurement	Error
1	806 <i>nH</i>	791 <i>nH</i>	821 <i>nH</i>	3.65 %
2	49.12 μH	49.11 μH	52.20 μH	5.73 %
3	5.97 μH	5.97 μH	5.85 μH	2.05 %
4	11.18 μH	11.15 μH	11.35 μH	1.76 %
5	6.91 μH	6.89 μH	7.12 μH	3.23 %
6	11.44 μH	11.43 μH	11.50 μH	0.61 %
7	2.49 μH	2.48 μH	2.43 μH	2.06 %
8	2.27 μH	2.25 μH	2.35 μH	4.26 %
9	1.22 μH	1.22 μH	1.28 μH	4.69 %
10	7.12 μH	7.10 μH	7.24 μH	1.93 %

The method used to measure mutual inductances is as follows. First of all, the coils are set in the position for which the mutual inductance is wanted to be measured. Two successive

Chapter 2. Coreless transformer modeling

measurements are then required. First, both coils are connected in series, and the inductance L_A thus obtained is defined as:

$$L_A = L_1 + L_2 + 2L_{12} \quad (2.19)$$

where L_1, L_2 are the self inductances of the coils and L_{12} is the mutual inductance. Secondly, the terminals of one of the coil are inverted, which gives the inductance L_B defined as:

$$L_B = L_1 + L_2 - 2L_{12} \quad (2.20)$$

The mutual inductance is then deduced by:

$$L_{12} = \frac{1}{4}(L_A - L_B) \quad (2.21)$$

The mutual inductance can be deduced only from (2.19) if the self inductance of both coils is known. However, performing the second measurement provides more accurate results as the error due to the connection cables is automatically compensated in the subtraction of (2.21).

In Table 2.7, the measured mutual inductances between different couples of coils 1 to 6 are compared with computed ones. The relative error is given between the results computed with the Neumann's formula and the measurements. They are in good agreement with errors remaining below 5 %.

Table 2.7: Results of the mutual inductance computations and measurements.

Coupled coils	Airgap	Stoke	Neumann	Measurement	Error
1-2	15 mm	2.51 μH	2.48 μH	2.58 μH	3.88 %
1-2	30 mm	1.63 μH	1.62 μH	1.69 μH	4.14 %
3-4	2.5 mm	4.72 μH	4.71 μH	4.80 μH	1.88 %
3-4	5 mm	3.66 μH	3.65 μH	3.78 μH	3.44 %
5-6	5 mm	5.11 μH	5.11 μH	4.91 μH	4.07 %

Finally, in Fig. 2.10, the mutual inductance between coils 1 and 2 is measured when the air gap is varied, and the mutual inductance between coils 5 and 6 is measured when the lateral displacement is varied, as for Fig. 2.9. In both cases the relative error between measured and computed values remains smaller than 8 %.

2.3 Equivalent electric circuit modeling

The goal of this section consists in calculating the electric parameters of the transformer once the inductances and the resistances are known. It is possible to determine the voltages and

2.3. Equivalent electric circuit modeling

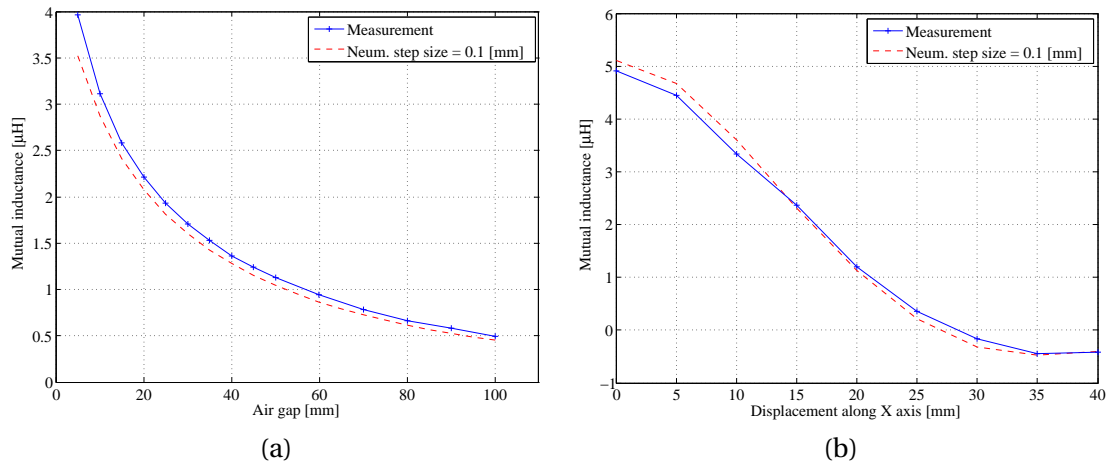


Figure 2.10: (a) Measured and computed mutual inductance between coils 1 and 2. (b) Measured and computed mutual inductance between coils 5 and 6.

currents in the primary and secondary sides with the voltage equations of the transformer, and consequently the power generated by the source or consumed by the load. In the second part of this section, the choice of the compensation capacitors and their evaluation are discussed.

The main electric parameters of coreless transformers are listed in Table 2.8.

Table 2.8: Electric parameters.

Parameter	Definition
L_1	Primary inductance
L_2	Secondary inductance
L_{12}	Mutual inductance
R_1	Primary resistance
R_2	Secondary resistance
R_L	Load resistance
C_1	Primary compensation capacitor
C_2	Secondary compensation capacitor
I_1	RMS source current
I_{L1}	RMS current in the primary coil
I_2	RMS load current
I_{L2}	RMS current in the secondary coil
ω	Electric pulsation

2.3.1 General electric circuit

Let us consider the electric circuit in the simplest case, *i.e.* when no compensation capacitors are present. This circuit is shown in Fig. 2.11. The approach to solve the coreless transformer circuit is similar to the one proposed in [38], [37], [90], but is adapted and treated more in detail. The system is assumed to be excited by a perfect sine wave in a steady state condition.

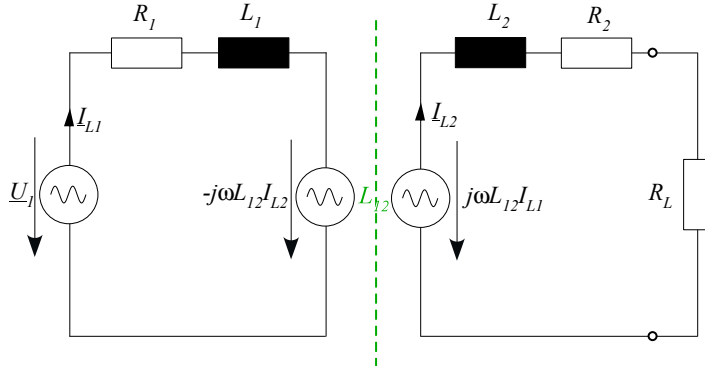


Figure 2.11: Electric circuit of the coreless transformer.

In this section, a distinction is made between the current delivered by the source \underline{I}_1 and the current flowing in the primary coil \underline{I}_{L1} . Similarly for the secondary side, a distinction is made between the current in the load \underline{I}_1 and the current in the secondary coil \underline{I}_{L1} . However, when there are no compensation capacitors or when they are placed in series with the self inductances, those currents are respectively equal (*i.e.* $\underline{I}_1 = \underline{I}_{L1}$ and $\underline{I}_2 = \underline{I}_{L2}$). This can be observed in Fig. 2.13.

As a result, when there are no compensation capacitors, the primary and secondary voltage equations are respectively given by:

$$\underline{U}_1 = R_1 \underline{I}_{L1} + j\omega L_1 \underline{I}_{L1} - j\omega L_{12} \underline{I}_{L2} \quad (2.22)$$

and

$$\underline{U}_2 = j\omega L_{12} \underline{I}_{L1} = (R_2 + R_L) \underline{I}_{L2} + j\omega L_2 \underline{I}_{L2} \quad (2.23)$$

Here, the first equality of the second voltage equation is not so trivial. It provides the basic information on how inductive coupling works and governs the condition that allows to obtain higher voltage levels at the secondary. Indeed, the voltage induced in the secondary coil is proportional to the frequency, the mutual inductance and the current of the primary coil. If the transferred power is wanted to be increased for a given application, at least one of these three parameters has to be increased.

2.3. Equivalent electric circuit modeling

An usual way to solve the circuit consists in analyzing the effect of the complete secondary circuit on the primary side. Basically, the secondary circuit is viewed from the primary voltage supply as an impedance, namely the reflected impedance \underline{Z}_R which is highly dependent on the geometric configuration of the primary and secondary coils. The electric circuit of the coreless transformer can be fully determined in four steps, as shown in Figs. 2.11 and 2.12.

1. **Step 1:** The electric circuit of the coreless transformer is given in Fig. 2.11. The unknown variables are the current in the primary coil I_{L1} and the current in the secondary coil I_{L2} ;
2. **Step 2:** The secondary circuit is reduced to a single impedance \underline{Z}_2 (Fig. 2.12(a));
3. **Step 3:** The whole secondary circuit is replaced by the reflected impedance \underline{Z}_R in the primary (Fig. 2.12(b));
4. **Step 4:** Knowing the total equivalent impedance \underline{Z}_{eq} viewed from the voltage supply (Fig. 2.12(c)), it is possible to determine I_{L1} and then to deduce I_{L2} .

To determine the reflected impedance, it is convenient to write the secondary components as a single impedance, that is the total secondary impedance \underline{Z}_2 given by:

$$\underline{Z}_2 = R_2 + R_L + j\omega L_2 \quad (2.24)$$

Then by substituting I_{L2} from (2.23), the term $j\omega L_{12}I_{L2}$ of (2.22) becomes:

$$j\omega L_{12}I_{L2} = -\frac{\omega^2 L_{12}^2}{\underline{Z}_2} I_{L1} = -\underline{Z}_R I_{L1} \quad (2.25)$$

As a result, the reflected impedance can be expressed as follows:

$$\underline{Z}_R = \frac{(R_2 + R_L)\omega^2 L_{12}^2}{(R_2 + R_L)^2 + \omega^2 L_2^2} - j \frac{\omega^3 L_{12}^2 L_2}{(R_2 + R_L)^2 + \omega^2 L_2^2} \quad (2.26)$$

where the first term is respectively the real part and the second term the imaginary part of the reflected impedance. With this, (2.22) becomes:

$$\underline{U}_1 = (R_1 + j\omega L_1 + \underline{Z}_R)I_{L1} = \underline{Z}_{eq}I_{L1} \quad (2.27)$$

with \underline{Z}_{eq} the total impedance seen by the voltage supply. It is determined by combining the primary and secondary circuits. Assuming that the sinusoidal voltage amplitude of the supply \underline{U}_1 is known, (2.27) allows to calculate the current I_{L1} that flows in the primary coil. The power P_{12} transferred from the primary coil to the secondary is given by the real part of the reflected

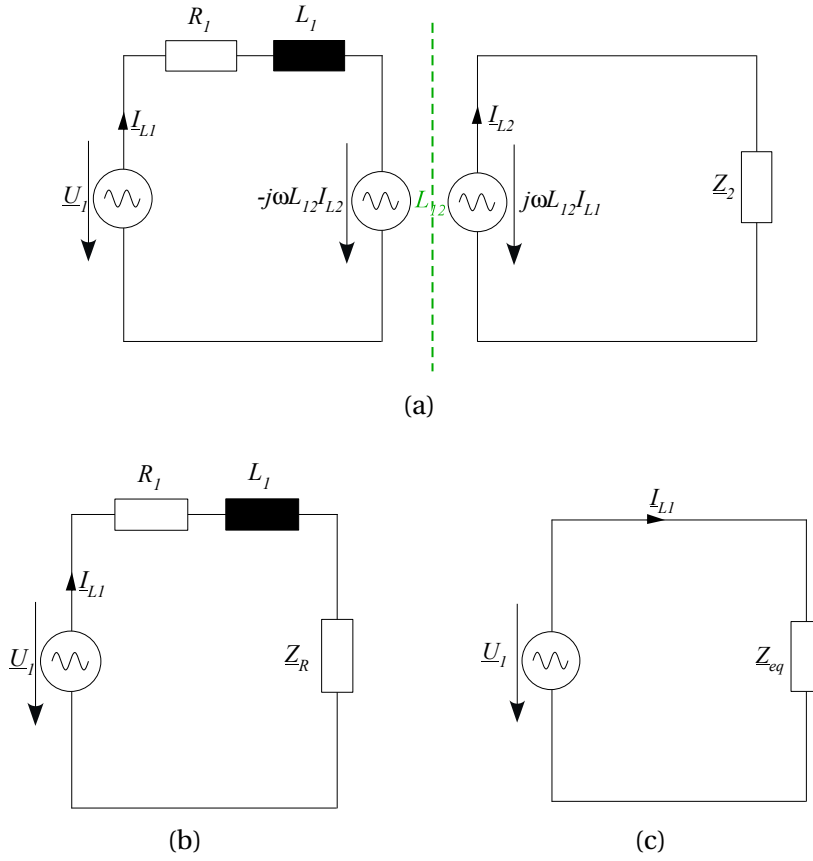


Figure 2.12: (a) Step 2: Simplification of the secondary circuit. (b) Step 3: Reflected impedance of the secondary circuit. (c) Step 4: Total equivalent impedance of the coreless transformer.

impedance multiplied by the square of the primary current magnitude as follows:

$$P_{12} = \Re \underline{Z}_R I_{L1}^2 \quad (2.28)$$

Assuming that the input voltage \underline{U}_1 is perfectly sinusoidal, the difference between the input power P_{in} delivered by the voltage supply and the transferred power P_{12} corresponds to the Joule losses in the resistance of the primary coil. Furthermore, the power transferred to the load is defined as the load resistance multiplied by the square of the secondary current amplitude:

$$P_L = R_L I_{L2}^2 \quad (2.29)$$

Similarly, the difference between the transferred power P_{12} and the load power P_L is due to the Joule losses in the resistance of the secondary coil. So basically, considering the simple

coreless transformer presented in this subsection, three issues can be stated:

1. The losses in coreless transformers are caused only by the Joule effects in respectively the primary and secondary coils. Therefore, these resistances are wanted to be as small as possible. In the same time, the self-inductances of the coils have to be maximized, since they represent their ability to generate a magnetic flux density for a given current. Generally, a high inductance goes with a high resistance, so there is a trade-off with an optimal solution for every application which has to be investigated. The goal is then to use coils with the highest possible quality factor.
2. For a coreless transformer without secondary resonant capacitors the power transferred to the load can not be sufficient unless the input voltage is large. The reason is that the secondary coil impedance $R_2 + j\omega L_2$ is generally great and therefore is responsible for a significant current drop in the load resistance. The simplest way to circumvent this issue is to increase the input voltage so that the power transferred to the load is sufficient. But this solution is not optimal because it requires higher current amplitudes in the primary coil, which in turn generates greater Joule losses. This may lead to dramatic results in terms of efficiency and Joule losses.
3. The previous point leads to the necessary addition of resonance capacitors to the primary and secondary circuits. By decreasing or even cancelling the large reactance of a coil, the resonance capacitors allow to reduce the current amplitudes and therefore to improve the efficiency of coreless transformers, and the optimum is reached at the resonance frequency. Resonant circuits are widely used to enhance inductive power transmission. They involve an alternating exchange of energy between the capacitor and the inductance of the coil, and the amount of energy required to maintain the oscillation is minimal. To understand this effect, it can be compared to the movement of a swing, where the energy of each push is added to the total energy if applied at the right time. There are many different possible configurations for the capacitors, as discussed in the following subsection. They have also an impact on the equations presented above.

2.3.2 The four topologies

In addition to the case where they are not present, the resonance capacitors can be placed in parallel or in series with the inductance of the coil. In the scope of this thesis, only the cases when they are present are considered of interest. This gives four different possible configurations. In the following, the letter S stands for a capacitor in series with the coil and P for a capacitor in parallel. The four topologies shown in 2.13 are labelled as SS, PS, SP and PP, where the first letter identifies the primary capacitor and the second one identifies the

secondary capacitor.

Each different topology has its advantages and drawbacks. The choice has to be made according to the specifications of the application to develop. In [120], [125], [126], [127], these advantages and drawbacks are discussed more in detail. However, the different topologies are discussed without taking into account the resistances of the coils because they are assumed to be insignificant.

Therefore, in the following points, each topology is briefly discussed. The addition of the capacitors modifies the equations presented in the previous section. The new formulations for the different topologies are presented and the resistances of the coils are also included in the model.

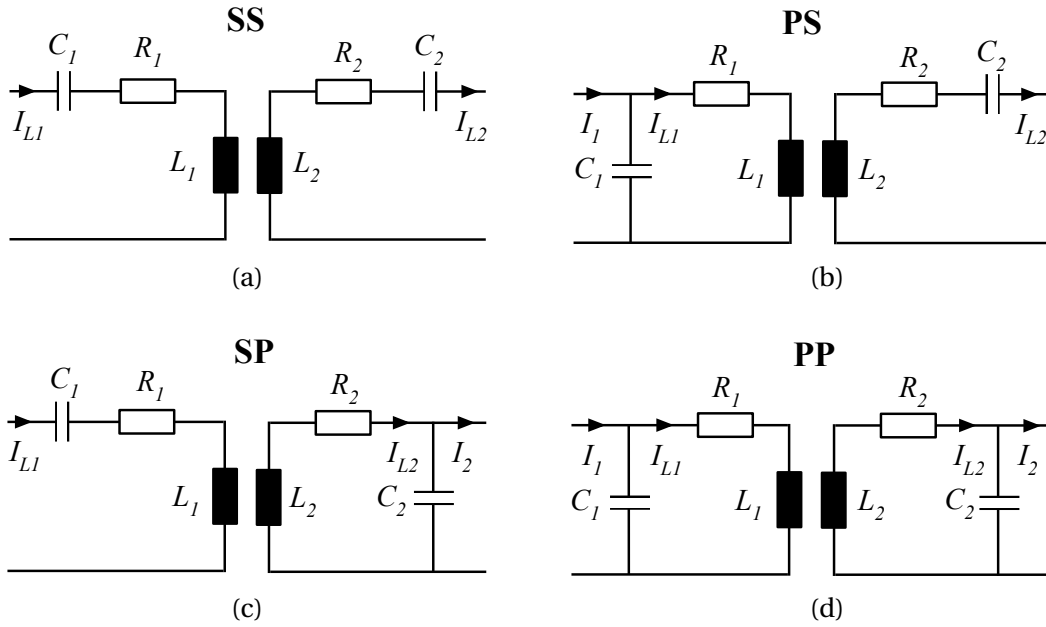


Figure 2.13: (a) Series-Series (SS) topology. (b) Parallel-Series (PS) topology. (c) Series-Parallel (SP) topology. (d) Parallel-Parallel (PP) topology.

Series compensated secondary

With the addition of a series capacitor, the secondary impedance (2.24) and the reflected impedance (2.26) can be rewritten as follows:

$$\underline{Z}_2 = R_2 + R_L + j\omega L_2 - j \frac{1}{\omega C_2} \quad (2.30)$$

and

$$\underline{Z}_R = \frac{\omega^4 C_2^2 L_{12}^2 (R_2 + R_L)}{(\omega^2 C_2 L_2 - 1)^2 + \omega^2 C_2^2 (R_2 + R_L)^2} - j \frac{\omega^3 C_2 L_{12}^2 (\omega^2 C_2 L_2 - 1)}{(\omega^2 C_2 L_2 - 1)^2 + \omega^2 C_2^2 (R_2 + R_L)^2} \quad (2.31)$$

To obtain the maximal power transferred from the primary to the secondary of (2.28), the goal is to maximize the real part of the reflected impedance and to cancel the imaginary part. By working at the resonance frequency, an advantage of a series compensation capacitor is that the secondary impedance and therefore the reflected impedance are purely resistive. So there is no reflected reactance generating additional losses. The secondary resonance frequency is given by:

$$\omega_0 = \frac{1}{\sqrt{L_2 C_2}} \quad (2.32)$$

At the resonance frequency, the total secondary impedance \underline{Z}_2 becomes:

$$\underline{Z}_2 = R_2 + R_L + j(\omega_0 L_2 - \frac{1}{\omega_0 C_2}) = R_2 + R_L \quad (2.33)$$

As a result, the reflected impedance is given by:

$$\underline{Z}_R = \frac{\omega_0^2 L_{12}^2}{R_2 + R_L} \quad (2.34)$$

which is purely resistive. This shows with (2.28) that a series compensated secondary behaves like a voltage source and is well suited to supply a stable load voltage when the coreless transformer is supplied by a current source. This statement is verified through a set of calculations in appendix A.

Another advantage of the secondary compensated capacitor is that the resonant frequency is independent on the mutual inductance, which is interesting for applications where the secondary coil position is expected to be variable.

Parallel compensated secondary

With the addition of a parallel capacitor, the secondary and reflected impedances are respectively given by:

$$\underline{Z}_2 = R_2 + j\omega L_2 + \frac{1}{\frac{1}{R_L} + j\omega C_2} \quad (2.35)$$

and

$$\underline{Z}_R = \frac{\omega^2 L_{12}^2 (1 + \omega^2 L_2^2 R_L^2) (R_2 + R_L + \omega^2 L_2 C_2 R_L)}{(R_2 + R_L + \omega^2 L_2 C_2 R_L)^2 + (\omega L_2 - \omega C_2 R_L R_2 - \omega C_2 R_L^2)^2} - j \frac{\omega^2 L_{12}^2 (1 + \omega^2 L_2^2 R_L^2) (\omega L_2 - \omega C_2 R_L R_2 - \omega C_2 R_L^2)}{(R_2 + R_L + \omega^2 L_2 C_2 R_L)^2 + (\omega L_2 - \omega C_2 R_L R_2 - \omega C_2 R_L^2)^2} \quad (2.36)$$

Here, just to simplify the expression and to highlight the impact of the parallel compensated capacitor, the resistance of the secondary is neglected, keeping in mind that it is not the case in the model. At the resonant frequency, the reflected impedance is then reduced to:

$$\underline{Z}_R = \frac{L_{12}^2 R_L}{L_2^2} - j \frac{\omega_0 L_{12}^2}{L_2} \quad (2.37)$$

Thereby, the reflected impedance has a capacitive reactance when the secondary capacitor is in parallel. Of course, this reactance can be also compensated by the primary inductance together with the primary capacitor.

Given that the coreless transformer is supplied by a current source, (2.28) with (2.37) show that a parallel compensated secondary behaves like a current source and is well suited to supply a stable secondary load current. This statement can be verified through a set of computations given in appendix A.

Series compensated primary

A series compensated primary can be used to cancel the inductance of the coil at resonance frequency. This allows to reduce the voltage of the source to manageable levels. The total impedance \underline{Z}_{eq} seen by the voltage supply is given by:

$$\underline{Z}_{eq} = R_1 + j\omega L_1 + \frac{1}{j\omega C_1} + \underline{Z}_R, \quad (2.38)$$

where the imaginary part is cancelled at resonance frequency. A great advantage of this primary topology is that the reactive impedance compensation of the primary coil is independent on the mutual inductance and the load resistance. To perform this, the capacitor has to be simply designed so that it exactly cancels the impedance of the primary inductance:

$$C_1 = \frac{1}{\omega_0^2 L_1}. \quad (2.39)$$

However, this topology has also two disadvantages. First, when the load becomes small or

when the mutual inductance becomes weak (which happens when the secondary coil is removed from the CET system for example), the primary circuit will draw very large currents from the source. This is due to the decrease of the reflected impedance and to the fact that the primary inductance is cancelled by the primary capacitor. To solve this problem, a current limitation has to be implemented.

Secondly, if the load increases (that is the load resistance decreases) or if the mutual inductance increases (that is when the primary and secondary coils are well aligned), the reflected impedance will greatly increase, which in turn will cause the primary current to decrease and thus result in a smaller power transferred to the load. This is unacceptable to ensure a minimal voltage induced in the load. To solve this problem, a primary current regulation should be implemented.

Parallel compensated primary

A parallel capacitor is generally used to generate large currents in the primary coil, which in return may require a large voltage supply because of the intrinsic large impedance of the primary coil at high frequency. The total impedance \underline{Z}_{eq} seen by the voltage supply is given by:

$$\underline{Z}_{eq} = \frac{1}{j\omega C_1 + \frac{1}{R_1 + j\omega L_1 + \underline{Z}_R}} \quad (2.40)$$

In this configuration, the interesting point is that the voltage applied to the primary coil is also the voltage applied to the capacitor. At resonance frequency, the current and the voltage delivered by the sinusoidal voltage supply should have a zero phase angle. This way they are exactly in phase and no reactive loss is generated.

The strategy to design the primary capacitor consists in considering the total circuit without the capacitor itself and to write its corresponding impedance as follows:

$$\underline{Z}_t = R_1 + j\omega L_1 + \underline{Z}_R = R_t + jX_t \quad (2.41)$$

where \underline{Z}_t is the total impedance seen by the voltage source without the primary capacitor, R_t and X_t are respectively the real part and the imaginary part of this impedance. The total impedance in (2.40) can then be rewritten as follows:

$$\underline{Z}_{eq} = \frac{R_t}{(1 - \omega C_1 X_t)^2 + \omega^2 C_1^2 R_t^2} + j \frac{X_t - \omega C_1 R_t^2 - \omega C_1 X_t^2}{(1 - \omega C_1 X_t)^2 + \omega^2 C_1^2 R_t^2} \quad (2.42)$$

Here, the condition of zero phase angle is reached only if \underline{Z}_{eq} is purely resistive. Therefore the

primary capacitor has to be designed so that the imaginary part of (2.42) is cancelled. This is achieved with:

$$C_1 = \frac{X_t}{\omega(R_t^2 + X_t^2)} \quad (2.43)$$

For example, in the specific case of a series compensation of the secondary coil and at the resonance frequency, the primary capacitor takes the following form:

$$C_1 = \frac{L_1(R_2 + R_L)^2}{\omega_0^4 L_{12}^4 + \omega_0^2 (2R_1 L_{12}^2 (R_2 + R_L) + L_1^2 (R_2 + R_L)^2) + R_1^2 (R_2 + R_L)^2} \quad (2.44)$$

A similar development can be made for a parallel compensated secondary. The main drawback of a parallel compensation at the primary is that the compensation of the reactive part of the whole circuit is a function of the mutual inductance and the load. However, the reflected impedance is generally much smaller than the primary coil impedance and therefore the impact of its variation is not critical for the primary capacitor design.

2.3.3 Discussion

In this section, the equivalent electric circuit of the coreless transformer has been presented. The different topologies with or without compensation capacitors have been analyzed through the general equations of transformers. The main contributions here are the integration of the resistances in the model and the discussion on the advantages and drawbacks of the different existing topologies.

2.4 Conclusion

In this chapter, different aspects of the coreless transformer have been addressed. First, the analytical and numerical models for the inductances have been presented. The model has then been validated through multiple sets of measurements. A special effort has been put in determining the right compromise between the computation time and the accuracy in anticipation of the forthcoming problem of optimization.

In the second part of this chapter, the equivalent electric circuit of the coreless transformer has been thoroughly analyzed, allowing to highlight the advantages and drawbacks of the different existing compensation topologies.

High frequency effects

Summary

3.1 Introduction	52
3.1.1 Definition of the skin and proximity effects	52
3.1.2 Equivalent electric circuit of a coil	53
3.1.3 Joule losses and efficiency issues	56
3.1.4 Problem definition	56
3.2 First numerical method	59
3.2.1 Current density modeling	59
3.2.2 Resistance calculation	61
3.2.3 Internal self inductance calculation	62
3.2.4 Validation and measurements	63
3.3 Numerical modeling using FEM	65
3.3.1 Introduction	65
3.3.2 Geometrical structure and model of a coil	65
3.3.3 Meshing of the conductors	67
3.3.4 Physical and electrical definition	68
3.3.5 Validation and measurements	70
3.4 Discussion	70
3.5 Exploitation of FEM simulations	72
3.5.1 Design of experiments	72
3.5.2 Complete output mapping	74
3.6 Effective impact of the high frequency on CET	76
3.7 Overall conclusion	77

This chapter addresses the high frequency (HF) effects in the coils. Two different methods are investigated. The first one is based on the resolution of Maxwell's equations. The second one uses FEM simulations. A strategy to exploit effectively the results is then developed. Finally, the main repercussions of HF effects on coreless transformers are analyzed in terms of losses and efficiency.

3.1 Introduction

3.1.1 Definition of the skin and proximity effects

Working at high frequency gives rise to effects that alter the behavior of electric currents in conductors. A time-varying current flowing inside a conductor generates a magnetic field that interacts with the current itself. More specifically, the varying magnetic field induces currents that oppose the one generated by the external source at the center of the cross-section, and that strengthen it at the periphery.

If a single conductor is involved, this results in a current accumulation at its periphery, and the higher is the operating frequency, the greater becomes this accumulation. This is referred to as the skin effect. For multiple close conductors, the current undergoes interactions from one conductor to another, and the current also tends to accumulate at their periphery. This is referred to as the proximity effect. Both skin and proximity effects are caused by the same physical phenomenon. They can be modeled in a similar way, and they define how the resistance and the internal self inductance of a coil varies with the frequency. Many works in literature have tried to define high frequency effects in conductors, and a short review of the most interesting ones is proposed here.

For a single circular conductor, the skin effect can be easily expressed in an analytical form with Bessel equations [54], [93], [118]. For multiple neighboring conductors, a numerical solution is derived from 2D-FEM simulations in [117].

In [26], [66], the impedance of rectangular conductors is computed by dividing the cross-section into several subbars, which allows to obtain a numerical solution for single and multiple conductors.

Another interesting method for multiple conductors of rectangular cross-section is presented in [44], [43], [42], based on the evaluation of the electric field and the current density on each segment of the discretized perimeter cross-sections.

In [61], the skin and proximity effects are evaluated through 2D-FEM simulations. Corrective

coefficients are derived and integrated to the impedance of the coil. These coefficients are functions of the frequency, the geometry and the fill factor of the conductors.

Finally, The PEEC (Partial Element Equivalent Circuit) method can be used to extract the electric parameters such as the resistance and the self inductance from the geometry of the conductors. It is well adapted to model structures that contain different kinds of metallic conductors. Multiple publications deal with the PEEC method [36], [47], and commercialized softwares exist such as the InCa3D solver by Cedrat [22]. The main advantage of this solution compared to the FEM one is that only the conductors have to be meshed and not the surrounding air, which allows to reduce the computation time.

3.1.2 Equivalent electric circuit of a coil

Formulations for DC resistance R_{DC} and DC internal self inductance $L_{i,DC}$ of coils are respectively discussed in sections 2.2.1 and 2.2.3. However, CET is performed at high frequencies, generally situated from 10 kHz to 5 MHz, which may induce changes in the magnitudes of resistance and inductance. To differentiate them from the DC case, we speak of AC resistance R_{AC} and AC internal self inductance $L_{i,AC}$. Furthermore, the modeling of the inductor coil proposed in Fig. 2.2 is no longer valid at high frequencies, as the parasitic capacitance may be no more negligible.

The multiple parallel turns of the coil gives rise to an equivalent parasitic capacitance in parallel to the resistance and inductance of the coil, as illustrated in Fig. 3.1. This parasitic capacitance C_{par} is relatively small (in the order of 10 pF) which makes it insignificant at low frequencies but not at very high frequencies (> 5 MHz).

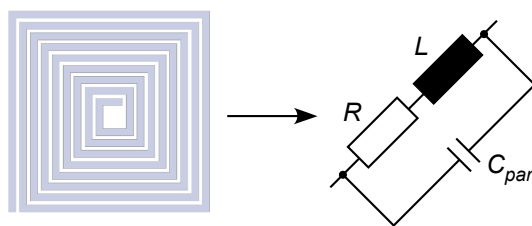


Figure 3.1: Equivalent electric circuit of a coil at high frequency.

As a result, the impedance of a coil is defined as follows:

$$\underline{Z}^{-1} = j\omega C_{par} + \frac{1}{R + j\omega L} \quad (3.1)$$

where R and L are respectively the resistance and the self inductance of the coil. This gives

respectively the following real and imaginary parts for the coil impedance:

$$\Re \underline{Z} = \frac{R}{(1 - \omega^2 LC_{par})^2 + (\omega RC_{par})^2} \quad (3.2)$$

$$\Im \underline{Z} = \frac{\omega L - \omega R^2 C - \omega^3 L^2 C_{par}}{(1 - \omega^2 LC_{par})^2 + (\omega RC_{par})^2} \quad (3.3)$$

For the modeling of the coreless transformers, it is not necessary to compute accurately the parasitic capacitance, as its impedance is insignificant compared to the one of the other components. For example, the measured parasitic capacitance of coil 5 (from Table 2.3) is 88 pF. This is a great value because of the large track width and the two copper layers. The corresponding impedance of the parasitic capacitance is about 9 k Ω at 200 kHz and 0.9 k Ω at 2 MHz. It is much greater than the impedance of the self inductance that is 8.67 Ω at 200 kHz and 86.70 Ω at 2 MHz. For comparison, the measured parasitic capacitance of coil 10 is 1.14 pF. At 200 kHz, the impedance of its parasitic capacitance is about 70 k Ω and the impedance of its self inductance is 8.92 Ω , and at 2 MHz, they are respectively 7 k Ω and 89.22 Ω .

So the parasitic capacitance can be neglected for the modeling of the coreless transformer. However, it may have an impact on the measurement of the resistance and the self inductance of a coil and therefore has to be taken into account. The reason comes from that the parasitic capacitance and the self inductance form a resonant circuit which leads to a huge increase of impedance at resonance frequency. Fig. 3.2 shows a typical impedance variation of a coil with hypothetical values of $R = 1 \Omega$, $L = 5 \mu\text{H}$, $C_{par} = 10 \text{ pF}$. The self resonance frequency f_s of a coil can be calculated by:

$$f_s = \frac{1}{2\pi\sqrt{LC}} \quad (3.4)$$

This results for the values given above (corresponding to Fig. 3.2) to a self resonance frequency of 22.50 MHz.

In practice, the resistance and self inductance of a coil cannot be measured by direct means with a RLC meter at high frequency, because the resistance, the self inductance and the parasitic capacitance cannot be physically dissociated. Instead, the real and imaginary parts of its impedance \underline{Z} are easily obtained. The self resonance frequency is determined by analyzing the measured curves and the value of the parasitic capacitance can be derived from (3.4). The effective measured resistance and self inductance are then obtained by resolving the system of equations (3.2) and (3.3).

Furthermore, a few remarks concerning the operating frequency can be made. The operating

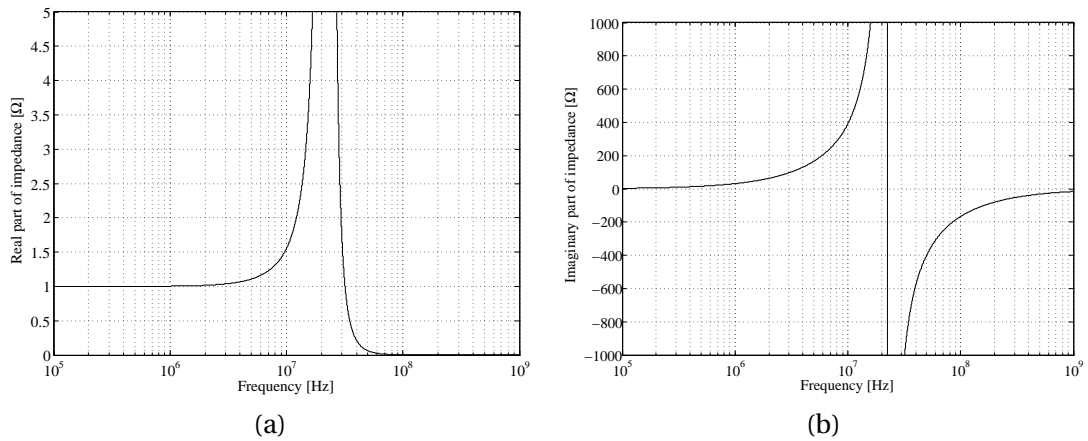


Figure 3.2: Typical impedance of a coil versus the frequency, with hypothetical values $R = 1 \Omega$, $L = 5 \mu\text{H}$, $C = 10 \text{ pF}$ (a) Real part. (b) Imaginary part.

frequency has to be smaller or equal to the resonance frequency, because above it, the coil behaves as a capacitor rather than an inductor. In some specific cases, the parasitic capacitance can be used as a parallel compensation capacitor or part of it [57]. But this possibility has been tested only for the secondary coil and for transferring a low power (about 0.1 W in [57]). For applications that require a larger power transfer, further research should be undertaken concerning the current distribution in the coil at resonance frequency.

In a series compensated topology, the self resonance frequency has to be avoided because the self inductance of the coil, the parasitic capacitor and the compensation capacitor form a more complex circuit that may generate resonance phenomena that are difficult to predict and control. In [112], it is stated that the operating frequency should be at least 10 times smaller than the resonance frequency so as to avoid the side effects of the parasitic capacitance in a CET system involving a series compensation topology. This factor here is overly estimated, and using adequately equations (3.2) and (3.3) allows to reduce this factor. Practically, for every coil encountered in this thesis, a factor of 5 has revealed to be sufficient to obtain precise measurements and the expected behavior of the coreless transformer.

In summary for the equivalent circuit of a coil, the parasitic can be neglected in the modeling of coreless transformers, but has to be taken into account for the measurements of the parameters of the coil. The maximal operating frequency has to be at least 5 times lower than the self resonance frequency of the coils, as follows:

$$f \leq \frac{f_s}{5} \quad (3.5)$$

where f_s is the self resonating frequency. For single-layer coils, the self resonance frequency

is generally situated between 30 MHz and 100 MHz. Their maximal operating frequency is then set to 5 MHz. However, for two-layers coils, the self resonating frequency can be situated between 5 and 10 MHz. Therefore, the maximal frequency for two-layers coils is frequently set to 1 or 2 MHz.

3.1.3 Joule losses and efficiency issues

Assuming there is no metallic material in vicinity, the only losses that are generated when a current is flowing through a coil are the Joule losses. Considering the equivalent circuit of Fig. 3.1, the Joule losses P_j are defined as:

$$P_j = \Re Z I^2 \quad (3.6)$$

where I is the amplitude of the current (AC rms) in the coil and Z the impedance of the coil. Given that condition (3.5) is respected, the only source of Joule losses are the resistances of the coils. Then, by considering only the losses in the coreless transformer (and not the ones generated in electronic components), the efficiency is given by:

$$\eta = \frac{P_{in}}{P_{out}} = \frac{P_{in}}{P_{in} + P_{loss}} = \frac{P_{in}}{P_{in} + \sum_{i=1}^m P_{j,i}} \quad (3.7)$$

where m is the number of coils in the coreless transformer and $P_{j,i}$ their associated Joule losses.

3.1.4 Problem definition

Most experts and designers of CET systems involving PCB coils (this is also valid for Litz coils) agree that, below 200 kHz, high frequency effects can reasonably be neglected [50], [51]. But the veracity of this statement cannot be proven for every case and the limits of its applicability are fuzzy. Furthermore, over 200 kHz these effects can be no more neglected and have a large impact on the Joule effects. The aim of the following sections should be to generate a numerical model of the high frequency effects on the resistance and internal self inductance. However, at this point, the focus of this chapter can be substantially restricted thanks to two reasons.

First, the skin and proximity effects for conductors of circular cross-section has been thoroughly addressed in [117]. Therein, experimental factors derived from FEM simulations are introduced in the analytical solution of the resistance and internal self inductance for a single circular cross-section. As a result it is possible to compute R_{AC} and $L_{i,AC}$ as a function of

the frequency, the radius of the wire, the number of turns, the number of layers of turns, the vertical space between turns, and the horizontal space between turns. For more details the reader should refer to [117]. The key point of the proposed method is the existence of an analytical solution for the current distribution in a conductor of circular cross-section [54], [93], [118]. Unfortunately, there is no such analytical solution for a rectangular cross-section, and therefore another numerical method has to be investigated for PCB coils.

Secondly, preliminary measurements on PCB coil samples have shown that the internal self inductance does not significantly change when the frequency is varied up to 5 MHz. Different AC resistances and AC self inductances (measured on coils 5, 7 and 10 defined in Table 2.3) are plotted respectively in Figs. 3.3 and 3.4. This shows that the frequency has a great impact on the resistance but a small one on the self inductance.

As a recall, the measurements of inductance are performed at 200 kHz by default in this thesis. The maximal relative difference obtained for self inductances considering the whole spectrum (from 10 kHz to 5 MHz) compared to this default value does not exceed 5 % for all the coils tested in this work. For instance, the maximal error obtained for coil 5 (in Fig. 3.4) is 4.13 %. In this case, the fluctuation is due to the the large width of the track combined with the distribution of the turns in two layers. However, this difference is not significant and does not require a proper care for optimization purposes. Furthermore, this difference can be compensated by adapting the resonance capacitors consequently. For comparison, the resistance of coil 7 in Fig. 3.3 is 27 % greater at 5 MHz than at low frequency. This increase of resistance is relatively weak compared to most encountered coils, due to the small width and thickness of the track. But such a variation of resistance can not be neglected and affects largely the losses of CET systems.

Regarding the few previous statements, it has been decided to focus the domain of study of HF effects to the resistance of PCB coils, that is for rectangular cross-section conductors. Therefore in the following sections, the aim is to modelize the AC resistance of PCB coils at frequencies from 10 kHz to 5 MHz. The upper limit is set at 5 MHz essentially because of electronics and hardware issues at higher frequencies. The lower limit is set at 10 kHz as it is not expected to go below for CET systems to transfer a minimal amount of power. Since the DC resistance is already defined by eq. (2.1), the goal is to obtain a multiplicative coefficient r_{AC} that modifies this DC resistance as follows:

$$R_{AC} = r_{AC}R_{DC} \tag{3.8}$$

This coefficient is a function of the coil geometry and of the operating frequency. It is interesting to isolate this coefficient instead of using the absolute value of AC resistance, because it provides a pragmatic quantification of the high frequency effects.

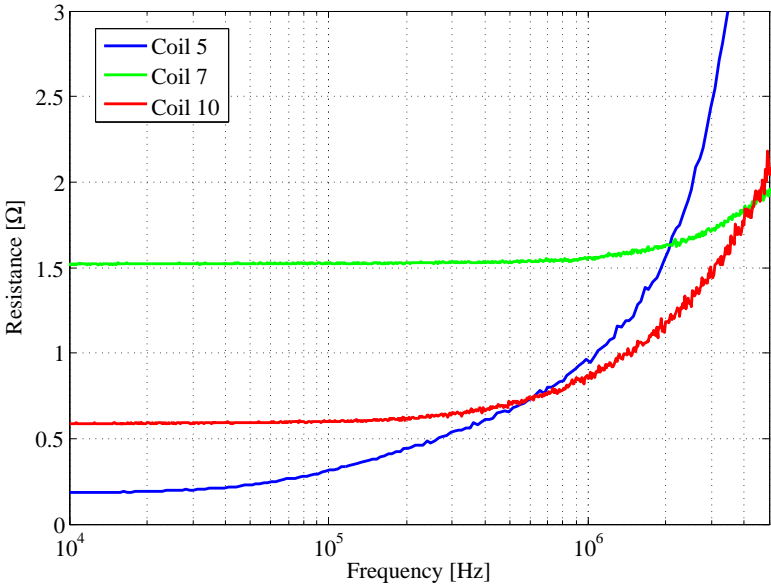


Figure 3.3: Typical variation of the resistance versus the frequency for coils 5, 7 and 10.

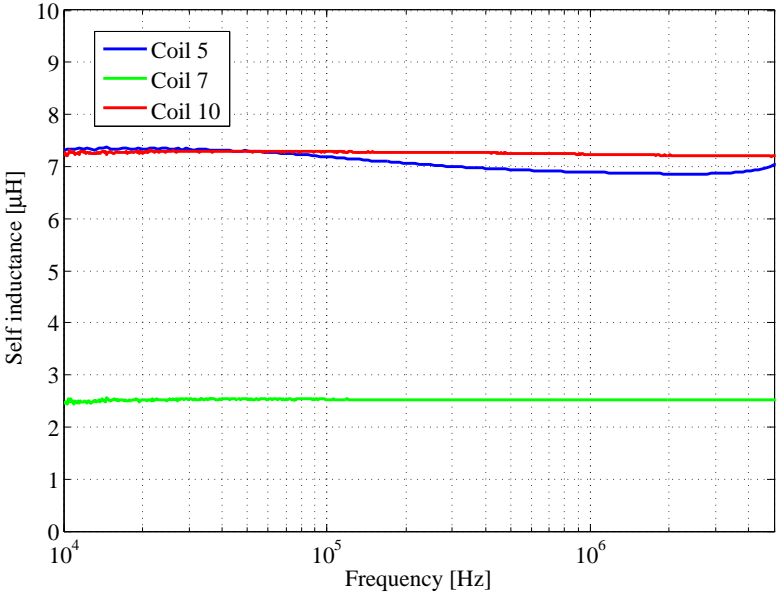


Figure 3.4: Typical variation of the self inductance versus the frequency for coils 5, 7 and 10.

Two different methods are investigated to provide the AC resistance of a coil. The first one is presented in section 3.2 and the second one in section 3.3.

3.2 First numerical method

3.2.1 Current density modeling

This numerical method is based on [26]. The first step to modelize the high frequency effects consists in evaluating the current distribution on the cross-section of the conductor. The shape of the cross-section as well as the number of parallel conductors are also free parameters in this method. Furthermore, the conductors are assumed to be infinite in length and the current flows in the z -direction only.

Through a theoretical development that can be found in [26], [65], [109], the magnetic vector potential, that is also solely z -directed, is given in the (x, y) -plane by:

$$A(x, y) = \frac{\mu_0}{2\pi} \int_S J(x', y') \ln \sqrt{(x - x')^2 + (y - y')^2} dx' dy' \quad (3.9)$$

where S is the cross section of the conductor. The current density $J(x, y)$ is defined by the integral equation:

$$J(x, y) = -\frac{j\omega\mu_0\sigma}{2\pi} \int_S J(x', y') \ln \sqrt{(x - x')^2 + (y - y')^2} dx' dy' + J_{\omega=0}(x, y) \quad (3.10)$$

Here, μ_0 is the permeability of free space, σ is the conductivity of the copper, and $J_{\omega=0}(x, y) = -\sigma|\nabla V|$ is the current density generated by the voltage supply, and corresponds to the current density at low frequencies. By solving this last equation, it is possible to calculate the current density distribution over the cross-section. But, except for a circular cross-section, it has no analytical solution, that is why a numerical one is used to solve the problem. It is an integral equation with the unknown function $J(x, y)$. As it is not possible to solve it under this form, it will be approximated by a matrix equation and then solved by inversion.

To do so, the cross-section is divided into multiple rectangular subbars, as shown in Fig. 3.5. Each subbar can be different in width w_i and thickness t_i , resulting in a section S_i . If the subbars are sufficiently small (that is smaller than half the skin depth), the current density can be assumed constant over their cross-section. It allows to rewrite equation (3.10) under the

form of a sum, as follows:

$$J(x_m, y_m) = -\frac{j\omega\mu_0\sigma}{2\pi} \sum_{n=1}^N J(x_n, y_n) \int_{S_n} \ln \sqrt{(x_m - x')^2 + (y_m - y')^2} dx' dy' + J_{\omega=0}(x_m, y_m) \quad (3.11)$$

Here, (x_m, y_m) is the position of the m -th subbar.

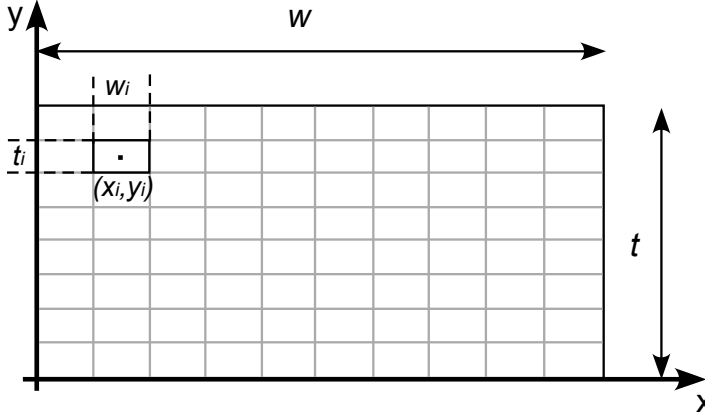


Figure 3.5: Conductor of rectangular cross-section.

In order to transform equation (3.11) into a matrix form, it is necessary to solve the integral of this last equation. Three different computation methods can be used [63], [110], [109], [65], and are discussed in appendix B. They lead to the determination of the integral:

$$Q_{mn} = \int_{S_n} \ln \sqrt{(x_m - x')^2 + (y_m - y')^2} dx' dy' \quad (3.12)$$

and equation (3.11) takes the simpler form:

$$J(x_m, y_m) = -\frac{j\omega\mu_0\sigma}{2\pi} \sum_{n=1}^N J(x_n, y_n) Q_{mn} + J_{\omega=0}(x_m, y_m) \quad (3.13)$$

Equation (3.11) may be applied for all subbars $m = 1, \dots, N$. This gives a set of complex equations that can be written using matrix notation:

$$\begin{bmatrix} c_{1,1} + 1 & c_{1,2} & \cdots & c_{1,N} \\ c_{2,1} & c_{2,2} + 1 & \cdots & c_{2,N} \\ \vdots & \vdots & \ddots & \vdots \\ c_{N,1} & c_{N,2} & \cdots & c_{N,N} + 1 \end{bmatrix} \begin{bmatrix} J_1 \\ J_2 \\ \vdots \\ J_N \end{bmatrix} = \begin{bmatrix} J_{\omega=0,1} \\ J_{\omega=0,2} \\ \vdots \\ J_{\omega=0,N} \end{bmatrix} \quad (3.14)$$

with $J_1 = J(x_1, y_1)$, $J_2 = J(x_2, y_2), \dots, J_N = J(x_N, y_N)$ and the coefficients c_{mn} defined as follows:

$$c_{mn} = \frac{j\omega\mu_0\sigma Q_{mn}}{2\pi} \quad (3.15)$$

Equation (3.14) can be expressed under its algebraic form:

$$(\mathbf{C} + \mathbf{U})\mathbf{J} = \mathbf{J}_{\omega=0} \quad (3.16)$$

where \mathbf{U} is the unit matrix, \mathbf{C} is the matrix of the coefficients c_{kl} , \mathbf{J} is the vector of the z -oriented current densities and $\mathbf{J}_{\omega=0}$ the vector of the current densities at a zero-frequency. Solving (3.16) allows to compute the current density for every subbar, and the distribution of the potential vector \mathbf{A} is calculated by resolving equation (3.9). With the assumption that the current is constant over each subbar, the vector potential in the m -th subbar becomes:

$$A_m = A(x_m, y_m) = \frac{\mu_0}{2\pi} \sum_{n=1}^N J_n Q_{mn} \quad (3.17)$$

This way, the vector potential can be evaluated for every subbar.

3.2.2 Resistance calculation

Knowing the current distribution in the conductor, it is possible to calculate the linear resistance R_{lin} of the conductor. The idea consists in equating the total power dissipated in the conductor S to the sum of the powers in every individual subbar as follows:

$$R_{lin}|I_{tot}|^2 = \sum_{n=1}^N \frac{\rho}{S_n} |I_n|^2 = \rho \sum_{n=1}^N |J_n|^2 S_n = \rho \int_S |J|^2 dS \quad (3.18)$$

where I_{tot} is the total current flowing in the conductor and is obtained by summing the currents in each subbar as follows:

$$I_{tot} = \sum_{n=1}^N I_n = \sum_{n=1}^N J_n S_n = \int_S J dS \quad (3.19)$$

Combining (3.18) and (3.19) yields the linear resistance:

$$R_{lin} = \frac{\rho \int_S |J|^2 dS}{\left| \int_S J dS \right|^2} \quad (3.20)$$

3.2.3 Internal self inductance calculation

In the introduction of this chapter, it is mentioned that it is not necessary to model the AC self inductance, because its variation with the frequency is not significant. However, with the method presented here, it is possible to calculate the internal part of the self inductance.

The linear internal self inductance $L_{i,lin}$ is also obtained using energy relations. The total energy in the internal inductance is equated to the energy stored in the magnetic field within the conductor, as follows:

$$L_{i,lin}|I_{tot}|^2 = \int_S |\nabla \times A|^2 dS = \frac{1}{\mu_0} \int_S |B|^2 dS = \frac{1}{\mu_0} \sum_{n=1}^N |B_n|^2 S_n \quad (3.21)$$

As a remark, the factor 1/2 has been removed from both sides of the equation. This leads to the following formulation for the linear internal inductance:

$$L_{i,lin} = \frac{\int_S |B|^2 dS}{\mu_0 \left| \int_S J dS \right|^2} \quad (3.22)$$

Therefore, to be able to compute $L_{i,lin}$, it is necessary to evaluate the magnetic flux density \mathbf{B} . Since the the vector potential is solely z -directed, the magnetic flux density has two spatial components along x -axis and y -axis, and is zero along z -axis ($B_z = 0$):

$$\mathbf{B} = \nabla \times \mathbf{A} = \begin{pmatrix} +\frac{\partial A}{\partial y} \\ -\frac{\partial A}{\partial x} \\ 0 \end{pmatrix} = \begin{pmatrix} B_x \\ B_y \\ 0 \end{pmatrix} \quad (3.23)$$

With equations (3.23) and (3.17), it is possible to calculate the magnetic flux density in the center position of each subbar S_m as follows:

$$B_{m,x} = B_x(x_m, y_m) = \frac{\mu_0}{2\pi} \sum_{n=1}^N J_n \frac{\partial Q_{mn}}{\partial y} \quad (3.24)$$

$$B_{m,y} = B_y(x_m, y_m) = -\frac{\mu_0}{2\pi} \sum_{n=1}^N J_n \frac{\partial Q_{mn}}{\partial x} \quad (3.25)$$

where $B_{m,x}$ and $B_{m,y}$ are respectively the magnetic flux density in the x - and y -directions. The norm is then easily calculated with the relation:

$$|B_m| = \sqrt{B_{m,x}^2 + B_{m,y}^2} \quad (3.26)$$

The numerical methods used to compute $\partial Q_{mn}/\partial x$ and $\partial Q_{mn}/\partial y$ are presented in appendix B.

3.2.4 Validation and measurements

To verify this model, two series of comparisons are made. The first one takes advantage from that the numerical method can be applied to any conductor shape. More specifically, it means that the subbars can be arranged at will so as to create the desired conductor shape. Then, a convenient way to verify the accuracy of the model consists in applying it to a case which has an analytical solution. For example, the skin effect for a conductor with circular cross-section has an analytical solution which can therefore easily be compared to the computation method proposed in this section.

At low frequencies, the linear resistance and the internal self inductance are given respectively by $R_{dc,lin} = \rho/S$, and $L_{i,lin} = \mu_0/8\pi$. For a circular copper conductor with a radius of 0.1 mm, the linear resistance and linear internal inductance are given respectively by 0.54 Ω/m and 50.00 nH/m. The values obtained with the model presented in this section are 0.54 Ω/m and 49.92 nH/m. Furthermore, it is also interesting to validate the model for higher frequencies. To do this, the well-known analytical equations of the linear resistance and internal inductance for a circular cross-section are used [54], [93], [118]. Their formulation is given in appendix B.4 and are compared in Fig. 3.6 with the numerical method for different conductors radii. Here as well, the size of the subbars is chosen so that their width w_i and thickness t_i are at least smaller than half the skin depth. The results do match very well.

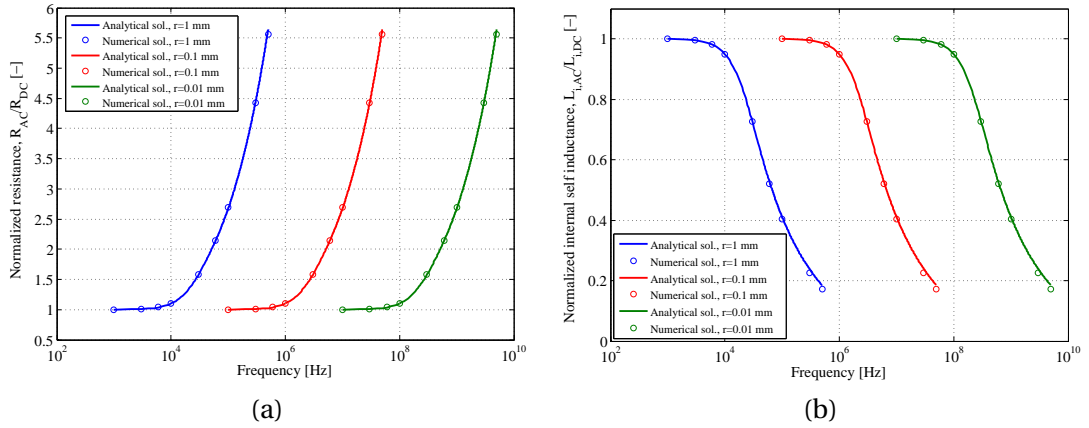


Figure 3.6: Comparison between the analytical solution and the numerical one for the linear resistance (a) and for the linear internal inductance (b). The linear resistance and the linear internal inductance are normalized to the DC value.

In the second set of comparisons, the numerical solutions are compared with measurements performed on real coils. According to [112], the numerical method provides more accurate

Chapter 3. High frequency effects

results by considering a number of neighboring conductors that is below the number of turns of the coil. This assumption is assessed by varying the number of parallel conductors during the computation of the AC resistance. Fig. 3.7 shows the comparison for coils 4, 5, 7 and 10 (defined in Table 2.3). The impedances have been measured using an *Agilent precision impedance analyzer 4294A (40 Hz-110 MHz)*. The real and imaginary parts of the coil impedance are exported to Matlab and treated using equations (3.2) and (3.3) so as to retrieve its AC resistance. This AC resistance is then normalized to the DC resistance, which gives the multiplicative coefficient r_{AC} .

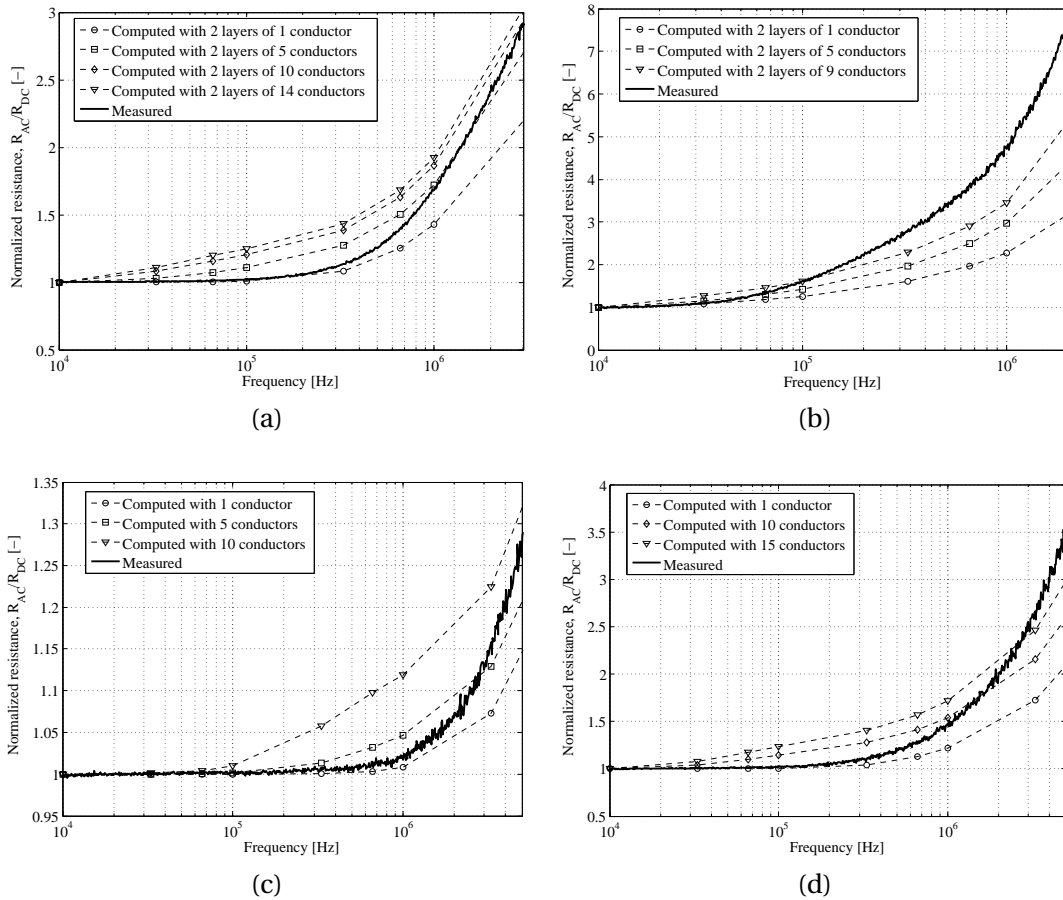


Figure 3.7: Comparison between the numerical solution and the measurements on (a) coil 4, (b) coil 5, (c) coil 7, and (d) coil 10.

The results of the comparison between the numerical model and the measurements have to be analyzed. First, the model is good, since the relative difference rarely exceeds 30 %, which is not a bad score considering the complexity of high frequency effects. In the four considered coils, a maximal relative difference of 33 % is obtained for coil 5 at the highest frequency. Secondly, the assumption made in [112], stating that the number of neighboring

conductors has to be adapted according to the tested coil has revealed to be true. This is an issue because it is difficult, in a designing process, to guess *a priori* the number of conductors to be evaluated for the coils.

As a conclusion for this first numerical method, our opinion is that it is well suited to generate a general evaluation of the AC resistance for the design of CET systems. However, it is considered insufficient for an optimization purpose.

3.3 Numerical modeling using FEM

3.3.1 Introduction

In this section, the second numerical method is discussed. It is based on finite element (FE) models and simulations to evaluate the AC resistance of the coils.

For the design and optimization of systems that are too complex to be studied analytically (or in which the analytical solution simply does not exist), the finite element method (FEM) appears to be an interesting candidate. It consists of a numerical technique that allows to resolve the differential equations describing a physical system. The solution obtained is an approximation resulted from the subdivision of a complicated domain into multiple smaller regions in which the governing equations are more easily solved. The approximation becomes more accurate when the number of subregions is increased, but in return requires more computational time and effort.

The FE software used, *Flux* from Cedrat [20], can solve electromagnetic and thermal physics problems, both in two dimensions and three dimensions. It has proven to be capable of computing Eddy currents in metallic materials, and of handling skin and proximity effects in conductors [35], [73], [117]. In this section, the two-dimensional *Flux2d* will be used. The following developments describe how simulations are carried out and how the resistance of the simulated coils is extracted.

3.3.2 Geometrical structure and model of a coil

As the current in the conductors is assumed to be sinusoidal, the simulations for estimating the skin and proximity effects are performed using the **steady state AC magnetic 2D** module. In this section, the FE model of a coil will be represented through a simple but typical example. Fig. 3.8 shows the geometrical description of this example, in which the conductors are artificially enlarged for readability purposes.

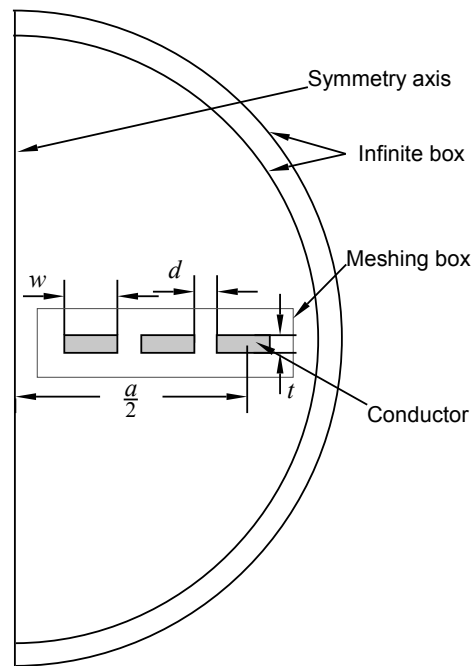


Figure 3.8: Geometrical design of a coil with Flux2d.

The different geometrical and electric parameters involved in the simulations are presented in Table 3.1. The values used in the example depicted in Fig. 3.8 are given in the third column.

Table 3.1: Input parameters for the FEM simulations

Parameter	Definition	Example values
n	Number of turns	3
N	Number of layers	1
t	Copper thickness	105 μm
w	Track width	0.5 mm
d	Spacing between two turns	0.2 mm
a	External size	30 mm
δ	Spacing between two layers	N/A
f	Operating frequency	200 kHz
I	Current in the conductors	1 A (AC rms)

The design in the FEM software can take advantage of the symmetry of the coils. Indeed, it includes a vertical symmetry axis at the center of the physical coil (axisymmetric model). The boundary conditions have to be chosen so that the magnetic field is tangential to this symmetry axis.

Fig. 3.9 shows the intensity of the magnetic flux density in the example defined above, and Fig.

3.10 shows the magnetic field lines around the coils. As expected, they are perpendicular to the plane formed by the coil and parallel to the symmetry axis.

Using this symmetry axis offers a great advantage. Of course, it reduces by half the geometrical domain of simulation, but mainly it resolves the problem of the first numerical method linked to the local form of the magnetic field. Indeed, in the first method, the conductors were considered infinite in length and were deployed towards a single direction. With the symmetry axis in FEM, the simulation takes into account the interaction of the opposite side of the coil as well, and in this sense, is closer to reality.

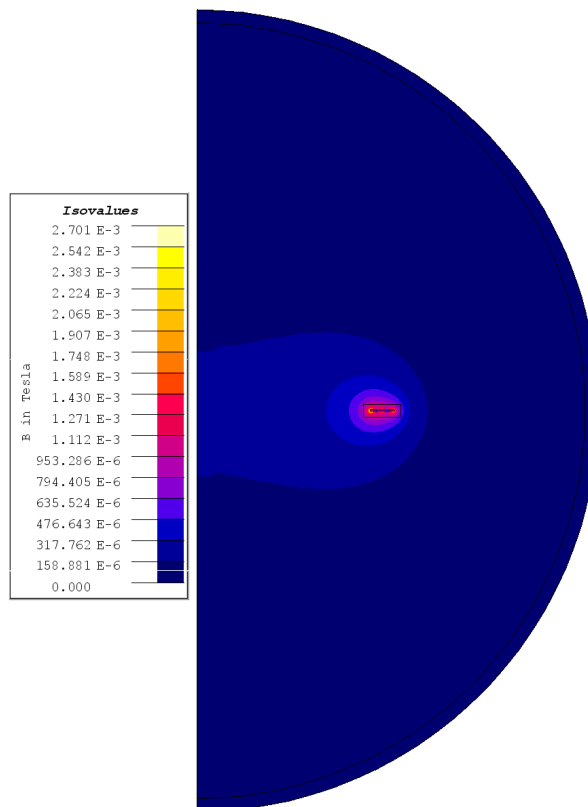


Figure 3.9: Intensity of the magnetic flux density around the coil showing the boundary condition of the design.

3.3.3 Meshing of the conductors

The 2D design of the coils consists only in copper rectangular structures corresponding to the cross-sections of the conductors surrounded with air. The main difficulty concerning the meshing of the conductors is linked to the size of the meshes at high frequency. The conventional rule for FEM HF simulations consists in using a mesh size that is at least smaller

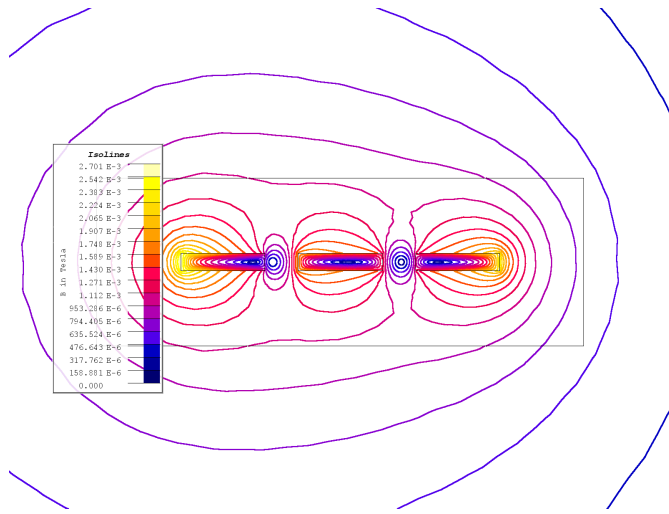


Figure 3.10: Magnetic field lines zoomed in the conductors region.

or equal to half the skin depth. The skin depth is defined as follows:

$$\delta_{sd} = \frac{1}{\sqrt{\pi f \mu_0 \sigma}} \quad (3.27)$$

where μ_0 is the magnetic permeability and ρ the resistivity of the conductor.

Considering copper as the conductive material and the highest frequency of 5 MHz for the current application, the resulting skin depth is equal to 30 μm . Following the rule formulated above, the mesh size for the conductors is set to 15 μm . In order to reduce the number of elements for the simulations and to increase the quality of the meshing, an intermediate box is created around the conductors where the mesh size is refined, as shown in Fig. 3.8. A practical example of the meshing box and the meshing of conductors is shown in Fig. 3.11.

3.3.4 Physical and electrical definition

Each turn of the coil is physically represented in the simulation by a rectangular solid conductor. Then, all these conductors are electrically connected in series and are supplied by a current source of $I = 1$ A (AC rms). Fig. 3.12(a)-(b) gives two examples of the current density distribution inside the conductors, respectively at 200 kHz and 5 MHz. At 200 kHz the current distribution is nearly uniform on the entire cross-sections, and at 5 MHz, there is an obvious crowding of current at their periphery.

The strategy to evaluate the resistance of the coil consists then in computing the Joule losses

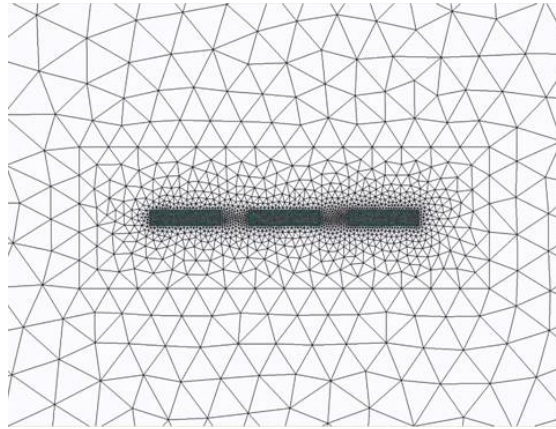
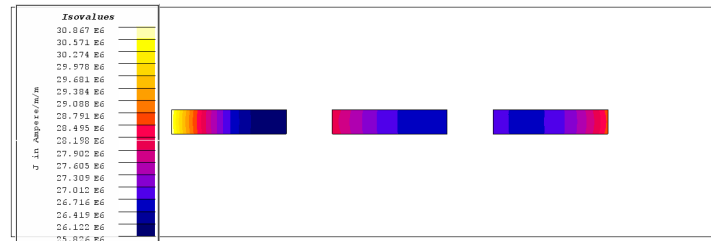
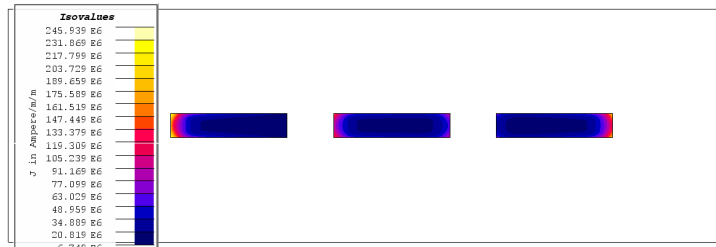


Figure 3.11: Meshing of the intermediate box and the conductors.



(a)



(b)

Figure 3.12: Current density distribution in the conductors at (a) 200 kHz and (b) 5 MHz.

inside the conductors with:

$$P_j = \int_S \rho J^2 dS \quad (3.28)$$

where S is the surface defined by the conductors and J the current density. Knowing the

current I that is generated in the conductors, the resistance R_{AC} can be deduced from:

$$R_{AC} = \frac{P_j}{I^2} \quad (3.29)$$

The value obtained is then normalized to the DC resistance obtained with (2.1) so as to obtain the multiplication coefficient r_{AC} .

3.3.5 Validation and measurements

To validate the FEM model, comparisons with measurements are performed on coils 4, 5, 6, 7, 10, 11 (defined in Table 2.3). The results are shown in Fig. 3.13. The conditions of measurements are the same as those defined in Section 3.2.4.

The FEM solution was first thought to be used as a verification for the first numerical method, but at last it appeared to be much more accurate than it according to the measurements. For every coils tested in this work, the relative error between FEM computations and measurements rarely exceeds 15 %. For example, the largest relative difference (of 19.5 %) for the 6 coils compared in Fig. 3.13 is obtained for coil 6 at about 800 kHz.

As a conclusion, the FEM method provides more accurate results than the first method. An error that generally remains below 15 % is really good for the AC resistance of a coil. Furthermore, the FEM method does not require to adjust the number of conductors to be modeled.

3.4 Discussion

Both methods have different advantages and drawbacks. In summary, the first method, presented in section 3.2, is less expensive in terms of computation time but provides less accurate results. Our belief is that this first method is sufficient for general design purposes and prototyping. However, for an optimization method, more accurate results are preferable so as to prevent an eventual erroneous convergence.

The second method, presented in section 3.3, provides more accurate results but in return is much more time consuming, since it is necessary to launch the FEM software, create the meshing, solve the equations and retrieve the results. Knowing that one simulation can easily last more than one minute, this solution can definitely not be applied by direct means to the optimization process, in which the number of simulations is expected to be in the order of 40'000.

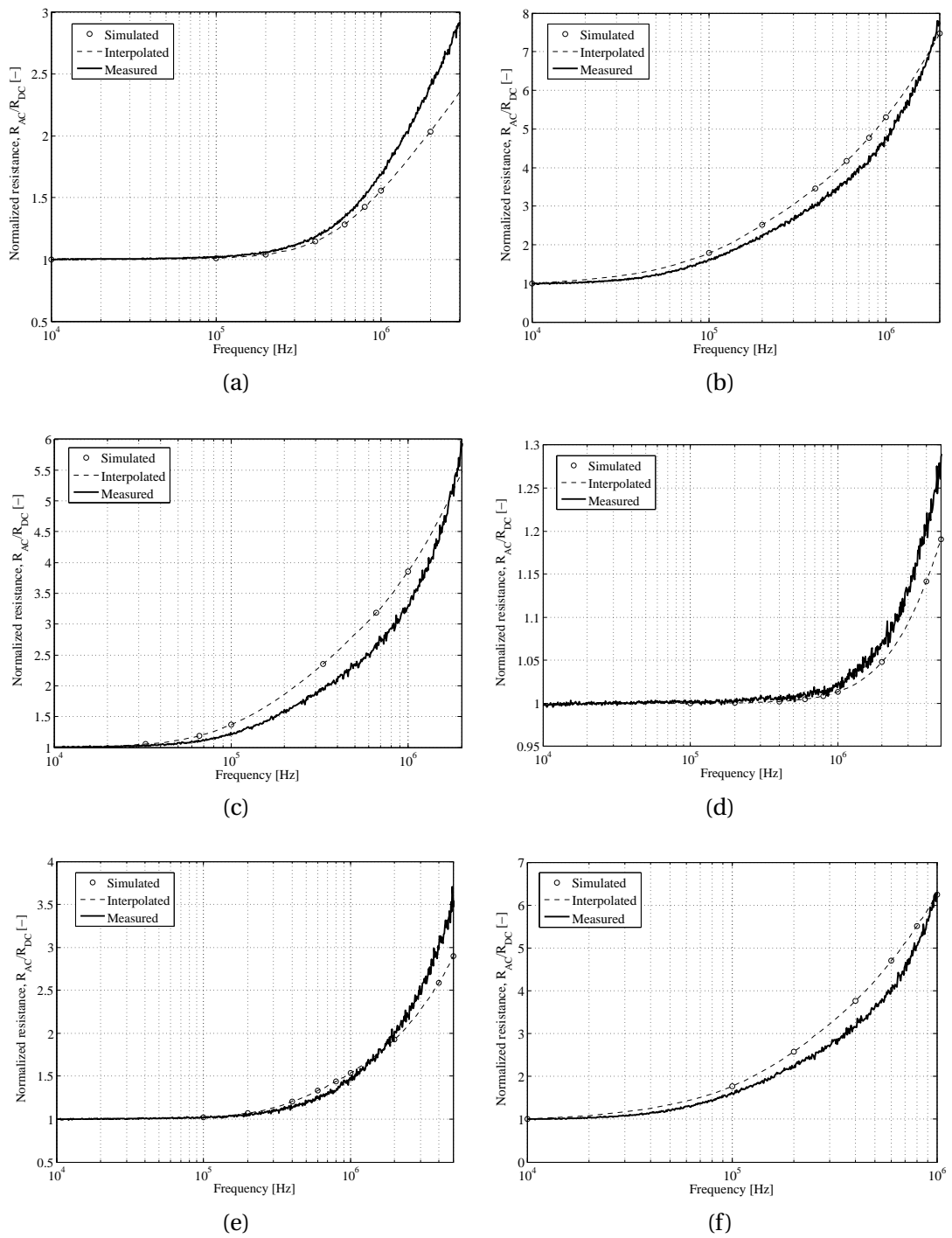


Figure 3.13: Comparison between measured and computed AC resistance. The AC resistance is normalized to the DC resistance. (a) Coil 4, (b) Coil 5, (c) Coil 6, (d) Coil 7, (e) coil 10, (f) coil 11.

Therefore, the simulations have to be exploited in a way that make them usable in the optimization method. This issue is discussed in the following section. Then, some practical observations are made in section 3.6 concerning the effect of the high frequency on the coils and more generally on CET systems.

3.5 Exploitation of FEM simulations

3.5.1 Design of experiments

The concepts of design of experiments (DOE) are thoroughly discussed in [52]. It consists basically in a strategy for planning the experiments linked to a given research problem. Properly designed experiments allow to retrieve a maximum of information from as few experimental tests as possible. The results thus obtained can be analyzed using relatively simple statistical tools that make the information easily readable and interpretable.

DOE techniques are generally used in practical measurements or tests, more rarely in simulations. But DOE applied to FEM simulations has been successfully performed in numerous works [52], [98], [84]. Therein, each different experimental run would require its own prototype which is most often inconceivable in electromagnetic applications. In this sense it is advantageous to replace the practical measurements by simulations.

Theoretically, DOE can be used to model a system in its entire experimental domain with only a few simulations, the number of necessary experimental runs depending on the design itself. Traditionally, the most common plan of experiments consists in varying one parameter at a time, all the other ones being held constant. Such a simple plan only allows to study the effect of the concerned factor on the system, and does not take into account the possible interactions between factors. In this sense, well structured plans (or designs) bring along a substantial improvement, as all parameters are simultaneously varied. Many different designs do exist, such as full factorial designs, fractional designs, Hadamard designs or composite designs. Every design has its advantages and drawbacks, but in this thesis, only full factorial designs are used.

In full factorial designs, the parameters are generally evaluated on two levels that correspond to their lower and upper limit. Then, to model a system defined by 5 parameters, the number of required experiments is $2^5 = 32$. With such a design, it is possible to generate a polynomial linear model that takes into account the interactions between factors.

In the specific case, the number of variables can be reduced to 5. First knowing that the number of layers for the turns distribution is either one or two, both cases can be treated

separately. In the two-layers case, the spacing between two layers is set to 0.2 mm. The current generated in the coil is set to 1 A (rms). The remaining variables are the 5 input parameters, namely the frequency f , the number of turns n per layers, the track width w , the spacing between two turns d and the external turn position a . The output parameter (or researched solution) is the resistance normalized to its DC value. Table 3.2 gives the variation range for the input parameters.

Table 3.2: Variation range of the input parameters

Param.	Min	Max	Unit
f	10^4	$5 \cdot 10^6$	[Hz]
n	1	25	-
w	0.2	2.0	[mm]
d	0.2	1.5	[mm]
a	20.0	50.0	[mm]

The most straightforward way to model the resistance in the entire experimental domain would be to apply a full factorial design with the five factors described above. But this is not feasible because the coil suffers from a geometrical constraint that can be defined as follows:

$$\frac{a}{2} \geq \frac{n}{N}(w + d) + cst \quad (3.30)$$

where cst is a constant that generates a free space in the center of the coil, in case where additional structures have to be integrated. In other words, this geometrical constraint states that it is impossible for a coil to have more turns than the available space can include. Typically, a high number of turns is not compatible with a large track thickness and a large spacing between tracks. This leads to a significant part of the experimental domain that is geometrically unfeasible and where no coherent results can be obtained by simulation. The problem with conventional DOE resides in that the entire experimental domain has to be available, especially the full factorial design that uses the extreme values of the experimental domain to generate a model.

Therefore, another solution has to be investigated. The final method used for the resistance evaluation is a combination of a complete output mapping and DOE, as discussed in the following subsections.

3.5.2 Complete output mapping

Definition

A complete output mapping consists in generating the solutions of the problem for all possible combinations of parameters. For continuous variables, some predetermined values within their variation range have to be fixed. The number of these values will determine the number of simulations to be done and therefore influence drastically the computation time. The result is a grid of points that are distributed in the experimental domain.

The goal is then to predict the solution for a point where no simulation has been performed. The simplest method is to choose the existing combination of parameters that comes closest to the desired evaluation point. A more complex approach is to guess the solution by interpolation.

The challenge consists then in realizing a huge number of simulations and saving the data in a form that is easily and quickly accessible during an optimization process. In the present case, the simulations can take advantage of the FEM software to simplify the management of data. By creating a specific scenario during the solving of the simulations, it is possible to define the frequency f as a variable parameter and then to compute the solutions for a single coil at multiple different frequencies.

The complete output mapping is fully managed by Matlab. A routine has been created that allows to launch automatically the simulations with the desired set of parameters and then to retrieve the results. A total grid of 500'000 points have been evaluated this way, and the results have been stored in text files that are quickly accessible for further use.

Interpolation Strategy

As already mentioned, the simplest way to find the solution for a random point in the experimental domain is to choose the one of the complete output mapping that is closest. This strategy can easily be tested using 2000 samples randomly chosen in the experimental domain. Fig. 3.14 shows the discrepancy between FEM simulation and the complete output mapping with the closest pick for these 2000 points. Obviously this strategy gives rise to errors that could be avoided by performing interpolations.

First, let us note that the number of turns n does not require any interpolation since it can take only integer values. Then, two different types of interpolation are used for the different parameters of Table 3.2. The first interpolation concerns the frequency f .

During the simulation, the resistance of the coil is calculated for 10 different values evenly

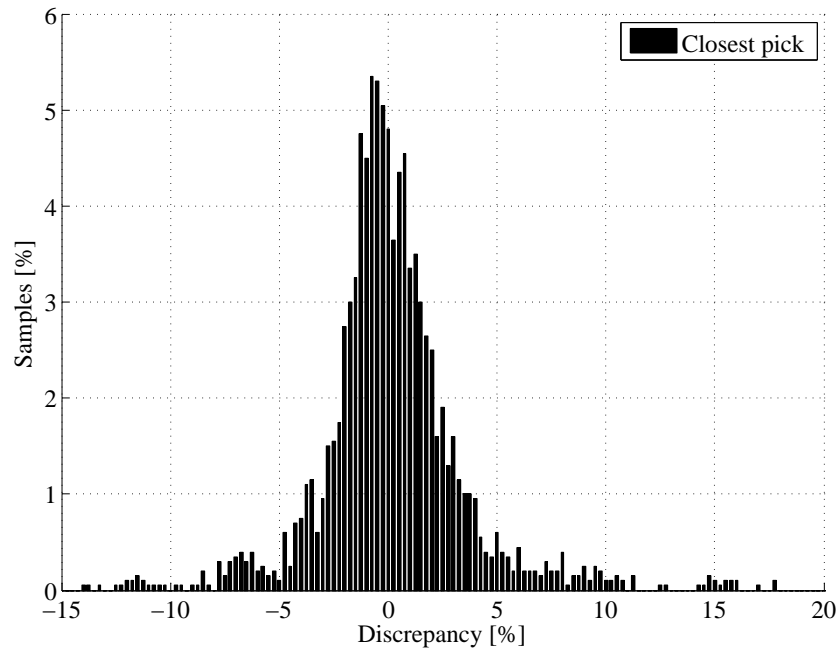


Figure 3.14: Discrepancy between FEM simulations and the complete output mapping used with the closest pick strategy. A total of 2000 samples randomly generated in the experimental domain have been evaluated.

distributed inside the frequency variation range. To evaluate the resistance for intermediate values situated between those 10 ones, a spline interpolation is applied.

The second interpolation concerns the track width w , the spacing between two tracks d and the external turn position a . For these three parameters, a factorial plan can be applied to the complete output mapping in order to generate a linear model between each of its points. Two different models have been tested using the same 2000 random samples as in Fig. 3.14: the linear model with interactions and the linear model without interactions.

Fig. 3.15 shows the discrepancy between FEM simulations and the complete output mapping with both interpolations discussed above. They are in good agreement. The difference between the model with interactions and the model without interactions is not significant, but the former is preferred as its issued standard deviation ($std = 0.41$) is slightly lower than for the latter ($std = 0.42$). For comparison, the standard deviation obtained with the closest pick strategy was much larger ($std = 3.41$).

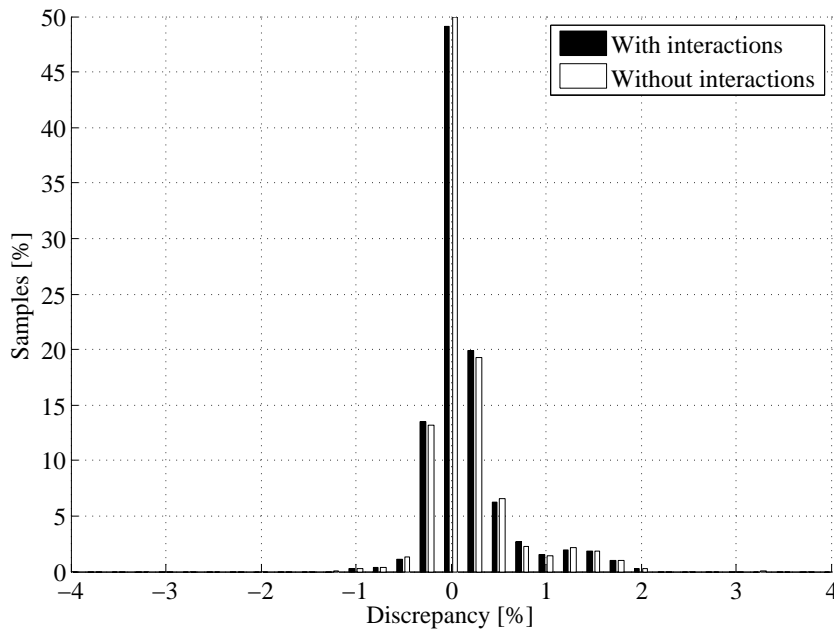


Figure 3.15: Discrepancy between FEM simulations and the complete output mapping with interpolation. The results obtained from the model with interactions and without interactions are compared. The same 2000 samples as in Fig. 3.14 have been evaluated.

3.6 Effective impact of the high frequency on CET

An good manner to verify if it is advantageous for a certain coil to increase the operating frequency is to compute its quality factor (2.18) on the whole frequency range. Fig. 3.16 shows the quality factor Q as a function of the frequency for the coils measured in Fig. 3.13. For all tested coils, the increase of resistance with the frequency is lower than the increase of inductive reactance. Therefore the quality factor can be only increased with the frequency. This statement can be generalized for all PCB coils in the frequency range considered in this thesis, given that the condition (3.5) is respected. As a result, it seems advantageous to work at the highest operating frequency as possible. However, the quality factor defines the coils individually whereas a CET system is much more complex and involves additional components (multiple coils, electronics, devices to be supplied, ...) that bring other issues at high frequency. At this point it is too early to state that the highest operating frequency is the best suited. This can be easily verified by evaluating the losses in a coreless transformer when the frequency is varied and the output power is fixed.

Then, to measure the impact of the high frequency on CET systems, an example using the coreless transformer composed of coils 5 and 6 as respective primary and secondary coils is proposed. The efficiency of the coreless transformer and the power losses are plotted versus

the frequency in Fig. 3.17. Two cases are represented. In the first one, the HF effects are not taken into account (the DC value of the resistances is used over the whole frequency range), and in the second one, they are taken into account. In this example, the current of the primary coil is adjusted so as to obtain exactly 5 W on a load resistance of 10 Ω .

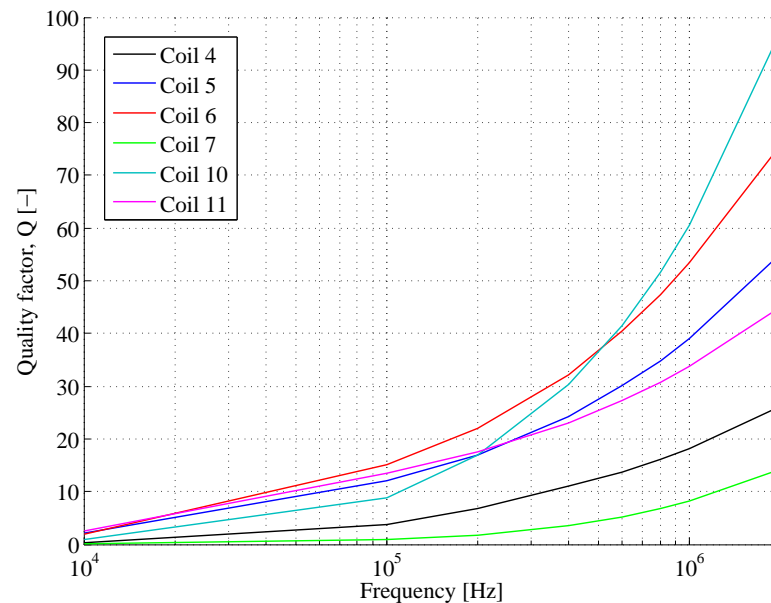


Figure 3.16: Computed quality factor for different coils.

This example shows how crucial it is to take into account the variation of the resistance with the frequency. As this variation depends on the coils geometry as well, a deeper analysis of complete CET systems and the inherent losses has to be performed in order to obtain an optimal solution. This matter is discussed in the next chapter.

3.7 Overall conclusion

As an overall conclusion, two methods to characterize the HF effects have been presented. After comparison, the FEM method has been chosen for the forthcoming optimization since it provided more accurate results. The main issue from this method is the computation time that was not acceptable, knowing that the average time for a single evaluation is more than one minute.

Therefore, a complete output mapping and an interpolation strategy using DOE have been implemented in order to exploit effectively the results of FEM simulations. Doing so allows to reduce the evaluation time of a single coil to about 0.2 seconds compared to more than 60 seconds that would be required to perform the full simulation. The final result offers an

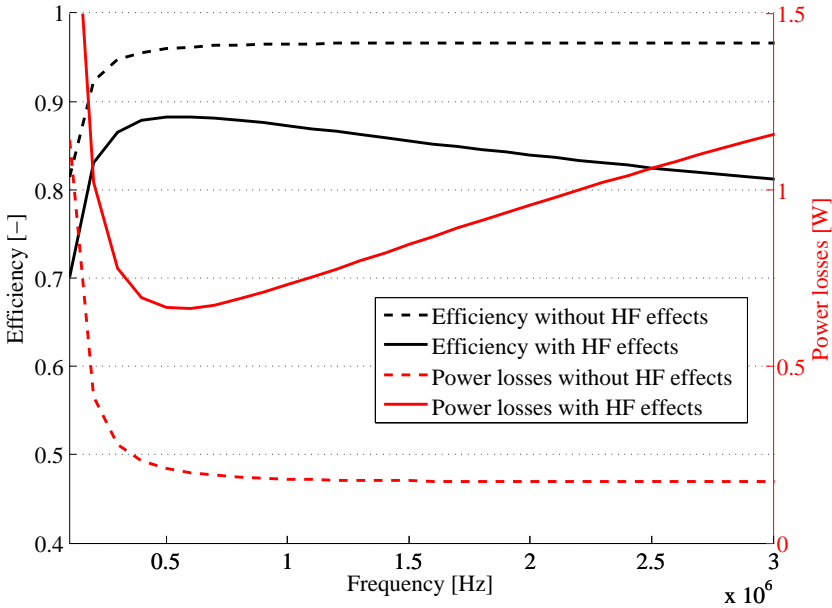


Figure 3.17: Efficiency and power losses versus the frequency for the coreless transformer made of coils 5 and 6. Dashed curves show the case where the HF effects are not taken into account, and plain curves when they are.

excellent compromise between accuracy and computation cost.

Finally, the importance of integrating the HF effects in the CET model has been highlighted through a concrete example.

Design and optimization of CET systems

Summary

4.1 Problem definition	80
4.2 Sensitivity analysis	83
4.2.1 Analysis context	83
4.2.2 Effect of the number of turns	83
4.2.3 Effect of the track width	85
4.2.4 Effect of the space between tracks	85
4.2.5 Effect of the size of the coils	86
4.2.6 Effect of the displacement of the secondary coil	87
4.2.7 Effect of the frequency	88
4.2.8 Discussion	90
4.3 Optimization methods	91
4.4 Genetic algorithms	92
4.4.1 Generalities	92
4.4.2 Genetic algorithm implementation	93
4.4.3 Genetic algorithm testing	94
4.5 Multiobjective genetic algorithms	98
4.5.1 Pareto optimality	98

Chapter 4. Design and optimization of CET systems

4.5.2	Generalities	99
4.5.3	Multiobjective genetic operators	100
4.5.4	Multiobjective genetic algorithm implementation	102
4.5.5	MOGA testing	103
4.6	Design of the CET table	107
4.6.1	Context and specifications	107
4.6.2	Choice of the coils geometry	108
4.6.3	Choice of the compensation topology	109
4.6.4	CET table Optimization	110
4.7	Overall conclusion	115

This chapter addresses the problem of CET systems design for most possible applications realized using PCB coils. In this context the most interesting research purpose consists in proposing a general methodology to find the optimal solution to each individual applications. The first part of this chapter defines the CET problems to be optimized in general and in the scope of this thesis. The second part proposes a sensitivity analyzis on the main parameters for CET systems in order to give a better global understanding of coreless transformers and possibly to simplify the forthcoming optimization. Then the optimization of CET systems is discussed and a new genetic algorithm (GA) is developed and tested. Finally, this new GA is applied to the design of the CET table.

4.1 Problem definition

The first chapters of this thesis have presented a good overview of the different choices that an engineer faces when he has to design coreless transformers for CET applications. Among these choices, one can find notably the compensation topology, the shape of the coils, the number of layers for the turns distribution, the operating frequency and the input voltage or current. Thus, designing a coreless transformer is not a trivial task. Frequently, the influence of each parameter is analyzed individually so as to deduce the tendencies and then make a choice. In this chapter, the goal is to present a method that is able to find the global optimum.

As pointed out in Chapter 1, two different kinds of CET systems can be optimized. The first one concerns relatively simple applications involving a static coreless transformer with only one primary coil and one secondary coil. The second one addresses more complicated CET systems with multiple primary coils or multiple secondary coils working simultaneously. The design of these two cases is approached with the same method in this chapter, but some differences still remain.

Indeed, the former can be resolved in a straightforward way, by evaluating only a single

situation that corresponds to the case where both coils are well aligned, or where the CET is most critical. The latter involves a larger charging surface, where a minimal amount of power has to be ensured at every positions. Without going too much into details as this matter will be discussed later in this work, such systems require multiple evaluations corresponding to different scenarios that may occur during the CET process. In brief, both problems are solved with the same optimization method, the main difference resides in the function to be optimized. In this chapter, the focus is first made on the first kind of CET systems through a simple problem that allows to test and validate the optimization algorithm. Then, the optimization of the second kind of CET systems will be discussed in section 4.6, where the goal is to design a CET table.

In general for CET systems, the specifications are based on the application to perform, and generally concern the dimensions of the CET platform, the input voltage and output voltage, or the power to be transferred. The design criteria tend to maximize the efficiency η or maximize the power transferred to the load P_L . In this thesis, as the application deals with low consumption peripherals (≤ 5 W), it is difficult to obtain really high efficiencies (≥ 90 %) because of the intrinsic nature of CET systems. Indeed, the addition of electronics and the presence of intermediate primary and secondary coils generate losses that cannot be avoided. This is the price to pay when using CET systems. But still, they can be minimized by making the good choices. That is why, in our opinion, it is more adequate to use the losses P_{loss} as design criterion instead of the efficiency. This is even more true considering that the main limitation for CET is the heat generated by the current in the coils, which is directly linked to the Joule losses.

This work is done in the academic world, where economical aspects are generally not an issue. However, for the design of a future industrial application, they have to be kept in mind. In the scope of this thesis, the goal consists in building prototypes that show and validate the theoretical developments, and economical issues remain secondary but still can be anticipated to some extent. Furthermore, the cost estimation for a prototype designed and built during this work would be far from an industrial reality where the price of the components highly depends on their quantity. This is even more true for PCBs as the price of a single PCB is really high compared to a multitude of identical PCBs for which the price per units is drastically reduced. In this sense, the PCB is a good candidate for the coils of a CET application, in addition to some obvious advantages that it offers during the fabrication and integration.

With this description, two objective functions have to be optimized, *i.e.* the output power and

the power losses:

$$O_1 = P_{loss} \quad [W] \tag{4.1}$$

$$O_2 = -P_{out} \quad [W] \tag{4.2}$$

Here, the first objective function O_1 represents the sum of Joule losses generated in every coil of the CET system, and O_2 represents the total power transferred to the terminals of the secondary coil. To P_{out} is assigned the negative sign because every optimization problem discussed in this chapter are turned into a minimization problem.

At a first glance, minimizing those two objective functions seems equivalent to maximizing the efficiency. In fact, the problem is much more subtle, and the experience shows that both objective functions have to be used to obtain the desired result. The different ways to deal with multiobjective problems is discussed later in this chapter.

One of the main difficulties concerning the design of CET systems is the number of parameters, because the geometry is quite complicated. As the output power is generally defined by the specifications, the remaining free parameters for CET systems are given in Table 4.1, where indices 1 and 2 are used to characterize respectively the primary and the secondary coils.

Table 4.1: Free parameters of CET systems.

Parameter	Value
$Sh_{1,2}$	The choice of the coils shape
To	The choice of the compensation topology
U_{in} or I_{in}	The input voltage or the input current
f	The operating frequency
$N_{1,2}$	The number of layers
$n_{1,2}$	The number of turns
$a_{1,2}$	The external dimension of the coils
$w_{1,2}$	The track width
$d_{1,2}$	The space between two tracks
$t_{1,2}$	The copper thickness
g	The air gap

The design comes up with a total of 18 parameters or choices for simple CET systems. Complicated CET systems (that belong to the second kind described above) include additional factors such as the number of primary and secondary coils and how they are distributed.

The variation of each single parameter leads to different solutions that could possibly fulfill the specifications of a given application. From this point, the problem can be solved in several

ways. Before going directly into optimization considerations, a good strategy consists in performing a sensitivity analysis on the different parameters.

The advantage of a sensitivity analysis is threefold. First, it provides a general understanding of the CET behavior and the impact of the main parameters on the whole system. Secondly, it allows to determine which parameters can be fixed so as to lighten the optimization process. Thirdly, it allows to determine the variation range of the parameters.

4.2 Sensitivity analysis

4.2.1 Analysis context

The goal of this section is to analyze the effect of the main geometrical parameters on CET systems. As a design reference for this analysis, the coreless transformer obtained with coils 5 and 6 (from Table 2.3) as primary and secondary coils is used. By default, the parameters of both coils are the ones presented in Table 2.3. A PS compensation topology is used because it is the one that will be used for the CET table. This choice will be justified later. Both capacitors are assumed to be perfectly designed according to the resonance frequency of 250 kHz, and the load is a resistor of 10 Ω . The input voltage U_1 applied to the coreless transformer is set to 12 V (rms).

4.2.2 Effect of the number of turns

In this first part, the effect of the number of primary turns n_1 and secondary turns n_2 is studied. The geometrical definition of a coil is such that the first turns are placed on its external size. The additional turns are then added towards the center of the coil by superimposed pairs. The number of primary turns n_1 is varied from 2 to 18 (*i.e.* $n_1 = 2, 4, \dots, 18$) and the number of secondary turns is varied from 2 to 20 (*i.e.* $n_2 = 2, 4, \dots, 20$), and the other parameters are kept constant.

Fig. 4.1(a) shows the mutual inductance L_{12} of the coreless transformer as a function of n_1 and n_2 . As expected, the results show that the mutual inductance increases when the number of primary and secondary turns is increased and that internal turns have less impact than external ones.

Fig. 4.1(b) presents the output power P_{out} of the coreless transformers as a function of n_1 and n_2 . The results show that when n_2 is increased, the output power is also increased. On the contrary, increasing n_1 leads to a decrease of the output power. The reason is that the impedance of the primary coil, given by $\underline{Z}_1 = R_1 + j\omega L_1$, becomes greater with the number of

Chapter 4. Design and optimization of CET systems

turns and therefore limits the current I_{L1} flowing through it when a PS topology is used. From the second voltage equation (2.23), it is obvious that it leads to a decrease of the secondary current I_2 . Actually this effect dominates the increase of the mutual inductance. However, using a small amount of primary turns so as to transfer a large power may be inappropriate in terms of Joule losses and efficiency.

Fig. 4.1(c) presents the efficiency η of the coreless transformer as a function of n_1 and n_2 . Only the Joule losses are taken into account. The efficiency is thus defined as follows:

$$\eta = \frac{P_{out}}{P_{out} + P_{loss}} \quad (4.3)$$

So using a sufficiently large number of turns ensures to have a good efficiency, especially for the number of secondary turns.

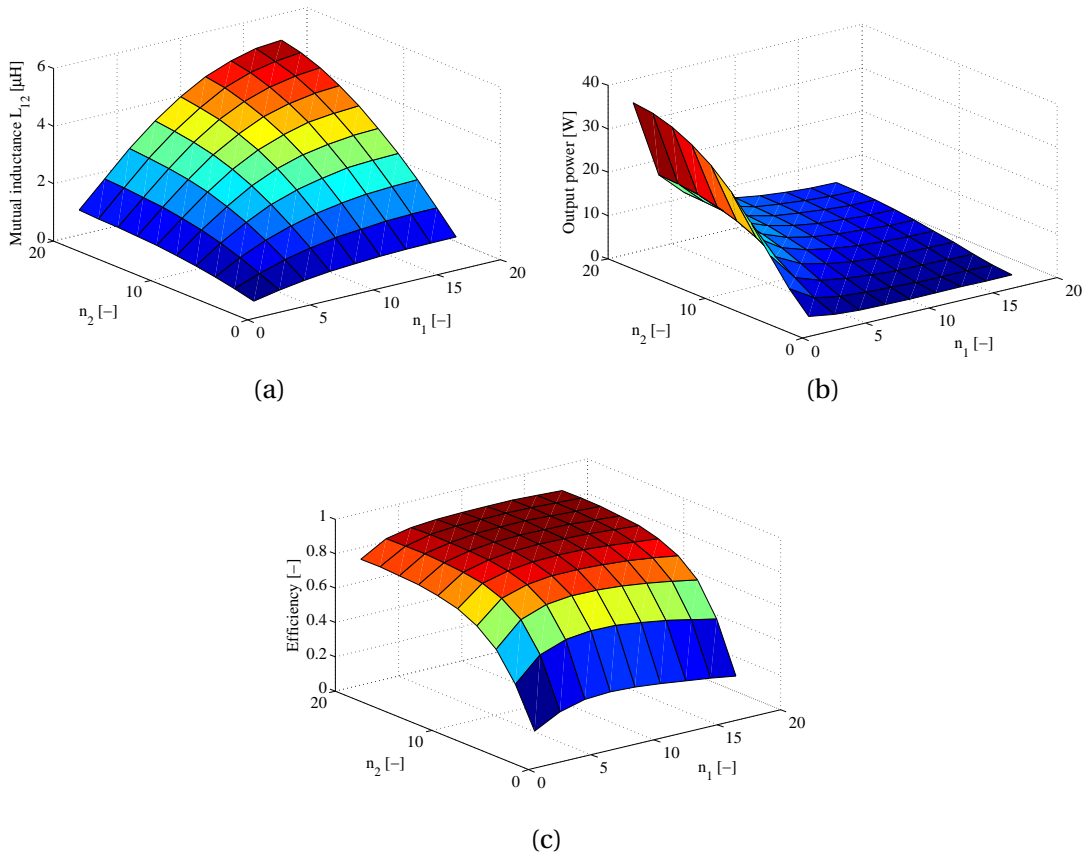


Figure 4.1: (a) Mutual inductance, (b) output power, and (c) efficiency versus the number of primary turns and the number of secondary turns.

4.2.3 Effect of the track width

Here, the primary and secondary track widths w_1 and w_2 are varied while the other parameters are kept at their default value except for n_1 and n_2 that are set to 12, which allows to have a larger range variation for w_1 and w_2 , that is from 0.2 mm to 2.0 mm ($w_{1,2} = 0.2, 0.4, \dots, 2.0$ mm). Thus, the external size of the coils remains unchanged (their default value being $a_1 = a_2 = 40$ mm), and the position of the turns is automatically adapted according to the track width.

Fig. 4.2(a) presents the mutual inductance as a function of w_1 and w_2 . The results show that the mutual inductance is greater for small values of track widths. It is so because small track widths allow to concentrate the turns at the periphery of the coils, which leads to an increase of self and mutual inductances.

Figs. 4.2(b) and 4.2(c) present respectively the output power and the efficiency of the coreless transformer as a function of w_1 and w_2 . In this case, the sensitivity analyzis shows a great interest because the results are not consistent with the intuition. The output power increases when w_1 is increased, and on the contrary decreases when w_2 is increased. Also, one could expect to obtain the best efficiency when the track widths are maximal, but actually this is not true. Here, for example, the best efficiency is obtained for intermediate values of widths (that are $w_1 = 1.2$ mm and $w_2 = 0.8$ mm). This is mainly due to the skin and proximity effects that have a greater impact on larger track widths.

4.2.4 Effect of the space between tracks

Here, the space between two tracks d_1 and d_2 respectively for the primary and secondary coils are varied from 0.2 mm to 1.5 mm (*i.e.* $d_{1,2} = 0.2, 0.3, \dots, 1.5$ mm). n_1 and n_2 are set to 12 so as to obtain the maximal range of variation for d_1 and d_2 . The other parameters are kept at their default value.

Fig. 4.3(a) shows the mutual inductance of the coreless transformer as a function of d_1 and d_2 . It is logically greater for small values of d_1 and d_2 as the turns are more concentrated at the periphery of the coils.

Fig. 4.3(b) presents the output power as a function of d_1 and d_2 . Increasing the primary inter-track space causes the impedance of the primary coil and mutual inductance to decrease, and then more current is generated into the primary coil which results in more transferred power. On the contrary, increasing the secondary inter-track space leads to a decrease of the output power.

As shown in Fig. 4.3(c), d_1 does not have a great impact on the efficiency of the coreless

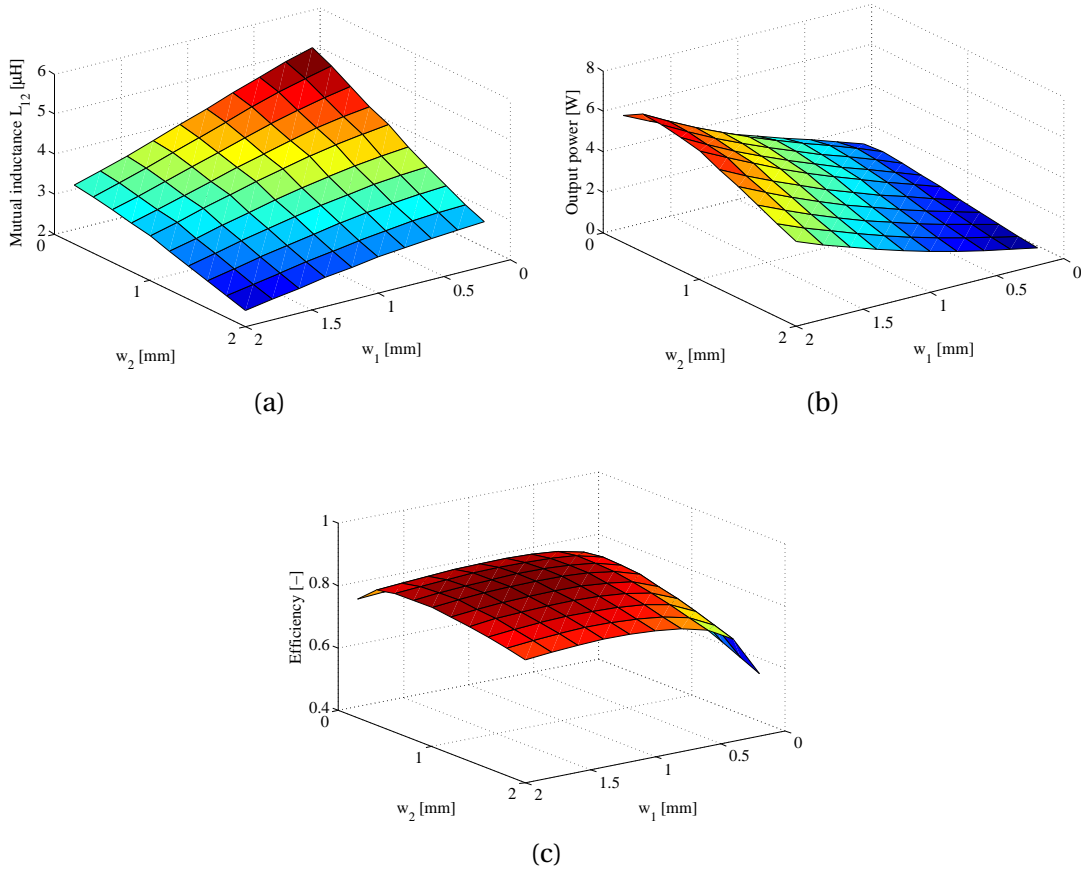


Figure 4.2: (a) Mutual inductance, (b) output power, and (c) efficiency versus the primary track width and the secondary track width.

transformer. Even so it is slightly more interesting to have a small value for d_2 . Here again, the maximal efficiency is obtained with intermediate values of d_1 and d_2 (that are $d_1 = 0.6 \text{ mm}$ and $d_2 = 0.5 \text{ mm}$), instead of the smallest values as intuition could suggest.

4.2.5 Effect of the size of the coils

Here, the external lengths a_1 and a_2 are varied from 28 mm to 50 mm. n_1 and n_2 are set to 12 so as to obtain a sufficiently large range of variation. The other parameters are kept at their default value.

Fig. 4.4(a) shows the mutual inductance as a function of a_1 and a_2 . Of course it becomes greater when both coils become larger as well. But there is another condition to satisfy in order to obtain a maximal mutual inductance, which is for both coils to have a similar external size.

Fig. 4.4(b) presents the output power as a function of a_1 and a_2 . It is difficult to predict the

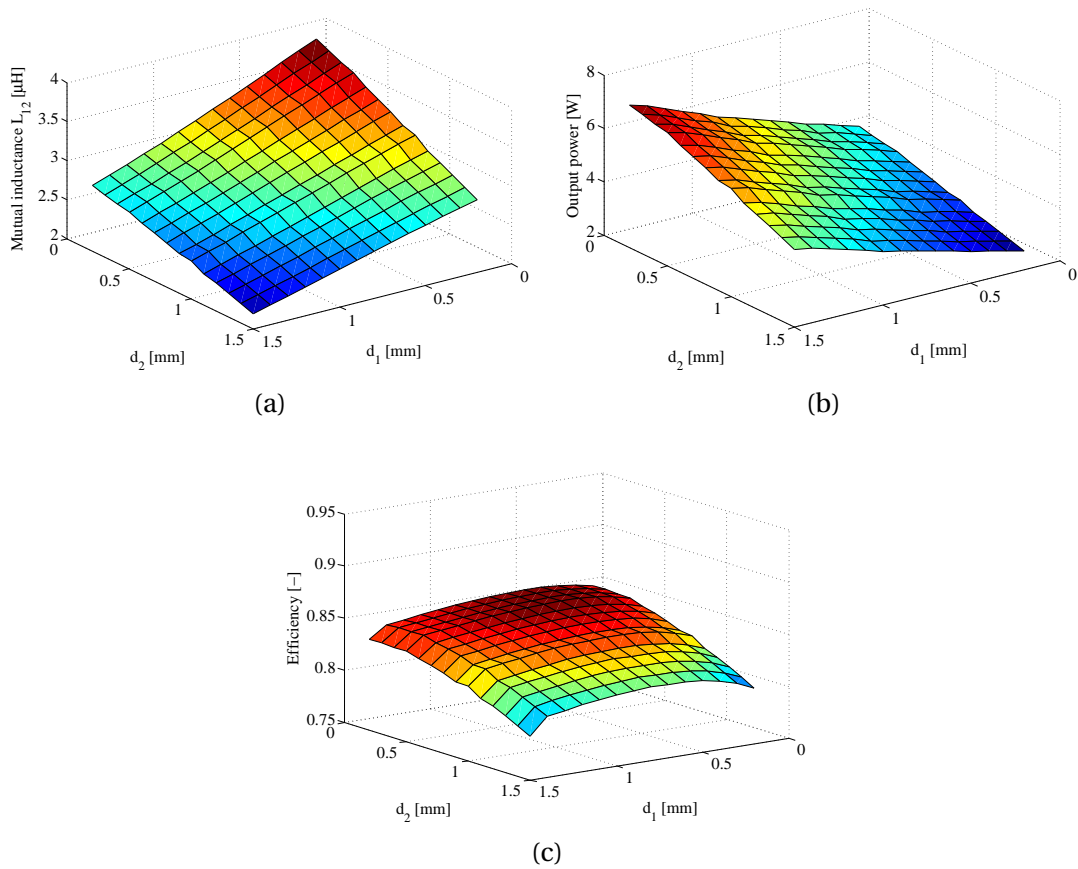


Figure 4.3: (a) Mutual inductance, (b) output power, and (c) efficiency versus the primary inter-track space and the secondary inter-track space.

behavior of the output power. However, an interesting result is that using a larger secondary coil than the primary one allows to increase the transferred power, as long as the difference in size is not excessive.

Fig. 4.4(c) shows that it is interesting to have coils as large as possible in term of efficiency, and this statement is equivalently valid for the primary and the secondary coils.

4.2.6 Effect of the displacement of the secondary coil

Here, the secondary coil is displaced above the primary one. The lateral displacements are defined by x_d along the X-axis and by y_d along the Y-axis. The displacements are varied from 0 mm (which corresponds to the case where the coils are perfectly aligned) to 30 mm.

Fig. 4.5(a) shows the mutual inductance and Fig. 4.5(b) shows the output power as a function of x_d and y_d . In this case, the primary coil does not undergo a change of impedance as its

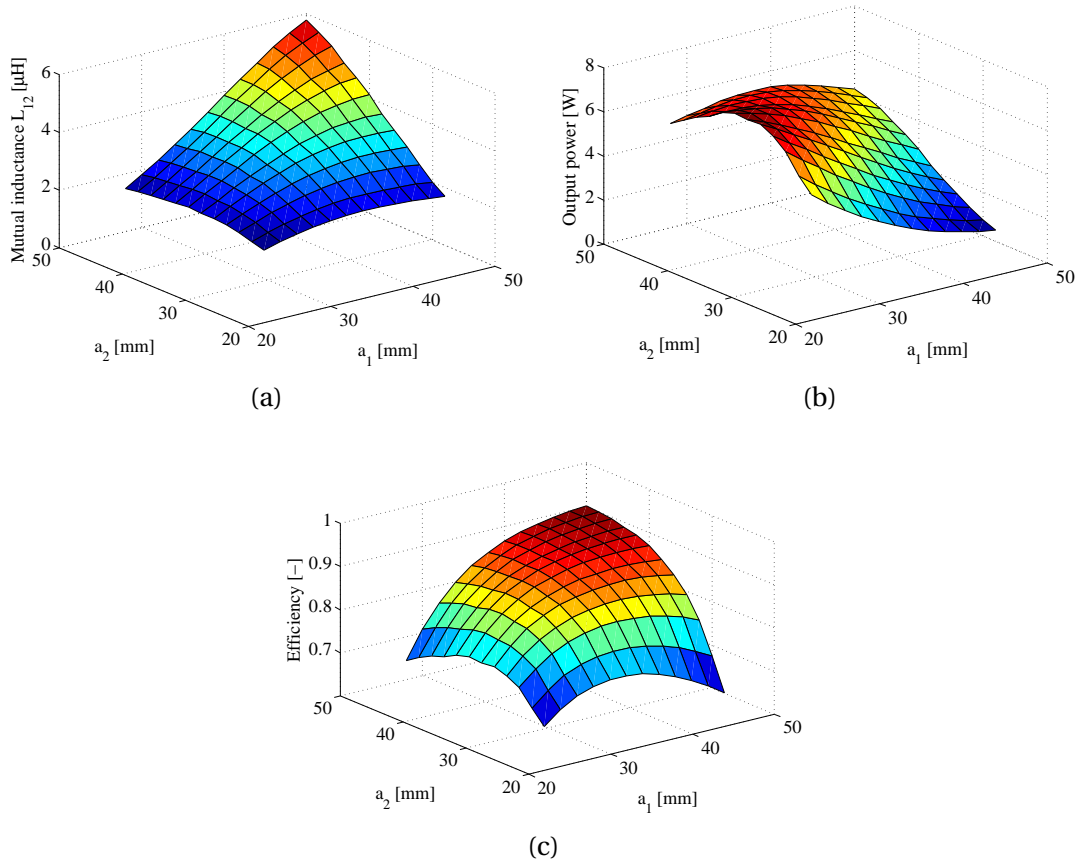


Figure 4.4: (a) Mutual inductance, (b) output power, and (c) efficiency versus the primary coil size and the secondary coil size.

geometrical parameters are not changed. Then, there is only a small increase of current in the primary coil due to the decrease of the mutual inductance when the secondary one is displaced. As a result, the variation of the output power is largely dominated by the mutual inductance.

Fig. 4.5(c) shows the efficiency as a function of x_d and y_d . The efficiency drops when the mutual inductance and the output power become too weak. It is caused by the Joule losses generated in the primary coil that become more significant compared to the output power.

4.2.7 Effect of the frequency

The effect of the frequency has already been shortly discussed in section 3.6, but here the focus is made on the output power and on the efficiency. To show the general effect of the frequency on the coreless transformer, the frequency f is varied from 100 kHz to 2 MHz, and all the other parameters are kept constant.

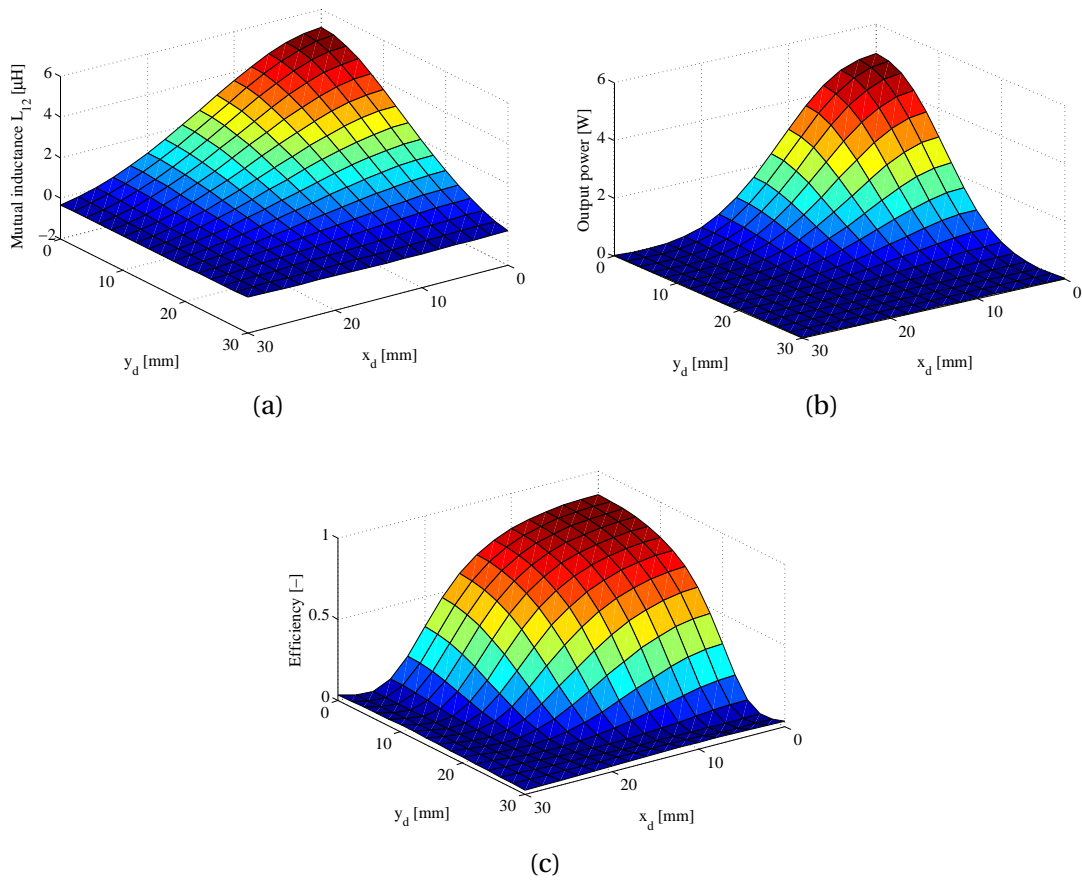


Figure 4.5: (a) Mutual inductance, (b) output power, and (c) efficiency versus the displacements x_d and y_d of the secondary coil.

Fig. 4.6(a) and (b) show respectively the output power and the efficiency as a function of the operating frequency.

Interestingly, for a PS topology, the frequency has a similar effect as n_1 on the coreless transformer. Indeed, an increase of the frequency leads to an increase of the impedance of the primary self inductance and of the mutual inductance, while the secondary self inductance can still be compensated by adapting the secondary capacitor C_2 . This leads to a decrease of the current in the primary coil and consequently to a decrease of transferred power. Fig. 4.6(a) clearly shows this effect. As a result, it is necessary to increase the input voltage so as to obtain an acceptable output power at high frequencies. Furthermore, as mentioned in section 3.6, it is obvious that using higher frequencies is not necessarily favorable in term of efficiency, because of the increase of resistance (Fig. 4.6(b)).

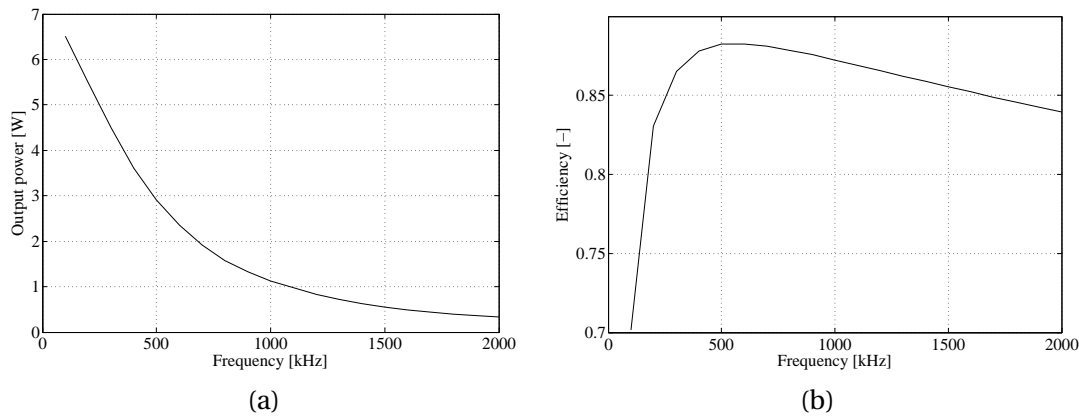


Figure 4.6: (a) Output power and (b) efficiency versus the operating frequency.

4.2.8 Discussion

It is difficult to draw precise rules for the behavior of the coreless transformer. But a few generalities can be formulated.

On the one hand, the mutual inductance is a good indicator for the efficiency, as a large mutual inductance is generally accompanied by a large efficiency. But on the other hand, it does not help to predict the output power.

With regard to the primary coil, increasing the number of turns and the frequency, decreasing the track width and the space between tracks leads to an increase of the impedance of the coil, which in return reduces the current generated in it, which finally reduces the output power. With regard to the secondary coil, increasing the number of turns and decreasing the space between tracks leads to an increase of the output power. Finally, both primary and secondary coils should be as large as possible, as it enhances both the output power and the efficiency.

In conclusion for the sensitivity analysis, the intuition concerning the behavior of the coreless transformer is often wrong. Besides, the few general remarks formulated here can be observed for most of coreless transformers, but they are valid only for a PS compensation topology.

The main drawback of such a study is that it does not take into account the interactions between the parameters. In this sense, a global optimization is the best solution.

Beyond providing a general understanding of the coreless transformers, the main benefit from this sensitivity analysis is that it allows to restrict the boundaries of some free parameters for the forthcoming optimization.

4.3 Optimization methods

Many optimization methods do exist for finding the best solution to a problem issued from engineering design. As a preliminary introduction to the optimization methods, the different terms used in the following sections are defined as follows:

- Objective function: Function to be minimized or maximized
- Free parameters: Factors that have an influence on the objective function
- Search space: Domain in which the objective function can be evaluated
- Constraint: Condition that restricts the search space to admissible solutions
- Admissible space: Region of the search space where all constraints are respected

The most obvious method for finding an optimum consists in evaluating all the possible solutions of a given problem. This is actually the only solution which allows to say with certainty that the global optimum is reached. But its computation cost is generally huge and increases greatly with the number of free parameters. Indeed, for problems involving many parameters (*i.e.* 10 or more) such as the CET systems studied in this thesis, this method is clearly not an option.

Besides, there are two kinds of optimization algorithms, the deterministic and the stochastic algorithms [100].

A deterministic algorithm is an algorithm that behaves in a predictable and repeatable way. Given a certain function to be maximized or minimized, it will produce at each execution the same result and will pass through the same algorithm sequences. In other words, deterministic algorithms produce a solution that is highly dependent on the initial conditions. The most used and probably most efficient deterministic method is the gradient-based algorithm, in which the partial derivations of the function to optimize are computed in order to reach a local optimum where the gradient of the function is zero. The main problem for this kind of strategy is that there is no way to certify that the resulting solution is a global optimum and not a local one. The designer has to try multiple initial conditions to increase the chances to reach the global optimum. Moreover, this method is well suited for problems having an analytical solution that is stable and differentiable. But the modeling of CET systems includes discrete parameters (such as the number of turns and the number of layers), and uses numerical solutions where the analytical solution does not exist (for example the inductance calculation). For all these reasons, deterministic algorithms such as the gradient method are discarded from the possible optimization methods in this thesis.

The stochastic methods use randomly generated parameters within their variation range. Thus, each separate execution of a stochastic algorithm evaluates different solutions. The problem of global or local convergence does not exist anymore, even if it remains difficult to prove that a local or global optimum is reached. A stochastic algorithm has greater chances of converging to the global optimum if the number of iterations or objective function evaluations is large. Furthermore, it is possible to solve problems involving discrete parameters and non-differentiable functions. Many stochastic algorithms exist, such as the simulated annealing, the ant colony optimization or the genetic algorithms. The only one studied in this thesis is the genetic algorithms (GA) for two reasons. First, it is the most intuitive and convenient. Secondly, the research group in which this thesis work has been realized has a good experience of GAs and has already developed a few efficient algorithms [99], [98], [106], [30], [85], [84].

4.4 Genetic algorithms

4.4.1 Generalities

Historically, the first GA was proposed by John Holland in 1975 [64]. But GAs became popularized later in 1989, after David Goldberg published his book [59]. GAs belong to the larger class of evolutionary algorithms (EA). The main concept is based on the simple principle that if the evolution has been able to optimize natural biological processes, it can be used as a paradigm to find optimal solutions to any other problems. Then, GAs take their inspiration on the natural evolution as in Darwin's theory, in which the selection, the reproduction, and the exchange of genes play a central role.

In a GA, a population of individuals is generated. After their evaluation, a few of them (the best ones according to the law of the survival of the fittest) are selected as parents in order to generate the next generation. During the process, their genetic material can be exchanged or undergo different mutations. Over successive generations, the population is supposed to evolve towards an optimal solution.

In this section, only the main concepts involved in GAs are mentioned so as to make the future developments coherent and understandable to the reader. More details are presented in appendix C.1, and multiple references may complete those descriptions [98], [95], [111], [70].

The specific rules that govern GAs are often called operators. They are responsible for the definition of the processes that lead to the creation of the new generations and determine how they replace the former ones. They are generally 5 for conventional GAs:

- The **evaluation** of individuals: During this phase, each individual is evaluated and qualitatively quantified in anticipation for the parents selection.
- The **selection** of the parents: The selection phase consists in generating a new population of parents. They are chosen on the basis of the evaluation through an appropriate method.
- The **crossover**: The crossover is an operation that allows to exchange the genetic material of the parents so as to create one or multiple children.
- The **mutation**: The mutation is a phase in which random modifications are applied to the children.
- The **replacement**: The replacement strategy defines how the children are inserted into the next generation and therefore how they replace the parents.

A scheme of the working of usual GAs is presented in Fig. 4.7. A description of the different operators and their implementation is given in appendix C.1.

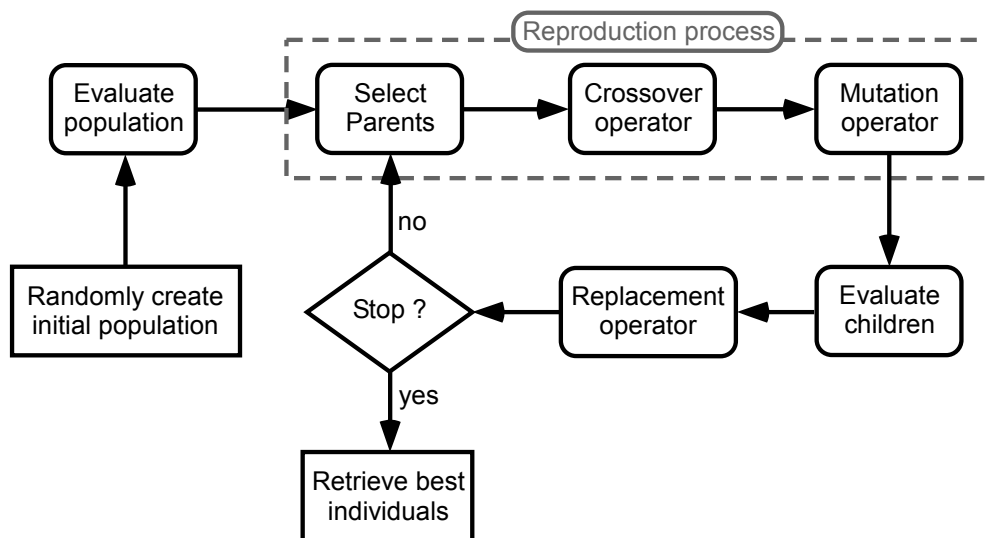


Figure 4.7: Schematic description of a conventional GA.

4.4.2 Genetic algorithm implementation

As a first attempt, the function *ga.m* from Matlab optimization toolbox [21] was tested, but the probabilities of mutation and crossover were difficult to adjust and the management of the constraints was not compatible with the ones associated with CET applications. Therefore, [106] and [98] have developed their own GA by including to it three main improvements.

The first improvement is related to the mutation and crossover operators. It consists of the adaptation of a method proposed in [128] that allows to regulate automatically the crossover and mutation probabilities according to the population diversity. At the beginning, a great diversity is imposed so as to ensure a good exploration of the search space. The diversity is then progressively decreased and oriented towards a local search at the end. As a result, the searchability of the GA is increased.

The second improvement concerns the crossover operator. It is adapted from [72] and consists of a specific arithmetic crossover applied to three parents instead of two parents. According to [72], this crossover increases the convergence speed and in the same time avoids a premature convergence.

The third improvement concerns the introduction of a local search in the GA. It is based on [72] and consists in exploring the neighbourhood of the best children at each generation. Basically, if a so generated individual is better than its original child, it takes his place in the next generation. This method increases the convergence speed and maintains the diversity in each generation. In return, it requires some computation time, since the objective functions of the new individuals have to be evaluated.

4.4.3 Genetic algorithm testing

This last GA has proven to be very effective and has allowed to optimize the design of a surgical ultrasonic transducer in [98] and a linear actuator in [84]. However, the former involves 11 free parameters and no constraint. The latter involves 4 free parameters and 2 constraints. For the optimization of CET systems using PCB coils, there are at least 10 free parameters and two geometrical constraints defined by (3.30). The problem to be solved is then obviously more complicated. Furthermore, as previously mentioned, two objectives are to be optimized for CET systems, namely the losses (to be minimized) and the output power (to be maximized). It is then interesting to test the GA with a simple CET application before to investigate the more complicated design of the CET table.

In order to test the GA for CET systems, a simple application (called *Prob1*) is created. It consists of a simple coreless transformer made up of two well-aligned coils. The goal is to transfer a power of 5 Watts to a load of $10\ \Omega$, and the maximal size of the coils was fixed to $50\ \text{by}\ 50\ \text{mm}^2$. These specifications are rather general and could refer to a typical application such as recharging a portable phone. *Prob1* makes a good candidate for testing the GA presented above. In this simple case, the compensation topology is parallel-series (PS) and the geometry of the coils is reduced to square and single-layered ones. The input voltage is set

to 12 V (AC rms). With this, the parameters limits (LU) are:

$$100 < f < 500 \quad [kHz] \quad (4.4)$$

$$1 < n_1, n_2 < 50 \quad [-] \quad (4.5)$$

$$20.0 < a_1, a_2 < 50.0 \quad [mm] \quad (4.6)$$

$$0.2 < w_1, w_2 < 2.0 \quad [mm] \quad (4.7)$$

$$0.2 < d_1, d_2 < 1.5 \quad [mm] \quad (4.8)$$

In most cases, it is sufficient to optimize only one of two objectives and set the other one as a constraint. In a first optimization attempt, the objective function to be minimized is chosen to be the power losses, and the output power is defined as a constraint. The power losses P_{loss} generated in the coreless transformer are defined as follows:

$$P_{loss} = P_{j1} + P_{j2} \quad (4.9)$$

with P_{j1} and P_{j2} the Joule losses of the primary and secondary coils.

The inequality constraints are defined as follows:

$$n_1(w_1 + d_1) + cst < \frac{a_1}{2} \quad (4.10)$$

$$n_2(w_2 + d_2) + cst < \frac{a_2}{2} \quad (4.11)$$

$$P_{out} > 5 \quad (4.12)$$

Prob1 has been submitted to the GA and led to bad results because the GA failed to converge properly. The reason comes from the fact that the problem to be solved is too much constrained. Indeed, the three constraints prevented the GA from converging adequately. Therefore, to solve this problem, the GA has been applied to another objective function that allows to eliminate the last constraint.

According to [81], a simple solution to deal with multiobjective problems consists in expressing a single objective function in the form of a weighted summation, as follows:

$$O = \alpha P_{loss} - (1 - \alpha) P_L \quad (4.13)$$

where O is the new objective function to be minimized. The term of the output power and the losses are weighted by a factor α that allows to assign a degree of importance to both criteria. This parameter has to be fixed according to the application to develop, and theoretically, each

different value of α could lead to a different solution. One can note here that maximizing the efficiency would be equivalent to minimizing (4.13) for a single and specific value of α .

The GA has been run to optimize *Prob1* with this new objective function. Unlike in the preceding attempt, there is no more problems of convergence, but the results remain unsatisfactory. The reason is that it is impossible to find the right value for α that corresponds exactly to the specifications. To illustrate this problem, two runs of optimizations are executed for different values of α . The results are presented in Fig. 4.8.

In the first run, α takes the successive values:

$$\alpha = 0.89, 0.90, 0.91, \dots, 0.98 \quad (4.14)$$

With this, a linear relation between the losses and the output power can be observed, but the spacing between each solution that corresponds to different values of α is too large to obtain a satisfactory solution. Therefore the variation range for α is refined in the second run, as follows:

$$\alpha = 0.9110, 0.9115, 0.9120, \dots, 0.9195 \quad (4.15)$$

All solutions are also situated on the vicinity of the same straight line as before, but it is impossible to extract a solution that corresponds to the desired specifications. The set of solutions undergoes some fluctuations along the straight line when the spacing between the different values of α is reduced. This can be observed in Fig. 4.9, where the output power versus α is plotted. The best solution, that is the closest one to the fulfilment of the specifications of *Prob1*, would provide an output power of 6.08 W and generate power losses of 0.53 W. This solution is obtained with $\alpha = 0.9170$. It is not bad in itself, but it is far from being optimal according to the specifications of *Prob1*. Indeed, the desired output power is 5 W, and a solution that is able to provide 6.08 W is sure to generate more Joule losses than one that would be closer to 5 W. In this sense it is not optimal.

Other solutions have been tried to minimize (4.13). For example, many attempts to assign different weighting factors and to vary them separately have been carried out, but with similar unsatisfactory results. Therefore, a new GA has to be implemented, that allows to provide at least one good solution. So far, a multiobjective problem was reduced to a single-objective one so as to find its optimum. In the following section, an optimization method that exploits simultaneously two objective functions is introduced and developed.

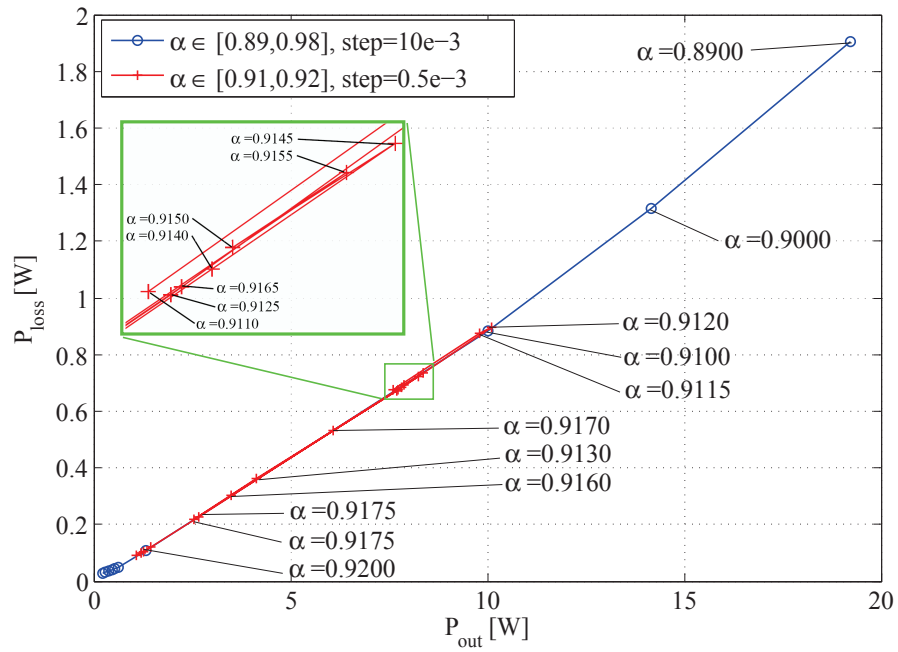


Figure 4.8: Power losses versus output power for different solutions obtained from two runs of optimization and with different values of α .

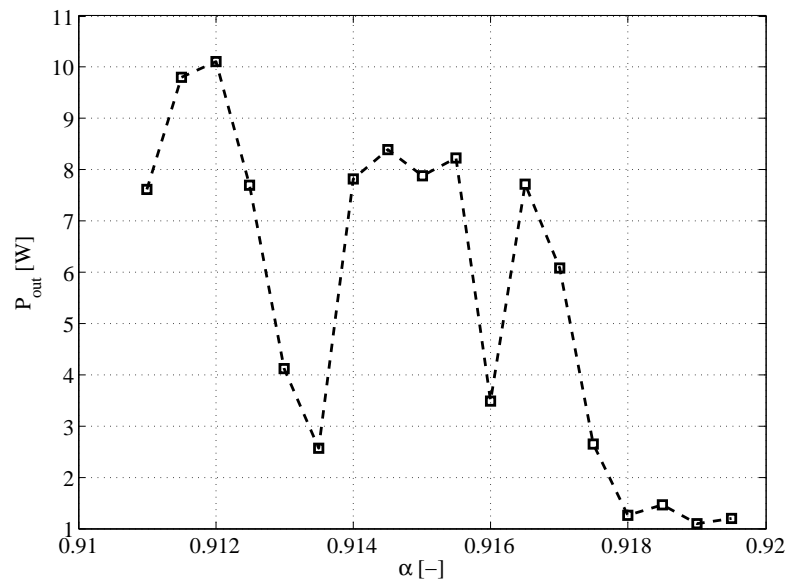


Figure 4.9: Output power versus α showing the fluctuations of the solutions obtained with the second run.

4.5 Multiobjective genetic algorithms

4.5.1 Pareto optimality

Before entering multiobjective optimization considerations, it is necessary to define the concept of Pareto optimality. Vilfredo Pareto (1848-1923) was a sociologist and economist who developed several theories on the study of income distribution and in the analysis of individual's choices. He was the one who first introduced a notion of optimality that consists in defining an optimum as an individual's state (of welfare for instance) that cannot be improved without making at least another individual's state worse off [23].

In the field of multiobjective minimization, a solution is a Pareto optimum if there is no other solution that allows to decrease an objective without increasing another one. To illustrate this, the example of two objectives to be minimized is often used. The concepts of Pareto domination and Pareto optimum are depicted in Fig. 4.10.

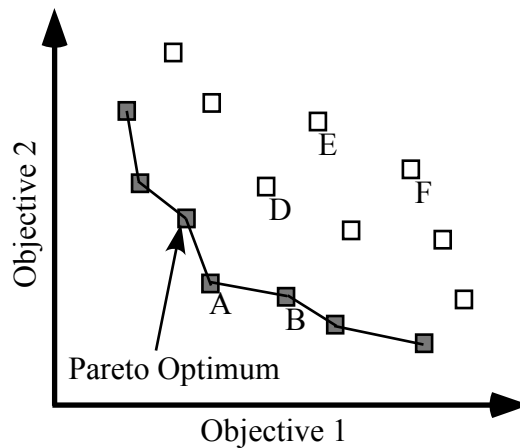


Figure 4.10: Explanation of the Pareto optimality. Here, the point D dominates the points E and F, because its two objectives are better. A and B belong to the set of Pareto optima, because no other solution dominates them.

Multiple algorithms, in which the Pareto optimality is used, do exist. Some are based on the simulated annealing method. One can mention for example the PASA (Pareto archived simulated annealing) or MOSA (Multiobjective simulated annealing) methods that are frequently presented in literature [121], [28]. In this section, the focus is made on the multiobjective genetic algorithms (MOGAs).

4.5.2 Generalities

The organization and the general concepts of the single objective GAs presented in the previous section remain valid for MOGAs, except for a few differences that will be explained further. The MOGA provided with the Matlab toolbox has been tried, with the same conclusion as in the previous section, especially the management of constraints that allows to define only linear constraints in the search space, which is not sufficient for the optimization of CET systems. Thus a new MOGA has to be implemented.

There are many kinds of MOGAs, but the most recent and popular ones are the strength Pareto evolutionary algorithm (SPEA, [133]), the Pareto-archived evolution strategy (PAES, [74]), and the non-dominated sorting genetic algorithm (NSGA, [116]). The common point to all these MOGAs is that they integrate the concept of Pareto domination in the evaluation of the individuals. In this thesis, the developed MOGA is based on the NSGA-II, which is an improvement of the NSGA, created so as to respond to the main criticism that was formulated by the scientific community. This algorithm has been chosen essentially because of its relatively simple implementation and because it is currently one of the most efficient [41].

Compared to single objective GAs, the main difference with MOGAs comes from the strategy to maintain the diversity inside the population and to keep a high convergence pressure so as to obtain a set of solutions that are well spread and uniformly spaced. In the NSGA-II, the convergence pressure is assured by the elitism operator, which defines how the individuals are evaluated and then selected inside a population. The diversity is maintained with the niche operator, which prevents the crowding of solutions in a region of the search space.

With the NSGA-II, there are thus two new operators:

- The **elitism** operator: It consists of a process that evaluates the individuals of a population based on their degree of non-domination. The elitism is also influenced by the replacement strategy and the niche operator.
- The **niche** operator: This method allows to limit the number of similar individuals that are passed to the next generation. In other words, it defines the ability of a MOGA to spread properly the individuals along the set of Pareto optimal solutions.

The different phases of the MOGA implemented in this thesis (called *NSGAimp*) are depicted in Fig. 4.11. Therein, N_p is the number of parents, N_c the number of children, and N_{tot} the total number of individuals inside the population. Typical values are given for those parameters.

The differences with the single objective GA and the main improvements carried out on the NSGA-II are described in the following subsections.

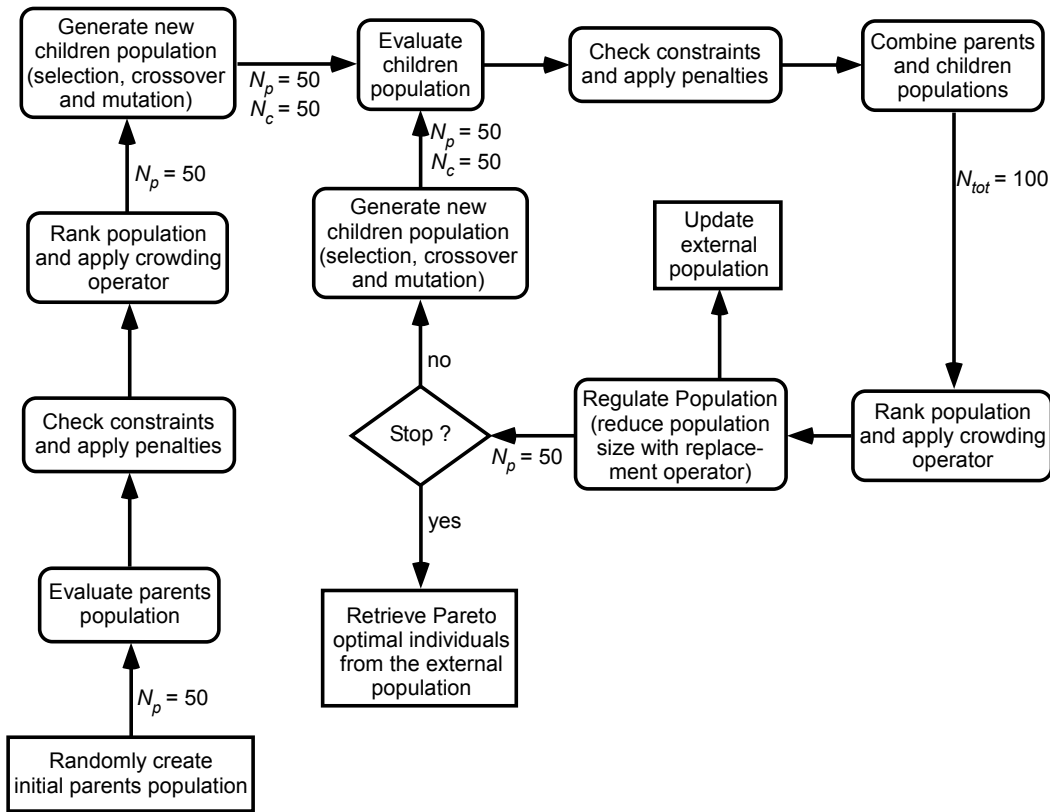


Figure 4.11: Schematic description of the MOGA implemented for CET systems.

4.5.3 Multiobjective genetic operators

Elitist Individual Evaluation

First of all, in the evaluation process of an individual, both objective functions to be minimized are calculated. Then, multiple possibilities exist to apply the constraints and evaluate the fitness functions. In the *NSGAimp*, two fitness values are associated to the corresponding objective functions by applying to each one of them the same penalty defined by (C.6) and (C.7) in appendix C.1.2.

Based on this fitness values, the individuals are then sorted according to their degree of Pareto domination inside the population. The main concept consists first in selecting all the individuals that are not dominated by any other in the population and attributing them the rank 1. These individuals are then virtually removed from the population and the next set of individuals that are not dominated are associated the rank 2. This process is pursued until every individual is ranked. So far, each individual having the same rank is then considered as equivalent in term of fitness evaluation. But the niche operator will allow to set up a hierarchy

of each individual belonging to the same rank.

This ranking procedure together with the constraints management that involves the penalty applied to both objective functions gives a property to the MOGA that is interesting: the convergence towards feasible solutions in the early generations when there are potentially no feasible solutions. Especially for CET systems optimization, the constraints are very coercive and this is the reason why the single objective GA did not work. Here, the ranking procedure is also applied to individuals that do not satisfy the constraints, and an individual that violates 'less severely' a constraint than another one is sure to be assigned a lower rank in the population. Thanks to that, if there is no feasible solution at early generations, the MOGA evolves towards the admissible space, and once it is reached, it evolves towards the Pareto optimal set of solutions.

Niche operator

Niche is a term issued from ecology that describes the relational position of a population (or multiple species) in its ecosystem. Each species has its own characteristics and occupies a different niche. In MOGAs, this concept is reused to prevent the algorithm from converging to a single region of the search space. Among the niching methods, there is the fitness sharing [116], the crowding method [102], and the clearing procedure [96].

The fitness sharing consists in assigning to each individual a shared fitness that is equal to its raw fitness divided by a value defined by the number of similar individuals. The greater the number of similar individuals, the larger is this value. Thus, an isolated individual has a higher probability to generate offsprings. There are two main problems with this method. First, a large population should be used so as to reduce the risk of disappearance of subpopulations during the stochastic evolution of the algorithm. Secondly, this method requires additional parameters, such as the size of the niche.

The crowding method inserts the children in the population by replacing similar elements. To do so, the selection process is designed in a way that only couples of similar parents can be chosen to generate children that will then belong to the same niche. Another possibility is for the children to replace the individuals that are most similar to them in the population. This avoids the concentration of all individuals in a single niche.

The clearing procedure is similar to the fitness sharing, except that a maximal number of individuals per niche is decided, and the fitness is deteriorated only for individuals that exceed this number. For example, if each niche accepts k individuals, the clearing procedure preserves the fitness of the k best individuals and decreases the fitness of the other ones that belong to the same niche. The disadvantage of this method is that it requires additional parameters

(size of the niche, number of niches, maximal number of individuals per niche).

In the *NSGAimp*, the diversity is preserved using a crowded-distance approach similar to the one proposed in [48]. The crowded distance consists of an estimation of the density of the individuals surrounding the one that is evaluated. It is determined by summing the distance of the two individuals situated on either sides of the evaluated individual (in the objective space). This distance is then normalized to the extreme values of objective functions obtained in the population. In other words, a smaller crowded distance is assigned to individuals that are more crowded. All individuals of the population are given a crowded distance according to their rank. This method has the advantage not to require additional parameters. In brief, each individual is characterized by two values: its rank and its crowded distance.

Elitist replacement strategy

In a wide sense, an elitist strategy consists in preserving the best individuals from one generation to another. For MOGAs, it means that each individual belonging to the first rank have to be transferred to the next generation. This is easily performed during the first generations, for which the number of first rank solutions is smaller than the size of the children population. At an advanced stage of the MOGA, the population formed by parents and children may count more first ranked individuals than can be passed to the next generation. Here, the crowding operator comes into play and selects the individuals that are most isolated.

Thus, the replacement strategy applied to the MOGA developed in this thesis consists in selecting primarily the individuals belonging to the lowest ranks and secondarily the ones that are less crowded.

4.5.4 Multiobjective genetic algorithm implementation

The different phases of the MOGA implemented to optimize CET systems are shown in Fig. 4.11. In addition to the strategy that ensures the convergence towards feasible solutions at early generations, three main improvements are applied to the MOGA. These are probably our main contributions to the development of an efficient MOGA.

The first improvement is related to a new strategy that combines the strengths of two different crossover methods. First, a standard uniform crossover offers a good convergence pressure but limits the diversity of the population because the original parameters of the parents are transferred to the children. This results in a quick convergence at early generations, but a slower one when the algorithm becomes close to the optimal set of solutions. Secondly, the arithmetic crossover introduced in section 4.4.2, involving three parents to generate

two children, has a relatively low convergence pressure but allows to spread considerably the individuals in the search space, resulting in an excellent diversity inside the population. *NSGAimp* cumulates both advantages by using alternatively those two crossovers. Doing so improves the overall speed of convergence and introduces more diversity in the population.

The second improvement is based on [108]. The MOGA developed therein includes an external file that contains the optimal solutions of each generation. This file is updated at each generation and only the first ranked solutions are kept. In the *NSGAimp*, this idea is reused by updating at each generation an external population that contains all the optimal solutions. All individuals assigned to rank 1 at each generation are registered in the external population. Within this external population, the dominated individuals are removed. If the number of individuals in the external population is greater than its maximal admissible number N_{max} , the most similar individuals are removed using the crowded distance operator. The external population does not interfere in the MOGA, it is just a passive tool that prevents the loss of optimal solutions during the elitist evolution of the MOGA.

The third improvement concerns the mutation operator. The mutation operator developed for the *NSGAimp* involves a polynomial probability distribution P_p as described in [40], a multiplication coefficient c and the current value of the parameters X_i . The mutated value of a parameter is then calculated as follows:

$$X_{i,mutated} = X_i + cP_p X_i \quad (4.16)$$

The polynomial probability distribution is defined so that $-1 < P_p < 1$ and P_p has a larger probability to be in the vicinity of zero. For more details, the reader should refer to [40]. The multiplication coefficient c is dynamically varied during the evolution of the MOGA. Thus, c has been empirically defined so that, at generation k , it is given by:

$$c = \left(20 \cdot (25 \cdot 10^{-3})^{(1 - \frac{k}{T})^{0.5}} \right)^{-1} \quad (4.17)$$

with T the maximal number of generations. To show the effect of the coefficient c , as an example, the maximal number of generations is set to $T = 500$. The resulting value of c is shown in Fig. 4.12. This dynamical variation of c introduces an aggressive strategy of mutations at early generations and reduces progressively the mutation values so as to obtain very small perturbations at the end of the MOGA.

4.5.5 MOGA testing

Different test functions are frequently used to evaluate the MOGAs. Zitzler *et al.*, a reference in the world of MOGAs, proposed six unconstrained test functions in [132]. The first four of

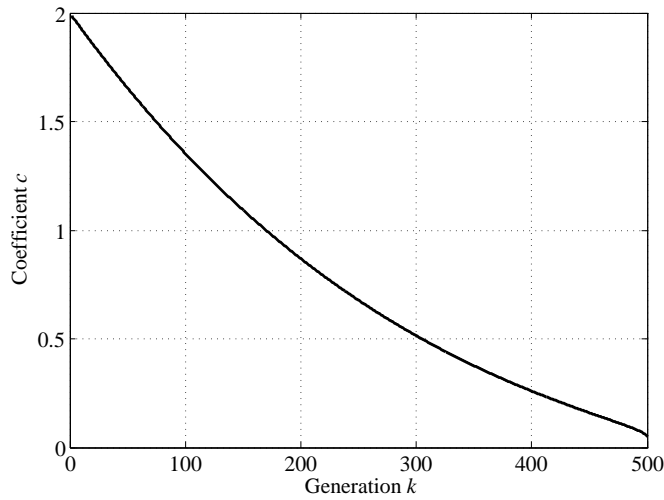


Figure 4.12: Multiplication coefficient evolution.

these six problems will be used in this section and are called *ZDT1*, *ZDT2*, *ZDT3*, and *ZDT4*. In addition, two constrained problems, called *Constr* [41] and *Tnk* [122] are tested. All these test functions are defined in detail and their Pareto front plotted in appendix C.2. Finally, the MOGA will be tested on *Prob1* that has been defined in section 4.4.3.

In all problems, the population size is set to $N_{tot} = 100$ individuals, in which $N_c = 50$ children are generated at each iteration. The number of generations is set to $T = 120$ which leads to a total of 6000 function evaluations, which is relatively low to reach an acceptable convergence for many problems. Each function is tested with the *NSGAimp* and the NSGA-II provided in the Matlab toolbox in order to compare their performance, except the *Tnk* function for which it is impossible because of the second order constraints.

For all unconstrained test functions, the worst, best and average results obtained over 15 runs are presented in Fig. 4.13. The number of parameters is set to 15 for *ZDT1*, *ZDT2*, *ZDT3*, and to 10 for *ZDT4*. The results show that *NSGAimp* is much more efficient in terms of convergence and number of Pareto solutions. Furthermore, each run provides similar results with *NSGAimp*, which is a guarantee of stability and repetitiveness.

For the constrained problems *Constr* and *Tnk*, equivalent results are obtained from different runs. Therefore, Fig. 4.14 shows the results of only single runs. The results show that for *Constr*, the convergence is equivalent for *NSGAimp* and Matlab's NSGA-II. However, the number of optimal solutions is greater for the former which makes it more interesting. Results on *Tnk* show that *NSGAimp* is able to handle effectively second order constraints.

Finally, *NSGAimp* is tested on the problem *Prob1*. The two objective functions to be optimized

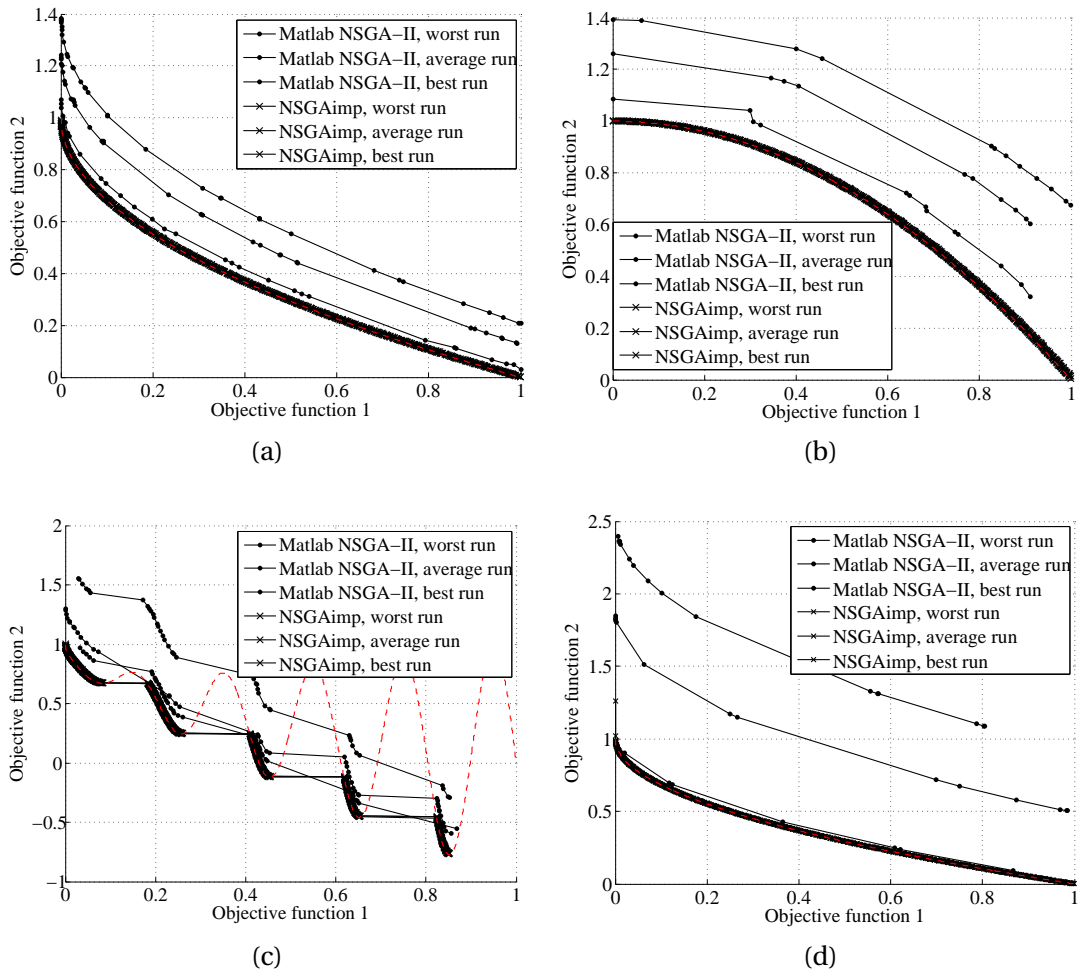


Figure 4.13: Obtained Pareto optimal solutions with *NSGAimp* and Matlab's *NSGA-II* on (a) *ZDT1*, (b) *ZDT2*, (c) *ZDT3*, (d) *ZDT4*.

are the Joule losses and the power transferred to the load. In order to limit the spread of the Pareto solutions within an acceptable range, two new constraints are defined so that the output power is situated between 2 and 10 W:

$$2 \leq P_{out} \leq 10 \tag{4.18}$$

This problem is interesting because it cumulates the difficulties of both constrained and unconstrained problems encountered above. Indeed, this problem involves a high number of parameters and complicated constraints. As this problem is more complex than the previous ones, the number of generations is increased to $T = 200$ for a total of 10000 function evaluations. The results of three successive runs are shown in Fig. 4.15. Interestingly, the results obtained are situated on the same line as in Fig. 4.8, with the difference that there are more

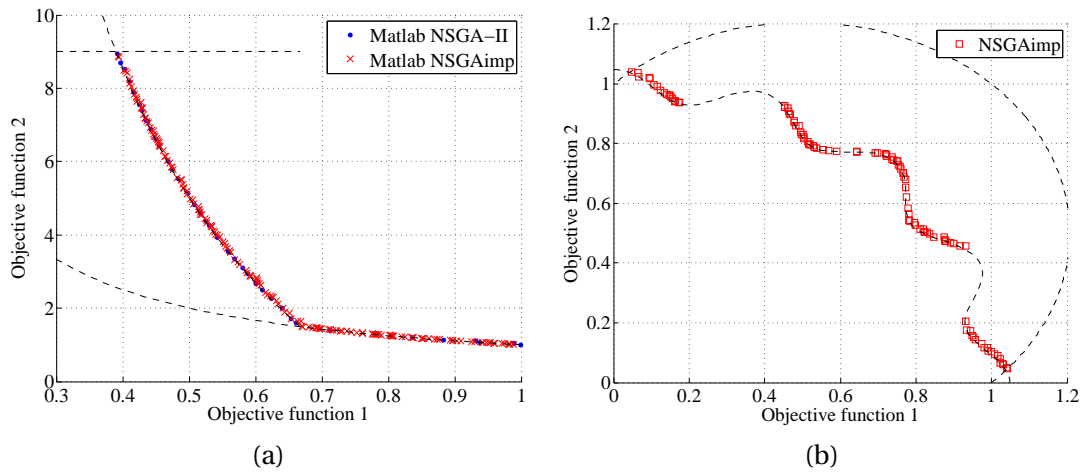


Figure 4.14: (a) Obtained Pareto optimal solutions with *NSGAimp* and Matlab's NSGA-II on *Constr*. (b) Obtained Pareto optimal solutions with *NSGAimp* on *Tnk*.

than 200 available solutions spread along this line for each run. In this case again, *NSGAimp* shows a good stability and effectiveness.

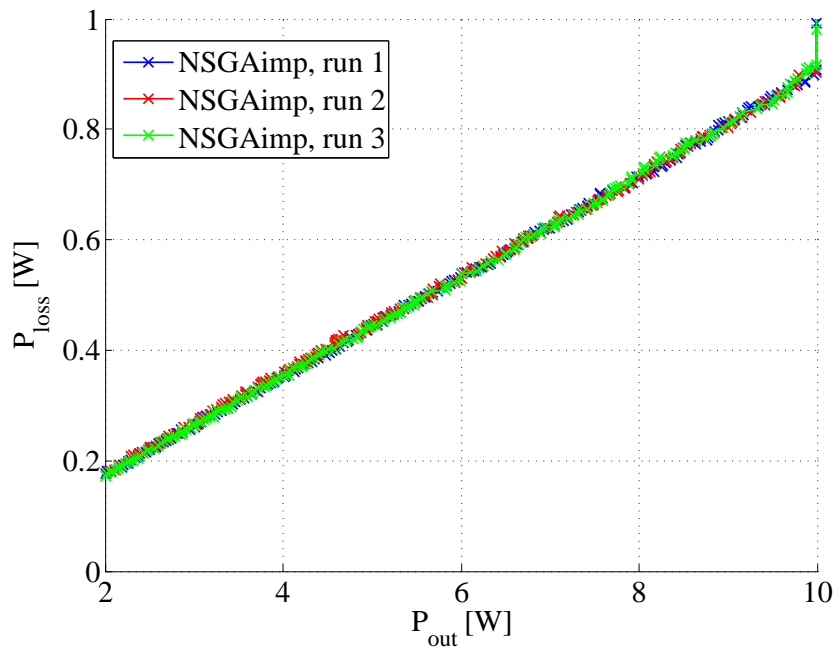


Figure 4.15: Pareto optimal solutions obtained for three successive runs of *NSGAimp* on the problem *Prob1*.

To determine the final solution for an application, one has only to choose the adequate solution that meets the specifications. For the problem *Prob1*, the goal is to obtain an output

power of 5 W, which is obtained with the set of input parameters given in Table 4.2. The calculated output power and power losses of the corresponding coreless transformer are given in Table 4.3. Finally, this solution has been realized and measured using the electronics and the setup that will be presented in section 5.1.3. The measured values are just mentioned here so as to compare them with the calculated ones.

Table 4.2: Free parameters.

Primary coil		Secondary coil	
Parameter	Value	Parameter	Value
n_1	9	n_2	10
a_1	49.60 mm	a_2	50.00 mm
w_1	1.21 mm	w_2	0.94 mm
d_1	0.47 mm	d_2	0.40 mm
f	500 kHz		

Table 4.3: Output parameters.

Parameter	Calc. value	Meas. value
P_{out}	5.03 W	5.05 W
P_{j1}	0.23 W	0.25 W
P_{j2}	0.21 W	0.22 W
P_{loss}	0.44 W	0.47 W
η	92 %	92 %

This validates the use of *NSGAimp* for simple CET applications. However, for more complicated CET systems such as the CET table, some preliminary remarks have to be done concerning the design. Based on the sensitivity analysis of section 4.2 and the MOGA developed in this section, a strategy to design the CET table is presented in the following section.

4.6 Design of the CET table

4.6.1 Context and specifications

The goal consists in designing a CET table for multiple low-powered loads. The expectations for such a CET table can be formulated as follows:

- It must be able to supply simultaneously small peripherals such as a mouse, a keyboard and a loudspeaker.

- The supply has to be performed continuously. This leads to another requirement, which is to activate only the portions of the table where the peripherals are localized.
- The CET system has to be as simple as possible so as to integrate it easily in the table and in the peripherals.

So as to identify the power that need to be transferred to different loads, three peripherals available on the market are tested. Their specifications have been measured and are reported in Table 4.4. Between those three peripherals, the most power-consuming one is the loudspeaker. But in order to ensure that a maximal number of existing peripherals can be supplied with this CET table, it has been decided that at least 5 W must be transferable everywhere on the surface.

Regarding the size of the coils, the secondary ones are limited by the size of the mouse. It is therefore limited to 50 mm, which allows to integrate it discretely under most of existing mice, even if the one used in the scope of this work would allow to have an external size that is even larger than 60 mm. The size of the primary coils is not limited and is determined according to the optimal design.

Table 4.4: Electric specifications of the mouse, keyboard and loudspeaker

Device	Voltage [V_{dc}]	Current [$mA_{dc,max}$]
Mouse	1.5	40
Keyboard	3.0	25
Loudspeaker	5.0	420

4.6.2 Choice of the coils geometry

At this point, the CET table can be made of an array of primary coils, and one or multiple secondary coils can be used for each peripheral. This gives rise to a multitude of possible geometric configurations. The primary coils can be distributed over one or multiple layers and can be of any shape. Fig. 4.16 shows a few possibilities for the disposition of the primary coils.

It has been mentioned earlier that only square and hexagonal coils are used in this work. This choice is justified here, because using circular coils (Figs. 4.16(a)-(b)) would create gaps between the coils where no magnetic field can be generated, which makes them not interesting for the CET table.

The configurations in which the primary coils are distributed over multiple layers (as in Fig. 4.16(f)) are also eliminated. This choice comes from the objective of simplifying as much as possible the electronics of the CET table. For instance, using two layers of primary coils would

double the number of electronic components, and that we wanted to avoid. In a similar way, using only a single secondary coil for each peripheral allows to limit the number of electronic components.

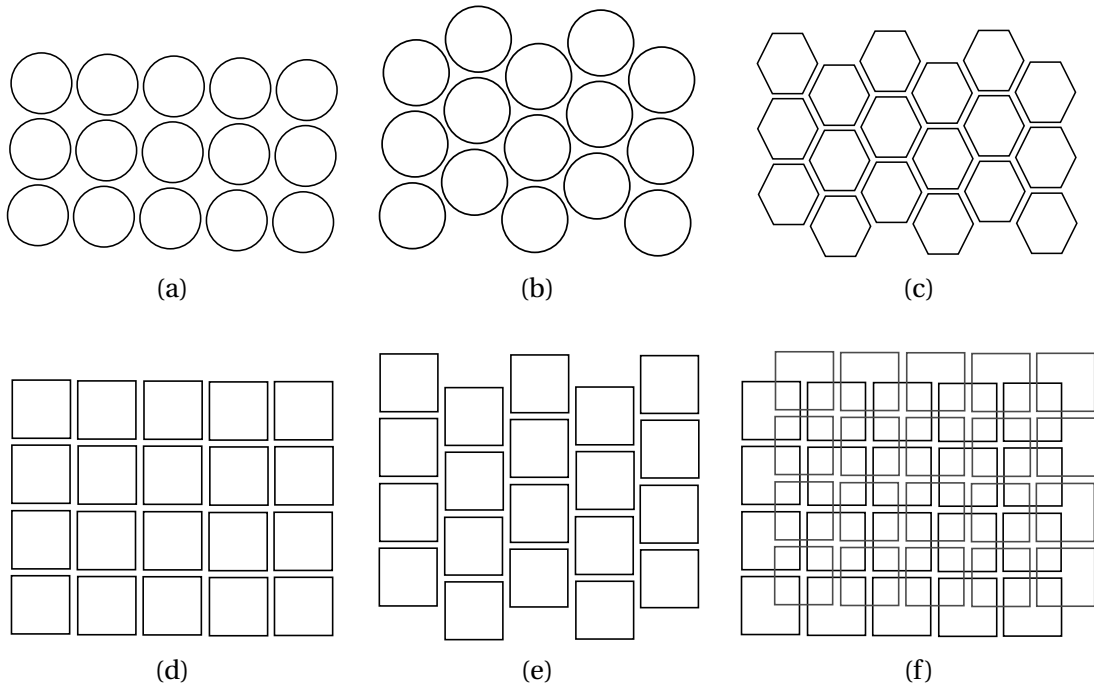


Figure 4.16: Arrays of (a)-(b) circular coils, (c) hexagonal coils, (d)-(e) square coils. (f) Two layers of primary square coils.

In brief, the remaining solution for the CET table is a primary array of square or hexagonal coils with one larger secondary coil for each peripheral. Two different configurations corresponding to Figs. 4.16(c) and 4.16(d) will be tested in chapter 5.

4.6.3 Choice of the compensation topology

The choice of the compensation topology is guided by the objective of restricting the number of electronic components. This choice is greatly related to the type of high-frequency converter used to generate the HF current into the primary coils. In the different applications developed in the next chapter, two configurations for the HF converter will be examined: the single-transistor converter and the full-bridge converter that are roughly outlined in Fig. 4.17. The full bridge generates purer sinusoidal signals than the single-transistor converter, but in return is more complicated to implement and to control.

Concerning the CET table, each coil of the primary array must have the ability to be individ-

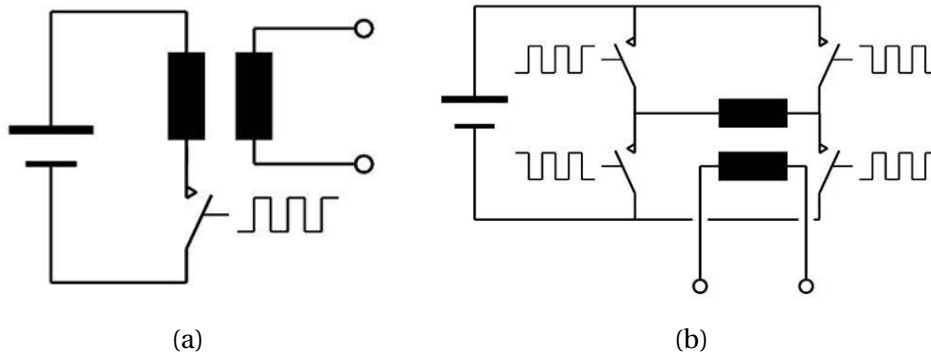


Figure 4.17: (a) Single-transistor converter. (b) Full-bridge converter

ually activated and deactivated. A large number of switches and electronic components are therefore required to control the whole CET table. For example, an interesting solution to a similar application is proposed in [112]. Therein, the electronics used to control a relatively small CET platform includes three transistors per primary coil, a demultiplexer, a multitude of drivers and other smaller components. The place it requires is really huge, much larger than the CET platform itself.

Because it allows to reduce the number of electronic components of the CET table developed in this thesis, a novel switching configuration based on the single-transistor converter is proposed. This will be discussed more into details in chapter 5.

To achieve the resonance with the primary inductance, it is necessary to place the primary compensation capacitor C_1 in parallel when using such a single-transistor converter. The secondary compensation is placed in series, because in this case the reflected impedance is strictly real and therefore the secondary circuit draws only active power.

4.6.4 CET table Optimization

In brief, the aim is to optimize a CET system composed of an array of primary coils and larger secondary coils. The losses are to be minimized and a minimal power of 5 W has to be transferred above the whole surface. The first idea that comes into mind to solve this problem consists in placing the secondary coil in the position where it is most difficult to reach this minimal amount of power and performing the optimization for this position. This method was tested and provided unsatisfactory results because the power was too much fluctuating as a function of the position of the secondary coil. Moreover, it did not allow to certify that the minimal power was transferred over the whole surface.

Then, the strategy adopted to optimize the CET table consists in separating the problem into different scenarios. Doing so allows to obtain a smaller fluctuation of the output power over the surface and ensures that the minimal power is transferred to the load.

For an array of square coils such as the one in Fig. 4.16(d), assuming that the secondary coil remains parallel to the primary ones, one can consider three different scenarios depicted in Fig. 4.18:

- The secondary coil is well aligned with a primary one. This corresponds to the position P_1 . In this case, only the concerned primary coil has to be activated.
- The secondary coil is placed above two adjacent primary coils. This corresponds to the position P_2 . In this case, both concerned primary coils have to be activated.
- The secondary coil is placed above four adjacent primary coils. This corresponds to the position P_3 . In this case, the four concerned primary coils have to be activated.

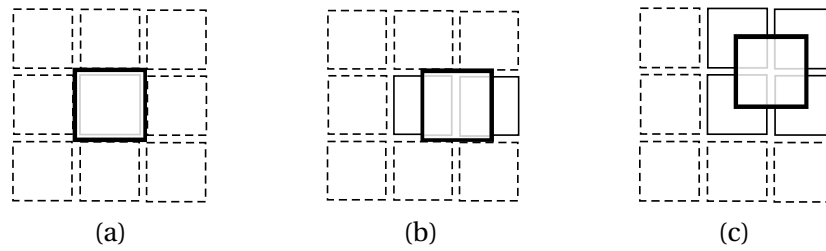


Figure 4.18: (a) Position P_1 , (b) position P_2 , (c) position P_3 .

Similarly for hexagonal coils, three different scenarios corresponding to positions P_a , P_b , P_c , can be considered and are described in Fig. 4.19. Different tests have shown that the optimization provides better results when the position P_a from the first scenario is laterally shifted by half the radius of a primary coil.

During the optimization, the three scenarios have to be taken into account. It is done by summing the respective output powers of each scenario in the first objective function and summing the respective power losses of each scenario in the second objective function. For example, applying this to an array of hexagonal coils as shown in Fig. 4.19 leads to the following objective functions (to be minimized):

$$O_1 = -P_{out,a} - P_{out,b} - P_{out,c} \quad (4.19)$$

$$O_2 = P_{loss,a} + P_{loss,b} + P_{loss,c} \quad (4.20)$$

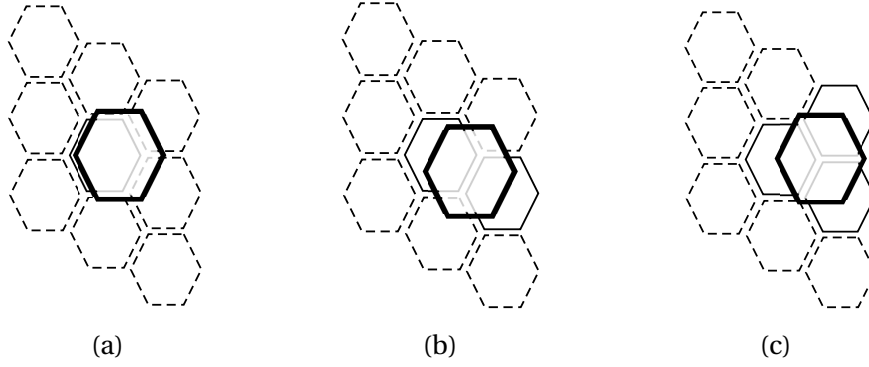


Figure 4.19: (a) Position P_a , (b) position P_b , (c) position P_c .

where $P_{out,a}$, $P_{out,b}$, and $P_{out,c}$ are the output powers obtained at positions P_a , P_b , and P_c . The corresponding power losses are defined as follows:

$$P_{loss,a} = P_{j1,a} + P_{j2,a} \quad (4.21)$$

$$P_{loss,b} = 2P_{j1,b} + P_{j2,b} \quad (4.22)$$

$$P_{loss,c} = 3P_{j1,c} + P_{j2,c} \quad (4.23)$$

Here, $P_{j1,a}$ corresponds to the Joule losses of the primary coil and $P_{j2,a}$ corresponds to the Joule losses of the secondary coil for the scenario (a). $P_{j1,b}$, $P_{j2,b}$, $P_{j1,c}$, $P_{j2,c}$ can be defined in a similar way.

The parameter limits are identical to the ones of *Prob1* presented in section 4.4.3 (*c.f.* equations 4.4 to 4.8). The only difference is that there are three additional free parameters, which are the input voltage U_{in} , the number of layers N_1 and N_2 for the distribution of the turns. The variation range for U_{in} is chosen between 12 and 24 V (AC rms) and the choice for N_1 and N_2 is limited to one or two layers in this work:

$$12.0 < U_{in} < 24.0 \quad [V (rms)] \quad (4.24)$$

$$N_1, N_2 = 1, 2 \quad [-] \quad (4.25)$$

To bound the solutions within an acceptable range of variation, the output power is constrained between 5 W and 10 W. This leads to a total of eight inequality constraints, defined as

follows:

$$\frac{n_1}{N_1}(w_1 + d_1) + cst < \frac{a_1}{2} \quad (4.26)$$

$$\frac{n_2}{N_2}(w_2 + d_2) + cst < \frac{a_2}{2} \quad (4.27)$$

$$P_{out,a} < 10 \quad (4.28)$$

$$P_{out,b} < 10 \quad (4.29)$$

$$P_{out,c} < 10 \quad (4.30)$$

$$P_{out,a} > 5 \quad (4.31)$$

$$P_{out,b} > 5 \quad (4.32)$$

$$P_{out,c} > 5 \quad (4.33)$$

As a recall, cst is a parameter that corresponds to the minimal free space inside the coils where no copper can be present. In this work, it is set to 2 mm.

The *NSGAimp* is then applied to this problem. As it is much more complicated than the previously encountered ones, the number of generations is set to $T = 400$, which gives a total of 20'000 function evaluations. The results of three consecutive runs are given in Fig. 4.20. In order to take advantage of the full potential offered by the multi-core computers, the “parallel computing toolbox” from Matlab has been used. Notably, the function “parfor” allows to distribute simultaneously different tasks to the four cores (clocked at 2.5 GHz) of the CPU. In this case, it has reduced the computation time by a factor of 3 to 3.5. As a result, a run typically requires between 8 and 10 hours of computing time.

As for *Probl*, the result of the three runs are similar. Each solution so obtained could fulfill the specifications. But in this specific case, the goal is to choose one that allows to provide at least 5 W at every position with the lowest Joule losses and with the lowest fluctuation of output power. Thus, a judicious choice consists in picking the solution with the lowest total Joule losses. The set of free parameters for this solution is given in Table 4.5 and the output parameters are given in Table 4.6. This solution will be experimentally tested in section 5.2.8.

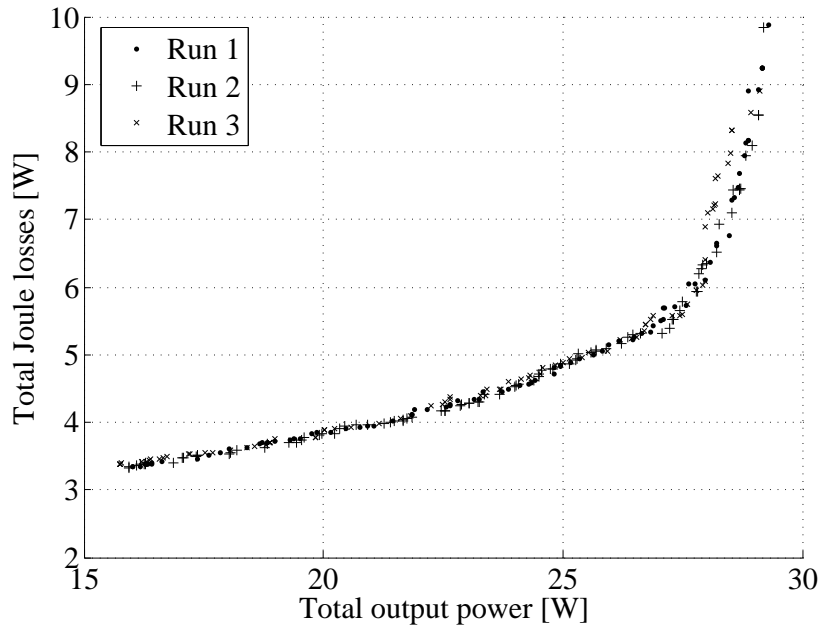


Figure 4.20: Results of three optimization runs giving the total output power ($-O_1$) versus the total Joule losses (O_2).

Table 4.5: Input parameters for the CET table.

Parameter	Value	Parameter	Value
n_1	20	n_2	18
N_1	2	N_2	2
a_1	38.99 mm	a_2	50.00 mm
w_1	0.45 mm	w_2	0.79 mm
d_1	0.39 mm	d_2	0.56 mm
f	500 kHz	U_{in}	24 V (AC rms)

Table 4.6: Output parameters for the CET table.

Parameter	Value	Parameter	Value	Parameter	Value
O_1	-15.93 W	O_2	3.38 W	U_{in}	24 V (rms)
$P_{out,a}$	5.07 W	$P_{out,b}$	5.74 W	$P_{out,c}$	5.12 W
$P_{loss,a}$	0.71 W	$P_{loss,b}$	1.17 W	$P_{loss,c}$	1.50 W
$P_{j1,a}$	0.30 W	$P_{j1,b}$	0.35 W	$P_{j1,c}$	0.36 W
$P_{j2,a}$	0.41 W	$P_{j2,b}$	0.47 W	$P_{j2,c}$	0.41 W

4.7 Overall conclusion

In this chapter, a general method to design CET systems is given. First, a sensitivity analysis is performed and allows to anticipate the variation range and the impact of the main parameters on a CET system.

Then, a new MOGA is developed so as to generate an optimal design for different CET systems. This new MOGA has been tested and has proven to provide excellent results in terms of convergence and diversity.

The main and innovative contribution of this chapter consists of the establishment of a method that allows to design and optimize both fixed and movable CET systems. The only difference resides in the number of scenarios to evaluate. Fixed position systems are designed by taking into account only a single position evaluation, and free position systems are designed by considering multiple scenarios for the position of the secondary coil. Thanks to this strategy, only the two objective functions have to be adapted, but the rest of the design process is left unchanged.

Experimental results and prototypes

Summary

5.1 Inductive notebook charger	118
5.1.1 Context and specifications	118
5.1.2 The coreless transformer	118
5.1.3 Electronics	120
5.1.4 Measurements	122
5.1.5 Conclusion	126
5.2 CET table	127
5.2.1 Introduction	127
5.2.2 First measurements	128
5.2.3 Second prototype	130
5.2.4 Supply strategy	131
5.2.5 Primary coils array circuit	134
5.2.6 Peripheral detection	138
5.2.7 Secondary coils circuit	142
5.2.8 Third prototype	144
5.3 Estimation of the magnetic field	146
5.4 Conclusion	148

In this chapter, the different prototypes built are measured and tested. The electronics used to drive the prototypes is presented. Finally, an estimation of the magnetic flux densities at stake are studied so as to address the problem of health and safety.

5.1 Inductive notebook charger

5.1.1 Context and specifications

As mentioned in chapter 1, the aim of this section is to design a CET system from the *Alto* platform (depicted in Fig. 1.2) to a notebook charger. To achieve this, Litz wires are used because the external size of the coils is quite large and because they offer in this case the best compromise between resistivity and integration. This prototype will allow to validate experimentally the modeling of coreless transformers presented in chapter 2.

A preliminary study has allowed to establish the specifications of the coreless transformer. The details of this study are presented in appendix D. A summary of the specifications is given in Table 5.1. The global electronics schematic of the CET system is presented in Fig. 5.1. It includes the following main parts (or functions):

- the input rectifier;
- the full-bridge converter;
- the coreless transformer;
- the output rectifier.

Table 5.1: Specifications of the CET notebook charger demonstrator

Specification	Description
Maximal coils size	240 mm by 160 mm
Airgap	10 mm
Input voltage	$U_1 = 355 \text{ V (AC rms)}$
Output voltage	$U_2 = 20 \text{ V (AC rms)}$
Load power	$P_L = 80 \text{ W}$

5.1.2 The coreless transformer

The choice of the compensation topology is based on the specifications. The notebook battery requires a stable voltage of 20 V (DC) even when the load fluctuates during the charging process. A good candidate for this specification is the PS topology. This choice will be verified by measurements.

The used Litz wire has a radius of 1 mm so as to support the current that flows through the coils. The space between two turns is chosen as small as possible so that each turn is in physical

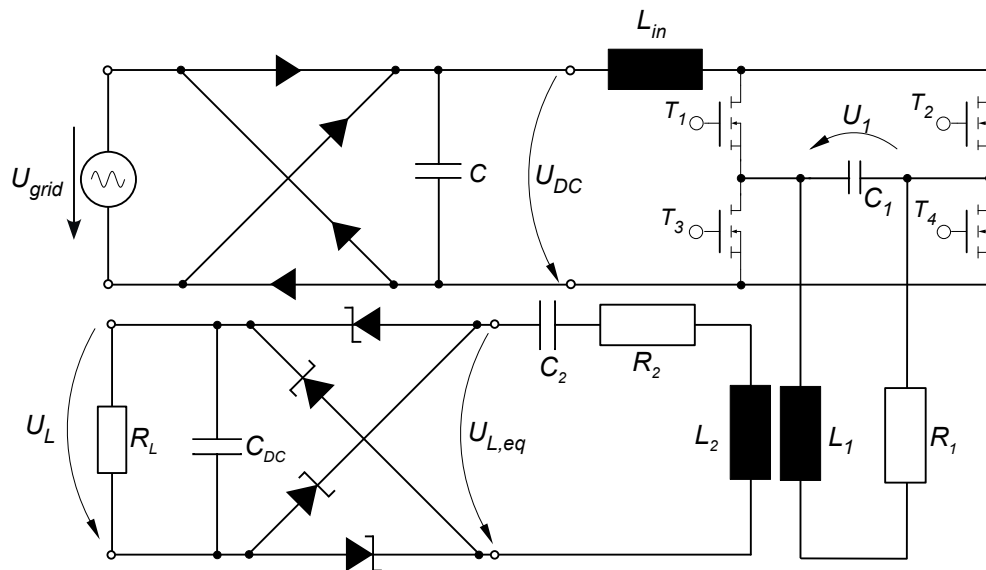


Figure 5.1: The CET system for the CET notebook charger.

contact with each other. Thus, the variable parameters for the design are number of primary turns n_1 , the number of secondary turns n_2 , the number of primary layers N_1 , the number of secondary layers N_2 , the primary first side length a_1 , the primary second side length b_1 , the secondary first side length a_2 , and the secondary second side length b_2 .

The design of the coreless transformer is performed through an iterative process that is presented in [90] and [88]. The design obtained for the coreless transformer is given in Table 5.2. This solution is then fabricated so as to test it and make measurements.

The operating frequency of the coreless transformer is set to 250 kHz. As expected, the number of primary turns is much larger than the number of secondary turns. This is a logical result because the aim of the coreless transformer is to generate an output voltage of 20 V (AC rms) from an input voltage of 355 V (AC rms). A large number of primary turns allows to reduce the current in the primary coil and a single secondary turn induces the correct voltage to the notebook battery.

The different values of the coreless transformer are given in Table 5.3. The measurements are performed at 250 KHz. As a result, the measured and calculated inductances are in good agreement, but there is a large difference between the measured and calculated resistances. It is mostly due to the contacts and partly due to the HF effects that are not taken into account for the calculated values. Even so, this difference does not alter the behavior of the coreless transformer because the resistance remains very low compared to the impedance of the self inductance for both primary and secondary coils.

Table 5.2: Final design of the coreless transformer for the Notebook.

Parameter	n_1	n_2	N_1	N_2	$a_{1,2}$	$b_{1,2}$
Value	10	1	3	1	220 mm	140 mm

Table 5.3: Calculated and measured parameters of the coreless transformer.

Parameter	L_1	L_2	L_{12}	R_1 ,	R_2
Calculated	49.11 μH	791 nH	2.98 μH	65 m Ω	7 m Ω
Measured	52.20 μH	821 nH	3.08 μH	210 m Ω	95 m Ω

5.1.3 Electronics

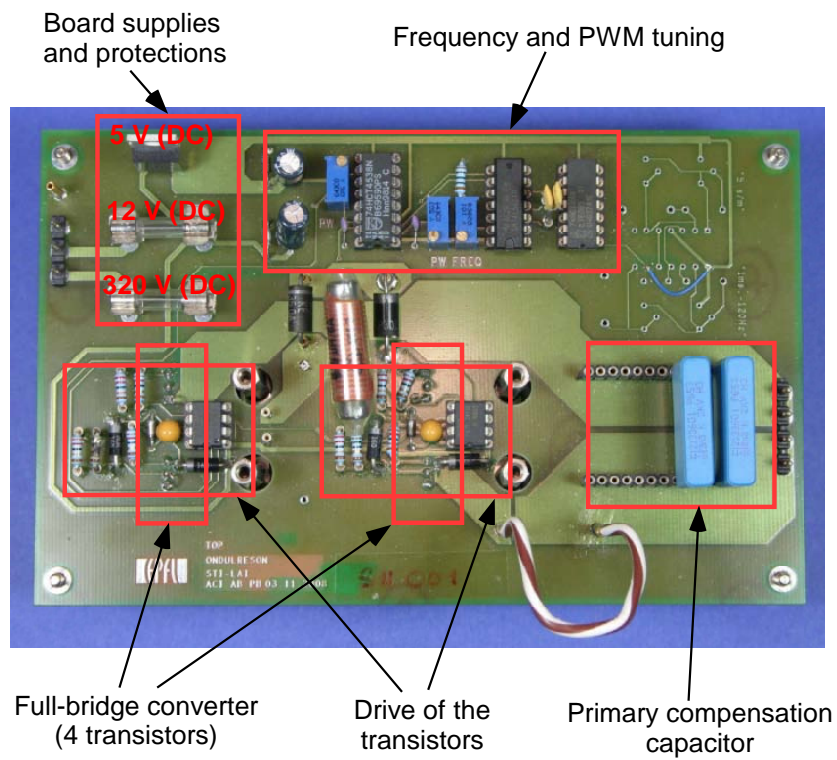
The full-bridge converter

The full-bridge converter is used to generate the HF signals into the primary coil from a DC voltage. The converter that is developed for the CET battery charger is based on the one presented in [57]. Therein, it was used for a low power CET application (about 10 W). The design has then be revisited to support a DC voltage of more than 320 V (DC) and a power in the order of 100 W.

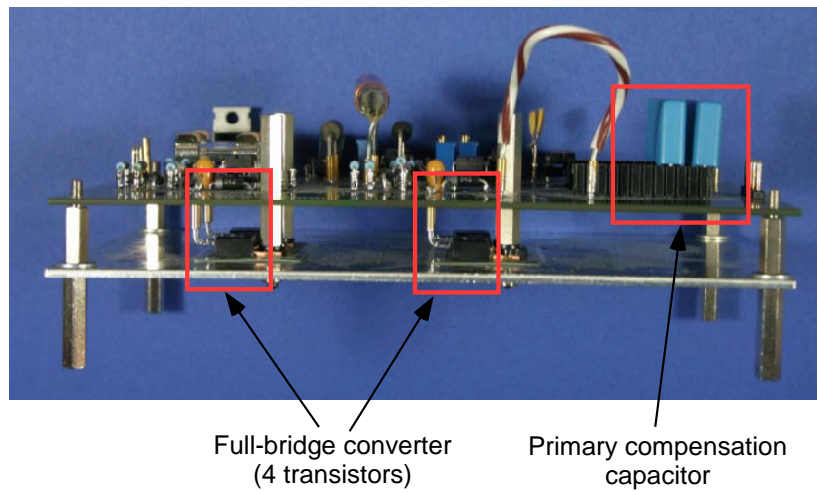
Fig. 5.2 shows a picture of the full-bridge converter. Its specific advantage is that the frequency and the PWMs can be manually adjusted by three potentiometers (typically from 200 kHz to 600 kHz).

The circuit is basically divided into three main parts. The first one concerns the logical circuit used to control and generate the PWMs. This part is supplied by a stable voltage of 5 V (DC). Secondly, the drivers of the transistors are supplied by a stable voltage of 12 V (DC). Finally, the power circuit has a stable voltage of 320 V at the input of the converter and gives rise to the 355 V (AC rms) at the output of the converter.

As shown in Fig. 5.2(b), the PCB is mounted on an aluminium plate that serves as a cooler for the transistors. More details on the electronics and the main components are given in appendix D.3.



(a)



(b)

Figure 5.2: (a) Top view and (b) side view of the full-bridge converter.

The output rectifier

The rectifier is situated at the output of the coreless transformer. Fig. 5.3 shows a photograph of the rectifier used to supply the notebook. More details on the components used in the rectifier are given in appendix D.3.

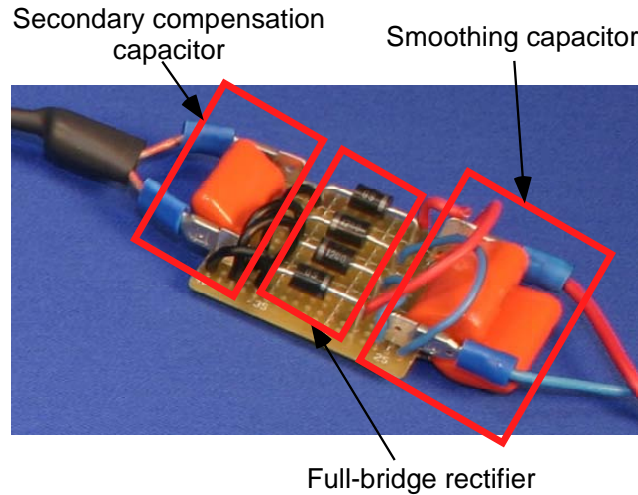


Figure 5.3: The output rectifier with the series compensation capacitor and the smoothing capacitor.

5.1.4 Measurements

Two sets of measurements are performed on the prototype. First, multiple measurements of voltages and currents are made at different steps of the CET system. Three cases are tested: when the coreless transformer has no load, when the coreless transformer is directly loaded by a resistor of $5\ \Omega$ (without rectifier), and when the coreless transformer is loaded by a resistor of $5\ \Omega$ through the output rectifier. This first set of measurements allows to analyze the effect of the load and of the full-bridge rectifier on the coreless transformer.

The second set of measurements is done with the rectifier and with a load varied from 2 to $15\ \Omega$ to show that the system is able to provide a stable voltage to the notebook battery.

First set of measurements: case 1

Fig. 5.4 shows the input voltage U_1 and the current in the primary coil I_{L1} when there is no load. This corresponds to the case in which there is no notebook on the platform. Since there is no load, only a small amount of active power is consumed in the CET system, due to the resistance of the primary coil and the losses in the transistors. The waveforms of the input

voltage and the current in the primary coil are perfectly sinusoidal.

Table 5.4 gives the values of voltages and currents at different steps of the CET system. As a recall, U_{DC} is the DC voltage at the input of the full-bridge converter, I_{DC} is the average current delivered to the full-bridge converter, U_1 is the input voltage (AC rms) of the coreless transformer and I_{L1} is the current (AC rms) in the primary coil. Those parameters can be observed in Fig. 5.1. From these measurements, the power losses are evaluated at 7 W when there is no load.

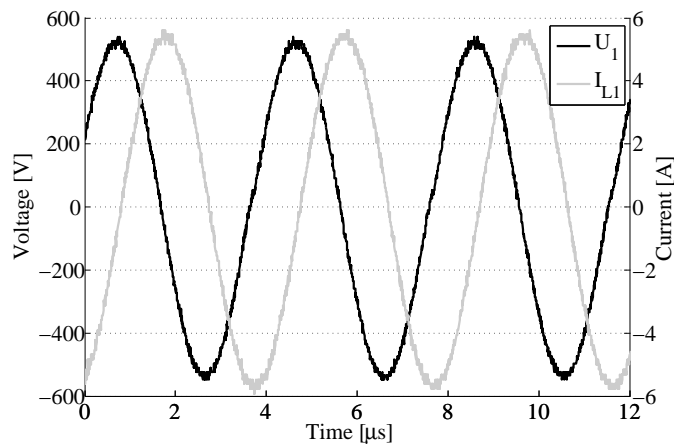


Figure 5.4: Measurement of the input voltage and the current in the primary coil when no load is present.

Table 5.4: Electrical values of the coreless transformer.

Parameter	U_{DC} (DC)	I_{DC} (DC)	U_1 (AC rms)	I_{L1} (AC rms)
Calculated	320 V	3.8 mA	355 V	4.32 A
Measured	322.7 V	22 mA	370.2 V	3.95 A

First set of measurements: case 2

Fig. 5.5(a) shows the voltage U_1 and the current in the coil I_{L1} when the coreless transformer is loaded by a resistor of 5Ω without rectifier. The result shows that the signals are very similar to the case without the load. The reason for this is that the impedance of the primary coil is much larger than the reflected impedance. In other words, the effect of the load and the secondary coil on the primary is very low. Fig. 5.5(b) shows the voltage measured on the load and the current in the secondary coil (which is equal to the current in the load). Their waveforms are perfectly sinusoidal.

Table 5.5 gives the values of voltages and currents at different steps of the CET system. As a

Chapter 5. Experimental results and prototypes

recall, U_L is the voltage (AC rms) obtained on the load and I_L is the current (AC rms) obtained in the load. The total losses generated in the coils and the full-bridge converter can be estimated from the measurements at 10.2 W, resulting in an efficiency of 88.9 %.

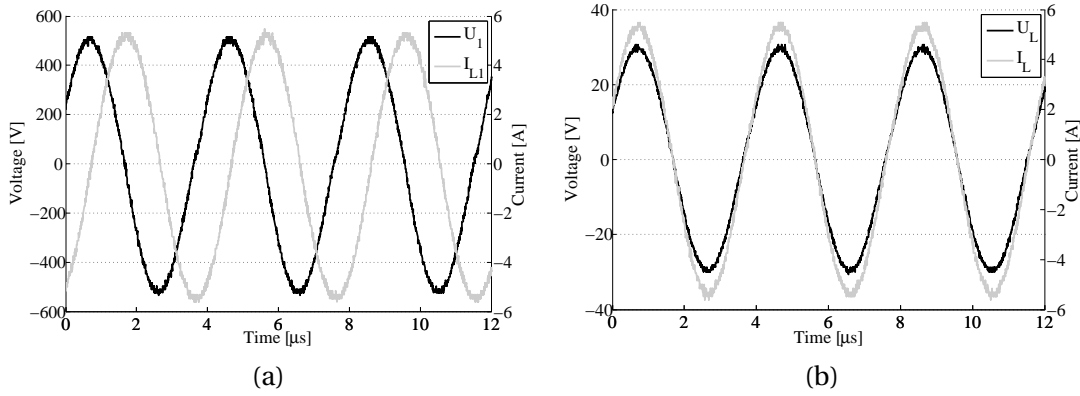


Figure 5.5: (a) Measurement of the input voltage and the current in the primary coil when the coreless transformer is loaded by a resistor of 5Ω without the rectifier. (b) Measurement of the voltage and the current in the load.

Table 5.5: Electrical values of the coreless transformer.

	U_{DC} (DC)	I_{DC} (DC)	U_1 (AC rms)	I_{L1} (AC rms)	U_L (AC rms)	I_L (AC rms)
Calc.	320 V	234 mA	355 V	4.21 A	20.18 V	4.05 A
Meas.	321.2 V	281.5 mA	358.1 V	3.80 A	21.16 V	3.79 A

First set of measurements: case 3

Fig. 5.6(a) shows the voltage U_1 and the current in the coil I_{L1} when the coreless transformer is loaded by a resistor of 5Ω through the rectifier. For the same reason formulated above, they are very similar to the previous cases. Fig. 5.6(b) shows the voltage $U_{L,eq}$ obtained at the input of the secondary rectifier and the current I_{L2} in the secondary coil. The waveforms are not sinusoidal because of the non-linearities introduced by the diodes.

Table 5.6 gives the values of voltages and currents at different steps of the CET system. Here, $U_{L,DC}$ and $I_{L,DC}$ are respectively the voltage and the current (DC) obtained in the load. The total losses generated in the coils, the full-bridge converter and the full-bridge rectifier can be estimated from the measurements at 22.6 W, resulting in an efficiency of 79.4 %.

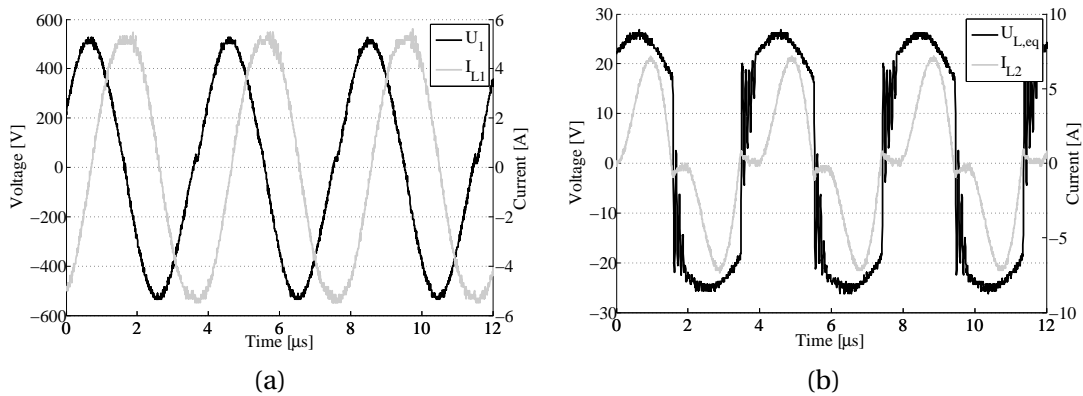


Figure 5.6: (a) Measurement of the input voltage and the current in the primary coil when the coreless transformer is loaded by a resistor of 5Ω with the rectifier. (b) Measurement of the voltage at the input of the secondary rectifier and the current in the secondary coil.

Table 5.6: Electrical values of the coreless transformer.

	U_{DC} (DC)	I_{DC} (DC)	U_1 (AC rms)	I_{L1} (AC rms)	$U_{L,DC}$ (DC)	$I_{L,DC}$ (DC)
Calc.	320 V	274 mA	355 V	4.34 A	20.06 V	4.01 A
Meas.	320.4 V	345.5 mA	359.9 V	3.89 A	21.7 V	4.05 A

Second set of measurements

As explained in appendix D.2.2, the load of the notebook battery can vary during the process of charging (as a function of the charge level, the screen brightness, CPU usage, ...), but in every case, a voltage situated around 20 V (DC) is required. Therefore, it is interesting to analyze the effect of the load variation of the system. To achieve this, an electronic load (HP 6050 DC) is used and varied from 2 to 15 Ω .

The load voltage $U_{L,DC}$ and the efficiency are plotted as a function of the load resistance in Fig. 5.7. The smaller is the load (that is the larger is its corresponding resistance), the higher is the DC voltage obtained on the load. This happens because the reflected impedance decreases when the load resistance is increased. This leads to a slight increase of current in the primary coil, which in turn increases the induced voltage in the secondary coil.

The measurements of efficiency take into account the losses in the transistors, in the coils and in the diodes of the secondary rectifier. The efficiency is maximal for a load resistance situated between 4 and 5 Ω , which corresponds to the value for which the coreless transformer is designed.

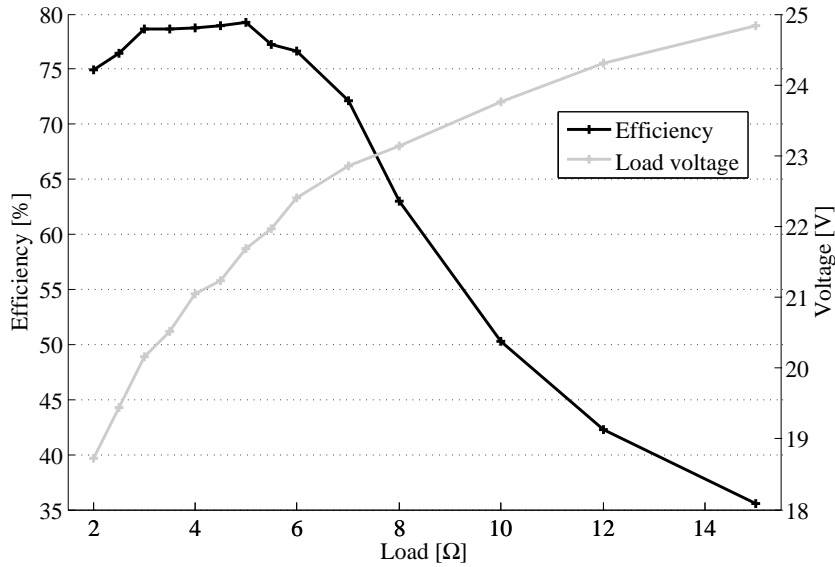


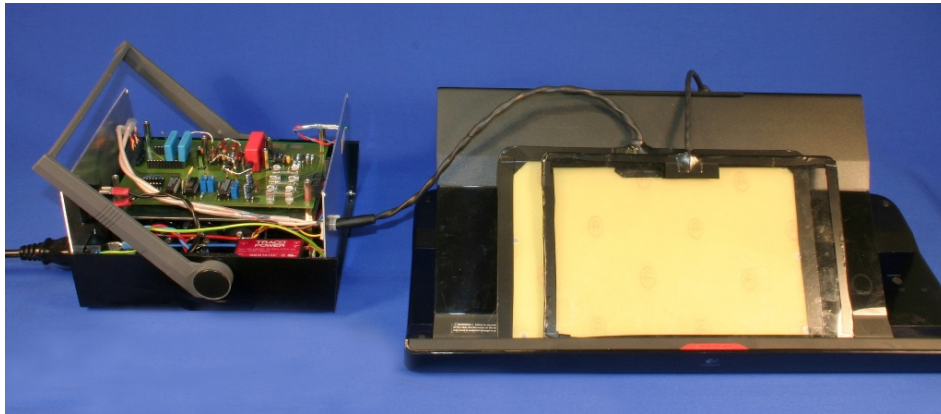
Figure 5.7: Efficiency and DC voltage level versus the load resistance.

5.1.5 Conclusion

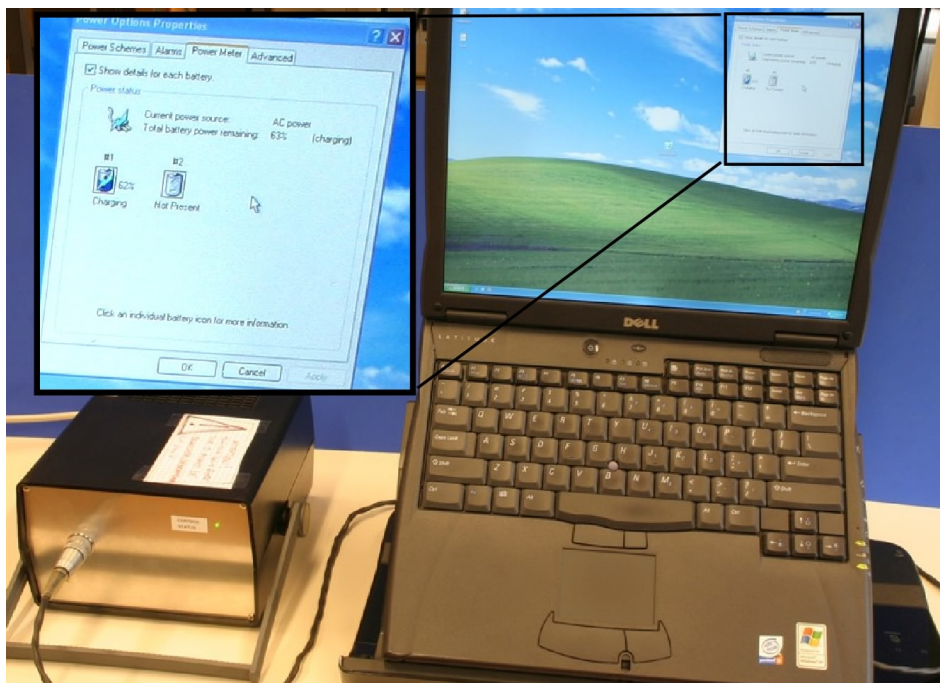
Thanks to a preliminary study presented in appendix D, it is possible to draw the specifications of the coreless transformer for the inductive notebook charger. With the analytical model presented in chapter 2, the design of the coreless transformer is performed and a prototype is built (*c.f.* Fig. 5.8(a)). The measurements show that the coreless transformer is able to provide a minimal and stable voltage of 20 V (DC) for different values of load resistances.

The presence of the secondary rectifier generates voltage and current disturbances in the secondary coil that deteriorate the efficiency of the whole system. The origin of this problem is assumed to come from the addition of capacitive and inductive elements (in the rectifier and the smoothing capacitor) that may be not consistent with the hypothesis that the equivalent load (D.4) is purely resistive. This issue must be further investigated so as to minimize the inherent efficiency drop.

Finally, the prototype has been tested directly on the battery while the notebook was working (*c.f.* Fig. 5.8(b)). We have been able to recharge completely the battery. For us, this first prototype allows to validate the modeling of coreless transformers.



(a)



(b)

Figure 5.8: (a) Picture of the prototype without the notebook. (b) Picture of the prototype while charging the notebook battery.

5.2 CET table

5.2.1 Introduction

Many aspects concerning the specifications and the design of the CET table and are discussed in section 4.6. The present section presents three different prototypes built during this thesis,

so as to validate the different models and the optimization method presented in the previous chapters.

First, preliminary measurements are made on two different arrays of coils. This allows to validate the accuracy of the analytical model when multiple coils are used, and in the same time, to identify some issues concerning the CET when using coils arrays. This first part is presented in section 5.2.2.

Secondly, a larger prototype is built in which a new method for the detection and local activation is implemented. This is probably the most important prototype developed in this thesis as it includes innovative developments concerning the detection and the supply of peripherals. The focus will be made on the electronics and the supply strategy of the CET table. This second part is presented in sections 5.2.3 to 5.2.7.

Finally, for the third prototype, the solution proposed in Tables 4.5 and 4.6 is implemented and measured so as to validate the optimization of the CET table. This third part is presented in section 5.2.8.

5.2.2 First measurements

First tests and measurements are done on two different primary coils arrays. The design of the coil 5 presented in Table 2.3 is replicated into multiple coils placed side by side. The first one is an array of nine primary coils distributed in one layer as shown in Fig. 5.9(a). The second one consists of an array of eighteen primary coils distributed in two shifted layers as shown in Fig. 5.9(b). A picture of the setup that is used for the measurements is given in Fig. 5.10 with the two-layers array and the full-bridge converter presented in section 5.1.3.

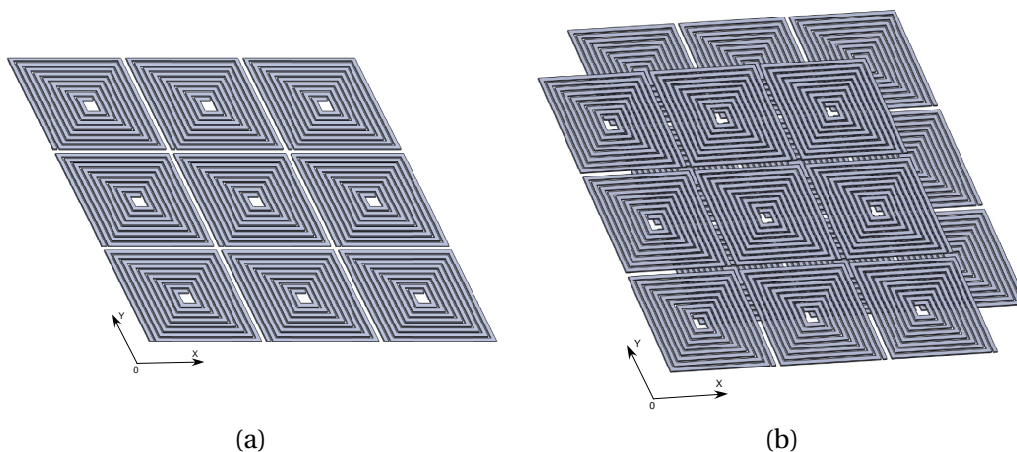


Figure 5.9: (a) The array of 9 coils. (b) The array of 18 coils.

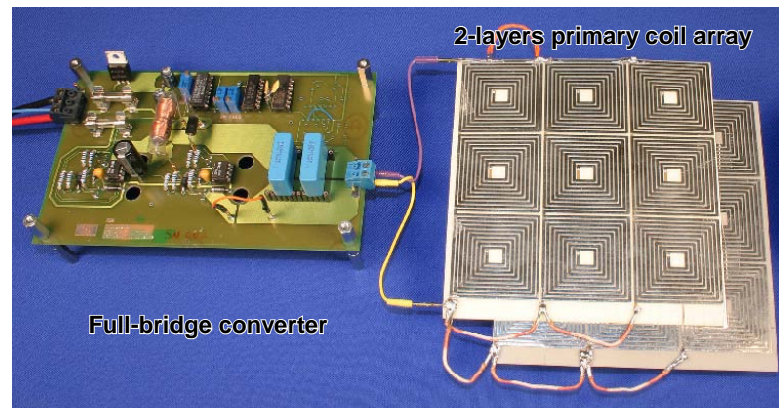


Figure 5.10: Picture of the setup with the array of 18 coils.

For the measurements, the coil 6 of Table 2.3 is displaced over the arrays. Fig. 5.11 shows the measured and calculated values of the voltage (AC rms) obtained on a load of $5\ \Omega$ as a function of the displacements x_d and y_d of the secondary coil. A grid of points separated by 5 mm is used. The vertical distance between the primary coils and the secondary one is 5 mm. The measurements are not performed above the whole arrays because the geometrical periodicity of the structures would make them repetitive. A current of 1 A (AC rms) is generated in the primary coils with the full-bridge converter working at a frequency of 220 kHz. The secondary coil is series-compensated with a capacitor of 47 nF.

Figs. 5.11(a) and 5.11(b) show respectively the calculated and the measured load voltage over the single-layer array. They are in good agreement. But the measurements show that a minimal voltage of 0.3 V (AC rms) is obtained when the secondary coil is placed exactly above the corners of four primary coils. Of course this value is not sufficient to supply electronic peripherals.

A possible solution to solve this problem consists in using two shifted layers. Figs. 5.11(c) and 5.11(d) show respectively the calculated and the measured load voltage above the two-layers array. The minimal voltage obtained under these conditions is about 3.3 V (AC rms).

In conclusion, this first study allows to validate the models presented in chapters 2 and 3 for primary coils arrays using PCB coils. Furthermore, it highlights the issues of CET with primary coils arrays, in which the voltage transferred to the load is not constant in function of the position, and may even be not sufficient to supply peripherals. A possible solution for this problem consists in using two layers of primary coils. But this method brings two main disadvantages. First, if it is true that a minimal amount of transferred power can be ensured at every position, it remains inconstant over the surface, for example between 3.3 and 5.5 V (AC rms) in Fig. 5.11(d). Secondly, concerning the problem of detection and local activation, two

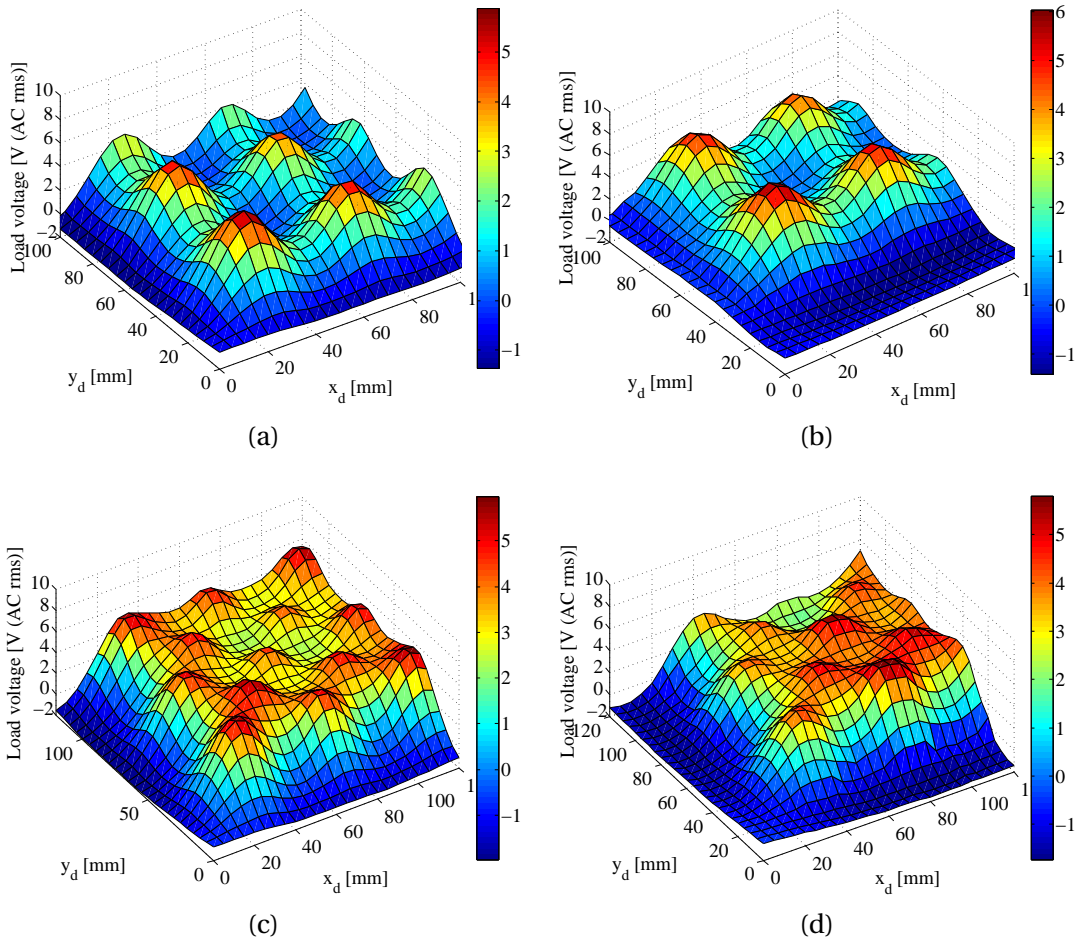


Figure 5.11: Load voltage versus the displacement along X axis and along Y axis. (a) Calculated and (b) measured over an array of 9 coils. (c) Calculated and (d) measured over an array of 18 coils distributed into two shifted layers.

layers of primary coils would lead to an increase of the electronic complexity and the number of components. These few remarks clearly illustrate the advantage of using a single layer of primary coils with larger secondary ones.

5.2.3 Second prototype

The goal of this second prototype is to implement hardware and software solutions to perform the peripheral detection and then the activation of the adequate primary coils. The design of the second prototype is not issued from the optimization presented in chapter 4, but from an iterative method presented in [89] and [91].

The geometrical parameters for the primary and the secondary coils are given in Table 5.7.

The operating frequency of the CET table is 200 kHz. At this frequency, the measured electrical parameters for the primary coil are a resistance of 0.25Ω and a self-inductance of $6,90 \mu\text{H}$. The measured electrical parameters for the secondary coil are a resistance of 0.95Ω and a self-inductance of $25,55 \mu\text{H}$.

Two pictures of the prototype are given in Fig. 5.12 showing respectively a top and a bottom view of the primary coils and electronics.

Table 5.7: Geometrical parameters of the coils for the second prototype.

Parameter	Value	Parameter	Value
a_1	40 mm	a_2	60 mm
n_1	18	n_2	20
N_1	2	N_2	2
w_1	1.5 mm	w_2	1.5 mm
d_1	0.5 mm	d_2	0.2 mm

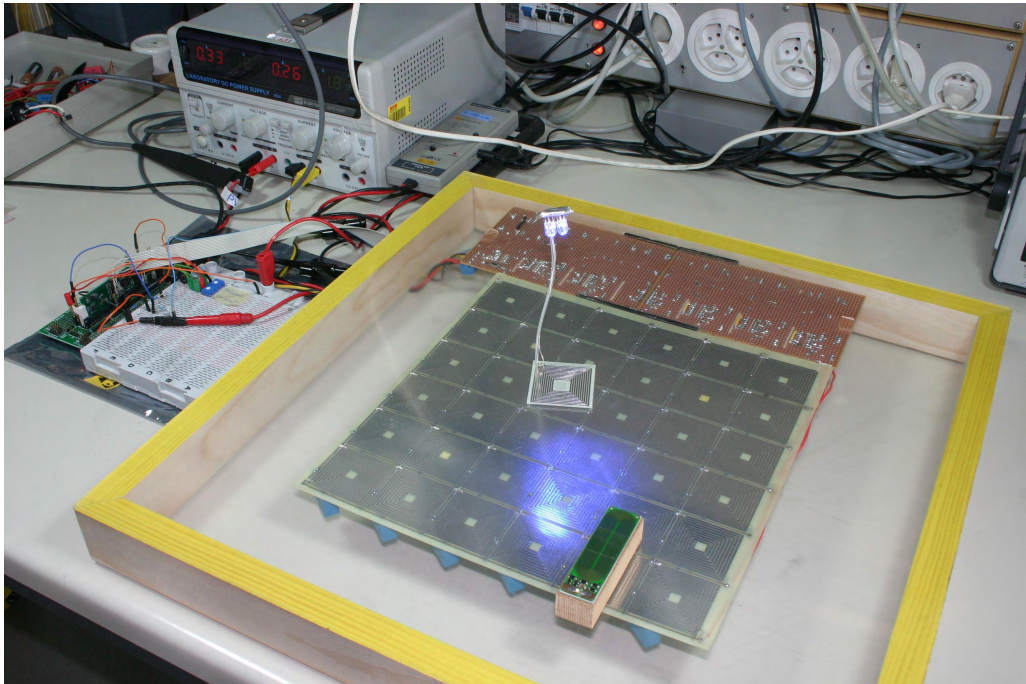
5.2.4 Supply strategy

The system has to be able to supply only the primary coils that are situated below the peripherals. Therefore, the CET table detects the presence and localizes the position of a peripheral. The detection methods are presented in the next section. Once the position of the peripherals is detected, the CET table activates only the corresponding coils. The whole process of detection and local activation is completely autonomous and sensorless.

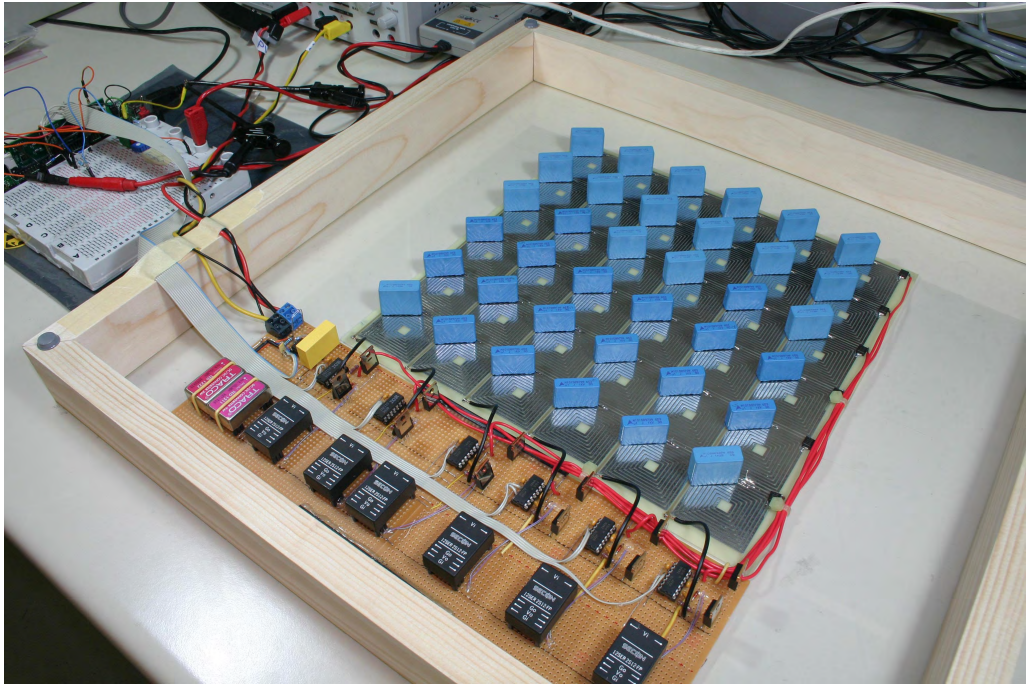
A DSP microcontroller (TI 28027 Piccolo) is used as the central control unit. It controls the transistors for the individual activation of primary coils, it processes the on-board measurements for the detection of peripherals, and it manages all the supply strategy of the CET table.

Basically, this strategy can be split into four main phases that are synthesized in Fig. 5.13. The first phase allows to calibrate the system, and the three following phases constitute an infinite loop that controls the load detection and the coil activation. The detection is performed by analyzing the electrical signals generated by the voltage supply. This issue is discussed in the following section. The four phases can be defined as follows:

1. The initialization phase realizes a first scanning of each primary coil with no peripheral on the table. The electrical signals of every single coil are measured and stored. This first set of measurements will then serve as the reference values.
2. The detection phase starts a new scanning of all coils. The primary signals are measured and compared to the reference values. A short (about 0.5 ms) analysis allows to determine the presence or the absence of a load above each primary coil.



(a)



(b)

Figure 5.12: (a) Top view and (b) bottom view of the prototype.

3. The supply phase activates the primary coils where a load has been detected. This phase takes most of time (about 0.5 s).
4. The clear phase deactivates all primary coils and leads to a new detection phase. This phase is very short (much less than 1 ms).

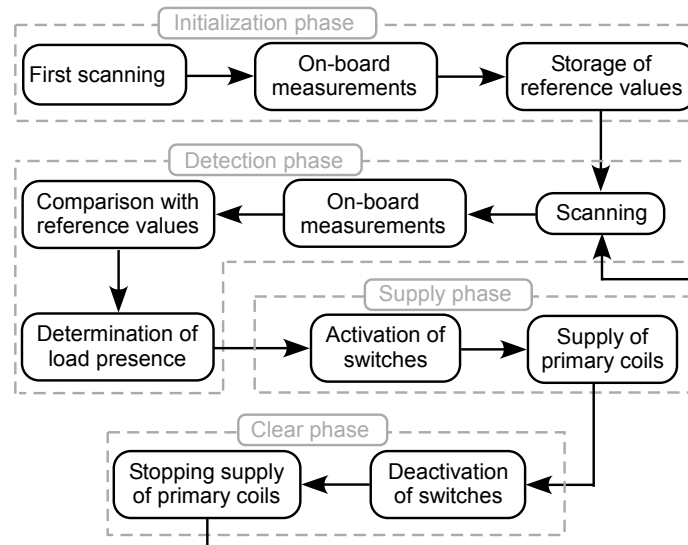


Figure 5.13: General strategy used for the CET table.

In brief, the operating strategy consists of an alternating sequence of detection phases and supply phases. Consequently, three different scales of time or frequency are used in the CET table, as explained in Fig. 5.14.

First, the supplying process is interrupted by the detection phases at intervals of about 0.5 s. This duration may be decreased depending on the desired reactivity of the peripherals detection. However, experimental tests have shown that the detection phase should be no longer than a few milliseconds in order not to perturb or interrupt the energy transfer. Keeping this value under 5 ms ensures no discontinuity of the peripherals supplying.

Secondly, the scanning of the primary coils consists in activating individually each coil during a very short time. Typically, the activation of every single coils lasts from 10 to 100 μ s, which is in agreement with the maximal duration of a few ms for the detection phase.

Thirdly, the activated coils are excited by a high-frequency current of about 200 kHz. This case occurs during the supply phase and during the short activation of every coils for the detection.

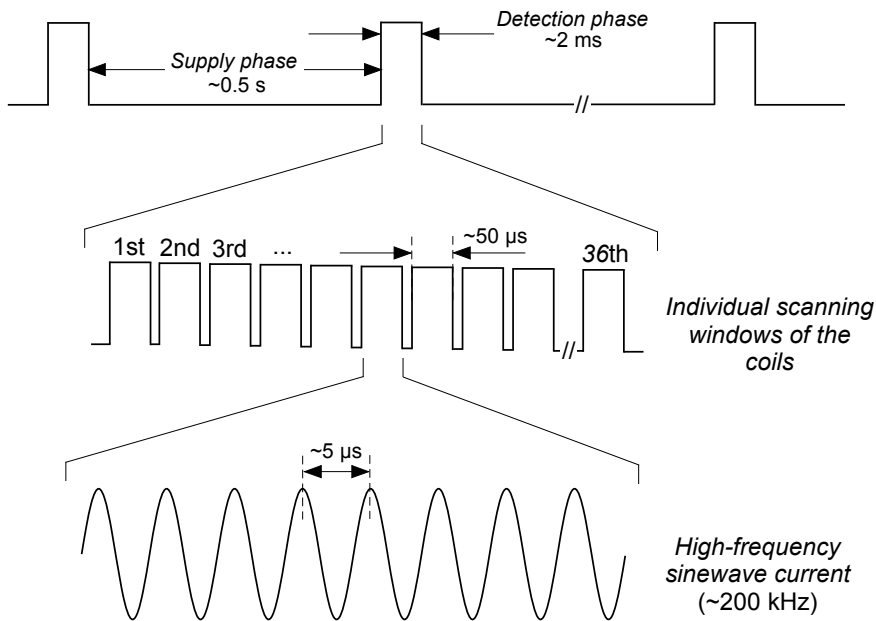


Figure 5.14: Different time scales for the signals applied to the primary coils array.

5.2.5 Primary coils array circuit

Primary layout

For a large CET surface, the number of electronic components may become very important and therefore the manufacturing cost and complexity of integration very high. In order to reduce the number of components, a specific electronic circuit allowing to activate individual primary coils has been developed. Its general layout is shown in Fig. 5.15. The coils are arranged in an array, where it is possible to control the rows and the columns independently. Each coil is represented by an inductor and a resistor in series.

The concept consists in managing all the primary coils as a function of their row and column arrangement. This is realized by connecting all the primary coils of a row to the same line and repeating the same process to columns. As a result, the column switches control the column lines and the row switches control the row lines. Switching on one row and one column allows to activate the corresponding single coil, as highlighted in Fig. 5.15.

A resonant capacitor is placed in parallel to each coil, so that if multiple primary coils are activated simultaneously, there is no need to tune the operating frequency. Furthermore, a diode must be added in series with every coil. This prevents the current from flowing back to other inactive coils.

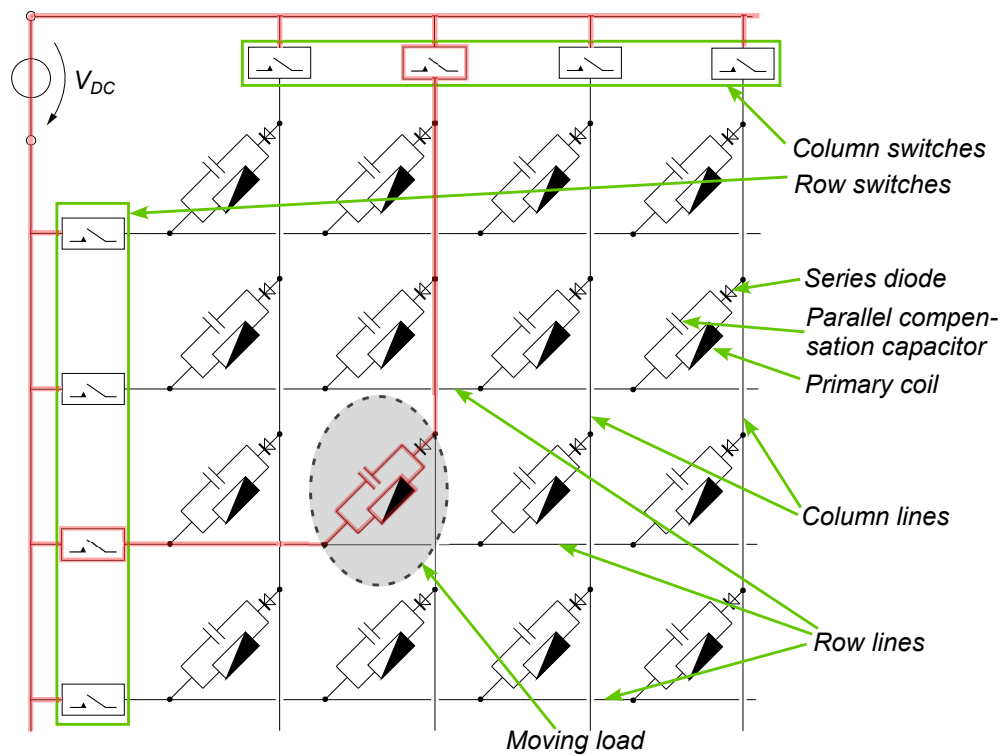


Figure 5.15: Primary circuit schematic.

All switches used in the primary circuit are identical MOS transistors, one per column and one per row. The column switches are simply opened or closed according to the presence of a load. The activation of the row switches is slightly different since they are in charge of generating the high frequency current in the primary coils. In other words, they are activated by applying a high frequency PWM (200 kHz) to their gate, and consequently they remain inactive when kept open. Therefore, when both a column switch and a row switch are activated, the system acts as a single-transistor converter for the concerned coil, as shown in Fig. 5.16. Such a single-transistor converter is based on a classical flyback converter and is often used in CET systems [107], [79], [29], [76].

Advantages and drawbacks

The array topology described in this section is completely different from conventional solutions that use one switch for each coil. It has its advantages and drawbacks, and it is interesting to compare this array topology with a conventional one.

Its most obvious benefit is the decreased number of electronic components it needs. For an array including ν rows and w columns, the required number of switches is only $\nu + w$ while

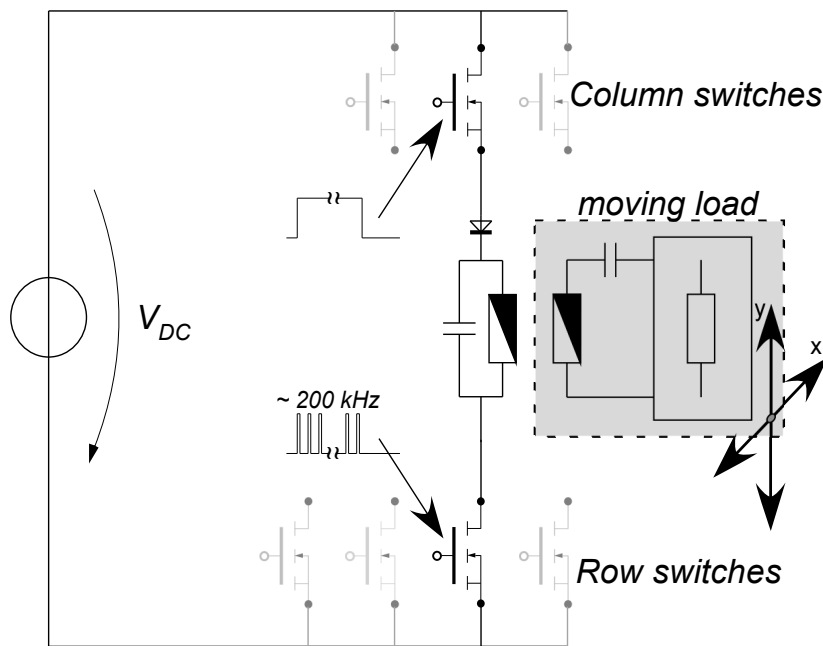


Figure 5.16: Single-transistor converter.

typical solutions use $v \cdot w$ switches. For instance, the prototype presented in this section uses only $6 + 6 = 12$ MOS transistors instead of 36 that would be necessary for each primary coil. Furthermore, the control of the activation is quite simple since only the 6 rows and the 6 columns have to be switched. Thanks to this small number of switches to be controlled, it is possible to connect them directly to the microcontroller without any demultiplexer.

The second advantage of this primary topology is that it allows to integrate a single detection system that is common to all the primary coils instead of using individual detection systems for each primary coil. This reduces drastically the number of components and wires required by the primary array.

However, this topology has also its drawbacks. The main one consists of an unwanted activation of some specific coils when multiple peripherals are placed on the table. Indeed, like for the activation of a single primary coil, when two coils belonging to the same row or column are activated, there is no problem. This case is shown in Fig. 5.17(a). But when two coils that belong to neither the same row nor the same column have to be activated, this automatically turns on two more coils situated at their opposite cross-sections. This case is shown in Fig. 5.17(b). It is not dramatic if the number of loads is not too high, but for a table that has a large surface, it could limit the number of peripherals that can be so supplied. A solution to this problem could be to fragment the table into multiple subparts that work independently of each other. But for the prototype that is presented in this section, this is not an issue.

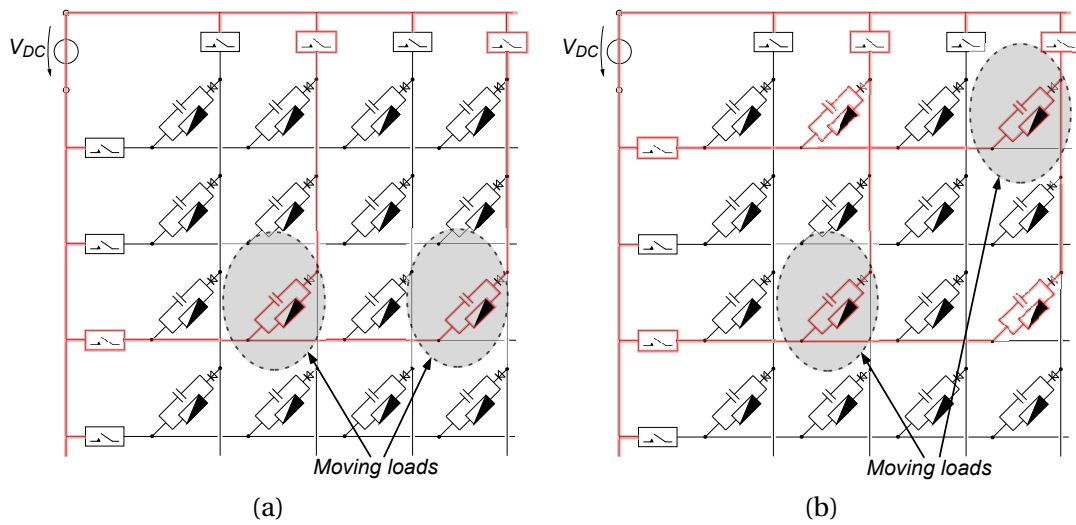


Figure 5.17: (a) Good scenario with two loads and two activated coils. (b) Bad scenario with two loads and four activated coils.

Implementation and measurements

The details of the implementation of the primary circuit and of the single-transistor converters are given in appendix E.1. Fig. 5.18(a) shows the voltage generated by the DSP and the low-side driver on the gate of the MOSFET, and Fig. 5.18(b) show respectively the measured input voltage U_{in} and the primary coil current I_{L1} when the system is transferring about 5 Watts to a secondary coil loaded by a resistor of $10\ \Omega$. The results show that the input voltage is not a pure sinusoid, because of the single-transistor converter. However, the primary current is almost perfectly sinusoidal.

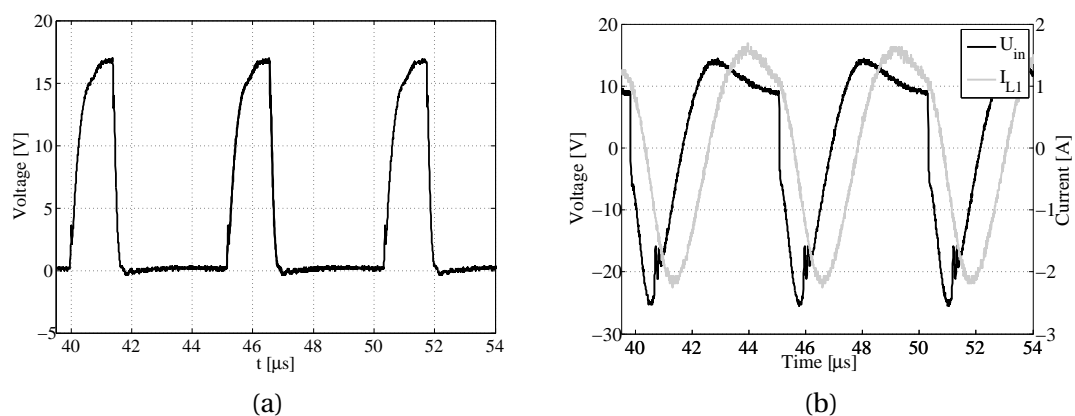


Figure 5.18: (a) Signal generated on the gate of the MOSFET. (b) Input voltage and primary coil current.

5.2.6 Peripheral detection

Detection methods

Depending on the presence of a load above a primary coil, the equivalent impedance seen by the voltage source is changed. As a result, the current and the voltage on the primary coil are as well changed. With the microcontroller and an adequate shaping electronic circuit, it is possible to detect these differences and determine the presence or absence of a peripheral. Basically, two main effects can be observed depending on the presence of a load and on the load itself.

The first one is the variation of the phase shift between the primary current and the input voltage. Theoretically, the resistance of the primary coil is insignificant compared to its inductive impedance. Then, if there is no load above it, the phase shift between the current and voltage of the primary coil is nearly $\phi = 90^\circ$ and no active power is consumed except for Joule losses in the primary coil. For instance, the phase angle of the primary coil defined in Table 5.7 is given by:

$$\phi = \arg(\underline{U}_{in}) - \arg(\underline{I}_{L1}) = \arg(R_1 + j\omega L_1) = 88.34^\circ \quad (5.1)$$

If there is a secondary coil with a load above it, then the phase shift decreases ($\phi < 90^\circ$), and the greater is the load the smaller is the phase shift. This means that active power is consumed in the CET process. For instance, if there is a secondary coil perfectly aligned with a primary coil and if the secondary coil is loaded by a resistor of 10Ω , the phase shift between the primary current and the voltage is given by:

$$\phi = \arg(\underline{U}_{in}) - \arg(\underline{I}_{L1}) = 54.81^\circ \quad (5.2)$$

So it is possible to use this effect to perform the peripherals detection. However, the phase shift detection circuit is complicated to implement because it requires two distinct measurement circuits for the current phase and the voltage phase [112].

The second effect that can be exploited is the amplitude of the primary coil current and the amplitude of the input voltage. Due to the PS compensation topology, the voltage amplitude is difficult to measure because its variation as a function of the load presence is not significant. The current amplitude is more convenient to measure, because it is a relatively pure sinusoid and because its amplitude variation is much more significant. The cause for this that the presence of a load creates a reflected impedance on the primary circuit which leads to a decrease of the primary current amplitude.

Implementing all the electronic circuits for the phase shift, the voltage amplitude and the

current amplitude could allow to evaluate accurately the total impedance of the system, and the impedance of the load itself could then be deduced. Such a system is proposed in [112]. However, it requires four distinct electronic circuits, which is not in adequation with the guideline of restricting the number of components.

Hence, it has been decided to implement only the current amplitude evaluation circuit presented in Fig. 5.19. The originality here is that this circuit is placed in series with the DC voltage supply so that its delivered current is measured. Doing so allows to use a single circuit for every primary coil. The strategy to determine the presence or the absence of a consumer simply consists in fixing a threshold value on the difference between the current amplitude measured during the calibration phase and the one measured during each detection phase. If this threshold value is exceeded, the presence of a load is declared positive for the concerned primary coil. All this process is continuously controlled by the DSP.

The main electronic components of the detection circuit are presented in details in appendix E.2. The current is evaluated by amplifying the voltage obtained on a shunt resistor R_S . A low-pass filter with a cut-off frequency of about 500 kHz is implemented to reduce the noise, and the resulting signal is then routed through a limiting current resistor to the analog-to-digital (A/D) converter of the microcontroller. As a result, the current amplitude of each coil can be evaluated, stored and compared to the calibrated values.

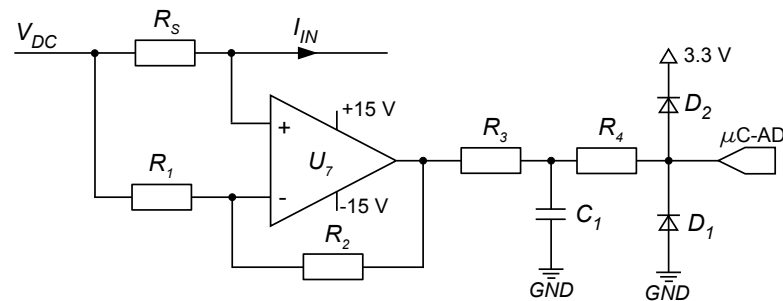


Figure 5.19: Circuit implemented for the estimation of the current.

Measurements

As a first set of measurements, the current generated by the voltage supply is measured in four different cases. First when there is no load on the tested coil, and then in the three cases presented in Fig. 4.18, that correspond respectively to when the secondary coil is perfectly aligned with a primary coil (case 1), when the secondary coil is placed between two primary coils (case 2), and when the primary coil is placed between four primary coils (case 3). The secondary coil is loaded by a resistor of 10Ω .

Fig. 5.20(a) shows the measurements of the current generated by the voltage supply, and Fig. 5.20(b) shows the measurements of the voltage provided to the A/D converter of the DSP (which corresponds to the output of the circuit presented in Fig. 5.19). Some noise is generated at the output of the detection circuit due to the switching transistors. However, it does not cause any problems because the A/D conversion is programmed to occur at the time where the voltage is at its maximum, thus avoiding the switching instant.

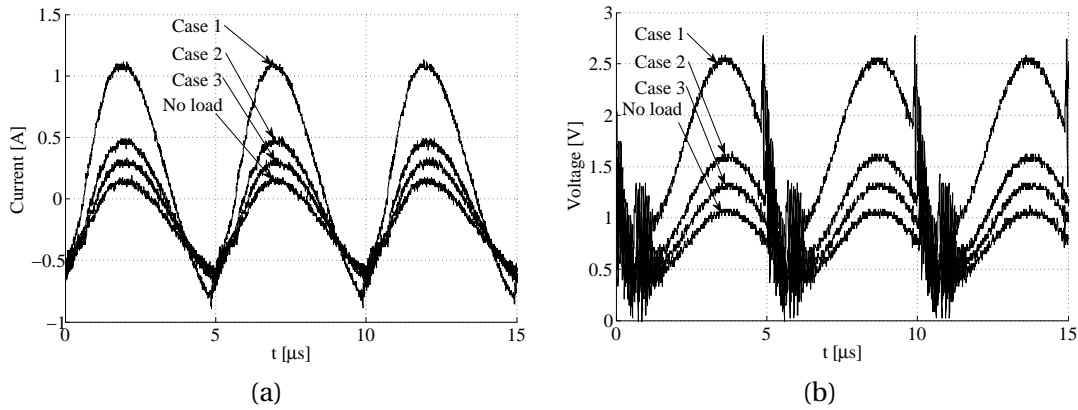


Figure 5.20: (a) Current generated by the voltage supply. (b) Voltage provided to the A/D converter of the DSP.

For the second set of measurements, the three different time scales depicted in Fig. 5.14 are presented. Fig. 5.21 shows the current delivered by the voltage supply for different cases.

In Figs. 5.21(a)-(b)-(c), the current is measured over a duration of 2 seconds when respectively no primary coil, one primary coil and two primary coils have detected the presence of a load and therefore are activated. For this time scale, the supply and detection phases can be observed. The supply phase shows different amplitudes of current as a function of the number of activated primary coils, and the detection phase takes the form of short peaks. As it can be observed, four detection phases per seconds are achieved so as to have a good reactivity for the peripheral detection.

In Figs. 5.21(d)-(e)-(f), a zoom is made on a single detection phase when respectively no primary coil, one primary coil and two primary coils have detected the presence of a load. A whole detection phase lasts for about 2 ms during which each primary coil is separately activated. In this specific case, 36 intervals can be observed (one per primary coil), and it is interesting to note that the current amplitude is higher for the coils that detect the presence of a load. For example, in Fig. 5.21(e), a secondary loaded coil is placed above the 24-th scanned coil and in Fig. 5.21(f), two secondary coils are placed above respectively the 12-th and 24-th coils.

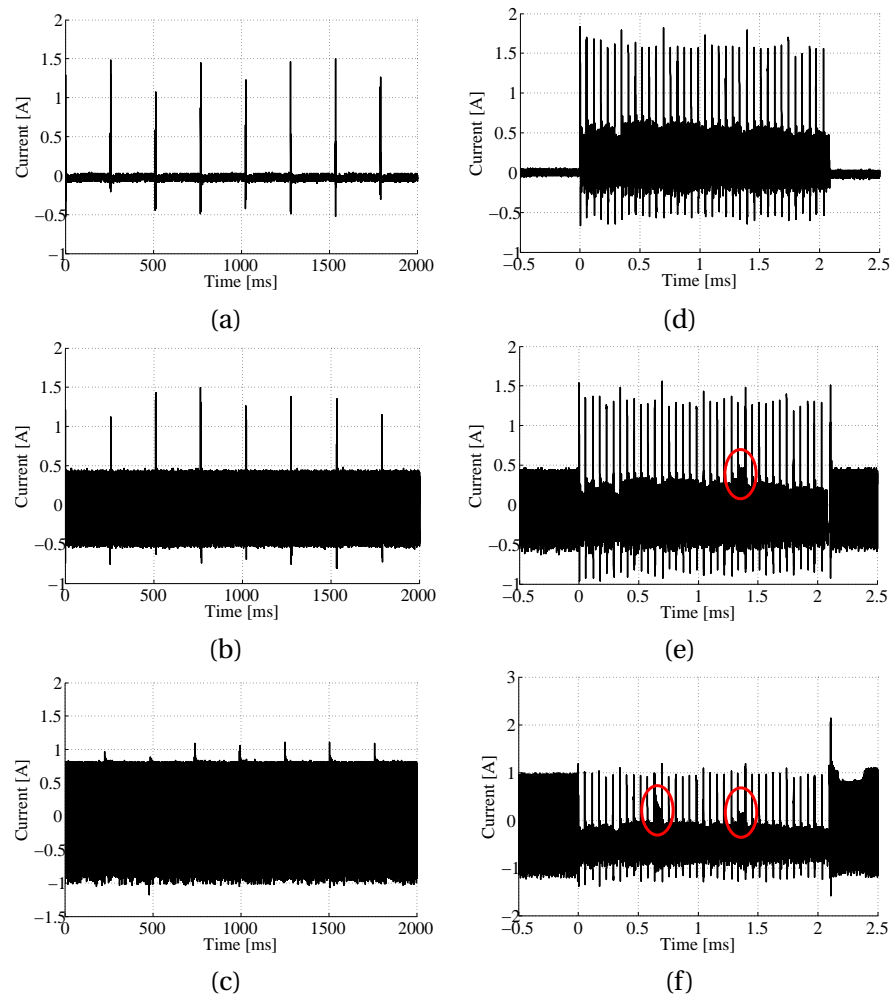


Figure 5.21: Current delivered by the DC voltage supply over a large time scale showing a few short detection phases between the supply phases with no load (a), one load (b), and two loads (c). View of the current during a single detection phase with no load (d), one load (e), and two loads (f).

Finally, in Fig. 5.22, the measured time window is still narrowed so as to focus on the high-frequency current generated by the voltage supply during the detection phase. Here specifically, a first measurement is performed with no load placed on the table and a second one with a load placed over the second scanned coil. This gives rise to an increase in the current amplitude of about 40 %. In this case, the secondary coil is well aligned with the primary one and loaded by a resistor of 100Ω (arbitrarily chosen). In order to get a good detection sensibility, the strategy consists then in triggering the A/D conversion at the moment of maximum current amplitude of the last peak for each primary coil. Waiting for the A/D conversion to be achieved on the 10-th peak allows to avoid the transient behavior at the activation of the coil, and thus ensures a good stability and repeatability of the peripheral detection.

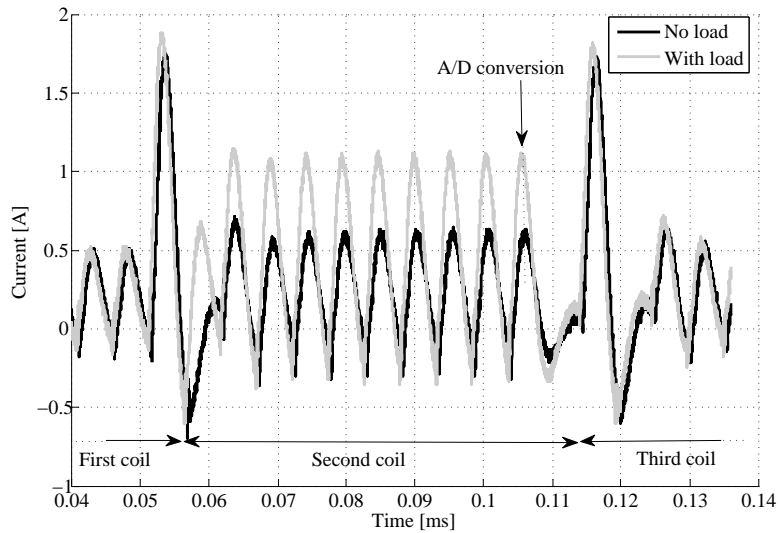


Figure 5.22: Zoom on the second coil scanning with and without load.

5.2.7 Secondary coils circuit

The schematic of the secondary circuit is shown in Fig. 5.23 and its main components are described in details in appendix E.3. A full-bridge rectifier with a smoothing capacitor allows to convert the 200 kHz induced voltage to a DC voltage. The level of the DC voltage is then adapted to the needs of the peripheral. For example, for the loudspeaker, a voltage regulator (called U_1 in Fig. 5.23) allows to obtain the required voltage of 5 V (DC). Similar circuits are used for the mouse and the keyboard.

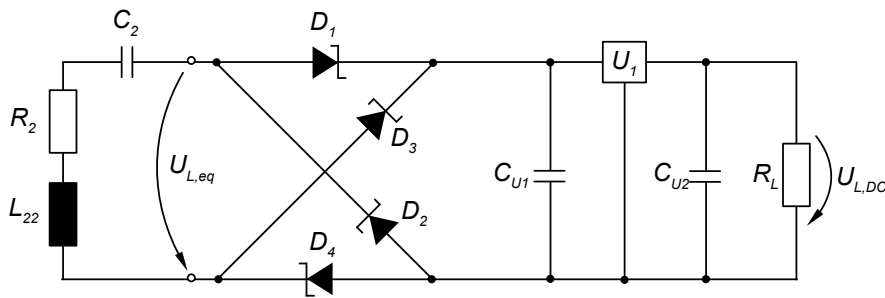


Figure 5.23: Secondary circuit scheme for the speaker providing a 5 V (DC) output.

Fig. 5.24 shows typical measurements of currents and voltages obtained on the secondary circuit. Here, they are made when the secondary coil is well aligned with a primary coil, but similar results are obtained for other scenarios. Two different cases are showed.

First, Fig. 5.24(a) gives the voltage U_L and the current I_L obtained on a load of 10Ω when there

is no rectifier and no voltage regulator.

Secondly, Fig. 5.24(b) gives the DC voltage $U_{L,DC}$ and current $I_{L,DC}$ obtained on a load of $10\ \Omega$ when there is a rectifier but no voltage regulator. The voltage $U_{L,eq}$ measured at the input of the rectifier and the secondary coil current I_{L2} are also shown.

The results show that the current generated in the secondary coil is nearly identical with and without rectifier. This confirms that the presence of the rectifier has no significant impact on the value of the load. The voltage U_L measured without rectifier is nearly sinusoidal, but when a rectifier is used, the voltage $U_{L,eq}$ has a square-wave shape. One can as well notice that the load voltage $U_{L,DC}$ shown in Fig. 5.24(b) is slightly lower than the amplitude of the square-wave voltage $U_{L,eq}$. This is due to the forward voltage drop in the diodes of the rectifier.

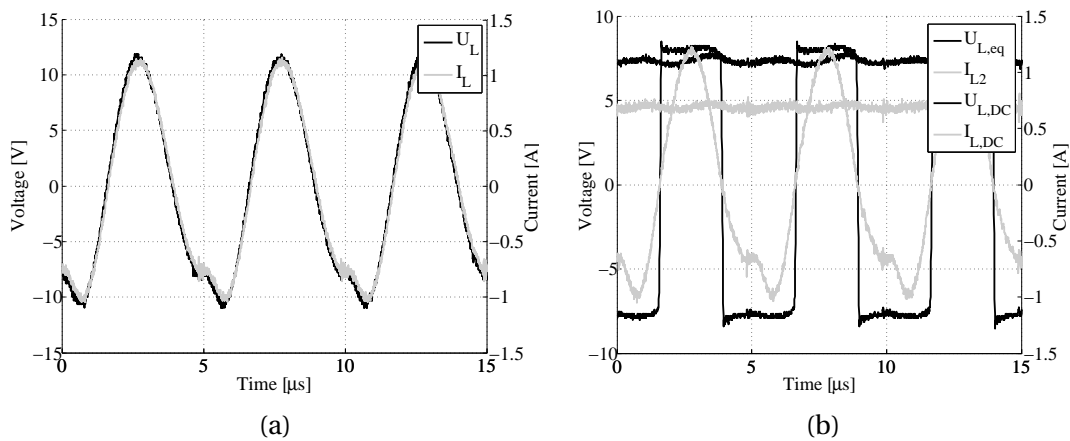


Figure 5.24: (a) Voltage and current measured on a load of $10\ \Omega$ without rectifier. (b) Voltage and current measured at the input and at the output of the rectifier loaded by a resistor of $10\ \Omega$.

Finally, Table 5.8 gives multiple measurements of power and efficiency using different loads in different scenarios. A rectifier is used for each measurement. The three different cases described in Fig. 4.18 are measured for a load of $5\ \Omega$, a load of $10\ \Omega$, a load of $100\ \Omega$ and the loudspeaker.

The voltage supply is set to $18\ \text{V}$ (DC) as this value allows to create an input voltage U_{in} of $12\ \text{V}$ (AC rms) on the primary coils. The power delivered by the source is then calculated by multiplying its DC voltage ($18\ \text{V}$ (DC)) by its average current. The voltage $U_{L,DC}$ obtained in the load is measured with a multimeter and the corresponding power P_L is easily derived. As a result, the efficiency η takes into account the losses in the transistors, in the coils and in the rectifier.

For the loudspeaker, the losses in the voltage regulator are also taken into account, and $U_{L,DC}$

Table 5.8: Power and efficiency measurements

	Load	$P_{in,DC}$ [W]	$U_{L,DC}$ [V]	P_L [W]	η [%]
Case 1	5 Ω	16.38	5.08	5.16	32
	10 Ω	12.78	7.48	5.60	44
	100 Ω	5.58	12.60	1.59	29
	loudspeaker	5.76	5.02	1.90	33
Case 2	5 Ω	23.58	6.07	7.37	31
	10 Ω	19.44	8.28	6.86	35
	100 Ω	10.26	13.05	1.70	17
	loudspeaker	12.43	5.05	1.91	15
Case 3	5 Ω	30.60	5.79	6.70	22
	10 Ω	24.48	7.45	5.55	23
	100 Ω	20.70	11.73	1.38	7
	loudspeaker	20.08	5.04	1.90	10

is thus the voltage obtained at the output of the regulator, that is 5 V (DC). The current drawn by the loudspeaker is measured at 0.37 A (DC), which leads to a power of 1.9 W.

In conclusion, the results presented in Table 5.8 show that it is possible to transfer at least 5 W everywhere on the surface. The efficiency is higher for a load resistance of 10 Ω than 5 Ω , because of the increase of current amplitude and consequently the Joule losses in the secondary coil when the load resistance is decreased.

5.2.8 Third prototype

In this section, a last prototype is presented. The design for the primary coils array is the one presented in Table 4.5. The aim of this prototype consists in validating the optimization of CET table proposed in chapter 4. A picture of the primary coils array with a secondary coil is given in Fig. 5.25.

First, Table 5.9 gives the calculated and measured values of the coil resistances and self-inductances. As the operating frequency of the prototype is 500 kHz, the measurements are performed at this frequency. Furthermore, multiple primary coils have been measured, and the values are highly similar (with less than 1 % of discrepancy between the different primary coils).

Then, the power and the Joule losses are measured in the three cases presented in Fig. 4.19. The results are given in Table 5.10. All voltages and currents are given in rms value. So as to preserve the conditions in which the optimization is performed, the secondary coil is loaded by a resistor of 10 Ω without rectifier, the airgap between the primary array and the secondary

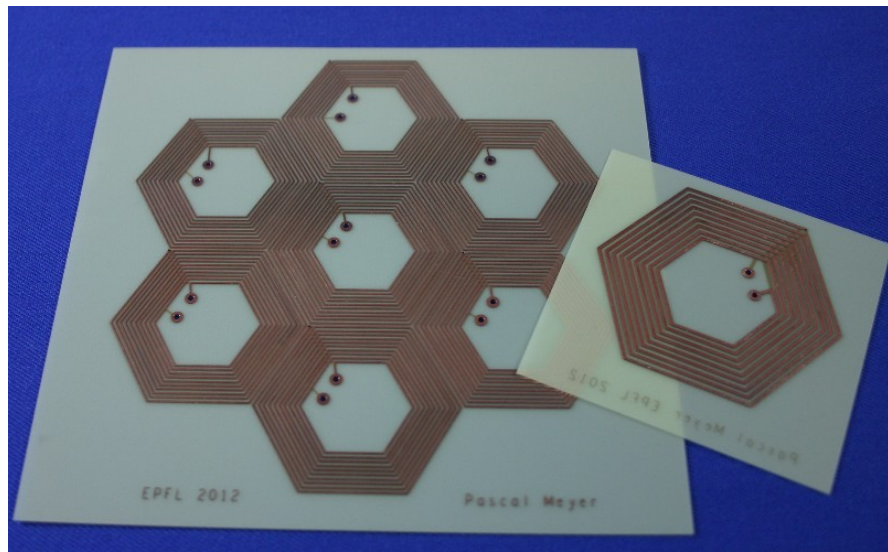


Figure 5.25: Picture of the primary coils array and the secondary coil.

Table 5.9: Parameters of the primary and secondary coils

	L_1 [μH]	R_1 [Ω]	L_2 [μH]	R_2 [Ω]
Measured	14.25	1.29	13.45	0.93
Calculated	13.42	1.03	13.12	0.82

coil is 5 mm. A voltage input of approximately 24 V (AC rms) is generated in the primary coils using the full-bridge converter presented in section 5.1.3. The Joule losses of the primary coils and of the secondary coil (respectively P_{j1} and P_{j2}) are calculated using the values of the measured resistances (respectively R_1 and R_2) and the values of the measured currents (respectively I_{L1} and I_{L2}). For the case b, the current in the two primary coils is measured, and for the case c, the current in the three primary coils is measured. Finally, The efficiency estimation takes into account only the Joule losses in the coils.

The measured results are in good agreement with the calculated ones. The main difference concerns the losses. Indeed, the calculated values for the losses are underevaluated. This is mainly due to the calculated resistances of the coils that are also slightly underestimated in the model. This difference is probably caused by imperfections of the PCB copper tracks, because even the calculated DC resistances have a lower value than the measured ones. However, this difference is not significant and the results obtained with this third prototype validate the optimization method presented in chapter 4.

Table 5.10: Measured and calculated electric parameters of the third prototype.

		U_{in} [V]	I_{L1} [A]	P_{j1} [W]	I_{L2} [A]	P_{j2} [W]	P_L [W]	P_{loss}	η
Case a	meas.	25.5	0.55	0.39	0.73	0.50	5.33	0.89	85
	calc.	24	0.54	0.30	0.71	0.41	5.07	0.71	88
Case b	meas.	25.6	0.60 0.56	0.46 0.41	0.77	0.55	5.92	1.42	80
	calc.	24	0.58	0.35	0.76	0.47	5.74	1.17	84
Case c	meas.	25.5	0.62 0.58 0.66	0.50 0.43 0.55	0.72	0.48	5.18	1.96	72
	calc.	24	0.59	0.36	0.71	0.41	5.12	1.50	78

5.3 Estimation of the magnetic field

The aim of this section consists in evaluating the magnetic flux density B on multiple points (x, y, z) situated in the vicinity of the CET table while it is working. It is then possible to determine if the amplitude of the magnetic flux density is acceptable in term of human health.

The magnetic field is calculated for the two last prototypes presented in the previous sections. For this, the Biot-Savart's law (2.3) is used, but it has to be adapted because it provides the amplitude for a field in magneto-static conditions. In the case of the CET table, the field is generated by an alternating current and therefore is also a wave that has the same frequency and phase angle. The amplitude of the magnetic flux density generated by an alternating current of pulsation ω and phase angle β is therefore given by:

$$B(t) = B e^{j(\omega t + \beta)} \quad (5.3)$$

where B is the norm of the magnetic flux density defined by (2.3). If multiple coils are excited by currents that have different phase angles, interferences occur and have to be taken into account for the calculation of the resulting magnetic field. For the CET table, since the secondary coil is series-compensated, the phase shift between the primary current and secondary current is $\pi/2$.

Table 5.11 gives the intensity of the magnetic flux density (rms values) at different points near the CET table. The cases 1 to 3 (*c.f.* Fig. 4.18) for the square-shaped prototype and the cases a to c (*c.f.* Fig. 4.19) for the hexagonal prototype are evaluated. In every case, the origin of the space coordinates is situated in the center of the primary coil(s). The values of the currents used to calculate the magnetic flux density are the ones measured on the prototypes while they are transferring 5 W to a load resistor of 10 Ω .

5.3. Estimation of the magnetic field

Table 5.11: Estimation of the magnetic flux density at different points above the two CET prototypes.

Prototype	Case	Position (x, y, z) [mm]	Mag. flux density [μ T]
Square coils	1	(0,0,20)	256.35
		(0,0,100)	6.80
		(50,0,20)	32.86
		(50,0,100)	4.56
		(100,0,20)	3.44
		(100,0,100)	1.91
	2	(0,0,20)	263.37
		(0,0,100)	8.29
		(50,0,20)	48.94
		(50,0,100)	5.65
		(100,0,20)	4.57
		(100,0,100)	2.41
	3	(0,0,20)	262.78
		(0,0,100)	10.83
		(50,0,20)	58.00
		(50,0,100)	7.59
		(100,0,20)	6.51
		(100,0,100)	3.39
Hexagonal coils	a	(0,0,20)	214.25
		(0,0,100)	3.05
		(50,0,20)	12.54
		(50,0,100)	2.01
		(100,0,20)	1.47
		(100,0,100)	0.84
	b	(0,0,20)	217.13
		(0,0,100)	3.86
		(50,0,20)	15.19
		(50,0,100)	2.57
		(100,0,20)	1.95
		(100,0,100)	1.09
	c	(0,0,20)	206.44
		(0,0,100)	4.69
		(50,0,20)	2.86
		(50,0,100)	28.62
		(100,0,20)	3.24
		(100,0,100)	2.83
		(100,0,100)	1.44

In [25], the limits for the human exposure to magnetic fields are defined. They are calculated on the basis of a maximal energy that can be absorbed in human tissues without being harmed. The basic restrictions for the current density generated in the body by a magnetic field are

precisely defined, but are practically difficult to measure. Besides those basic restrictions, the general limits of the magnetic field intensities are given, which allow to ensure that the basic restrictions are not exceeded. However, the converse is not necessarily true, that is if the general limits are exceeded, it does not mean that the basic restrictions are violated.

According to [25], the maximal intensity of the magnetic flux density is dependent on the frequency. For the square-shaped prototype working at 200 kHz, the general limit is fixed at $4.60 \mu\text{T}$. For the hexagonal-shaped prototype working at 500 kHz, the general limit is fixed at $1.84 \mu\text{T}$. The results of Table 5.11 show that these limits are often exceeded when the evaluation is performed very close to the coils. But when the distance of evaluation becomes greater than about 150 mm, the intensity of the magnetic flux density is acceptable.

Practically, for the CET table that aims to supply different peripherals, it means that only the hands and a small portion of the arms are immersed in potentially too intense magnetic fields. For us, as only a small portion of the body is concerned, the prototypes are estimated to be valid, but more tests should be done on samples of human tissues to definitely confirm this statement.

5.4 Conclusion

In this chapter, the different prototypes built during this thesis work are presented and tested. They contribute largely to the validation of the different models and the optimization method presented in the previous chapters.

The main effort has been placed in the prototype presented in sections 5.2.3 to 5.2.7. Therein, a specific primary coils topology has been developed so as to limit as much as possible the number of electronic components. In this sense, an efficient method to detect the peripherals and selectively activate the primary coils is presented. The system is controlled by a single DSP and is completely autonomous. Finally, different tests and measurements have shown that the system is able to provide at least a power of 5 W over the whole surface.

Finally, the last section gives a general overview of the magnetic field densities that are at stake when using a CET table and discusses the inherent health issues.

Conclusion

6.1 Overview

This thesis addresses the modeling, design and optimization of inductive CET systems. In the domain of electronic devices and especially desktop peripherals, inductive CET clearly appears as the technology to investigate. Just like wireless communication protocols, it responds to the omnipresent demand of electronic industry for removing cables, plugs, adaptors, chargers or batteries that pollute domestic and professional environments.

In preamble of this thesis, a state of the art presents available products and current researches dealing with inductive CET, highlighting the main issue concerning the design of such systems. Indeed, the developed solutions are designed only for single applications and are often not optimized. So there is an obvious lack of design and optimization methods applicable to any inductive CET problem, and the aim of this thesis is to fill this gap. To achieve this, the conception of the problem is separated into multiple subparts that can be individually modified or adapted for different applications. Such a modular approach is the key point of this thesis, as it allows to englobe a very large panel of CET solutions with a relatively simple design methodology. Furthermore, it endorses the accessibility to the developments made in the scope of this work, as they are expected to be reused by other engineers and researchers in the future. It would be indeed easy for them to modify individual parts or add developments of their own without compromising the rest of the design. Several issues concerning CET are

addressed, notably an analytical model of inductances and its numerical implementation, the FEM model allowing to calculate the resistance at high frequency, and the equivalent electric model of the coreless transformer through different compensation topologies. Besides, an optimizer using multiobjective genetic algorithms is developed in order to exploit effectively the modeling and to generate the design of different CET systems. Finally, as for validation of the modeling and optimization methods, fully functional prototypes are designed, built and successfully tested.

6.2 Main results and innovative contributions

The main results and original contributions are summarized in the following points:

- *Accurate modeling of coreless transformers:* Analytical and numerical models, taking into account coils resistance and different compensation topologies, allow to predict accurately the behavior of inductive coils and coreless transformers. They are implemented in a way that makes them highly adaptable and low-consuming in term of computation time. Besides, an estimation of the magnetic field intensities has made it possible to assess the related health risks.
- *High frequency effects for PCB coils:* A new method based on FEM simulations is presented and confronted to another numerical one issued from literature. The former outpasses by far the latter in term of accuracy, but in return requires larger computing resources. Therefore, a complete output mapping together with an interpolation strategy using DOE exploit cleverly FEM simulations so as to address this problem without compromising the accuracy of the results.
- *Multiobjective genetic algorithms:* A new MOGA based on the classical NSGA-II has been implemented. Some major improvements are brought to the general working of the algorithm and to different genetic operators. The new MOGA has then been submitted to different test functions and applied to the design of CET systems. It has proven to provide a fast convergence while maintaining an excellent diversity of solutions.
- *Design method for the CET table:* For free position systems, using a single-layer array of primary coils with a larger secondary one has been identified as the most interesting solution. A novel design method based on the evaluation of the transferred power and the Joule losses for multiple positions of the secondary coil is presented. It allows to generate an optimal solution in term of efficiency and, in the same time, it ensures the uniformity of the transferred power above the CET surface.
- *Implementation of the CET table and its detection system:* An innovative activation

strategy of the primary coils has been developed. It consists of specific coils connexions based on an arrangement of rows and columns so as to minimize the number of required electronic components. Besides the primary coil activation, a single detection system has been implemented for the whole CET table instead of multiple ones as encountered in earlier works. It is based on the analyzis of the current amplitude delivered by the voltage supply and in this sense is fully sensorless. Finally, digital control techniques have enabled the autonomous management of the peripherals detection and coils activation.

The collaboration with the industrial partner has enabled to have a clear view on the objectives that consisted in modeling and implementing different CET prototypes. So as to reach that goal, many scientific problems have been addressed. The inherent researches resulted to five publications presented in international conferences (ICEM2010, ECCE2010, ICEMS2011, EPE2011, ICEMS2012) and one article published in a transaction journal (Industry Applications 2011).

6.3 Outlook and perspectives

Having adopted a modular conception of CET systems encourages the promotion of further researches in this domain and consequently their integration to the ones achieved during this thesis work. The future developments that are more likely to share a link with this thesis, among the multitude of existing ones, are summarized in the following points:

- *Modeling of the losses in the transistors*: The models and optimization presented in this thesis are focused on the coreless transformer. It makes sense because this is the most sensitive part in CET systems. The losses in the transistor are very complex to modelize, and have been only studied superficially because it was not an issue for the success of the thesis objectives. However, it would be very interesting to develop a complete model of the losses in the transistors, as they have surely a significant impact on the overall efficiency of CET systems, especially when the operating frequency is increased. In the same vein, investigating the methods called zero voltage switching (ZVS) or soft switching could be of greatest interest.
- *Thermal modeling*: The increase of temperature in the coils when the CET system is loaded may become a limiting factor to the amount of transferred power. For the different prototypes presented in this thesis, this was not an issue as Joule losses were in the order of 0.5 W per coils, leading to temperatures that remained below 50 °C. However, a thermal modeling could be integrated to the ones of coreless transformer, so as to provide a multi-physic approach for the optimization of CET systems.

Chapter 6. Conclusion

- *Shielding*: The advantage of adding a shielding under the primary coils and above the secondary coils would be twofold. First it would increase the inductances of the coils and thus their quality factor. Secondly it would reduce the intensity of the radiated magnetic field in the surrounding of CET systems. The presence of ferro-magnetic and/or conductive material would have a significant impact on CET systems, which should be studied in detail.
- *Primary current control*: The different prototypes presented in this thesis are directly supplied by voltage supplies. It could be however interesting to implement a system that allows to control the current generated into the primary coil, by dynamically adapting the input voltage level for example. Doing so could lead to a real-time regulation of the transferred power.
- *Prototype*: Only a small version of the optimized design has been prototyped in order to verify and validate the optimization method. It could be interesting to realize a larger one that also integrates the digital control for the peripheral detection and local activation.
- *Load recognition*: A system allowing to recognize the load should be implemented. By analyzing thoroughly the current and the voltage of the primary coil, it should be possible to avoid the activation of CET if an undesired material is placed on the table. Still further, it should be possible to recognize exactly the load present on the table so as to adapt the power to transfer. The electronic implementation and the digital control of such a load recognition would be a great challenge.

Despite these possible improvements, this thesis has successfully proven the feasibility of a CET table for multiple peripherals. The different developments and researches can be easily reused by other engineers and leave a door open to the design of future CET applications.

In conclusion, a last reflexion is proposed concerning the ongoing standardization of CET systems. At the beginning of this thesis work, the WPC (Wireless Power Consortium) was in its very early days. But for a few years, it has been gaining more and more success and reputation from both industrial and academic worlds. Our intuition is that aiming to set the standards for inductive CET is the right strategy to further promote this technology. Not so far in the future, the WPC may become unavoidable for designing industrial CET products. We therefore strongly recommend to future CET engineers to keep a close watch on the WPC and, more generally, to the development of standards.

Electric Modeling Equations

A.1 Series Compensated Secondary: Voltage Source Behavior

A series compensated secondary in coreless transformers leads to a voltage source behavior. This can be easily verified using equations (2.28), and (2.30) to (2.34) for a given coreless transformer, as for instance the one composed of coils 5 and 6 (so defined in section 2.2.5). Fig. A.1(a) shows the load current versus the load voltage when the primary coil current is maintained at a constant value of 1 A (rms), and when the load resistance is varied from 10 to 100 Ω (arbitrarily chosen). This clearly shows that a secondary capacitor in series results in a stable voltage supply. The power in the load is then given by:

$$P_L = \frac{U_L^2}{R_L} \tag{A.1}$$

where U_L is the voltage on the load and R_L the load resistance.

In Fig. A.1(b), the power transferred to the load versus the resistance of the load is plotted. The curve is a typical one of a voltage supply.

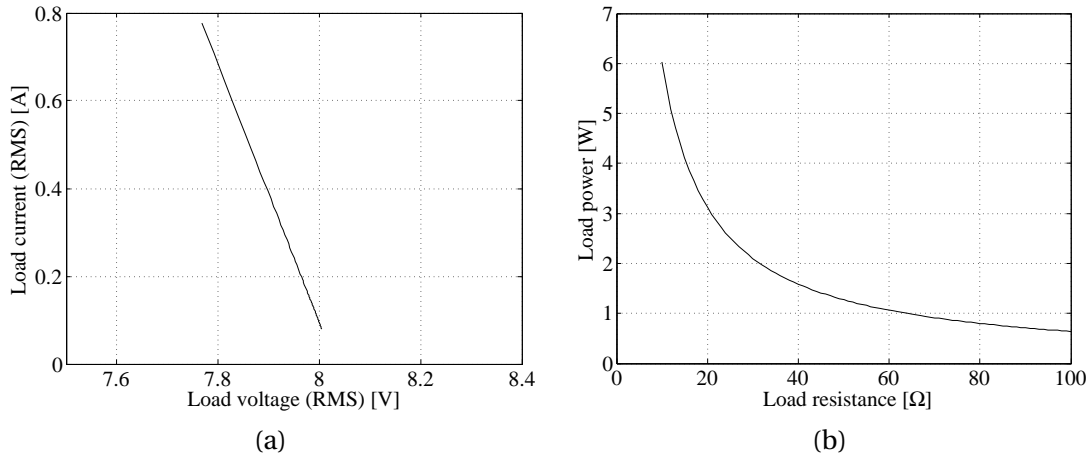


Figure A.1: Behavior of the coreless transformer (coils 5 and 6) when the load resistance varies from 10 to 100 Ω .

A.2 Parallel Compensated Secondary: Current Source Behavior

A parallel compensated secondary in coreless transformers leads to a current source behavior. This can be easily verified using equations (2.28), and (2.35) to (2.37). Using the coreless transformer composed of coils 5 and 6 and maintaining the primary coil current at 1 A (rms), the characteristic of the load voltage versus the load current is illustrated in Fig. A.2(a). This clearly shows that a secondary capacitor in parallel results in a stable current source. The power in the load can thus be defined as follows:

$$P_L = R_L I_L^2 \tag{A.2}$$

where I_L is the current in the load.

In Fig. A.2(b), the power transferred to the load versus the resistance of the load is plotted. The curve is a typical one of a current source.

A.2. Parallel Compensated Secondary: Current Source Behavior

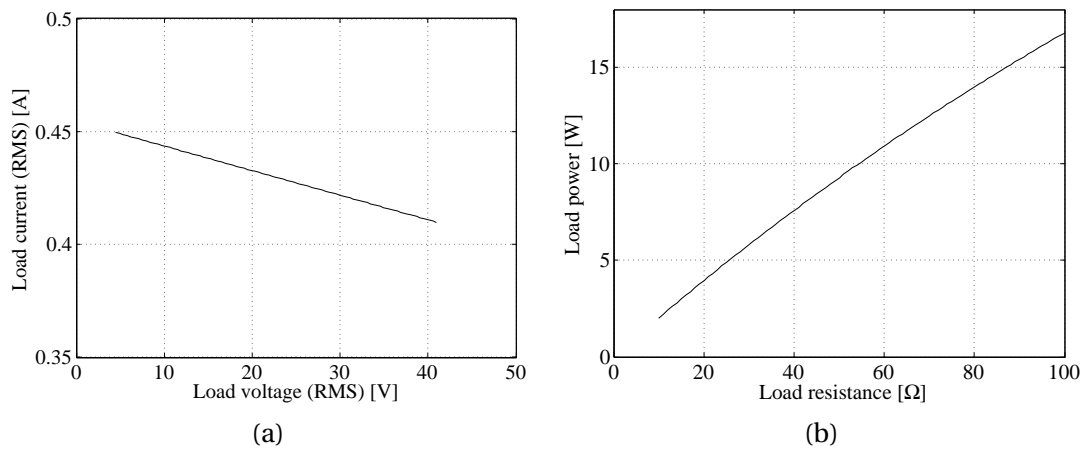


Figure A.2: Behavior of the coreless transformer (coils 5 and 6) when the load resistance varies from 10 to 100 Ω.

A.3 Behavior of the four topologies

In the two previous sections, the coreless transformer is assumed to be supplied by a constant current generated into the primary coil. This case refers to as a coreless transformer controlled by a current source. However, when it is supplied by a constant voltage source, the behavior may be completely different as a function of the compensation topology. This case refers to as a coreless transformer controlled by a voltage source. The behavior of the four different topologies is presented in Fig. A.3 (PS-PP) and Fig. A.4 (SS-SP). In all cases, the input voltage U_1 of the coreless transformer is set to 12 V (rms).

The results show that a PS topology behaves as a voltage supply for the load and that a SS topology behaves as a current source for the load. PP and SP topologies lead to behaviors that are more difficult to categorize and that are dependent on the geometrical parameters of the coreless transformer.

A.3. Behavior of the four topologies

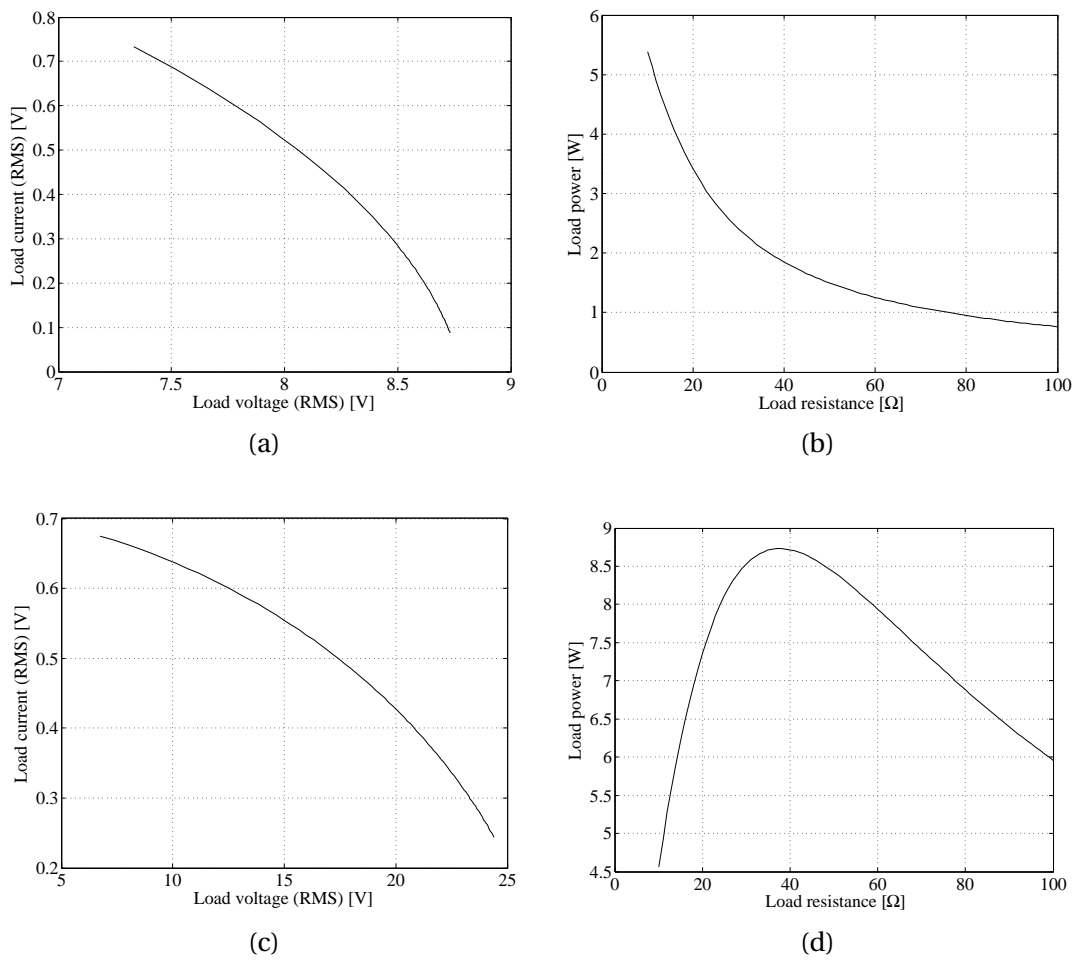


Figure A.3: Behavior of the coreless transformer (coils 5 and 6) when the load resistance varies from 10 to 100 Ω . (a)-(b) PS topology, (c)-(d) PP topology.

Appendix A. Electric Modeling Equations

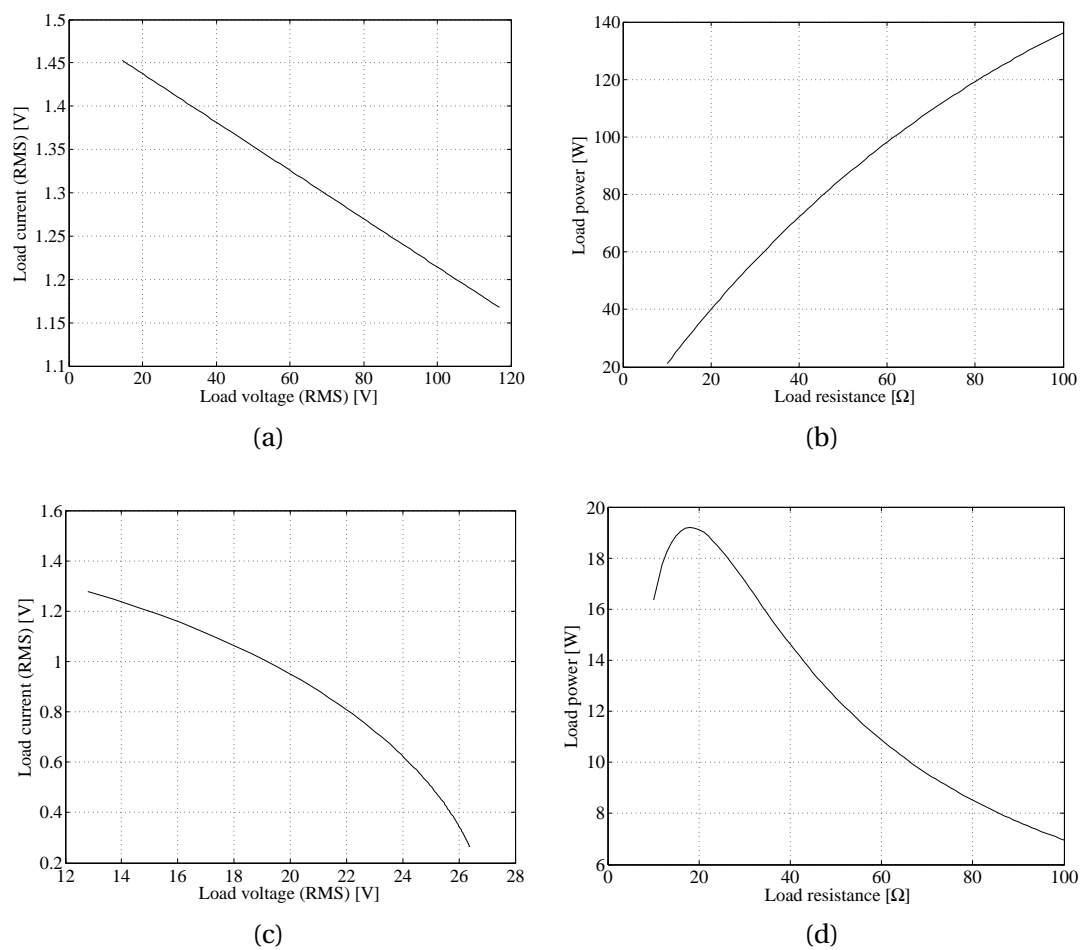


Figure A.4: Behavior of the coreless transformer (coils 5 and 6) when the load resistance varies from 10 to 100 Ω . (a)-(b) SS topology, (c)-(d) SP topology.

Numerical methods for the integral

B.1 Integral method

The first method is proposed in [109] and [65]. The integral method is the most straightforward one because it consists in solving numerically the integral of equation (3.11), which is possible with a computation software like Matlab. Then, for the solutions of $\partial Q_{mn}/\partial x$ and $\partial Q_{mn}/\partial y$, the integral Q_{mn} is derivated as follows:

$$\begin{aligned} \frac{\partial Q_{mn}}{\partial x} &= \int_{S_n} \frac{\partial}{\partial x_m} \ln \sqrt{(x_m - x')^2 + (y_m - y')^2} dx' dy' \\ &= \int_{S_n} \frac{x_m - x'}{(x_m - x')^2 + (y_m - y')^2} dx' dy' \end{aligned} \quad (\text{B.1})$$

and

$$\begin{aligned} \frac{\partial Q_{mn}}{\partial y} &= \int_{S_n} \frac{\partial}{\partial y_m} \ln \sqrt{(x_m - x')^2 + (y_m - y')^2} dx' dy' \\ &= \int_{S_n} \frac{y_m - y'}{(x_m - x')^2 + (y_m - y')^2} dx' dy' \end{aligned} \quad (\text{B.2})$$

These two last integrals can be directly evaluated by a computation software. This method gives accurate results for the computation of the AC-resistance and internal inductance, but requires an intensive resolution with a large number of integrals, which may result in a long computation time. Therefore, quicker solutions have to be used.

B.2 Approximated integral method

The second method is derived from the first one, but an approximation is made, that allows to remove the integrals from the computation process [109]. If the integral Q_{mn} is evaluated on a point $P(x_m; y_m)$ that is situated outside the n th subbar, then it can be assumed that the distance $\sqrt{(x_m - x')^2 + (y_m - y')^2}$ does not change much inside the integration surface of the n th subbar, so that it can be considered as constant. The integral Q_{mn} is then simplified to:

$$Q_{mn} = \int_{S_n} \ln \sqrt{(x_m - x')^2 + (y_m - y')^2} dx' dy' \approx \ln \sqrt{(x_m - x_n)^2 + (y_m - y_n)^2} S_n \quad (\text{B.3})$$

and the derivatives $\partial Q_{mn}/\partial x$ and *partial* $Q_{mn}/\partial y$ become:

$$\frac{\partial Q_{mn}}{\partial x} \approx \frac{x_m - x_n}{(x_m - x_n)^2 + (y_m - y_n)^2} S_n \quad (\text{B.4})$$

and

$$\frac{\partial Q_{mn}}{\partial y} \approx \frac{y_m - y_n}{(x_m - x_n)^2 + (y_m - y_n)^2} S_n \quad (\text{B.5})$$

This method has the advantage to be much quicker, and if the subbars are chosen sufficiently small, it provides accurate results with an absolute error that is smaller than 1 % in comparison with the integral method.

B.3 Geometrical mean distance method

For convenience, equation (3.10) is used as the start point for this third method and is integrated over the m -th subbar:

$$\int_{S_m} J(x, y) dx dy = - \frac{j\omega\mu_0\sigma}{2\pi} \int_{S_m} \int_S J(x', y') \ln \sqrt{(x-x')^2 + (y-y')^2} dx' dy' dx dy + \int_{S_m} J_{\omega=0}(x_m, y_m) dx dy \quad (\text{B.6})$$

If the subbars are sufficiently small, the current density is assumed constant over their cross-section, which allows to replace some integrals of equation (B.6) into sums as follows:

$$J(x_m, y_m) S_m = - \frac{j\omega\mu_0\sigma}{2\pi} \sum_{n=1}^N J(x'_n, y'_n) \cdot \int_{S_m} \int_{S_n} \ln \sqrt{(x-x')^2 + (y-y')^2} dx' dy' dx dy + J_{\omega=0}(x, y) S_m \quad (\text{B.7})$$

where N is the number of subbars. The geometrical mean distance R_{mn} between two subbars is defined by:

$$\ln R_{mn} = \frac{\int_{S_m} \int_{S_n} \ln \sqrt{(x-x')^2 + (y-y')^2} dx' dy' dx dy}{S_m S_n} \quad (\text{B.8})$$

and therefore equation (B.7) becomes:

$$J(x_m, y_m) = - \frac{j\omega\mu_0\sigma}{2\pi} \sum_{n=1}^N J(x'_n, y'_n) \ln R_{mn} S_n + J_{\omega=0}(x, y) \quad (\text{B.9})$$

The numerical method used to calculate $\ln R_{mn}$ are proposed in [26], [63], [110]. Since no solution to calculate $\partial \ln R_{mn} / \partial x$ and $\partial \ln R_{mn} / \partial y$ is proposed, this section presents a method deduced from the solution of $\ln R_{mn}$.

Appendix B. Numerical methods for the integral

First, the numerical solution for $\ln R_{mn}$ is given by:

$$\begin{aligned} \ln R_{mn} = & -25/12 + \frac{1}{2w_m t_m w_n t_n} \sum_{i=1}^4 \sum_{j=1}^4 (-1)^{i+j} \left[\left(\frac{e_i^2 p_j^2}{4} - \frac{e_i^4}{24} - \frac{p_j^4}{24} \right) \ln(e_i^2 + p_j^2) \right. \\ & \left. + \frac{e_i^3 p_j}{3} \tan^{-1}\left(\frac{p_j}{e_i}\right) + \frac{e_i p_j^3}{3} \tan^{-1}\left(\frac{e_i}{p_j}\right) \right] \end{aligned} \quad (\text{B.10})$$

where

$$\begin{aligned} e_1 &= E - \frac{w_m}{2} - \frac{w_n}{2} & p_1 &= P - \frac{t_m}{2} - \frac{t_n}{2} \\ e_2 &= E + \frac{w_m}{2} - \frac{w_n}{2} & p_2 &= P + \frac{t_m}{2} - \frac{t_n}{2} \\ e_3 &= E + \frac{w_m}{2} + \frac{w_n}{2} & p_3 &= P + \frac{t_m}{2} + \frac{t_n}{2} \\ e_4 &= E - \frac{w_m}{2} + \frac{w_n}{2} & p_4 &= P - \frac{t_m}{2} + \frac{t_n}{2} \end{aligned} \quad (\text{B.11})$$

In order to compute $\partial \ln R_{mn} / \partial x$ and $\partial \ln R_{mn} / \partial y$, eq. (B.10) is derivated. Since $\partial / \partial x \equiv \partial / \partial e_i \equiv \partial / \partial E$ and $\partial / \partial y \equiv \partial / \partial p_j \equiv \partial / \partial P$, it gives:

$$\begin{aligned} \frac{\partial \ln R_{mn}}{\partial x} = & \frac{1}{2w_m t_m w_n t_n} \sum_{i=1}^4 \sum_{j=1}^4 (-1)^{i+j} \left[\left(\frac{e_i p_j^2}{2} - \frac{e_i^3}{6} \right) \ln(e_i^2 + p_j^2) \right. \\ & + \left(\frac{e_i^2 p_j^2}{4} - \frac{e_i^4}{24} - \frac{p_j^4}{24} \right) \frac{2e_i}{e_i^2 + p_j^2} + e_i^2 p_j \tan^{-1}\left(\frac{p_j}{e_i}\right) - \frac{e_i^3 p_j^2}{3(p_j^2 + e_i^2)} \\ & \left. + \frac{p_j^3}{3} \tan^{-1}\left(\frac{e_i}{p_j}\right) + \frac{e_i p_j^4}{3(e_i^2 + p_j^2)} \right] \end{aligned} \quad (\text{B.12})$$

and

$$\begin{aligned}
 \frac{\partial \ln R_{mn}}{\partial y} = & \frac{1}{2w_m t_m w_n t_n} \sum_{i=1}^4 \sum_{j=1}^4 (-1)^{i+j} \left[\left(\frac{e_i^2 p_j}{2} - \frac{p_j^3}{6} \right) \ln(e_i^2 + p_j^2) \right. \\
 & + \left(\frac{e_i^2 p_j^2}{4} - \frac{e_i^4}{24} - \frac{p_j^4}{24} \right) \frac{2p_j}{e_i^2 + p_j^2} + \frac{e_i^3}{3} \tan^{-1} \left(\frac{p_j}{e_i} \right) + \frac{e_i^4 p_j}{3(e_i^2 + p_j^2)} \\
 & \left. + e_i p_j^2 \tan^{-1} \left(\frac{e_i}{p_j} \right) - \frac{e_i^2 p_j^3}{3(p_j^2 + e_i^2)} \right]
 \end{aligned} \tag{B.13}$$

This third method is much quicker than the first one but slightly longer than the second one. Still, if the subbars are sufficiently small, the obtained results with this method provides an error that is smaller than 1 % for the resistance and self internal inductance.

B.4 Linear resistance and internal self inductance for circular cross-section conductors

To calculate the linear resistance and the linear self inductance as a function of the frequency, there is an analytical solution for circular cross-section. It uses Bessel functions and is defined as follows [54], [93], [118]:

$$R = \frac{k'}{2\pi a\sigma} \frac{\text{ber}(k'a)\text{bei}'(k'a) - \text{bei}(k'a)\text{ber}'(k'a)}{(\text{ber}'(k'a))^2 + (\text{bei}'(k'a))^2} \quad (\text{B.14})$$

$$L_i = \frac{k'}{2\pi a\sigma\omega} \frac{\text{ber}(k'a)\text{ber}'(k'a) + \text{bei}(k'a)\text{bei}'(k'a)}{(\text{ber}'(k'a))^2 + (\text{bei}'(k'a))^2} \quad (\text{B.15})$$

where ber , bei , ber' , bei' are the real and imaginary parts of the Bessel function and respectively of the derivatives of the Bessel function, $k' = \sqrt{\omega\mu_0\sigma}$ and a is the radius of the conductor.

Genetic algorithms implementation and test functions

C.1 Genetic operators

C.1.1 Individual evaluation

An individual is generally represented by a vector \mathbf{X} that corresponds to a solution of the function to optimize. This vector contains the values of the parameters associated to this solution.

$$\mathbf{X} = (X_1, X_2, \dots, X_i) \tag{C.1}$$

So an individual \mathbf{X} contains the i parameters X_1, X_2, \dots, X_i . These parameters may take different forms, such as binary values or real values. The representation type is often called genotype. In this thesis, only the real values genotype is used. However, some of the parameters, such as the number of turns, have only integer values. This problem is circumvented during the individual (or child) creation by rounding the value of the affected parameters to its closest integer value, as follows:

$$X_{i,int} = \text{round}(X_i) \tag{C.2}$$

Appendix C. Genetic algorithms implementation and test functions

The choice of the genotype is important because it may influence the organization of the GA and the way of individuals evaluation.

To quantify the quality of an individual, a fitness function $F(\mathbf{X})$ has to be defined. Generally, the fitness function associates to each individual a real value that defines its probability to be chosen as a parent during the selection phase or to survive to the next generation. Often, the fitness function is the same as the objective function $O(\mathbf{X})$, except when a constraint is violated. In this specific case, a penalty is applied to the fitness function.

C.1.2 Constraints management

The m constraints g_1, g_2, \dots, g_m of a problem are organized in a vector \mathbf{G} as follows:

$$\mathbf{G} = (g_1, g_2, g_3, \dots, g_m) \quad (\text{C.3})$$

For all the individuals of a population, the constraints g_i are defined so that they are strictly positive only if they are violated. For example, the geometrical constraint related to the maximal number of turns (3.30) introduced in chapter 3 becomes:

$$g_1 = \frac{n}{N}(w + d) + cst - \frac{a}{2} \quad (\text{C.4})$$

Similarly, a possible constraint on the maximal admissible Joule losses $P_{j,max}$ for a coil would take the following form:

$$g_2 = P_j - P_{j,max} \quad (\text{C.5})$$

In these two examples, the constraints are violated if $g_1 > 0$ or $g_2 > 0$. If so, a penalty is imposed to the fitness function in a way that the concerned individual is at least worse than the worst of the individuals that does not violate any constraint. With those explanations and assuming a problem where the objective function is to be minimized, the fitness function is defined as follows [92]:

$$F(\mathbf{X}) = \begin{cases} O(\mathbf{X}) & \text{if } g_i \leq 0 \text{ for all } g_i \\ F_{max} + \sum_{i=1}^m v_i(\mathbf{X}) & \text{otherwise} \end{cases} \quad (\text{C.6})$$

where

$$v_i(\mathbf{X}) = \max\{0, g_i(\mathbf{X})\} \quad (\text{C.7})$$

and F_{max} is the worst fitness function among the individuals that do not violate any constraints. This strategy is interesting because it ensures that an individual that does not respect at least one constraint has less probability to survive than any other that respects every constraint.

C.1.3 Selection

Once a fitness is assigned to each individual of the population, some of them will be selected to begin the reproduction process. The greater is the individual fitness, the greater is his chance to be selected. This operator is then consistent with the concept of natural selection, as the most efficient individuals are more likely to be transferred to the next generation while the weakest ones tend to disappear. Theoretically, if neither the crossover nor the mutation were applied, the strongest individual would completely invade the population in a few generations, leading to a premature convergence of the GA.

This brings together the concepts of selection pressure and diversity. Selection pressure is an indication of the strength of a selection method and have a great influence on the speed of convergence. A too high pressure reduces the diversity in a population, which may result in a premature convergence. The diversity represents the ability of a GA to evaluate the whole search space. Maintaining it as high as possible reduces the probability of premature convergence but, in the same time, slows down the convergence. Thus, there is a trade-off between selection pressure and diversity.

Multiple selection methods exist and have in common to be dependent on the fitness of the individuals. In this thesis, only two methods are used as they are probably the most popular and efficient ones.

The *proportionate selection* (or *roulette-wheel selection*) consists in selecting an individual in proportion to its fitness. The roulette-wheel of a casino can illustrate the principle of this method. It would include as many cases as individuals in the population and each case would have a size that is proportional to the fitness value of the individual it represents. A random selection is then made as if the roulette-wheel was rolled. The specificity of this method is that a weak individual still has a chance to produce offspring even if the strongest ones are more likely to do so.

The *tournament selection* consists in randomly picking a few individuals in the population (generally between 2 and 10) and selecting the one (or the ones) that has (or have) the greatest fitness. The main advantage of this method is that the selection pressure can be easily adjusted by changing the number of individuals involved in the tournament. A large tournament size reduces the probability of weak individuals to be selected.

C.1.4 Crossover

The selection operator allows to create new individuals (children). To do so, it generally uses two parents selected during the preceding phase and generates one child or two children. This is integral part of the stochastic process as multiple applications of the crossover on the same parents can generate different children. Several crossover methods exist. One can cite uniform crossover, arithmetic crossover, one-point or two-point crossover. As they are already discussed and commented in literature [98], [30], only a short qualitative description is proposed here.

The *one-point crossover* consists in randomly choosing a cutting point in the genotype for both parents. This point can then be placed between any pair of parameters within the vector \mathbf{X} . The two children are obtained by exchanging the value of the parameters that are situated before (or after) this cutting point. Similarly, the *two-points crossover* involves two random cutting points in the genotype, and only the parameters situated between them (or outside them) are exchanged.

The *uniform crossover* consists in evaluating separately each parameter from two parents and choosing randomly between them to create the children. As a result, the genotype of the children is a mixture of the two parents. The probability to choose the parameters from a parent or the other one is generally set to $1/2$, but this ratio can be adjusted.

In the previous crossover methods, the exact parameters values of the parents are distributed to the children. However, especially for a real values genotype, it may be interesting to generate children with different parameters values from the ones of the parents. In this sense, the *arithmetic crossover* consists in taking the average values of the parameters from two parents to generate one child.

C.1.5 Mutation

The aim of the mutation is to randomly modify a number of parameters in the genotype of an individual, generally a recently born child. This operator allows to introduce some diversity in the population. More specifically, it gives to an individual trapped in a local optimum the opportunity to escape it. As for the other operators, multiple techniques exist, such as the simple *random mutation*, the *uniform mutation* or *gaussian mutation*.

C.1.6 Replacement

Once the children are created (selection and crossover operators) and mutated (mutation operator), the strategy of replacement has to be established. Basically the replacement operator defines how the children replace the parents for the next generation.

A *total replacement* consists in completely replacing the individuals from the old population by the children. However, the number of generated children at each generation is generally not as large as the number of individuals in the population. Then, a *reverse replacement* can be applied, which consists in replacing the k worst individuals from the old population by the k best children (or all children). Some additional conditions can be applied for the replacement. For example, the possibility for a child to replace an individual only if it has a better fitness value.

C.1.7 Genetic algorithm termination

A stop criterion has to be defined to decide when the execution of the GA ends. It can for example be the convergence to a solution or a maximal number of generations. In this thesis, the termination criterion will always be the number of objective function evaluations. This strategy allows to control the computation time, but in return generates the risk that the global optimum is not reached. Generally, if the maximum of objective function evaluations is sufficiently high, this is not an issue.

C.2 Multiobjective test functions

C.2.1 Unconstrained test functions

The different multiobjective test functions used in chapter 4 are defined in this appendix. Table C.1 presents the unconstrained test functions $ZDT1$, $ZDT2$, $ZDT3$, and $ZDT4$. Therein, p is the number of variables of a test function. The values of the Pareto front solutions are known and defined in the fifth column. In Fig. C.1, the Pareto fronts of the four test functions are plotted.

C.2.2 Constrained test functions

Two constrained test functions are used in chapter 4, called $Constr$ and Tnk . They are defined in Table C.2. As a reminder, the constraints g_i are defined in a way that they are not violated if they are smaller or equal to zero. In Fig. C.2, the Pareto fronts of $Constr$ and Tnk are plotted.

Appendix C. Genetic algorithms implementation and test functions

Table C.1: Unconstrained test functions that are often used to evaluate MOGAs.

Function	p	Variable limits	Objective functions	Pareto front solutions
<i>ZDT1</i>	15	[0,1]	$O_1 = X_1$ $O_2 = h(\mathbf{X}) \left[1 - \sqrt{\frac{X_1}{h(\mathbf{X})}} \right]$ $h(\mathbf{X}) = 1 + 9 \frac{(\sum_{i=2}^p X_i)}{p-1}$	$X_1 \in [0, 1]$ $X_i = 0, i = 2, \dots, p$
<i>ZDT2</i>	15	[0,1]	$O_1 = X_1$ $O_2 = h(\mathbf{X}) \left[1 - \left(\frac{X_1}{h(\mathbf{X})} \right)^2 \right]$ $h(\mathbf{X}) = 1 + 9 \frac{(\sum_{i=2}^p X_i)}{p-1}$	$X_1 \in [0, 1]$ $X_i = 0, i = 2, \dots, p$
<i>ZDT3</i>	15	[0,1]	$O_1 = X_1$ $O_2 = h(\mathbf{X}) \left[1 - \sqrt{\frac{X_1}{h(\mathbf{X})}} - \frac{X_1}{h(\mathbf{X})} \sin(10\pi X_1) \right]$ $h(\mathbf{X}) = 1 + 9 \frac{(\sum_{i=2}^p X_i)}{p-1}$	$X_1 \in [0, 1]$ $X_i = 0, i = 2, \dots, p$
<i>ZDT4</i>	10	$X_1 \in [0, 1]$ $X_i \in [-5, 5],$ $i = 2, \dots, p$	$O_1 = X_1$ $O_2 = h(\mathbf{X}) \left[1 - \sqrt{\frac{X_1}{h(\mathbf{X})}} \right]$ $h(\mathbf{X}) = 1 + 10(p-1) + \sum_{i=2}^p [X_i^2 - 10 \cos(4\pi X_i)]$	$X_1 \in [0, 1]$ $X_i = 0, i = 2, \dots, p$

Table C.2: Constrained functions that are often used to evaluate MOGAs.

Function	p	Variable limits	Objective functions	Constraints
<i>Constr</i>	2	$X_1 \in [0.1, 1.0]$ $X_2 \in [0, 5]$	$O_1 = X_1$ $O_2 = \frac{1+X_2}{X_1}$	$g_1 = 6 - X_2 - 9X_1$ $g_2 = 1 + X_2 - 9X_1$
<i>Tnk</i>	2	$X_1 \in [0, \pi]$ $X_2 \in [0, \pi]$	$O_1 = X_1$ $O_2 = X_2$	$g_1 = -X_1^2 - X_2^2 + 1 + 0.1 \cos(16 \arctan(X_1 / X_2))$ $g_2 = (X_1 - 0.5)^2 + (X_2 - 0.5)^2 - 0.5$

C.2. Multiobjective test functions

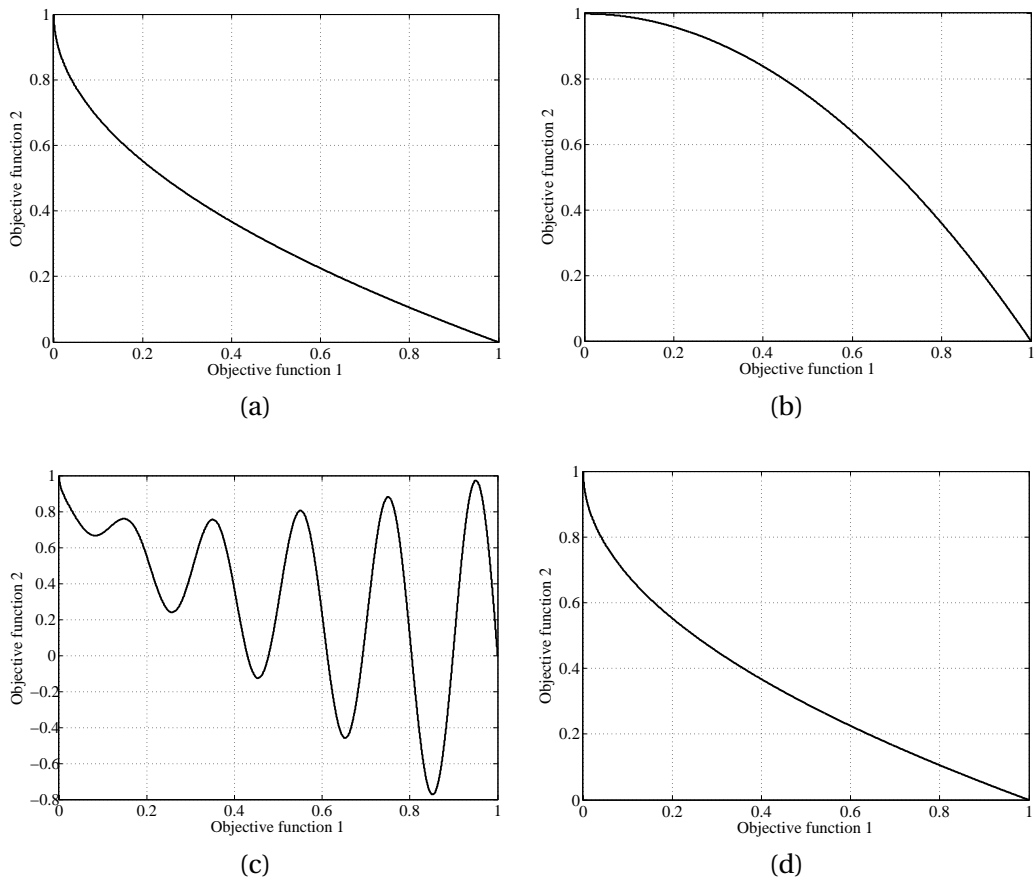


Figure C.1: (a) Pareto front line of (a) *ZDT1*, (b) *ZDT2*, (c) *ZDT3*, (d) *ZDT4*.

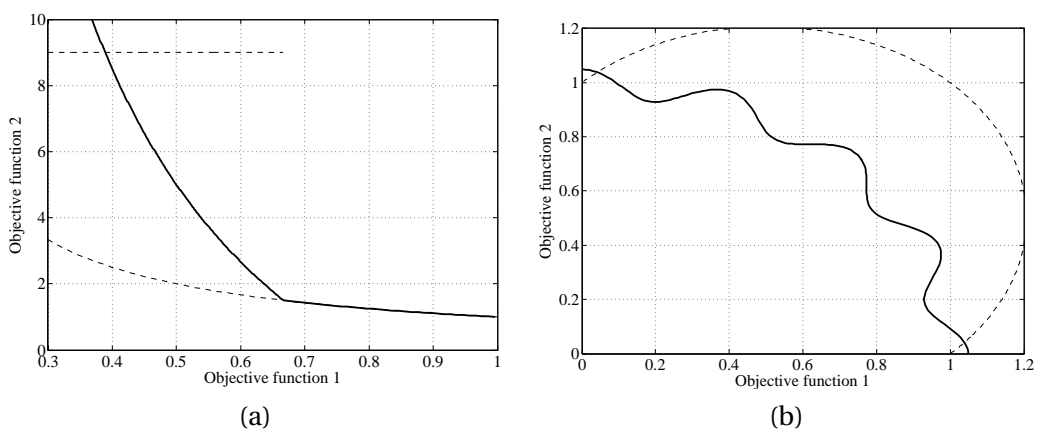


Figure C.2: (a) Pareto front line of (a) *Constr*, (b) *Tnk*.

Notebook charger: Preliminary study and electronics

D.1 Energy chain

To determine the specifications of the CET system for the notebook charger, the whole system has to be considered. Its energy chain is given in D.1. The different parts are the following ones:

1. the grid;
2. the input rectifier;
3. the high frequency converter;
4. the coreless transformer;
5. the output rectifier;
6. the notebook battery (load).

In order to determine the specifications of the coreless transformer, each part (or function) has to be analyzed separately. The following sections present the study that leads to the establishment of specifications for the coreless transformer.

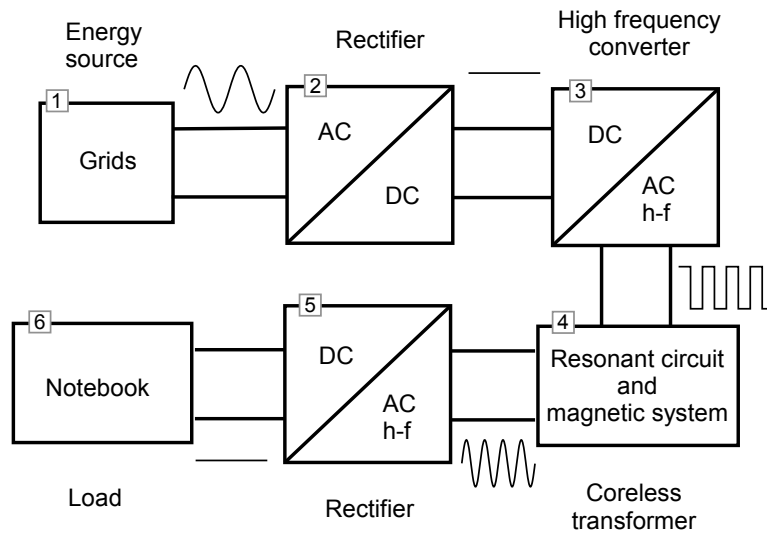


Figure D.1: Energy chain for the CET system of the notebook.

D.2 Charger and notebook specifications

D.2.1 Coils

The primary coil has to be integrated on the *Alto* platform in a way that it does not disturb its conventional use. The secondary coil has to be integrated under the notebook. The only restriction concerns the size of the coils that should not be larger than the one of the notebook, that is approximately 240 mm by 160 mm.

The vertical distance (or airgap) between the primary and the secondary coil is 10 mm, due to the thickness of the *Alto* platform and the integration of the primary coil.

D.2.2 Electrical requirements

As a first requirement, the battery charger has to draw its power directly from the grid. The user should plug it and the CET has to be working.

Secondly, the notebook used for this project is a Dell Latitude C840. The original charger is able to supply 20 V (DC) and 4.5 A (DC) to the notebook. Some measurements have been performed while the computer was being charged. For these measurements, the screen was set to a standard brightness and the CPU was not working. The measured voltage and current drawn by the notebook oscillate periodically between two states:

1. 18 V (DC), 3.2 A (DC) (during a few seconds)
2. 19.5 V (DC), 1.15 A (DC) (during a few seconds)

If the brightness of the screen is increased and the CPU is fully working, the current of the first state can be increased (a maximal of 3.8 A (DC) has been measured). The load is automatically managed by the internal electronics of the notebook. In brief, the goal is to realize a charger that provides a stable voltage $U_{L,DC}$ of 20 V (DC) for a power up to 80 W, which offers a large margin of security.

D.2.3 Input voltage of the coreless transformer

Fig. D.2 shows an electronic schematic of the primary side. The input voltage (AC) of the coreless transformer is obtained in two steps.

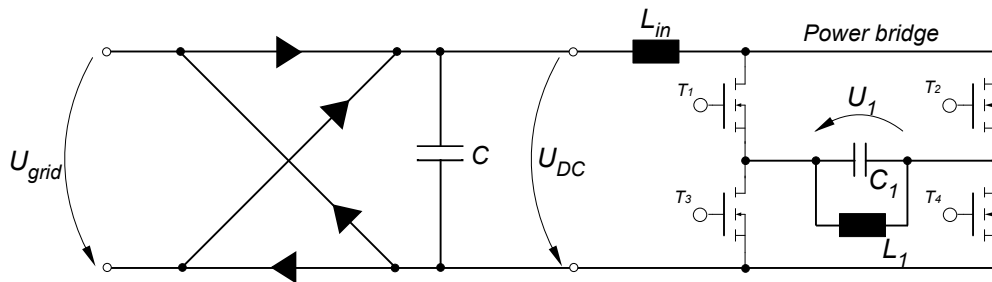


Figure D.2: Electronic schematic from the grid to the primary coil. The secondary side is not shown.

First, the grid voltage U_{grid} (240 V (AC rms), 50 Hz) is rectified by a full-bridge rectifier and a smoothing capacitor. The rectifier used in this project is a Diotec KBU6G and the smoothing capacitor is a standard one ($C = 470 \mu F$). This gives the voltage U_{DC} of 320 V (DC), obtained as follows:

$$U_{DC} = (U_{grid}\sqrt{2} - 2V_j)0.95 \approx 320 \text{ V} \quad (\text{D.1})$$

where $V_j = 0.7 \text{ V}$ is the forward voltage of the diodes. Here, a security margin of 5 % has been used due to the fluctuation of the DC voltage, as outlined in Fig. D.3. Doing so has been verified by measurement and shows a good agreement.

Secondly, a full-bridge converter (presented in section 5.1.3) allows to generate a HF voltage U_1 of 355 V (AC rms) on the primary coil. Theoretically, the converter applies a square wave voltage to the primary coil. But the primary resonant capacitor has the effect of filtering the higher harmonic voltages, which gives rise to a sine wave on the terminals of the primary coil.

This generates an incoherence of compatibility between the output of the rectifier U_{DC} and the input of the converter where the voltage takes the shape of rectified sine wave. That is why an inductor L_{in} has to be placed at the input of the bridge. Doing so turns the behavior of the system into a current source, and the difference of voltage is taken by the inductor.

Assuming the resonant circuit correctly designed and neglecting the losses in the full-bridge converter, the energy at the output of the converter is equal to the energy at its input. Hence, the DC voltage corresponds to the average AC voltage on half a period (Fig. D.4). Assuming the AC voltage is a perfect sine wave, its average is given by integration as follows:

$$\bar{U} = \frac{1}{T/2} \int_0^{T/2} \hat{U} \sin(\omega t) dt = \frac{2}{\pi} \hat{U}_1 = \frac{2\sqrt{2}}{\pi} U_1 \quad (D.2)$$

Here, T is the period of the voltage. Thus, the AC voltage is defined by:

$$U_1 = \bar{U} \frac{\pi}{2\sqrt{2}} = U_{DC} \frac{\pi}{2\sqrt{2}} \quad (D.3)$$

As a result the value of the input voltage U_1 is approximately 355 V (AC rms). This value is used to design the coreless transformer.

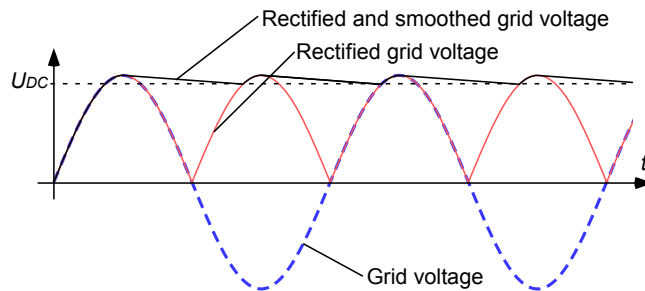


Figure D.3: Schematic view of the rectified and smoothed voltages.

D.2.4 Output voltage of the coreless transformer

At the output of the coreless transformer, a full-bridge rectifier with a capacitive filter is used in order to make the energy usable for the notebook (*c.f.* Fig. D.5(a)). The presence of the rectifier with the capacitive filter creates a square form of voltage at the input of the rectifier. Therefore, for the analysis of the AC signals, the fundamental component of the voltage must

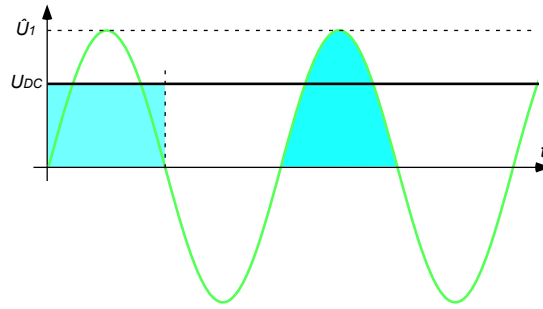


Figure D.4: Schematic view of the AC voltage at the converter output.

be used [119]. But the rectifier changes the impedance of the load for the resonant circuit because of the nonlinearity introduced by the rectifier. The resulted impedance formed by the rectifier and the load itself can be modeled by an equivalent resistor as shown in Fig. D.5(b). Its value is given by [46], [75]:

$$R_{eq} = \frac{8}{\pi^2} R_L \quad (D.4)$$

With this, the computation of AC voltages and currents remains valid by taking the fundamental components of the signals and by loading the resonant circuit with the equivalent load resistance. This leads to an equivalent load resistance R_{eq} of 4.6Ω for the first state of the supplying process (worst case). Furthermore the AC voltage required by the equivalent load is given by:

$$U_{L,eq} = \frac{2\sqrt{2}}{\pi} U_{LDC} \quad (D.5)$$

By taking into account the voltage drop U_j in the diodes, the necessary AC voltage that ensures a DC voltage of 20 V (DC) to the notebook is:

$$U_{L,eq} = \frac{2\sqrt{2}}{\pi} U_{LDC} + 2U_j \quad (D.6)$$

In conclusion, the AC voltage $U_{L,eq}$ required at the output of the coreless transformer is 20 V (AC rms).

D.2.5 Summary

In conclusion, Table 5.1 gives a summary of the different specifications for the coreless transformer.

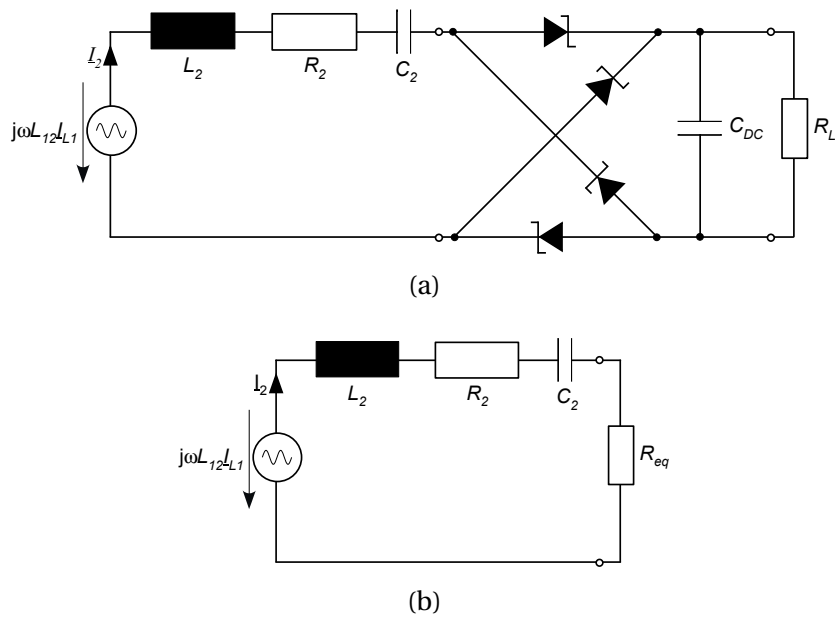


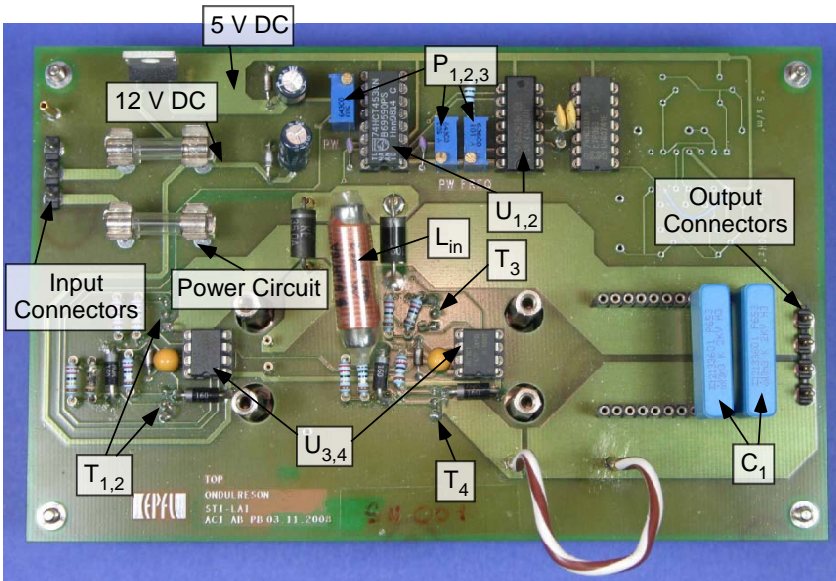
Figure D.5: (a) Electronic schematic of the secondary circuit. (b) Equivalent circuit.

D.3 Electronics

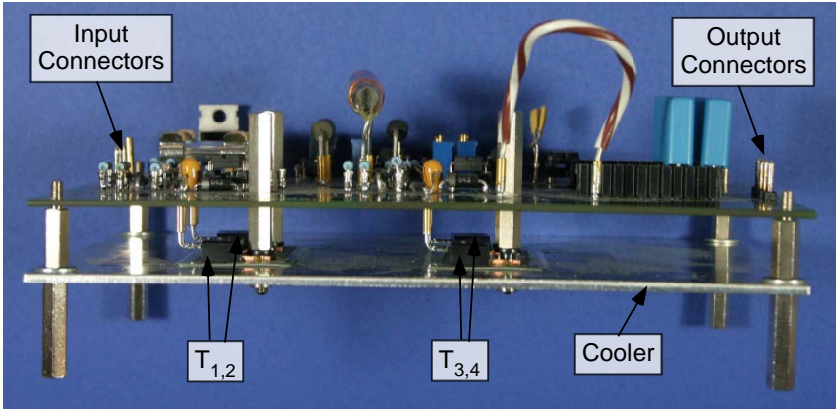
Two pictures of the full-bridge converter are given in Fig. D.6 with the identification of the main electronic components. Their definition is given in Table D.1.

Table D.1: Main components of the full-bridge converter

Component	Value	Definition
U_1	SN74LS624N	Voltage-controlled oscillator (VCO)
U_2	74HCT4538N	Monostable multivibrator
$U_{3,4}$	IR2101	High and low side drivers
P_1	100 Ω	Frequency tuning
$P_{2,3}$	50 k Ω	PWM tuning
$T_{1,2,3,4}$	IRFB9N65A	MOSFETs (TO-220 package)
L_{in}	250 μ H	Self-inductance
C_1	6.9 nF	First resonant capacitor.



(a)



(b)

Figure D.6: (a) Top view and (b) side view of the full-bridge converter.

Appendix D. Notebook charger: Preliminary study and electronics

A picture of the full-bridge rectifier is given in Fig. D.7 with the identification of the main electronic components. Their definition is given in Table D.2.

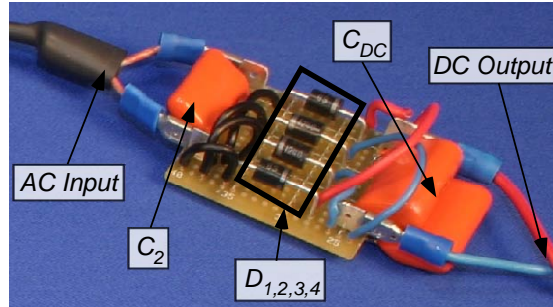


Figure D.7: The output rectifier with the series compensation capacitor and the filter capacitor.

Table D.2: Components used in the rectifier.

Component	Value	Definition
$D_{1,2,3,4}$	SB1240	Schottky Barrier Rectifiers.
C_2	470 nF	Second resonant capacitor.
C_{DC}	1.68 μ F	Filter capacitor.

CET table: electronics

E.1 Primary coils array implementation

The main electronics used in the primary side and a portion of the primary coils array are shown in Fig. E.1. The main components are then defined in Table E.1.

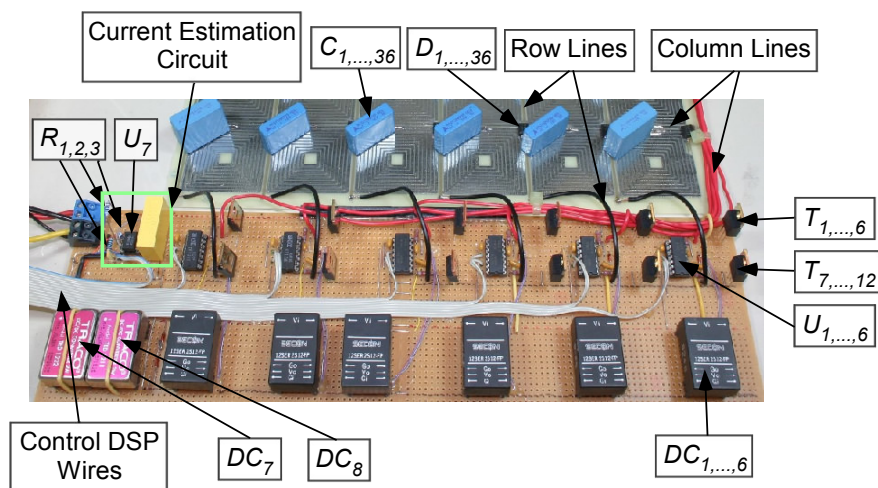


Figure E.1: Photograph of the primary electronic circuit and a portion of the primary coils array.

Appendix E. CET table: electronics

Table E.1: Description of the main components used in the primary circuit.

Component	Value	Definition
$T_{1,\dots,6}$	IRF530N	MOSFETs driving the column lines
$T_{7,\dots,12}$	IRF530N	MOSFETs driving the row lines
$U_{1,\dots,6}$	IR2110	Low-side and high-side drivers
U_7	-	Part of the detection circuit
$R_{1,2,3}$	-	Parts of the detection circuit
$DC_{1,\dots,6}$	Traco TME 1212S	12 V/12 V DC/DC converter for the high-side drivers
DC_7	Traco TEL 1210 2 Watts	DC/DC converter with an output of 3.3 V.
DC_8	Traco TED 1222 2 Watts	DC/DC converter with an output of ± 15 V.
$C_{1,\dots,36}$	Low ESR ceramic 100 nF	Primary parallel compensation capacitors.
$D_{1,\dots,36}$	30BQ100	Shottky diodes.

Basically, the switch functions are achieved by using 12 MOSFET transistors that require drivers to be activated. Therefore, 6 separate ICs ($U_{1,\dots,6}$) are used, each of them containing a low-side driver for the row switches and a high-side driver for the column switches. The high frequency PWMs generated by the microcontroller are then routed to the input of the low-side drivers while the logic signals for controlling the column switches are routed to the high-side inputs. The 6 DC/DC converters $DC_{1,\dots,6}$ are used to generate the high-side floating supply voltage and the DC/DC converter DC_7 is used to generate the logic supply voltage (3.3 V) corresponding to the output level of the microcontroller. Furthermore, 36 capacitors $C_{1,\dots,36}$ are used as primary resonant for each coil, and 36 diodes are placed in series with each primary coil and capacitor in order to prevent the current from flowing back into other coils.

E.2 Detection method implementation

The different electronic components used for the detection system are presented in Table E.2.

Table E.2: The main components used in the detection circuit.

Component	Value	Definition
U_7	TL072CP	Low-noise operational amplifier for the current estimation circuit.
R_S	0.1 Ω SMS-R100-1.0	Shunt resistor.
R_1	10 k Ω	Amplifier resistor.
R_2	22 k Ω	Amplifier resistor.
R_3	100 k Ω	Low-pass filter resistor.
R_4	1 k Ω	Limiting current resistor.
C_1	3.3 nF	Low-pass filter capacitor.
$D_{1,2}$	BAT48	Small signal shottky diodes.

E.3 Secondary circuit implementation

The different electronic components used in the secondary circuit are presented in Table E.3.

Table E.3: Description of the main components used in the primary circuit.

Component	Value	Definition
L_{22}	25.45 μH	Measured secondary coil self inductance.
R_2	0.95 Ω	Measured secondary coil resistance.
C_2	25.3 nF	Secondary resonant capacitor.
U_1	LM2990T-5.0	Negative low dropout regulator.
$D_{1,\dots,4}$	SB1240	Shottky diodes with a low forward voltage.
C_{U1}	0.47 μF	Electrolytic capacitor.
C_{U2}	0.22 μF	Electrolytic capacitor.

To supply the mouse and the keyboard, a linear adjustable regulator LM317 is used with the right resistors configuration so as to obtain respectively 1.5 V (DC) and a 3 V (DC) at their output.

Bibliography

- [1] Alto picture. [Online], <http://www.caron-informatique.fr/catalog/images/...cordless.jpg>, June 2010.
- [2] Alto picture. [Online], <http://static.pcinpact.com/images/bd/news/33768-alto-logitech.jpg>, June 2010.
- [3] Car wireless charging by haloipt. [Online], <http://www.haloipt.com/>, September 2011.
- [4] Contactless electric vehicle charging prototype by bmw and siemens. [Online], <http://techprezz.com/2011/04/bmw-and-siemens-introduces-induction-based-wireless-charging-ev-concept/>, September 2011.
- [5] Contactless energy transfer of the ecoupled table. [Online], <http://ecoupled.com/>, September 2011.
- [6] Contactless energy transfer system for a small dockstation. [Online], <http://www.hpwebos.com/us/products.../accessories/touchstone-technology.html>, September 2011.
- [7] Inductive charging toothbrushes. [Online], <http://www.oralb.com/>, September 2011.
- [8] Inductive powering mouse. [Online], <http://www.a4tech.com/>, September 2011.
- [9] Logitech. [Online], <http://www.logitech.com>, September 2011.
- [10] The maximum power transfer as a function of the coils size and the frequency with respect to the health restrictions recommended by the international commission on non-ionizing radiation protection. [Online], <http://www.wirelesspowerconsortium.com/technology/maximum-power-transfer-into-space.html>, September 2011.
- [11] The philips sonicare website. [Online], <http://www.sonicare.com>, September 2011.
- [12] Powermat product line. [Online], <http://www.powermateu.com/H>, September 2011.
- [13] The swissmetro website. [Online], <http://www.swissmetro.ch>, September 2011.

Bibliography

- [14] Tesla's experiments. [Online], <http://www.neuronet.pitt.edu>, September 2011.
- [15] The westinghouse electric corporation website. [Online], <http://www.westinghouse.com>, September 2011.
- [16] Wireless charging platform. [Online], <http://www.qualcomm.com>, September 2011.
- [17] Wireless charging platform. [Online], <http://www.mojomobility.com/>, September 2011.
- [18] The wireless power consortium. [Online], <http://www.wirelesspowerconsortium.com/>, September 2011.
- [19] Witricity contactless system for electric vehicles. [Online], <http://www.witricity.com/pages/ev-charging-system.html>, September 2011.
- [20] Cedrat website. [Online], <http://www.cedrat.com/>, January 2012.
- [21] Genetic algorithm toolbox. [Online], <http://www.mathworks.com/>, January 2012.
- [22] Inca3d from cedrat website. [Online], <http://www.cedrat.com/InCa3D>, August 2012.
- [23] Vilfredo pareto's life. [Online], <http://en.wikipedia.org/wiki/VilfredoPareto>, February 2012.
- [24] J. Achterberg, E. A. Lomonova, and J. de Boeij. Coil array structures compared for contactless battery charging platform. *Magnetics, IEEE Transactions on*, 44(5):617–622, May 2008.
- [25] A. Ahlbom, U. Bergqvist, J. H. Bernhardt, J. Cesarini, L. A. Court, M. Grandolfo, M. Hietanen, A. F. Mckinlay, M. H. Repacholi, D. H. Sliney, J. A. J. Stolwijk, M. L. Swicord, L. D. Szabo, M. Taki, T. S. Tenforde, H. P. Jammet, and R. Matthes. Guidelines for limiting exposure to time-varying electric, magnetic, and electromagnetic fields (up to 300 GHz). International Commission on Non-Ionizing Radiation Protection. *Health Phys*, 74(4):494–522, Apr. 1998.
- [26] G. Antonini, A. Orlandi, and C. Paul. Internal impedance of conductors of rectangular cross section. *Microwave Theory and Techniques, IEEE Transactions on*, 47(7):979–985, jul. 1999.
- [27] A. Balakrishnan, W. Palmer, W. Joines, and T. Wilson. The inductance of planar structures. In *Applied Power Electronics Conference and Exposition, 1993. APEC '93. Conference Proceedings 1993., Eighth Annual*, pages 912–921, mar 1993.
- [28] S. Bandyopadhyay, S. Saha, U. Maulik, and K. Deb. A simulated annealing-based multi-objective optimization algorithm: Amosa. *Evolutionary Computation, IEEE Transactions on*, 12(3):269–283, june 2008.
- [29] T. Bieler, M. Perrottet, V. Nguyen, and Y. Perriard. Contactless power and information transmission. *Industry Applications, IEEE Transactions on*, 38(5):1266–1272, Sep/Oct 2002.

- [30] A. Bourquard. Optimisation d'un instrument chirurgical ultrasonique par algorithmes genetique. Semester project, Ecole Polytechnique Federale de Lausanne (EPFL), 2008.
- [31] H. Chan, K. Cheng, and D. Sutanto. A simplified neumann's formula for calculation of inductance of spiral coil. In *Power Electronics and Variable Speed Drives, 2000. Eighth International Conference on (IEE Conf. Publ. No. 475)*, pages 69–73, 2000.
- [32] D. K. Cheng. *Field and Wave Electromagnetics*. The Addison-Wesley series in electrical engineering. Addison-Wesley, 1989.
- [33] B. Choi and J. Nho. Contactless energy transfer using planar printed circuit board windings. *Electronics Letters*, 37(16):1007–1009, 2 Aug 2001.
- [34] B. Choi, J. Nho, H. Cha, T. Ahn, and S. Choi. Design and implementation of low-profile contactless battery charger using planar printed circuit board windings as energy transfer device. *Industrial Electronics, IEEE Transactions on*, 51(1):140–147, Feb. 2004.
- [35] H. Chung and M. Pong. Effect of switching frequency and number of winding layers on copper loss of an inductor. In *Power Electronics and Motion Control Conference, 2000. Proceedings. IPEMC 2000. The Third International*, volume 3, pages 1312–1317 vol.3, 2000.
- [36] K. Coperich, A. Ruehli, and A. Cangellaris. Enhanced skin effect for partial-element equivalent-circuit (peec) models. *Microwave Theory and Techniques, IEEE Transactions on*, 48(9):1435–1442, sep 2000.
- [37] J. de Boeij, E. Lomonova, J. Duarte, and A. Vandenput. Contactless energy transfer to a moving load part ii: Simulation of electrical and mechanical transient. *Industrial Electronics, 2006 IEEE International Symposium on*, 2:745–750, July 2006.
- [38] J. de Boeij, E. Lomonova, and A. Vandenput. Contactless energy transfer to a moving load part i: Topology synthesis and fem simulation. *Industrial Electronics, 2006 IEEE International Symposium on*, 2:739–744, July 2006.
- [39] J. de Boeij, E. A. Lomonova, and A. J. A. Vandenput. Optimization of contactless planar actuator with manipulator. *Magnetics, IEEE Transactions on*, 44(6):1118–1121, June 2008.
- [40] K. Deb and M. Goyal. A Combined Genetic Adaptive Search (GeneAS) for Engineering Design. *Computer Science and Informatics*, 26:30–45, 1996.
- [41] K. Deb, A. Pratap, S. Agarwal, and T. Meyarivan. A fast elitist multi-objective genetic algorithm: Nsga-ii. *IEEE Transactions on Evolutionary Computation*, 6:182–197, 2000.
- [42] T. Demeester and D. de Zutter. Applications of the dirichlet-to-neumann boundary operator in transmission line modeling. In *Electromagnetic Compatibility, 2009 20th International Zurich Symposium on*, pages 25–28, jan. 2009.
- [43] T. Demeester and D. De Zutter. Internal impedance of composite conductors with arbitrary cross section. *Electromagnetic Compatibility, IEEE Transactions on*, 51(1):101–107, feb. 2009.

Bibliography

- [44] D. DeZutter and L. Knockaert. Skin effect modeling based on a differential surface admittance operator. *Microwave Theory and Techniques, IEEE Transactions on*, 53(8):2526–2538, aug. 2005.
- [45] R. M. Dickinson. Wireless power transmission technology state of the art the first bill brown lecture. *Acta Astronautica*, 53(4-10):561–570, 2003.
- [46] A. Ecklebe and A. Lindemann. Analysis and design of a contactless energy transmission system with flexible inductor positioning for automated guided vehicles. *IEEE Industrial Electronics, IECON 2006 - 32nd Annual Conference on*, pages 1721–1726, Nov. 2006.
- [47] M. Enohnyaket and J. Ekman. Peec models for air-core reactors modeling skin and proximity effects. In *Power Electronics Specialists Conference, 2007. PESC 2007. IEEE*, pages 3034–3038, june 2007.
- [48] H. Eskandari and C. D. Geiger. A fast pareto genetic algorithm approach for solving expensive multiobjective optimization problems. *Journal of Heuristics*, 14(3):203–241, June 2008.
- [49] A. Esser. Contactless charging and communication for electric vehicles. *Industry Applications Magazine, IEEE*, 1(6):4–11, nov/dec 1995.
- [50] C. Fernandez, O. Garcia, R. Prieto, J. Cobos, S. Gabriels, and G. Van Der Borghet. Design issues of a core-less transformer for a contact-less application. *Applied Power Electronics Conference and Exposition, 2002. APEC 2002. Seventeenth Annual IEEE*, 1:339–345 vol.1, 2002.
- [51] C. Fernandez, R. Prieto, O. Garcia, P. Herranz, J. Cobos, and J. Uceda. Modelling core-less high frequency transformers using finite element analysis. *Power Electronics Specialists Conference, 2002. pesc 02. 2002 IEEE 33rd Annual*, 3:1260–1265 vol.3, 2002.
- [52] J. Fernandez Lopez. *Modeling and optimization of ultrasonic linear motors*. PhD thesis, Ecole Polytechnique Federale de Lausanne (EPFL), 2006.
- [53] A. Garcia, J. Carrasco, J. Soto, F. Maganto, and C. Morón. A method for calculating the magnetic field produced by a coil of any shape. *Sensors and Actuators A: Physical*, 91(1-2):230–232, 2001. Third European Conference on Magnetic Sensors & Actuators.
- [54] O. Gatous and J. Pissolato. Frequency-dependent skin-effect formulation for resistance and internal inductance of a solid cylindrical conductor. *Microwaves, Antennas and Propagation, IEE Proceedings -*, 151(3):212–216, 2004.
- [55] P. Germano and M. Jufer. Contactless power transmission: Frequency tuning by a maximum power tracking method. *EPE '97, 7th European Conference on power electronics and applications, Trondheim*, IV:693–697, September 1997.
- [56] P. Germano, N. Macabrey, and M. Jufer. Contactless power transmission: Linear positioning of the moving element. Technical report, Swiss Federal Institute of Technology, Lausanne (EPFL) DE-LEME / ELG, 1998.

- [57] P. Germano, I. Stefanini, and Y. Perriard. Stimulation colique pour le traitement des troubles de la motilité - projet colostim. Technical report, LAI-CHUV, 2007.
- [58] P. Germano, I. Stefanini, and Y. Perriard. Contactless system dedicated to colic stimulation. *ICEM 2008, Vilamoura, Portugal*, 2008.
- [59] D. E. Goldberg. *Genetic Algorithm in Search, Optimization, and Machine Learning*. Addison-Wesley, New York, 1989.
- [60] H. Greenhouse. Design of planar rectangular microelectronic inductors. *Parts, Hybrids, and Packaging, IEEE Transactions on*, 10(2):101–109, Jun 1974.
- [61] J. Gyselinck and F. Robert. Frequency- and time-domain homogenization of windings in two-dimensional finite-element models. In *Power Electronics and Applications, 2005 European Conference on*, pages 10 pp. –P.10, 0-0 2005.
- [62] K. Hatanaka, F. Sato, H. Matsuki, S. Kikuchi, J. Murakami, M. Kawase, and T. Satoh. Power transmission of a desk with a cord-free power supply. *Magnetics, IEEE Transactions on*, 38(5):3329 – 3331, sep. 2002.
- [63] T. J. Higgins. Formulas for the geometric mean distances of rectangular areas and of line segments. *Journal of Applied Physics*, 14:188–195, 1943.
- [64] J. H. Holland. *Adaptation in Natural and Artificial Systems*. University of Michigan Press, 1975.
- [65] S. R. H. Hoole. *Computer-Aided Analysis and Design of Electromagnetic Devices*. Elsevier, New York, 1989.
- [66] A. Hu, W. Ma, and Z. Zhao. New numerical methods of computing internal inductance of conductors of rectangular cross section. In *Electromagnetic Compatibility and 19th International Zurich Symposium on Electromagnetic Compatibility, 2008. APEMC 2008. Asia-Pacific Symposium on*, pages 674 –677, may 2008.
- [67] S. Hui and W. Ho. A new generation of universal contactless battery charging platform for portable consumer electronic equipment. *Power Electronics, IEEE Transactions on*, 20(3):620–627, May 2005.
- [68] W. Hurley and M. Duffy. Calculation of self and mutual impedances in planar magnetic structures. *Magnetics, IEEE Transactions on*, 31(4):2416–2422, Jul 1995.
- [69] W. Hurley and M. Duffy. Calculation of self- and mutual impedances in planar sandwich inductors. *Magnetics, IEEE Transactions on*, 33(3):2282–2290, May 1997.
- [70] O. A. Jadaan, L. Rajamani, and C. Rao. Improved selection operator for ga. *Journal of Theoretical and Applied Information Technology*, 2005-2008.
- [71] H. E. S. Jr., J. C. Schuder, and J. W. Mackenzie. Energy transport through tissue by inductive coupling. *The American Journal of Surgery*, 114(1):87 – 94, 1967.
- [72] P. Kaelo and M. Ali. Integrated crossover rules in real coded genetic algorithms. *European Journal of Operational Research*, 176(1):60 – 76, 2007.

Bibliography

- [73] M. Klauz and D. Dorrell. Eddy current effects in a switched reluctance motor. *Magnetics, IEEE Transactions on*, 42(10):3437–3439, oct. 2006.
- [74] J. Knowles and D. Corne. The pareto archived evolution strategy: a new baseline algorithm for pareto multiobjective optimisation. In *Evolutionary Computation, 1999. CEC 99. Proceedings of the 1999 Congress on*, volume 1, pages 3 vol. (xxxvii+2348), 1999.
- [75] R. Laouamer, J. P. Ferrieux, H. Benqassmi, O. Normand, and N. Buchheit. A comparison of resonant converter topologies with three and four energy storage elements for automatic inductive charging application. *Electric Machines and Power Systems*, 27:221–236, March 1999.
- [76] J. Li, Y. Shi, Z. Niu, and D. Zhou. Modeling, simulation and optimization design of pcb planar transformer. In *Electrical Machines and Systems, 2005. ICEMS 2005. Proceedings of the Eighth International Conference on*, volume 3, pages 1736–1739 Vol. 3, sept. 2005.
- [77] X. Liu and S. Hui. Optimal design of a hybrid winding structure for planar contactless battery charging platform. *Power Electronics, IEEE Transactions on*, 23(1):455–463, Jan. 2008.
- [78] X. Liu and S. Hui. Simulation study and experimental verification of a universal contactless battery charging platform with localized charging features. *Power Electronics, IEEE Transactions on*, 22(6):2202–2210, Nov. 2007.
- [79] S. Llorente, F. Monterde, J. Burdio, and J. Acero. A comparative study of resonant inverter topologies used in induction cookers. In *Applied Power Electronics Conference and Exposition, 2002. APEC 2002. Seventeenth Annual IEEE*, volume 2, pages 1168–1174 vol.2, 2002.
- [80] E. Lou, N. Durdle, V. Raso, and D. Hill. Measurement of the magnetic field in the near-field region and self-inductance in free space due to a multturn square-loop. *Science, Measurement and Technology, IEE Proceedings -*, 144(6):252–256, nov 1997.
- [81] Y. Louvrier. *Etude et optimisation multicritère d'un convertisseur DC-DC à canaux multiples entrelacés*. PhD thesis, Ecole Polytechnique Federale de Lausanne (EPFL), 2010.
- [82] N. Macabrey. *Alimentation et guidage linéaire sans contact*. PhD thesis, Ecole Polytechnique Federale de Lausanne (EPFL), 1998.
- [83] V. Marian, C. Vollaie, B. Allard, and J. Verdier. Low power rectenna topologies for medium range wireless energy transfer. In *Power Electronics and Applications (EPE 2011), Proceedings of the 2011-14th European Conference on*, pages 1–10, 30 2011-sept. 1 2011.
- [84] J. Maridor. *Design, optimization and sensorless control of a linear actuator*. PhD thesis, Ecole Polytechnique Federale de Lausanne (EPFL), 2011.
- [85] J. Maridor, M. Markovic, Y. Perriard, and D. Ladas. Optimization design of a linear actuator using a genetic algorithm. In *Electric Machines and Drives Conference, 2009. IEMDC '09. IEEE International*, pages 1776–1781, may 2009.

- [86] H. Matsuki, M. Shiiki, K. Murakami, K. Nadehara, and T. Yamamoto. Flexible transcutaneous transformer for artificial heart system. *Magnetics, IEEE Transactions on*, 26(5):1548–1550, sep 1990.
- [87] H. Matsuki, M. Shiiki, K. Murakami, and T. Yamamoto. Investigation of coil geometry for transcutaneous energy transmission for artificial heart. *Magnetics, IEEE Transactions on*, 28(5):2406–2408, Sep 1992.
- [88] P. Meyer, P. Germano, M. Markovic, and Y. Perriard. Design of a contactless energy transfer system for desktop peripherals. In *Energy Conversion Congress and Exposition (ECCE), 2010 IEEE*, pages 2253–2258, 2010.
- [89] P. Meyer, P. Germano, M. Markovic, and Y. Perriard. Design of a contactless energy-transfer system for desktop peripherals. *Industry Applications, IEEE Transactions on*, 47(4):1643–1651, july-aug. 2011.
- [90] P. Meyer, P. Germano, and Y. Perriard. Modelling and design of a contactless energy transfer system for a notebook battery charger. In *Electrical Machines (ICEM), 2010 XIX International Conference on*, pages 1–6, 2010.
- [91] P. Meyer, P. Germano, and Y. Perriard. Contactless energy transfer system for computer peripherals. In *Power Electronics and Applications (EPE 2011), Proceedings of the 2011-14th European Conference on*, pages 1–10, 30 2011-sept. 1 2011.
- [92] Z. Michalewicz. A survey of constraint handling techniques in evolutionary computation methods. In *Proceedings of the 4th Annual Conference on Evolutionary Programming*, pages 135–155, 1995.
- [93] W. Mingli and F. Yu. Numerical calculations of internal impedance of solid and tubular cylindrical conductors under large parameters. *Generation, Transmission and Distribution, IEE Proceedings-*, 151(1):67–72, 2004.
- [94] S. Mohan, M. del Mar Hershenson, S. Boyd, and T. Lee. Simple accurate expressions for planar spiral inductances. *Solid-State Circuits, IEEE Journal of*, 34(10):1419–1424, Oct 1999.
- [95] P. C. Pendharkar and J. A. Rodger. An empirical study of impact of crossover operators on the performance of non-binary genetic algorithm based neural approaches for classification. *Comput. Oper. Res.*, 31:481–498, April 2004.
- [96] A. Petrowski. A clearing procedure as a niching method for genetic algorithms. In *Evolutionary Computation, 1996., Proceedings of IEEE International Conference on*, pages 798–803, may 1996.
- [97] B. D. Popovic. *Introductory Engineering Electromagnetics*. Addison-Wesley, 1971.
- [98] D. Porto. *Design Methodology and Numerical Optimization of Ultrasonic Transducers for Spinal Surgery*. PhD thesis, Ecole Polytechnique Federale de Lausanne (EPFL), 2009.
- [99] D. Porto, A. Bourquard, and Y. Perriard. Genetic algorithm optimization for a surgical ultrasonic transducer. In *Ultrasonics Symposium, 2008. IUS 2008. IEEE*, pages 1457–1460, nov. 2008.

Bibliography

- [100] P. Ragot. *Modélisation analytique multiphysique pour la conception optimale de moteurs synchrones à aimants permanents*. PhD thesis, Ecole Polytechnique Federale de Lausanne (EPFL), 2008.
- [101] E. A. Rose, A. C. Gelijns, A. J. Moskowitz, D. F. Heitjan, L. W. Stevenson, W. Dembitsky, J. W. Long, D. D. Ascheim, A. R. Tierney, R. G. Levitan, J. T. Watson, N. S. Ronan, P. A. Shapiro, R. M. Lazar, L. W. Miller, L. Gupta, O. H. Frazier, P. Desvigne-Nickens, M. C. Oz, V. L. Poirier, and P. Meier. Long-term use of a left ventricular assist device for end-stage heart failure. *New England Journal of Medicine*, 345(20):1435–1443, 2001.
- [102] B. Sareni and L. Krahenbuhl. Fitness sharing and niching methods revisited. *Evolutionary Computation, IEEE Transactions on*, 2(3):97–106, Sept. 1998.
- [103] F. Sato, H. Matsuki, S. Kikuchi, T. Seto, T. Satoh, H. Osada, and K. Seki. A new meander type contactless power transmission system-active excitation with a characteristics of coil shape. *Magnetics, IEEE Transactions on*, 34(4):2069–2071, Jul 1998.
- [104] F. Sato, J. Murakami, H. Matsuki, S. Kikuchi, K. Harakawa, and T. Satoh. Stable energy transmission to moving loads utilizing new clps. *Magnetics, IEEE Transactions on*, 32(5):5034–5036, Sep 1996.
- [105] T. Sato, F. Sato, and H. Matsuki. New functional electrical system using magnetic coils for power transmission and control signal detection. *Magnetics, IEEE Transactions on*, 37(4):2925–2928, jul 2001.
- [106] T. Schaffter. Optimisation d'un moteur synchrone à l'aide des algorithmes génétiques. Semester project, Ecole Polytechnique Federale de Lausanne (EPFL), 2007.
- [107] H. Shiroyama, H. Matsuo, and Y. Ishizuka. Quasi-resonant converter with divided resonant capacitor on primary and secondary side. In *Telecommunications Energy Conference, 2009. INTELEC 2009. 31st International*, pages 1–6, oct. 2009.
- [108] C. Silva and E. B. Jr. Genetic algorithm development for multi-objective optimization of batch free-radical polymerization reactors. *Computers & Chemical Engineering*, 27(8 - 9):1329–1344, 2003.
- [109] P. Silvester. *Modern Electromagnetic Fields*. Prentice-Hall, Inc., Englewood Cliffs, N.J., 1968.
- [110] A. Sinclair and J. Ferreira. Analysis and design of transmission-line structures by means of the geometric mean distance. In *AFRICON, 1996., IEEE AFRICON 4th*, volume 2, pages 1062–1065 vol.2, Sept. 1996.
- [111] A. Sokolov and D. Whitley. Unbiased tournament selection. In *Proceedings of the 2005 conference on Genetic and evolutionary computation, GECCO '05*, pages 1131–1138, New York, NY, USA, 2005. ACM.
- [112] C. Sonntag. *Contactless Energy Transfer Platform using Air-cored Planar Inductors*. PhD thesis, Eindhoven University of Technology, 2010.

- [113] C. Sonntag, E. Lomonova, and J. Duarte. Implementation of the neumann formula for calculating the mutual inductance between planar pcb inductors. In *Electrical Machines, 2008. ICEM 2008. 18th International Conference on*, pages 1–6, 2008.
- [114] C. Sonntag, E. Lomonova, and J. Duarte. Variable-phase contactless energy transfer desktop part i: Design. pages 4460–4465, oct. 2008.
- [115] C. Sonntag, E. Lomonova, J. Duarte, and A. Vandenput. Specialized receivers for three-phase contactless energy transfer desktop applications. *Power Electronics and Applications, 2007 European Conference on*, pages 1–11, 2-5 Sept. 2007.
- [116] N. Srinivas and K. Deb. Multiobjective optimization using nondominated sorting in genetic algorithms. *Evolutionary Computation*, 2:221–248, 1994.
- [117] I. Stefanini. *Méthodologie de conception et optimisation d'actionneurs intégrés sans fer*. PhD thesis, Ecole Polytechnique Federale de Lausanne (EPFL), 2006.
- [118] I. Stefanini, M. Markovic, and Y. Perriard. 3d inductance and impedance determination taking skin effect into account. In *Electric Machines and Drives, 2005 IEEE International Conference on*, pages 74–79, May 2005.
- [119] R. Steigerwald. A comparison of half-bridge resonant converter topologies. *Power Electronics, IEEE Transactions on*, 3(2):174–182, Apr. 1988.
- [120] O. Stielau and G. Covic. Design of loosely coupled inductive power transfer systems. *Power System Technology, 2000. Proceedings. PowerCon 2000. International Conference on*, 1:85–90 vol.1, 2000.
- [121] R. Suresh and K. Mohanasundaram. Pareto archived simulated annealing for permutation flow shop scheduling with multiple objectives. In *Cybernetics and Intelligent Systems, 2004 IEEE Conference on*, volume 2, pages 712–717, 2004.
- [122] M. Tanaka, H. Watanabe, Y. Furukawa, and T. Tanino. Ga-based decision support system for multicriteria optimization. In *Systems, Man and Cybernetics, 1995. Intelligent Systems for the 21st Century., IEEE International Conference on*, volume 2, pages 1556–1561 vol.2, oct 1995.
- [123] S. Tang, S. Hui, and H.-H. Chung. Characterization of coreless printed circuit board (pcb) transformers. *Power Electronics, IEEE Transactions on*, 15(6):1275–1282, Nov 2000.
- [124] D. Thrimawithana and U. Madawala. A three-phase bi-directional ipt system for contactless charging of electric vehicles. In *Industrial Electronics (ISIE), 2011 IEEE International Symposium on*, pages 1957–1962, june 2011.
- [125] C.-S. Wang, G. Covic, and O. Stielau. Power transfer capability and bifurcation phenomena of loosely coupled inductive power transfer systems. *Industrial Electronics, IEEE Transactions on*, 51(1):148–157, Feb. 2004.
- [126] C.-S. Wang, G. Covic, and O. Stielau. Investigating an lcl load resonant inverter for inductive power transfer applications. *Power Electronics, IEEE Transactions on*, 19(4):995–1002, July 2004.

Bibliography

- [127] C.-S. Wang, O. Stielau, and G. Covic. Design considerations for a contactless electric vehicle battery charger. *Industrial Electronics, IEEE Transactions on*, 52(5):1308–1314, Oct. 2005.
- [128] R.-L. Wang and K. Okazaki. An improved genetic algorithm with conditional genetic operators and its application to set-covering problem. *Soft Computing - A Fusion of Foundations, Methodologies and Applications*, 11:687–694, 2007. 10.1007/s00500-006-0131-1.
- [129] H. Wu, A. Hu, P. Si, D. Budgett, C. Tung, and S. Malpas. A push-pull resonant converter with dual coils for transcutaneous energy transfer systems. In *Industrial Electronics and Applications, 2009. ICIEA 2009. 4th IEEE Conference on*, pages 1051–1056, may 2009.
- [130] W. Zhong, X. Liu, and S. Hui. Analysis on a single-layer winding array structure for contactless battery charging systems with free-positioning and localized charging features. In *Energy Conversion Congress and Exposition (ECCE), 2010 IEEE*, pages 658–665, 2010.
- [131] W. Zhong, X. Liu, and S. Hui. A novel single-layer winding array and receiver coil structure for contactless battery charging systems with free-positioning and localized charging features. *Industrial Electronics, IEEE Transactions on*, 58(9):4136–4144, sept. 2011.
- [132] E. Zitzler, K. Deb, and L. Thiele. Comparison of Multiobjective Evolutionary Algorithms: Empirical Results. *Evolutionary Computation*, 8:173–195, 2000.
- [133] E. Zitzler and L. Thiele. Multiobjective evolutionary algorithms: a comparative case study and the strength pareto approach. *Evolutionary Computation, IEEE Transactions on*, 3(4):257–271, nov 1999.

Curriculum Vitae

Pascal MEYER
Born July 10, 1984
Swiss Citizen
pascal.meyer@a3.epfl.ch

Studies and professional experience

- 2008-to date Teaching assistant and Ph.D. student at the Integrated Actuators Laboratory (LAI), Ecole Polytechnique Fédérale de Lausanne (EPFL), Switzerland.
- 2003-2008 Master of Science in Microengineering, Ecole Polytechnique Fédérale de Lausanne (EPFL), Switzerland.
- 1998-2003 High School Diploma in Latin/Sciences, Saint-Maurice, Switzerland

Publications

P. Meyer, P. Germano, and Y. Perriard. Modelling and design of a contactless energy transfer system for a notebook battery charger. In *Electrical Machines (ICEM), 2010 XIX International Conference on*, pages 1-6, 2010.

P. Meyer, P. Germano, M. Markovic, and Y. Perriard. Design of a contactless energy transfer system for desktop peripherals. In *Energy Conversion Congress and Exposition (ECCE), 2010 IEEE*, pages 2253-2258, 2010.

P. Meyer, P. Germano, M. Markovic, and Y. Perriard. Design of a contactless energy transfer system for desktop peripherals. *Industry Applications, IEEE Transactions on*, 47(4):1643-1651, july-aug. 2011.

P. Meyer and Y. Perriard. Skin and proximity effects for coreless transformers. In *Electrical Machines and Systems (ICEMS), 2011 International Conference on*, pages 1-5, aug. 2011.

P. Meyer, P. Germano, and Y. Perriard. Contactless energy transfer system for computer peripherals. In *Power Electronics and Applications (EPE 2011), Proceedings of the 2011- 14th European Conference on*, pages 1-10, 30 2011-sept. 1 2011.

P. Meyer, P. Germano, and Y. Perriard. FEM modeling of skin and proximity effects for coreless transformers. To appear in *Electrical Machines and Systems (ICEMS), 2012 International Conference on*.